



**HAL**  
open science

# Prospective crystal-chemistry : relaxors, ferroics and low temperature SPS

Thomas Hérisson de Beauvoir

► **To cite this version:**

Thomas Hérisson de Beauvoir. Prospective crystal-chemistry : relaxors, ferroics and low temperature SPS. Material chemistry. Université de Bordeaux, 2017. English. NNT : 2017BORD0678 . tel-02275778

**HAL Id: tel-02275778**

**<https://theses.hal.science/tel-02275778>**

Submitted on 2 Sep 2019

**HAL** is a multi-disciplinary open access archive for the deposit and dissemination of scientific research documents, whether they are published or not. The documents may come from teaching and research institutions in France or abroad, or from public or private research centers.

L'archive ouverte pluridisciplinaire **HAL**, est destinée au dépôt et à la diffusion de documents scientifiques de niveau recherche, publiés ou non, émanant des établissements d'enseignement et de recherche français ou étrangers, des laboratoires publics ou privés.

THÈSE PRÉSENTÉE  
POUR OBTENIR LE GRADE DE  
**DOCTEUR DE**  
**L'UNIVERSITÉ DE BORDEAUX**

ÉCOLE DOCTORALE DES SCIENCES CHIMIQUES  
SPÉCIALITÉ : Chimie et Physico-Chimie des Matériaux

Par **Thomas HERISSON DE BEAUVOIR**

---

**Prospective crystal-chemistry : relaxors, ferroics and low  
temperature SPS**

---

Sous la direction de : Michaël JOSSE

Soutenance prévue le 26 Septembre 2017

Membres du Jury :

|                                |   |            |
|--------------------------------|---|------------|
| <b>Mr RANDALL Clive</b>        | Professeur, MRI, State College            | Rapporteur |
| <b>Mr ESTOURNES Claude</b>     | Directeur de Recherche, CIRIMAT, Toulouse | Rapporteur |
| <b>Mr ALARY Jean-André</b>     | R&D manager, IMERYS                       | Examineur  |
| <b>Mme ELISSALDE Catherine</b> | Directrice de Recherche, ICMCB            | Examineur  |
| <b>Mr MAGLIONE Mario</b>       | Directeur de Recherche, ICMCB             | Examineur  |
| <b>Mr JOSSE Michaël</b>        | Maitre de conférences, ICMCB              | Directeur  |



# Remerciements

Mes premiers remerciements vont naturellement à Mario Maglione, directeur de l'Institut de Chimie de la Matière Condensée de Bordeaux, pour m'avoir accueilli au sein du laboratoire. Je le remercie aussi pour les discussions qui m'ont été utiles à la réalisation de ce travail.

Je tiens ensuite à remercier ceux qui ont porté un regard très attentif sur ce manuscrit afin d'en juger la pertinence, Claude Estournes et Clive Randall qui ont accepté d'être rapporteur de ce travail. Je remercie également les autres membres du jury, Jean André Alary, Mario Maglione et Catherine Elissalde pour avoir accepté d'assister à la soutenance et participer à de longues discussions.

Je tiens à remercier profondément Michael Josse qui m'a guidé tout au long de ces trois (finalement très courtes) années. Sa passion et son optimisme infaillible m'ont porté et inspiré à travers les incertitudes autour de cet indomptable et capricieux SPS qui aura fini par nous montrer des facettes plus joyeuses. Merci pour les moments de café/science qui représentent sûrement le moyen le plus efficace et le plus agréable (les chouffes/sciences sont quand même en rude compétition) pour discuter de manière non sérieuse de choses très sérieuses. Merci aussi à Graziella et Cathy, sans qui je n'aurais pas eu le courage de quitter mon poste de lieutenant chez les pompiers pour m'engager dans une aventure sans vision à long terme et sans certitude, je sais que ça a pu leur causer des inquiétudes mais je les rassure, ça a toujours été sans regret tout au long de ces trois ans, merci.

Merci à tous ceux qui font que le travail puisse se dérouler de bonne manière et que le labo tourne rond, notamment un grand merci à Carole, Sandrine, Éric, Sébastien, Lionel, Dominique, U-Chan, Rodolphe, Laetitia.

J'en viens naturellement à remercier maintenant les personnes sans qui ce travail n'aurait sûrement pas été aussi complet et grâce à qui la lecture de ce manuscrit devient interminable, à tel point que j'en viens à douter de ma capacité à le relire moi-même, et je tiens à m'en excuser pour les prochains étudiants qui devront reprendre la suite de ces travaux. Je veux bien sûr parler de tous les stagiaires qui sont passés dans le groupe et ont travaillé avec moi, mais aussi et surtout ont participé à la vie du groupe et le maintien d'une ambiance à laquelle j'ai

rapidement pris goût et qui j'espère perdurera encore longtemps. Merci à Tom et Anna qui ont été les premiers stagiaires que j'ai encadré pendant ma première année de thèse et qui ont dû faire face, l'un comme l'autre, à de nombreux imprévus, et à de nombreux doutes sur la faisabilité des manip avec des moyens rudimentaires, parfois même un peu archaïques. Merci à Vincent qui a suivi au cours de ma deuxième année, une fois la machine mise en route, et qui a travaillé sur un matériau pendant deux mois sans savoir ce qu'il était, mais tout en étant sûr qu'il n'était pas celui que l'on visait... pour finalement se révéler être un des résultats les plus intéressants de cette thèse. Merci à Michael, ce colosse Gallois dont la bonne humeur à toute épreuve a été contagieuse. Finalement en dernière année de thèse est arrivé Bastien, toujours curieux et intéressé, qui a lui aussi participé à rendre les moments passés au labo agréables, et qui a encore une fois beaucoup apporté au travers d'un stage au cours duquel ma disponibilité commençait à faire parfois défaut, merci encore.

Vient finalement le phénomène Iñaki, ce bonhomme au cœur immense et à la timidité touchante, dont la contribution au présent travail, bien qu'évidente, pertinente et importante, reste incomparable avec la rencontre humaine et le partage. Anaiak gara !

J'en viens maintenant à mes compagnons de groupe, avec qui on a partagé beaucoup, beaucoup de café et bien trop de chouffe. D'abord, mes deux rencontres au cours de mes premiers mois au labo, un professeur breton qui m'a transmis beaucoup plus que je ne saurais m'en souvenir. Je ne saurais le remercier à la hauteur de son implication. Ensuite, David, mon codétenu avec qui j'ai dû apprendre à vivre, mais surtout ensuite dont j'ai dû apprendre à me passer, ce qui n'a jamais vraiment été achevé. Les mots ne suffiront pas à dire combien je lui dois, notamment l'honneur de me faire parrain de son fils. J'ai ensuite eu la chance de partager mon bureau avec deux physiciens, Sergey, un Russe au service de la couronne Belge, ainsi que Christopher, Mexicain infiltré en Allemagne, qui m'auront montré une humanité incroyable que je garde comme exemples. Durant une courte période j'ai dû évacuer mon bureau et je me suis invité dans le bureau de Lucile, que j'ai bien pris soin de détourner de sa rédaction dans les critiques pour elle, je ne sais pas si je dois te remercier ou m'excuser, probablement les deux. Vient le tour de Clément, avec qui j'ai passé un temps interminable à refaire le monde, mais comme toujours, il reste encore beaucoup à faire, mais nous continuons à nous astreindre à une rigueur exemplaire. Le flacon a changé mais la passion reste la même.

Merci enfin à mon collègue et ami Arnaud, avec qui j'ai passé des heures, des jours à échanger et partager, avec qui j'ai eu la chance de voyager et que je devrais rapidement retrouver, on a fait notre route ensemble tout au long de ces trois années et je sais qu'il nous reste encore un bon bout de chemin à faire ensemble.

Merci enfin à tous mes amis, mes proches, Mathieu, Bijou, Vincent, David, Diane, Pinou, Clio, Simon, Claire, ainsi qu'à mes collocs avec qui les journées se terminaient souvent par un bon moment de détente autour d'une bière et d'une partie de cartes, Clio, Timothée, Jakub, et Tahdhg. Merci ensuite à ma famille qui m'a soutenu tout au long de ce parcours auquel personne n'était vraiment familier, merci à mon frère sans qui je ne serais pas ce que je suis aujourd'hui. Merci enfin à Marie dont j'ai croisé la route au cours de cette aventure et qui m'a énormément aidé et soutenu, notamment tout au long de la rédaction et des moments difficiles.

Ces remerciements ont été écrits comme le reste de la thèse, dans une précipitation qui ne convient pas à l'importance qu'ils auraient mérité. Les années de thèse, au-delà de la production scientifique qui seule laisse des traces écrites, sont avant tout trois années (parfois quatre pour les gourmands) d'aventure et de découverte humaines, qui à seules suffiraient à en justifier l'intérêt. Ceci m'avait été résumé dès ma première semaine par Michaël en une simple phrase : *« l'important, c'est de se faire plaisir ».*

# Contents

|  |           |
|--|-----------|
| GENERAL INTRODUCTION .....   | 10        |
| <u>PART I: ON THE RELAXOR TO FERROELECTRIC CROSSOVER IN <math>BA_2NDfENb_4O_{15}</math>-BASED TTBS</u>                 |           |
| <b>CHAPTER 1: CONCERNING FERROELECTRICITY AND TTb MATERIALS.....</b>   | <b>18</b> |
| <b>1.1. DIELECTRIC PROPERTIES OF CERAMICS.....</b>   | <b>18</b> |
| 1.1.1 DIELECTRIC PROPERTIES AND CRYSTAL SYMMETRY.....  | 18        |
| 1.1.2 DIELECTRIC POLARIZATION.....   | 20        |
| 1.1.2.1 Different polarization nature .....  | 20        |
| 1.1.2.2 Case of ferroelectric ceramics .....   | 22        |
| 1.1.2.3 Piezoelectricity.....  | 24        |
| 1.1.2.4 Pyroelectricity.....   | 25        |
| 1.1.3 FERROELECTRIC PHASE TRANSITIONS.....   | 27        |
| 1.1.3.1 Classical ferroelectrics .....   | 27        |
| 1.1.3.1 Antiferroelectrics and ferrielectrics.....   | 31        |
| 1.1.3.2 Relaxor ferroelectrics .....   | 32        |
| 1.1.3.3 Relaxor to ferroelectric crossover .....   | 36        |
| <b>1.2. TETRAGONAL TUNGSTEN BRONZE STRUCTURE .....</b>   | <b>37</b> |
| 1.2.1 TTb CRYSTAL CHEMISTRY.....   | 38        |
| 1.2.2 DIELECTRIC PROPERTIES .....  | 40        |
| 1.2.3 PARTICULAR CASE OF $BA_2LNfENb_4O_{15}$ ( $LN$ =RARE EARTH) .....  | 42        |
| 1.2.4 MODULATED STRUCTURE OF TTb.....  | 46        |
| <b>1.3. CONCLUSION ON CHAPTER .....</b>  | <b>50</b> |
| <b>CHAPTER 2: STUDY OF STRUCTURE AND DIELECTRIC PROPERTIES OF LI SUBSTITUTED <math>BA_2NDfENb_4O_{15}</math> .....</b> | <b>52</b> |
| <b>2.1. SYNTHESIS OF SOLID SOLUTIONS.....</b>  | <b>52</b> |
| 2.1.1 CHOICE OF SOLID SOLUTIONS .....  | 52        |
| 2.1.2 SOLID STATE SYNTHESIS .....  | 53        |
| 2.1.2.1 Powder mixing .....  | 54        |
| 2.1.2.2 Pellet firing .....  | 54        |
| 2.1.2.3 Pellet sintering.....  | 55        |
| <b>2.2. POWDERS AND PELLETS CHARACTERIZATIONS.....</b>   | <b>55</b> |
| 2.2.1 STRUCTURAL CHARACTERIZATION OF FIRED POWDERS.....  | 55        |

|   |  |            |
|---|--|------------|
| 2.2.2   | <i>PELLET MICROSTRUCTURE</i> .....   | 57         |
| 2.2.3   | <i>DIELECTRIC MEASUREMENTS</i> .....   | 59         |
| 2.2.4   | <i>STRUCTURAL CHARACTERIZATIONS</i> .....  | 67         |
| <b>2.3.</b>   | <b>CONCLUSION</b> .....  | <b>76</b>  |
| <i>CHAPTER 3: INFLUENCE OF ELABORATION CONDITIONS ON <math>BA_2NdFeNb_4O_{15}</math> DIELECTRIC PROPERTIES</i>            |  |            |
|   | .....  | 77         |
| <b>3.1.</b>   | <b>MULTIPLE DIELECTRIC BEHAVIORS FOR A SINGLE PHASE</b> .....  | <b>77</b>  |
| <b>3.2.</b>   | <b>SYNTHESIS PARAMETERS, POST TREATMENTS OF CERAMICS</b> .....   | <b>79</b>  |
| 3.2.1   | <i>TWO STEP-FIRING</i> .....   | 79         |
| 3.2.2   | <i>SINTERING TIME AND POST-SINTERING HEAT TREATMENT</i> .....  | 85         |
| 3.2.3   | <i>POST ANNEALING TREATMENT</i> .....  | 88         |
| 3.2.4   | <i>PERSISTENCE OF PEROVSKITE PHASE</i> .....   | 89         |
| 3.2.5   | <i>PRECURSOR MILLING</i> .....   | 92         |
| <b>3.3.</b>   | <b>STRUCTURAL COMPARISON OF SAMPLES WITH DIFFERENT DIELECTRIC PROPERTIES</b> .....                     | <b>95</b>  |
| 3.3.1   | <i>RIETVELD XRD REFINEMENT</i> .....   | 95         |
| 3.3.2   | <i>ELECTRON DIFFRACTION</i> .....  | 98         |
| <br><i><u>PART 2: FERROIC, MULTIFERROIC AND MAGNETOELECTRIC PROSPECTIVE SEARCH USING SPARK PLASMA SINTERING (SPS)</u></i> |  |            |
| <b>CHAPTER 1: A STATE OF THE ART, FROM MULTIFERROIC AND MAGNETOELECTRIC MATERIALS TO LOW TEMPERATURE SINTERING</b> .....  |  |            |
|   |  | <b>116</b> |
| <b>1.1.</b>   | <b>DEFINITION, CLASSIFICATION OF (MULTI)FERROIC AND MAGNETOELECTRIC MATERIALS</b> .....                | <b>116</b> |
| 1.1.1   | <i>DEFINITION</i> .....  | 116        |
| 1.1.2   | <i>CLASSIFICATION OF MULTIFERROICS</i> .....   | 120        |
| 1.1.2.1   | <i>Type 1 multiferroics</i> .....  | 121        |
| 1.1.2.2   | <i>Type 2 multiferroic</i> .....   | 124        |
| 1.1.3   | <i>COMPOSITE MULTIFERROICS</i> .....   | 129        |
| 1.1.4   | <i>SINTERING, AN OPPORTUNITY FOR THE INVESTIGATION OF DIELECTRIC PROPERTIES THROUGH CERAMICS</i> ..... | 131        |

|             |  |                 |
|-------------|--|-----------------|
| <b>1.2.</b> | <b>SINTERING TECHNIQUES AND HOW TO REDUCE THE SINTERING TEMPERATURES</b>                 | <b>133</b>      |
| 1.2.1       | DEFINITION .....   | 134             |
| 1.2.2       | SINTERING TECHNIQUES OF CERAMICS.....  | 136             |
| 1.2.2.1     | Solid state sintering .....  | 136             |
| 1.2.2.2     | Pressure assisted sintering .....  | 142             |
| 1.2.2.3     | Liquid phase sintering.....  | 148             |
| 1.2.3       | CONCLUSION ON SINTERING.....   | 152             |
| <b>1.3.</b> | <b>EXPERIMENTAL APPROACH .....</b>   | <b>152</b>      |
|             | <b>CHAPTER 2: SPARK PLASMA SINTERING OF FRAGILE FERROIC MATERIALS AT LOW TEMPERATURE</b> | <b>.....154</b> |
| <b>2.1.</b> | <b>CANDIDATE MATERIALS SELECTION .....</b>   | <b>155</b>      |
| <b>2.2.</b> | <b>EXPERIMENTAL SPARK PLASMA SINTERING SETUP.....</b>                                    | <b>157</b>      |
| <b>2.3.</b> | <b>NH<sub>4</sub>FEP<sub>2</sub>O<sub>7</sub>.....</b>                                   | <b>159</b>      |
| 2.3.1       | STRUCTURE .....  | 160             |
| 2.3.2       | SYNTHESIS .....  | 160             |
| 2.3.3       | POWDER CHARACTERIZATION .....  | 161             |
| 2.3.4       | SINTERING .....  | 163             |
| 2.3.4.1     | Sintering conditions and pellet characterization .....                                   | 163             |
| 2.3.4.2     | Phase stabilization in SPS environment.....  | 166             |
| 2.3.5       | PHYSICAL PROPERTIES.....   | 167             |
| 2.3.5.1     | Magnetic measurements.....   | 167             |
| 2.3.5.2     | Dielectric measurements.....   | 168             |
| 2.3.6       | CONCLUSION ON NH <sub>4</sub> FEP <sub>2</sub> O <sub>7</sub> .....                      | 169             |
| <b>2.4.</b> | <b>A<sub>2</sub>CU(CO<sub>3</sub>)<sub>2</sub> (A = K, NA) .....</b>                     | <b>170</b>      |
| 2.4.1       | STRUCTURE AND PROPERTIES .....   | 170             |
| 2.4.1.1     | K <sub>2</sub> Cu(CO <sub>3</sub> ) <sub>2</sub> .....                                   | 170             |
| 2.4.1.2     | Na <sub>2</sub> Cu(CO <sub>3</sub> ) <sub>2</sub> .....                                  | 172             |
| 2.4.2       | SYNTHESIS .....  | 172             |
| 2.4.2.1     | K <sub>2</sub> Cu(CO <sub>3</sub> ) <sub>2</sub> .....                                   | 172             |
| 2.4.2.2     | Na <sub>2</sub> Cu(CO <sub>3</sub> ) <sub>2</sub> ·3H <sub>2</sub> O.....                | 174             |
| 2.4.3       | POWDER CHARACTERIZATION .....  | 178             |
| 2.4.3.1     | Structural characterization (XRD).....   | 178             |
| 2.4.3.2     | Thermal analysis (TGA).....  | 179             |

|             |  |            |
|-------------|--|------------|
| 2.4.3.3     | <i>Magnetic measurement (SQUID)</i> .....  | 180        |
| 2.4.4       | <i>SINTERING</i> .....   | 180        |
| 2.4.4.1     | <i>Sintering conditions and pellet characterization</i> .....  | 181        |
| 2.4.4.2     | <i>In-situ dehydration of <math>\text{Na}_2\text{Cu}(\text{CO}_3)_2 \cdot 3\text{H}_2\text{O}</math> into <math>\text{Na}_2\text{Cu}(\text{CO}_3)_2</math></i> ..... | 185        |
| 2.4.5       | <i>PHYSICAL PROPERTIES</i> .....   | 186        |
| 2.4.5.1     | <i>Magnetic measurements</i> .....   | 187        |
| 2.4.5.2     | <i>Dielectric and magnetocapacitance measurements</i> .....  | 187        |
| 2.4.6       | <i>CONCLUSION ON CARBONATES</i> .....  | 190        |
| <b>2.5.</b> | <b><i>MNSO<sub>4</sub></i></b> .....   | <b>191</b> |
| 2.5.1       | <i>POWDER CHARACTERIZATION</i> .....   | 192        |
| 2.5.2       | <i>SINTERING</i> .....   | 197        |
| 2.5.2.1     | <i>Effect of initial powder hydration level</i> .....  | 198        |
| 2.5.2.2     | <i>In-situ dehydration</i> .....   | 201        |
| 2.5.2.3     | <i>Effect of pressure, temperature and time</i> .....  | 206        |
| 2.5.2.4     | <i>Influence of <math>\alpha</math> to <math>\beta</math> transition</i> .....   | 209        |
| 2.5.3       | <i>PHYSICAL PROPERTIES</i> .....   | 214        |
| 2.5.3.1     | <i>Conclusion on <math>\text{MnSO}_4</math></i> .....  | 217        |
| <b>2.6.</b> | <b><i>COMPARISON OF SPARK PLASMA SINTERING AND SOLVOTHERMAL SINTERING OF <math>\text{MNSO}_4 \cdot \text{H}_2\text{O}</math></i></b> .....                           | <b>218</b> |
| 2.6.1       | <i>SPARK PLASMA SINTERING (SPS)</i> .....  | 218        |
| 2.6.2       | <i>SOLVOTHERMAL SINTERING OF <math>\text{MNSO}_4 \cdot \text{H}_2\text{O}</math></i> .....   | 223        |
| 2.6.3       | <i>DISCUSSION ON SINTERING OF <math>\text{MNSO}_4 \cdot \text{H}_2\text{O}</math></i> .....  | 228        |
| 2.6.4       | <i>PHYSICAL CHARACTERIZATION</i> .....   | 229        |
| 2.6.5       | <i>CONCLUSION ON <math>\text{MNSO}_4 \cdot \text{H}_2\text{O}</math></i> .....   | 230        |
| <b>2.7.</b> | <b><i>CHAPTER CONCLUSION</i></b> .....   | <b>231</b> |
|             | <i>CHAPTER 3: TOWARDS MOLECULAR CERAMICS</i> .....   | 234        |
| <b>3.1.</b> | <b><i>SYNTHESIS, SINTERING AND CHARACTERIZATION OF</i></b> .....   | <b>234</b> |
| <b>3.2.</b> | <b><i>PHYSICAL PROPERTIES</i></b> .....  | <b>240</b> |
| <b>3.3.</b> | <b><i>TOWARDS NEW MATERIALS</i></b> .....  | <b>241</b> |
|             | <i>PART CONCLUSION</i> .....   | 243        |
|             | <i>GENERAL CONCLUSION</i> .....  | 245        |
|             | <i>REFERENCES</i> .....  | 249        |

# General introduction

Dielectric or magnetic materials have a tremendous number of applications, from the massive use of capacitors in electronic devices of daily use (computer, cell phones...), to piezoelectric sensors, magnetic storage, sonars, medical imaging, non-linear optics or more generally communications... They are nowadays both important in everyday life and for specific high technology development. The necessity to develop smaller sizes and transportability, with the same level or even improved efficiency, is more than ever an important stake and requires advanced functional materials. Nowadays, the economic development is based on virtual economy and fast communication all around the world. However, technologies such as Big-Data storage necessitate tremendous storage capacities and very fast data transfer to be efficient. Realizing this passes through the development of real infrastructure and support that require advanced dielectric and magnetic materials. Among them are ferroics, multiferroics and magnetoelectrics, are highly touted candidates for the development of new type of memory cells, that of spintronics... Developing new materials requires the mobilization of multiple resources, skills and cultures, entailing interactions between chemistry, material science, physics and engineering which must be perfectly synchronized to be profitable. Beyond the search for such functional properties, other challenges have to be addressed for the development of future functional materials, such as:

- The use of non-critical constituents<sup>1</sup>
- The use of processing methods limiting their environmental footprints
- The development of materials and processes compatible with new generations of materials (functional polymers, molecular materials) and devices (organic, flexible, soluble electronics...)
- The development of materials favoring circular economy, through recyclability or at least by facilitating their retreatment

A way of creating breakthrough, thus, significantly improve any kind of domain, is to explore beyond usual limits of the (multi)disciplinary territory of this domain. This is the field of prospective research, which usually is a high-risk approach, since the exploration of unknown territories may take long time to achieve, and may even fail to deliver the expected results, as any research activity but with a larger probability. However, such approach may also reveal

unexpected great possibilities, and does not necessarily involves the exploration of virgin territories. Indeed, evolving context and unexpected discoveries can revive the potential of partially or even deeply (or thought so) explored territories, which may contain useful resources with respect to the aforementioned challenges.

In the present work, the central interest is concerned with ferroic materials<sup>2</sup>. These have the particularity of possessing a spontaneous polarization, magnetization or strain that can be reversed by the application of external field. Ferroic properties are the foundations of many applications and understanding their fundamental operation is a prior and essential step before any use can be made of them. The strong link between ferroic properties, crystal structure and chemical composition implies that diffraction studies and crystal-chemical approaches are particularly well-suited for the study of ferroic materials. Once the link has been established between crystal chemical aspects and properties, or while it is established, it is possible to design a material for a dedicated purpose. At this point, bridging the gap from chemistry to physics induces the development of material processing. The three of these aspects (crystal chemistry, materials processing and physical properties) represent the main pillars of the present study. As pointed out earlier, prospective research will be undertaken in this work, and, to mitigate their risks, two different research topics will be investigated, the study of relaxor to ferroelectric crossovers in Tetragonal Tungsten Bronze (TTB) niobates, and the development of low temperature Spark Plasma Sintering of fragile materials. The latter is an original and well-established topic, yet with (almost) unexplored facets, that bears limited risks, while the former is a high-risk, high reward and totally new direction, which may have breakthrough potential.

In a first part, the interest will be focused on understanding the crystal chemical background of ferroelectric materials crystallizing in tetragonal tungsten bronze structure<sup>3</sup>. These materials represent one of the most important class of ferroelectric materials<sup>4</sup>, but also possess non-linear optic<sup>5</sup> and ionic conduction<sup>6</sup> properties. The previous observations of aperiodic structural modulations in these materials have been recently linked to dielectric properties<sup>7</sup>. Moreover, the use of XRD technique was unable to solve the structure of these materials and the structure-property link remains unclear. The exploration of solid solution is a powerful tool to investigate structure-properties relationships. Thus, after a first chapter setting up the background associated to dielectric materials and more specifically TTBs, a second chapter will be

dedicated to the exploration of solid solutions and their characterization, to investigate the evolution of structural and dielectric properties in Li-substituted  $\text{Ba}_2\text{NdFeNb}_4\text{O}_{15}$ . Three different substitution schemes will be presented, which were designed to decipher the crystal chemical role of lithium, otherwise elusive in X-Ray diffraction studies. Upon discovery of unexpected relationships between processing conditions and dielectric properties, a third chapter will be specifically dedicated to their investigation, including a preliminary report of a crystallographic study by means of electron diffraction.

After a first part dedicated to the exploration of crystal chemistry of TTBs, a second part will be dedicated to the prospection for new ferroic, multiferroic or magnetoelectric fragile materials through the use of Spark Plasma Sintering (SPS) technique. Fragile materials here refers to materials displaying a limited thermal stability, which forbids their sintering by conventional means. The characterization of the dielectric properties of such materials, in prospective research, is hindered by their unavailability in ceramic form. Following seminal results acquired back in 2012, the present work aims at establishing a proof of concept concerning the sintering of fragile materials by low temperature SPS, to allow for the development of prospective research on these materials. A first chapter will provide a brief background concerning (multi)ferroics and magnetoelectrics, and give a rapid overview of the principles of sintering and the main processing methods. A second chapter will highlight the crystal chemical criteria that will be necessary to select interesting candidate materials, and present the experimental results associated with the densification of the four selected materials. A particular attention will be paid to the sintering of manganese sulfate, through which the sintering mechanisms involved in low temperature SPS will be investigated. In these works, SPS will be performed in unusual conditions while attempting to obtain dense measurable samples, for the subsequent investigation of their physical properties. A strong accent will be put on the behavior and stability of various materials during sintering with respect to various SPS parameters. In a third and last chapter, unexpected results issued from this exploratory study of low temperature SPS will be presented. These results may constitute a significant breakthrough in the field of ceramic materials and highlight the interest of exploratory studies, whatever their domain, and the fact that their outcome cannot be anticipated, as was stated almost a century ago by the inaugural director of the Bell Labs<sup>8</sup>:

*“No touchstone has been vouchsafed to us by which we can predetermine even approximately the usefulness of the scientific discoveries, which are to be made in the quest of a broader knowledge.”*

Finally, the main conclusions from this work will be summed up and perspectives will be drawn concerning the pursuit of both research directions, as well as their future impact.



**Part 1: On the relaxor to  
ferroelectric crossover in  
 $\text{Ba}_2\text{NdFeNb}_4\text{O}_{15}$ -based TTBs**

This first part is dedicated to the exploration of ferroelectric (FE) materials with particular dielectric behavior and interesting structures belonging to the tetragonal tungsten bronze (TTB) family<sup>3</sup>. This structure, derived from perovskite structure, is based on corner-sharing octahedra, and possesses a huge degree of compositional flexibility. The octahedral arrangement results in four different cationic sites. One is the center of octahedra, which often bears the FE properties of TTB materials<sup>9</sup>, while the others are situated in channels of different sizes. This variety of sizes is responsible for the large possibilities of chemical composition. In addition, TTB materials can also be stable with partial<sup>10</sup> or total<sup>11</sup> filling of these cationic channels, therefore increasing the compositions possibilities. The structural arrangement of these materials sometimes results in structural modulations that can be commensurate or incommensurate, which makes them interesting for structural exploration<sup>12-15</sup>.

More than their major chemical and structural flexibility, TTB materials are widely known and have been the object of many researches as FE materials<sup>7,11,16-22</sup>. They can present classical ferroelectric behavior<sup>21</sup>, relaxor behavior<sup>23</sup> or even both within a single composition<sup>24</sup>. They also have interesting piezoelectric and non-linear optical<sup>5,25</sup> properties. Thanks to their significant chemical flexibility<sup>9,12</sup>, it is possible to tune the dielectric properties of TTBs through the exploration of solid solutions<sup>7,17,25-28</sup>.

In the present work, a particular interest is focused on the exploration of  $\text{Ba}_2\text{NdFeNb}_4\text{O}_{15}$  composition<sup>13,29-32</sup> through two different aspects. The first one consists in the exploration of solid solutions to tune the dielectric response from a crossover (both relaxor and ferroelectric states) to a single relaxor (R) state. The strong relationship between dielectric properties and crystallographic structure of materials makes the diffraction techniques a useful tool, usually coupled to dielectric properties measurements. The previous observation of centrosymmetric structures and the total absence of structural phase transitions makes this material of great fundamental interest<sup>13</sup>. Following previous works on cationic substitutions in this TTB system, the present work aims at highlighting the structural and dielectric effect of Li insertion in the structure.

A second part will be dedicated to the particular case of the parent compound of all the solid solutions explored to study relaxor to ferroelectric crossovers,  $\text{Ba}_2\text{NdFeNb}_4\text{O}_{15}$ . After highlighting the effect of synthesis conditions on dielectric properties, a more detailed

crystallographic study of different samples will be performed to further understand this interesting material.

# Chapter 1: Concerning ferroelectricity and TTB materials

This chapter aims at reminding the different principles and definitions that will be useful to interpret the results presented in the following part of this work. A first part will be dedicated to dielectric material properties (pyroelectricity, piezoelectricity, ferroelectricity) and their crystal symmetry requirements. A second part will be focused on tetragonal tungsten bronzes (TTB in the following) structure. A description of their singular dielectric behavior (with both ferroelectric and relaxor states) also requires a more detailed description of TTB structures that includes superstructures with both periodic and aperiodic modulations.

## 1.1. Dielectric properties of ceramics

### 1.1.1 Dielectric properties and crystal symmetry

Dielectric, elastic, piezoelectric, ferroelectric and optical properties are closely related to crystal symmetry<sup>7,33,34</sup>. Within the 32 point groups, 11 are centrosymmetric. 20 of the 21 remaining groups possess a single polar axis and then can be polarized. In such symmetries, an offset between the barycenters of positive and negative charges is responsible for a local dipole moment<sup>35</sup>.

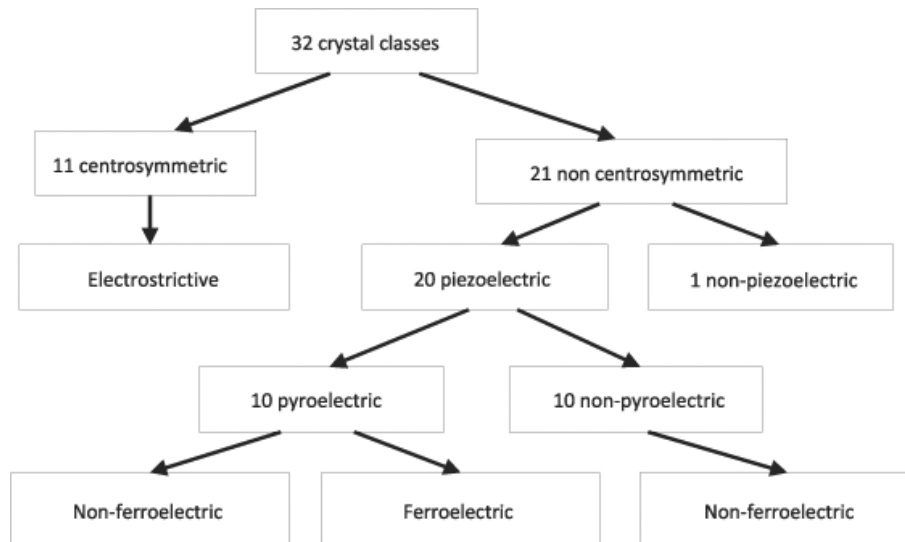


Figure 1: Schematic representation of dielectric symmetry groups

However, if local dipolar moments are compensated along the polar axis, no spontaneous polarization can occur. In the opposite case, a spontaneous polarization  $P_s$  can arise and is temperature dependent. These are pyroelectric. Among the 20 piezoelectric point groups, 10 are pyroelectric, allowing for the appearance of a spontaneous polarization and the 10 others are not. Ferroelectricity corresponds to materials in which a spontaneous polarization can be reversed with the application of an external electric field. However, if a point group allows ferroelectricity, a material adopting this group will not necessarily be ferroelectric.

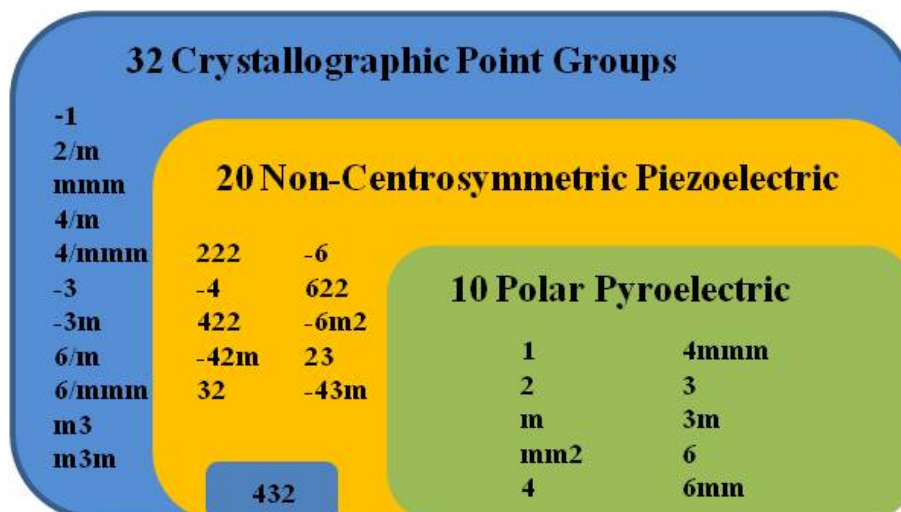


Figure 2: Representation of dielectric point groups

Figure 2 represents the list of point groups and their link with the possible dielectric behaviours. A ferroelectric group necessarily belongs to the pyroelectric and piezo electric groups, whereas the opposite is not mandatory. Ferroelectric materials then belong to the ten pyroelectric point groups listed above: 1, 2, m, mm2, 4, 4mm, 3, 3m, 6 and 6mm<sup>35</sup>.

## 1.1.2 Dielectric polarization

### 1.1.2.1 Different polarization nature

Polarization is a complex mechanism containing various contributions: electronic, atomic, dipolar, and space charges. The equation of polarization<sup>36</sup> under the application of an external electric field is:

$$P = P_e + P_i + P_d + P_c \quad \text{Eq. (1)}$$

These different polarization phenomena involve different kinds of charged species and mainly differ in their relaxation time and thus their size. Therefore, it is possible to highlight their contribution to global polarization through dielectric constant measurement versus frequency. Figure 3 displays the contribution of different mechanisms to the global polarization versus external electric field frequency.

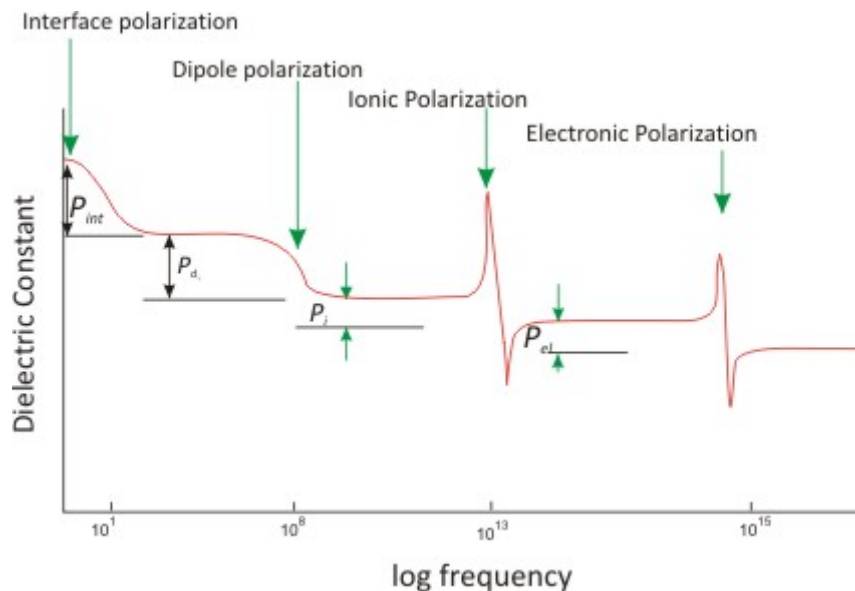


Figure 3: Evolution of polarization with frequency showing different relaxation modes: space charges, dipoles, ions and electrons

- Space charges ( $P_c$ ): In the lowest frequency range, the main part of polarization comes from interface polarization, *i.e.* space charges ( $P_c$ ). These consist in an accumulation of free charges at the interfaces of solids (typically at the sample/electrode interface, for example). In dielectric ceramics, this may also result from microstructures presenting high porosity level (and therefore many interfaces).
- Dipole polarization ( $P_d$ ): In the higher frequency range, the relaxation of space charges no longer contributes to the dielectric response, because voltage oscillations are too fast. This results in a drop of dielectric constant corresponding to the value of interfacial polarization  $P_c$ . Once  $P_c$  contribution becomes zero, dipole relaxation is the next most important polarization contribution, and remains so up to about  $10^6$  Hz. Dipole polarization corresponds to the orientation of polar molecules or atomic groups under the application of external field. In the latter, positive and negative charges barycenters do not coincide anymore. In dielectric oxides, the existence of such polarization is strongly linked to structural modification, and therefore to the symmetry of the material.
- Ionic or atomic polarization ( $P_i$ ): For the highest frequencies, dipoles and space charges no longer contribute to the polarization. Ionic and electronic polarization remain the only contributions. The ionic polarization consists of individual motions of atoms or ions. These correspond to fast movements that relax at higher frequencies, up to about  $10^9$  Hz. They are usually observed in vibrational spectroscopy.
- Electronic polarization ( $P_e$ ): This phenomenon is present in all dielectrics but its contribution is very small. It is due to the presence of local dipoles associated to an inhomogeneous distribution of electronic density (or fluctuations thereof) around atomic nuclei, which is affected by an external electric field.

In dielectric materials, the most interesting source of polarization is in the  $P_d$  range, which is expressed between  $10^2$  and  $10^6$  Hz in dielectric measurements. If the measurement is performed in a lower frequency range, the dielectric response could be dominated by space charges, whereas at higher frequencies, the contribution from dielectric polarization  $P_d$  vanishes.

In a dielectric, for low values of external electric fields, polarization  $P$  is related to the external field  $E$  as:

$$P = \epsilon_0 \chi E \quad \text{Eq. (2)}$$

where  $\chi$  is the dielectric susceptibility of the material and  $\epsilon_0$  is the dielectric permittivity of vacuum ( $=8.854 \cdot 10^{-12} \text{ F.m}^{-1}$ ).

The susceptibility of a medium is related to the relative permittivity  $\epsilon_r$  by:

$$\chi = \epsilon_r - 1 \quad \text{Eq. (3)}$$

with  $\epsilon_r$  the relative permittivity of the considered material.

In a ceramic considered homogeneous and isotropic and characterized by a linear dielectric response, one obtains:

$$\vec{D} = \epsilon_0 \vec{E} + \vec{P} = \epsilon_0 \vec{E} + \epsilon_0 \chi \vec{E} = \epsilon_0 (1 + \chi) \vec{E} = \epsilon_0 \epsilon_r \vec{E} \quad \text{Eq. (4)}$$

Here,  $\vec{D}$  is the electric displacement.

Considering a sinusoidal field  $\vec{E} = \vec{E}_0 \cdot e^{i\omega t}$ , where  $t$  is time and  $\omega$  is the frequency, the applied field and the resulting polarization are out of phase, depending on relaxation times of the different relaxation mechanisms:

$$\vec{P} = \vec{P}_0 \cdot e^{i\omega t} = \epsilon(t) \cdot \vec{E} \quad \text{Eq. (5)}$$

Dielectric permittivity in the frequency space becomes a complex value calculated from the Fourier transform of the dielectric response  $\epsilon_r(t)$ :

$$\epsilon_r(\omega) = \int_0^{\infty} \epsilon_r(t) \cdot e^{i\omega t} \cdot dt = \epsilon'_r(\omega) + i \epsilon''_r(\omega) \quad \text{Eq. (6)}$$

$\epsilon'_r(\omega)$  and  $\epsilon''_r(\omega)$  are respectively called real and imaginary parts of dielectric permittivity. The ratio  $\epsilon''_r(\omega) / \epsilon'_r(\omega)$  is called losses coefficient and is noted  $\tan\delta$ .

### 1.1.2.2 Case of ferroelectric ceramics

Let us focus on the particular case of ferroelectric polycrystalline materials under the application of an external electric field.

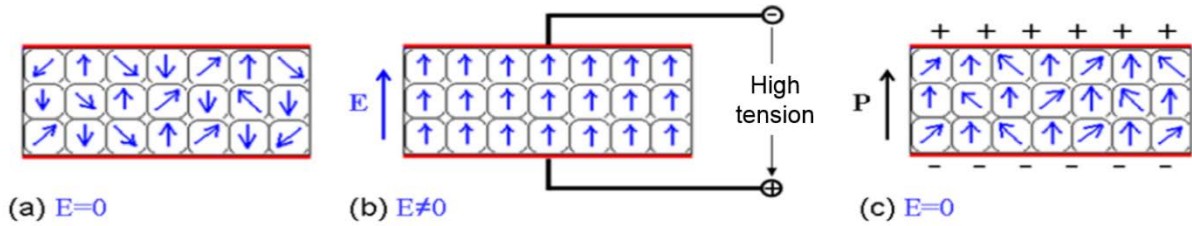


Figure 4: Schematic representation of dielectric polarization  $P$  of a ceramic (a) without external field, (b) with external field applied and (c) after poling

Above the ordering temperature, called the ferroelectric Curie temperature ( $T_C$ ), the material is in a paraelectric state. In this state, no dipole is spontaneously present. When decreasing the temperature below  $T_C$ , dipoles form and orientate cooperatively in the same direction over a certain distance. This results in the formation of ferroelectric domains. Different domains are separated by domain walls and are oriented in different directions when no electric field is applied (see Figure 4 a). Macroscopic polarization remains zero since all dipoles compensate each other's statistically. Under the application of external field of sufficient intensity, all dipoles orientate along the direction of external field ( $E$ ) (Figure 4 b). This results in a polarization called saturation polarization ( $P_S$ ) (Figure 5). After removing this external field, most of the dielectric dipoles have a memory of the previously applied field and a global polarization remains present even without external field. This polarization is called remnant polarization ( $P_r$ ) (Figure 5). To recover a zero polarization, it is necessary to apply a field in the opposite direction. The value of the field needed to remove polarization is called coercive field ( $E_C$ ).

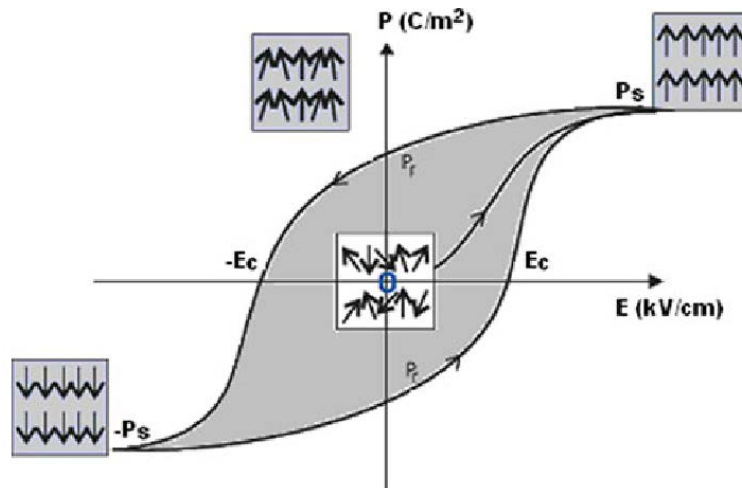


Figure 5: Ferroelectric  $P(E)$  hysteresis loop with first polarization curve

Whereas in the first cycle, the initial polarization is null ( $P = 0 \text{ C.cm}^{-2}$ ), in the further cycles the application of an opposite field  $-E_c$  (coercive field) is necessary to cancel polarization. This way, when cycling  $P(E)$  measurement, an hysteretic behavior is observed that is characteristic of ferroelectrics.

### 1.1.2.3 Piezoelectricity

While working on pyroelectricity in 1880, Pierre and Jacques Curie observed that an electric field could be generated when applying mechanical pressure on quartz crystals<sup>37</sup>. This phenomenon will further be called piezoelectric effect. After the predictions of the opposite effect, called inverse piezoelectric effect, by Gabriel Lippman, based on thermodynamical calculations<sup>38</sup>, they experimentally observed the deformation of such crystals under the application of electric field<sup>37</sup>. Using symmetry considerations, they predicted the presence of such behavior in other crystals like tourmaline, topaz and Rochelle salts.

The presence of piezoelectric effects in such crystals is demonstrated, but remains weak, and it is with the discovery of ferroelectricity, particularly with ferroelectric perovskites, that piezoelectricity attracted more attention. Currently, the prototype piezoelectric phase is the PZT perovskite ( $\text{Pb}(\text{Zr,Ti})\text{O}_3$ ) which is widely used as commercial piezoelectric phase for electric to mechanical energy conversion or vice-versa. They are mainly used as detectors, in electro-optics or as actuators<sup>39</sup>. Nowadays, particularly with the desire to replace lead-containing materials<sup>40</sup>, important efforts are focused on the research of alternatives to lead based materials, such as bismuth based titanates, BCTZ perovskites or alkaline niobates and tantalates<sup>41</sup>.

The origin of piezoelectric effect can be multiple: a rotation of dipolar moments under the application of electric field and dipolar moment modification through barycenters displacement. In order to describe piezoelectric effect, Voigt proposed the relation<sup>42</sup>:

$$\vec{P} = \epsilon \vec{E} + d \vec{T} \quad \text{Eq. (7)}$$

where  $d$  is the scalar piezoelectric coefficient and  $T$  is the elastic constraint.

Piezoelectric measurements can be performed using an impedance bridge, through the measurement of complex admittance with respect to frequency. The sample, depending on its shape and size, has a resonance frequency that can be determined, so that admittance

measurement can be performed in a narrow frequency range around this resonance, to characterize it. A typical measurement is displayed on Figure 6.

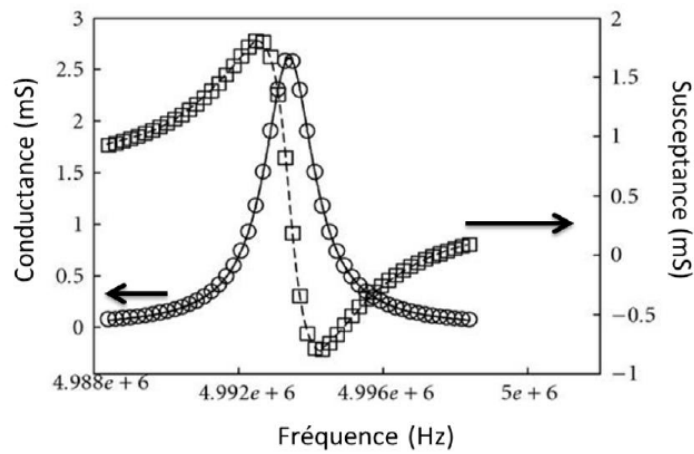


Figure 6: Conductance and susceptance as a function at the frequency resonance for a single crystal of quartz<sup>43</sup>

Different resonance modes coexist in the material depending on its shape and size. Therefore, depending on each mode, different resonance frequencies can be measured. Usually for pellets of about 10 mm diameter and 1 mm thick, radial modes are observed typically below 1 MHz and thickness modes above 1 MHz.

Beyond the search for piezoelectric properties, such measurements also allow to probe phase transitions related to polar order in relaxors and ferroelectrics, at least when piezoelectric coefficients are large enough for the piezoresponse to be detected.

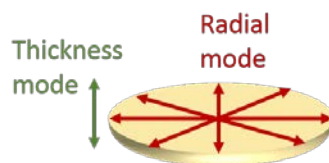


Figure 7: Representation of radial and thickness resonance modes of piezoelectric effect

#### 1.1.2.4 Pyroelectricity

In some materials possessing a spontaneous polarization, if not most, this spontaneous polarization evolves with temperature. This is in particular the case of pyroelectric materials.

This property settles below a Curie temperature  $T_C$ , and was discovered during the 18<sup>th</sup> century by Louis Lemery in tourmaline, which was called “firestone”<sup>44</sup>.

If polarization is important, it becomes possible to neglect vacuum polarization and to assimilate polarization  $P$  to electric displacement  $D$ . By definition, this one is a density of free charges on a sample surface. Therefore, the following equation is obtained:

$$D = \frac{Q}{S} \approx P \quad \text{Eq. (8)}$$

where polarization is usually expressed in  $\mu\text{C}\cdot\text{cm}^{-2}$

It is impossible to directly access to the spontaneous polarization, but an indirect measurement is possible. This one actually consists in the measurement of thermal depolarization currents and pyrocurrents, from which are deduced the spontaneous polarization. This kind of measurement is very sensitive to thermal ramp variations, therefore, a perfect control is necessary to perform accurate measurement. Depending on the accuracy of the experimental setup, pyrocurrent measurement can allow for the detection of very small signals (below the pA range), but require high quality samples to avoid spurious contributions from defects, interfaces (...), that can hinder the measurement. The measured current is directly linked to the charge variations versus time:

$$Q(t) = \int i(t)dt \quad \text{Eq. (9)}$$

Spontaneous polarization is linked to pyrocurrent:

$$P = \int \frac{i}{S} dt \quad \text{Eq. (10)}$$

Moreover, expressing partial derivatives of spontaneous polarization  $P_S$ :

$$\frac{dP_S}{dt} = \frac{\partial P_S}{\partial T} \cdot \frac{\partial T}{\partial t} \quad \text{Eq. (11)}$$

where  $\frac{\partial P_S}{\partial T}$  is called primary pyroelectric coefficient  $p$  and is a characteristic parameter of pyroelectricity.

Therefore, measurements are presented as the temperature dependence of spontaneous polarization and pyroelectric coefficient:

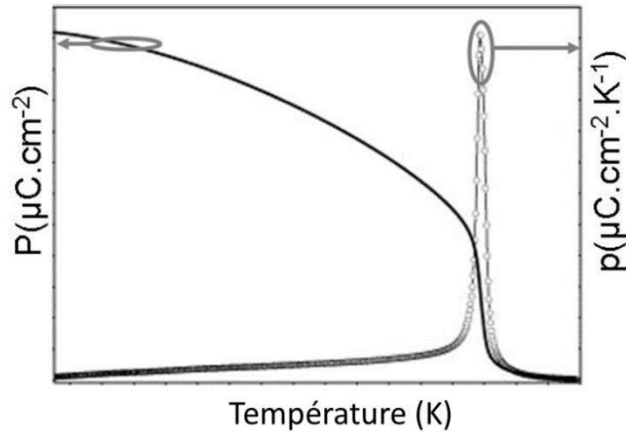


Figure 8: Temperature dependence of polarization and pyroelectric coefficient  $p$  of a usual ferroelectric material

### 1.1.3 Ferroelectric phase transitions

Ferroelectric (FE) materials have been previously presented as materials containing oriented dipoles. However the presence of these local dipoles is observed only in some particular conditions. Above their Curie temperature ( $T_C$ ), these dipoles either vanish or become disordered, and the resulting polarization becomes zero.

#### 1.1.3.1 Classical ferroelectrics

A usual way to characterize FE materials is to measure  $P(E)$  loops. As previously presented on Figure 5, the presence of an hysteresis loop is characteristic of ferroelectricity and results from the alignment of dipoles along an external electric field, and the remanence of this alignment after removing external field. The presence of dipole arises from the presence in the structure of a separation of the barycenters of positive and negative charges in the FE phase. However, at  $T_C$ , a phase transition occurs from this FE phase to a paraelectric (PE) phase, where dipoles are no longer present (displacive ferroelectrics) or are disordered (order-disorder ferroelectrics).

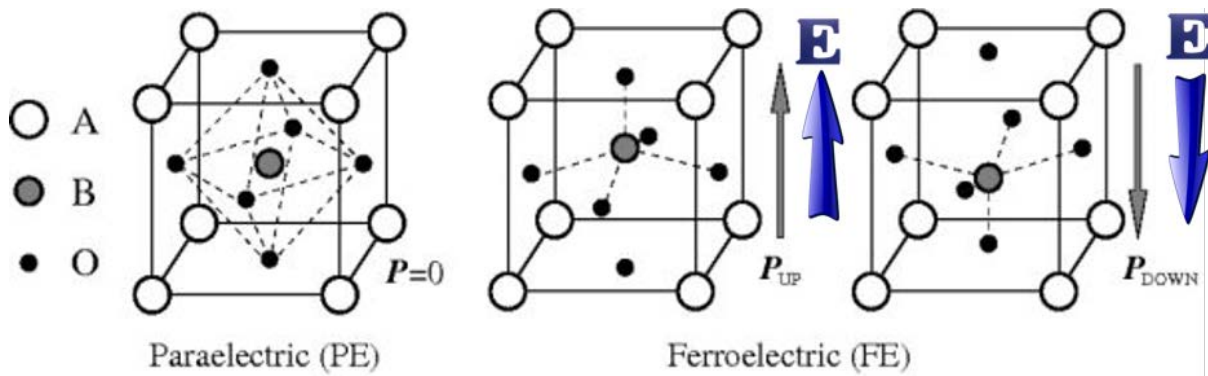


Figure 9: Representation of  $ABO_3$  perovskite in paraelectric and ferroelectric states. Both representation of ferroelectric state show the polarization reversal with external electric field (arrows represent the direction of field)

Figure 9 displays the representation of a single perovskite lattice in the PE state and in the two equivalent orientations of the FE state. In the PE state, the phase is centrosymmetric with the barycenters of A and B cations located at the same place as the barycenter of oxygens. Therefore, the resulting dipole moment, and thus polarization, is zero.

In the FE state, one can notice through the displacement of the central B cation that the barycenter of positive charges moves in the upper direction while the oxygens slightly move in the opposite direction. Then the polarization is non-zero and is oriented along the barycenter displacement direction. If the applied electric field is reversed, the B cation moves towards the lower position while oxygen move the opposite way, and the polarization is reversed. Applying an external field on the PE phase does not results in the characteristic hysteresis associated to the two FE states, and the PE phase can easily be distinguished from a pure FE phase (Figure 10).

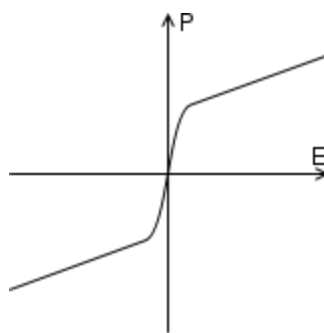


Figure 10: Representation of  $P(E)$  measurement for a material in the PE state

It is then possible, through  $P(E)$  measurements at different temperatures, to define the transition temperature  $T_C$  from PE to FE phase. However, this determination is more often performed

through permittivity measurements. As described earlier, at the transition temperature, a phase transition occurs from a higher symmetry in the high temperature range (PE) to a lower symmetry (FE). This transition is accompanied by the loss of inversion symmetry, that forbids the appearance of a spontaneous polarization.

Two types of transitions are possible, following Landau theory<sup>45</sup> (Figure 11).

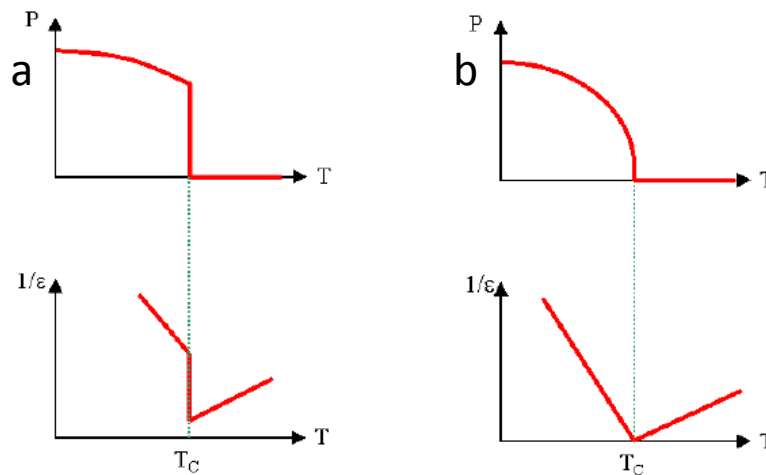


Figure 11: Evolution of polarization and inverse of dielectric permittivity versus temperature for (a) first order and (b) second order transitions<sup>46</sup>

In the case of first order transition, statistic Boltzmann law predicts a non-zero probability for polarization to switch from  $P = 0$  to  $P \neq 0$  at  $T_c$ . This switch can be abrupt, and results in an abrupt change in inverse of permittivity. Among first order FE materials, ammonium sulfate  $(\text{NH}_4)_2\text{SO}_4$ <sup>47</sup> or perovskites such as  $\text{BaTiO}_3$  and  $\text{PbTiO}_3$ <sup>48</sup> are good examples.

Second order transition FE materials represent fewer examples of ferroelectrics, among which the triglycine sulfate (TGS)<sup>49</sup>. In opposition with first order, their transition is more diffuse, and no abrupt change of polarization nor permittivity is observed.

In the high temperature phase, there is no macroscopic polarization. This can result from the absence of dipoles or the presence of local compensated dipoles. Therefore, two different ways can be followed to transit from PE to FE phase:

- Displacive transition. In this case, no dipole is present in the high temperature PE state and a decrease of temperature provokes ionic displacement in the lattice, resulting in

the formation of local dipoles. It is the main transition type in ferroelectrics, such as for  $\text{PbTiO}_3$ <sup>50</sup>.

- Order-disorder transition. In this case, the PE phase possesses dipoles but these ones are randomly oriented and finally orientate in the same direction at the FE transition. This is the case of some FE like Rochelle salts,  $\text{NaNO}_2$  or TGS<sup>51</sup>.

In the paraelectric phase, the thermal evolution of isothermal permittivity follows the Curie-Weiss law:

$$\varepsilon' = \frac{C}{T - T_{CW}} \quad \text{Eq. (12)}$$

C is called the Curie constant (in Kelvin).  $T_{CW}$  is the Curie-Weiss temperature and from it the nature and amplitude of interaction between dipoles, which can be parallel or antiparallel (in the case of antiferroelectric ordering), can be evaluated.

In order to characterize the FE to PE phase transitions, dielectric measurements are performed by measurement of capacitance C and loss coefficient  $\tan\delta$  which are related to dielectric permittivity  $\varepsilon'_r$  and  $\varepsilon''_r$  as a function of temperature and frequency.

$$C = \varepsilon_0 \varepsilon'_r \frac{A}{d} \quad \text{Eq. (13)}$$

$$\tan\delta = \frac{\varepsilon''}{\varepsilon'} \quad \text{Eq. (14)}$$

with A the surface area of the electrodes and d the distance between both electrodes, considering a sample with two parallel faces.

Figure 12 below displays a permittivity measurement of  $\text{BaTi}_{0.8}\text{Zr}_{0.2}\text{O}_3$  ceramic showing two different states. The high temperature state, above the peak temperature, is the PE state, and at  $T_C$  around 315 K, there is a peak in both real and imaginary parts of permittivity, with a maximum of  $\varepsilon$  at the transition temperature.

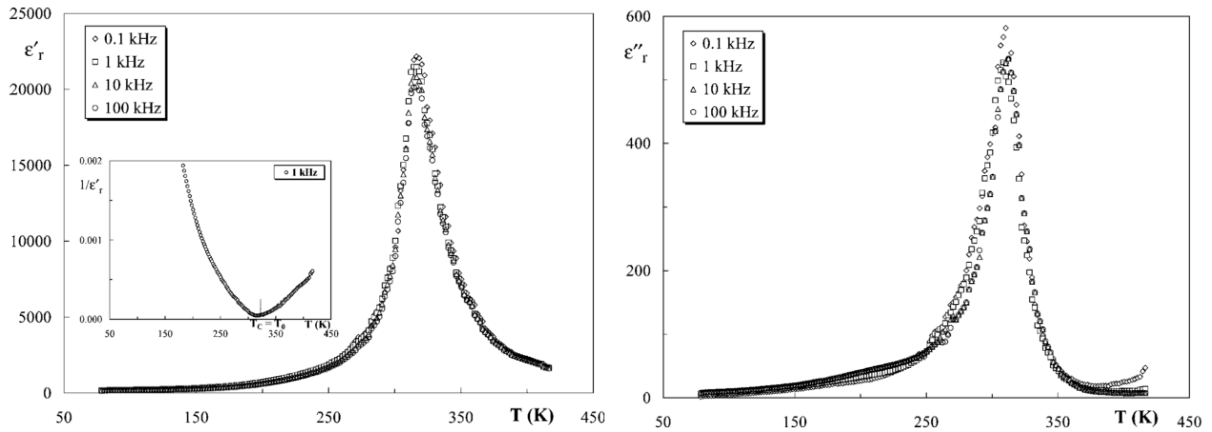


Figure 12: Permittivity measurement of  $BaTi_{0.8}Zr_{0.2}O_3$  ceramic<sup>22</sup>

### 1.1.3.1 Antiferroelectrics and ferrielectrics

Some materials, known to possess dipoles ordered at long range, do not display the presence of a FE hysteresis loop, but rather two different hysteresis, observable for applied electric field of sufficient amplitude. This is a characteristic signature of antiferroelectric materials (AFE).

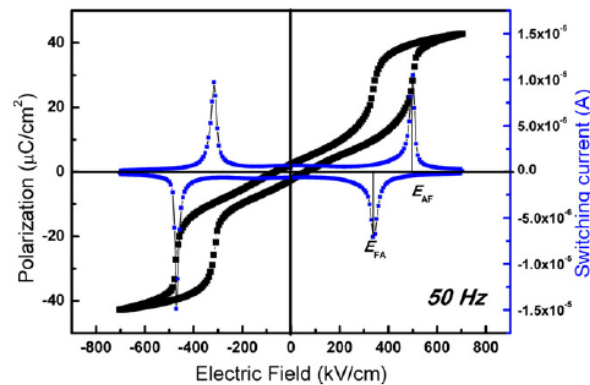


Figure 13: Double hysteresis loop and corresponding current curve of  $PbZrO_3$ <sup>52</sup>

Figure 13 displays  $P(E)$  measurement for  $PbZrO_3$  which is an AFE phase. It is visible that the measured response is composed of two separated symmetric hysteresis loops, separated by a domain characterized by a linear response. It implies that in the absence of electric field, the polarization of the sample is close to zero, whereas in the case of FE, after removing the field a polarization  $P_R$  remains. This specific situation is due to the local organization of dipoles.

The difference between FE and AFE phases lies in the interaction between neighboring dipoles. In the case of FE phase, all dipoles, up to the scale of domains, are spontaneously aligned in the same direction, whereas in the case of AFE, they adopt an antiparallel arrangement. This is a

situation that is very similar to that of antiferromagnetic materials (AFM), after which antiferroelectrics are named.

In this case, the transition temperature is no longer called Curie temperature but could be called Neel temperature  $T_N$  as for AFM materials. As discussed earlier, when fitting the permittivity curve in the paraelectric region with Curie-Weiss law, one will be able to determine a Curie constant that traduces the amplitude of the dielectric interactions between neighboring dipoles, and also a Curie-Weiss temperature  $T_{CW}$ , which is expected to be negative in the case of an AFE material.

In some cases, however, a more complex behavior can be observed: it is the case of ferrielectric materials. Different propositions have been made to define these materials. Kanzig<sup>53</sup> defined ferrielectrics as “crystals that exhibit at a given temperature antiferroelectric properties along one axis and ferroelectric properties along another”. Cross<sup>54</sup> used it to define a particular phase of ferroelectric and antiferroelectric mixed crystals. Pulvari suggests the possibility to obtain ferrielectricity in uncompensated AFE<sup>55</sup>. Ferrielectricity is observed for instance in solid solution between AFE composition such as  $\text{Na}(\text{V},\text{Nb})\text{O}_3$  perovskites<sup>55</sup> or layered phases such as  $\text{Bi}_4\text{Ti}_3\text{O}_{12}$ <sup>56</sup> of Aurivilius structure based on  $[\text{TiO}_6]$  octahedrons separated by  $\text{Bi}_2\text{O}_2$  layers.

#### 1.1.3.2 Relaxor ferroelectrics

Among dielectric materials, some present a particular behavior, with signs of polar order, polarization, and possibly pyro- and piezoelectric responses, but their overall behavior does not correspond to the typical response of a ferroelectric.

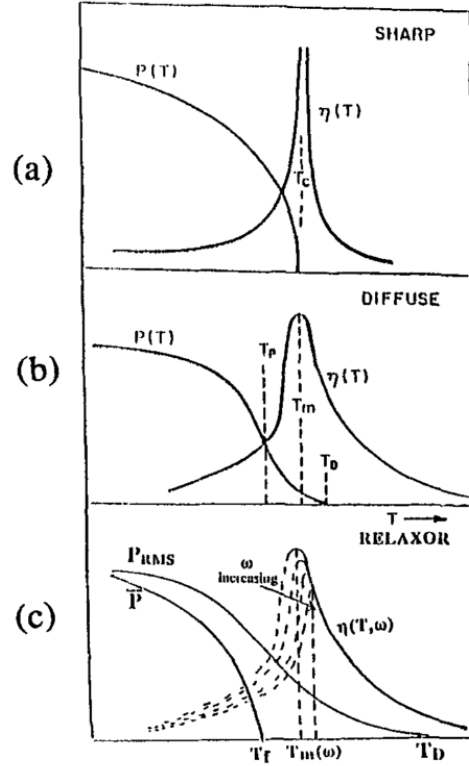


Figure 14: Types of Ferroelectric Phase Transitions. (a) simple proper ferroelectric: sharp second order phase change in highly perfect single crystal. (b) diffuse phase transition associated with macroscopic heterogeneity as in practical capacitor dielectrics. (c) relaxor ferroelectric defining  $T_m(\omega)$ ,  $T_D$ ,  $T_F$ .<sup>57</sup>

In the example of a classical second-order transition FE phase (Figure 14 a) there is a sharp transition from FE to PE phase accompanied by an abrupt loss of polarization at  $T_C$ . In the case of real materials, and as desired in practical applications, it is interesting to have a strong value of permittivity on a larger temperature range. This case is represented on Figure 14 b. In that case, polarization persists slightly above  $T_m$  and the transition is “rounder”. In the relaxor ferroelectrics, three features of the dielectric response are qualitatively different. The transition is clearly diffuse and rounded, but the response is now markedly dispersive below  $T_m$  and  $T_m$  is a function of frequency (Figure 14 c). In the polarization the root mean square value ( $P_{RMS}$ ) persists to a temperature ( $T_D$ ) 200 to 300°C above  $T_m$  but the mean polarization  $\bar{P}$  decays to zero at a temperature  $T_F$  which is well below  $T_m$ .<sup>57</sup>

These materials are referred to as “relaxor-ferroelectrics” or simply relaxors. Most of the known materials exhibiting such behavior are perovskites and tetragonal tungsten bronze structured materials, among which PMN ( $\text{PbMg}_{1/3}\text{Nb}_{2/3}\text{O}_3$ ) is the archetype<sup>58</sup>. It was first discovered by Smolenskii in the 1950’s<sup>59</sup> and has been of great interest since, thanks to its large permittivity.

The main difference with ferroelectrics is that transition from PE state to relaxor (R) state is not accompanied by a structural transition. In the polar R state, PMN remains surprisingly cubic below  $T_m$ . This compound has been explored under different forms<sup>60</sup> and became the prototype of relaxor materials<sup>61</sup>. After long researches on the possible origin of such behavior, it has been proposed by Bokov and Mylnikova<sup>62</sup> that this behavior is due to local heterogeneity, giving a range of Curie points, but that the scale was very small and therefore below the resolution of X-ray and optical probes. This was therefore evidenced, after the synthesis of single crystals and the development of imaging techniques, that the main explanation for relaxor behavior is the presence these polar regions at a nano scale<sup>63</sup> (called polar nano regions PNR), related to an inhomogeneous spatial distribution (at the nanoscale) and chemical ordering at the intermediate scale breaks up the long range cooperative alignment of dipoles.

Since there is a variation in the size of the different PNR, their dielectric response is characterized by a frequency dependence, which results in broad dielectric transition peaks. Because different PNR have slightly different polarization, size and compositions, the temperature at which the permittivity reaches its maximum depends on the measurement frequency. In this case, no single transition temperature can be extracted from the measurement like in the case of classical FE. In the present case, the maximum of permittivity is frequency dependent. Therefore, transition temperature  $T_m$  has to be given for a selected frequency, and the variation of transition temperature in a given frequency range,  $\Delta T_m$  is also a characteristic parameter of relaxors.

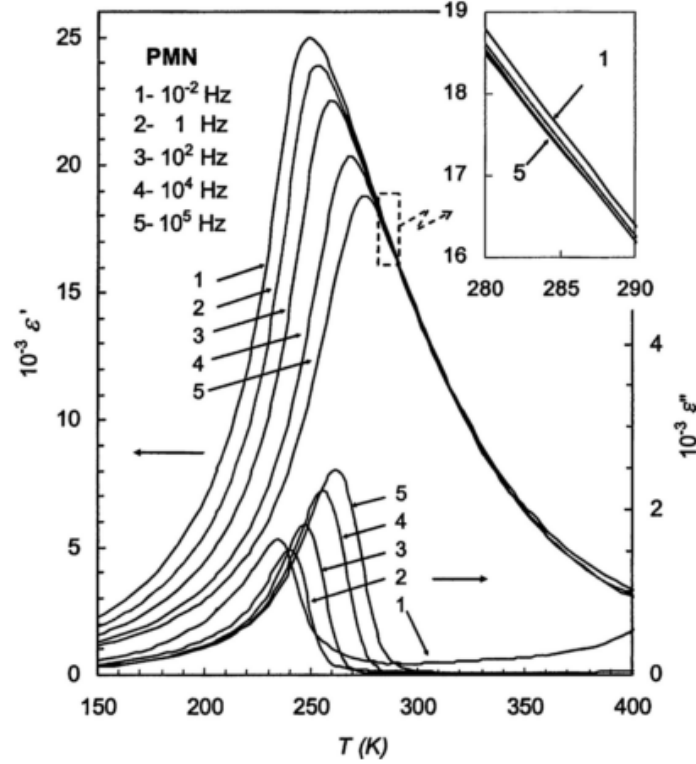


Figure 15: Real and imaginary part plot as a function of temperature and frequency<sup>58</sup>

This frequency dependence can be modeled using the Vogel-Fulcher (VF) law<sup>64,65</sup> which gives access to the corresponding activation energy, and the PNR freezing temperature  $T_{VF}$  of the domains. VF equation is simply a modified Arrhenius expression, which traduces an increasing degree of interaction between random local relaxation processes, until they are totally frozen, at the so-called freezing temperature. This process, in the case of relaxors, shapes the frequency dependence of their dipolar response.

$$f = f_0 \cdot e^{-\frac{Ea}{k(T-T_{VF})}} \quad \text{Eq. (15)}$$

where  $f$  is the frequency of the perturbation (applied ac field frequency, Hz);  $f_0$  is the Debye frequency (Hz), above which dipoles of a cluster only move individually<sup>66</sup>;  $Ea$  is the activation energy of local polarization (J);  $T_{VF}$  is the characteristic VF temperature (often described as the static freezing temperature) (K) and  $k$  is Boltzmann constant ( $1.38 \times 10^{-23} \text{ J.K}^{-1}$  or  $8.617 \times 10^{-5} \text{ eV.K}^{-1}$ ).

However, dielectric response are affected by microstructural parameters like density or grain size, and in such case it is difficult to fit the experimental data using this law, usually because

the actual value of  $T_m(f)$  is difficult to determine, and that frequency range explored is limited (usually  $10^2$  to  $10^6$  Hz).

In many cases, these relaxor materials are observed when exploring solid solution by substituting an element (usually non ferroelectrically active) in a ferroelectric perovskite phase. This can give rise to the so-called relaxor to ferroelectric crossover.

### 1.1.3.3 Relaxor to ferroelectric crossover

Cationic substitutions such as Ti by Zr in  $\text{BaTiO}_3$ <sup>22</sup> or Pb by La in  $\text{Pb}_{1-x}\text{La}_x(\text{Zr}_{1-y}\text{Ti}_y)_{1-x/4}\text{O}_3$  PLZT lead to the evolution of a classical ferroelectric to a relaxor ferroelectric. Such evolution with chemical composition is called “ferroelectric-relaxor crossover”.

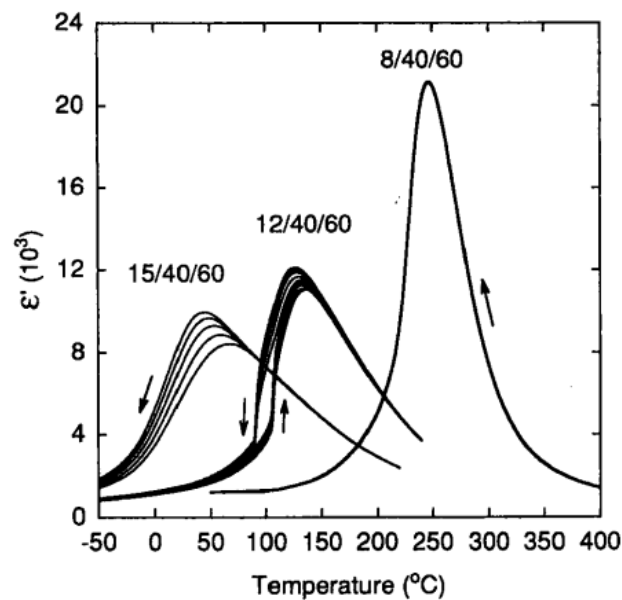


Figure 16: Dielectric measurement of PLZT ((Pb,Lu)Zr0.40Ti0.60O3) for three contents of La (15, 12 and 8 %) showing a normal ferroelectric to relaxor transition when increasing La content<sup>67</sup>

On Figure 16 are visible two different behaviors. The first one (8% La) is a classical ferroelectric transition with a frequency independent maximum at  $T_C$ , whereas for the two other at lower temperature (12 and 15% La), the transitions are frequency dependent, typical of a relaxor behavior. Moreover, the chemical substitution is accompanied with a decrease of the transition temperature.

As a second possibility, there may be some cases in which the presence of both transitions within a single material occurs. This behavior is often observed for TTB materials, such as

$\text{Ba}_2\text{NdTi}_{2+x}\text{Nb}_{3-x}\text{O}_{15-x/2}$ <sup>24</sup> (Figure 17). In this case, the starting composition exhibits a pure FE transition, and increasing oxygen deficiency (according to the proposed substitution scheme) leads to the observation of a second anomaly at lower temperature. In this case, the presence of R transition does not hinder the presence of the FE transition, and both transitions seem to emerge from different mechanisms, with a limited evolution of the corresponding transition temperatures with respect to the previous case.

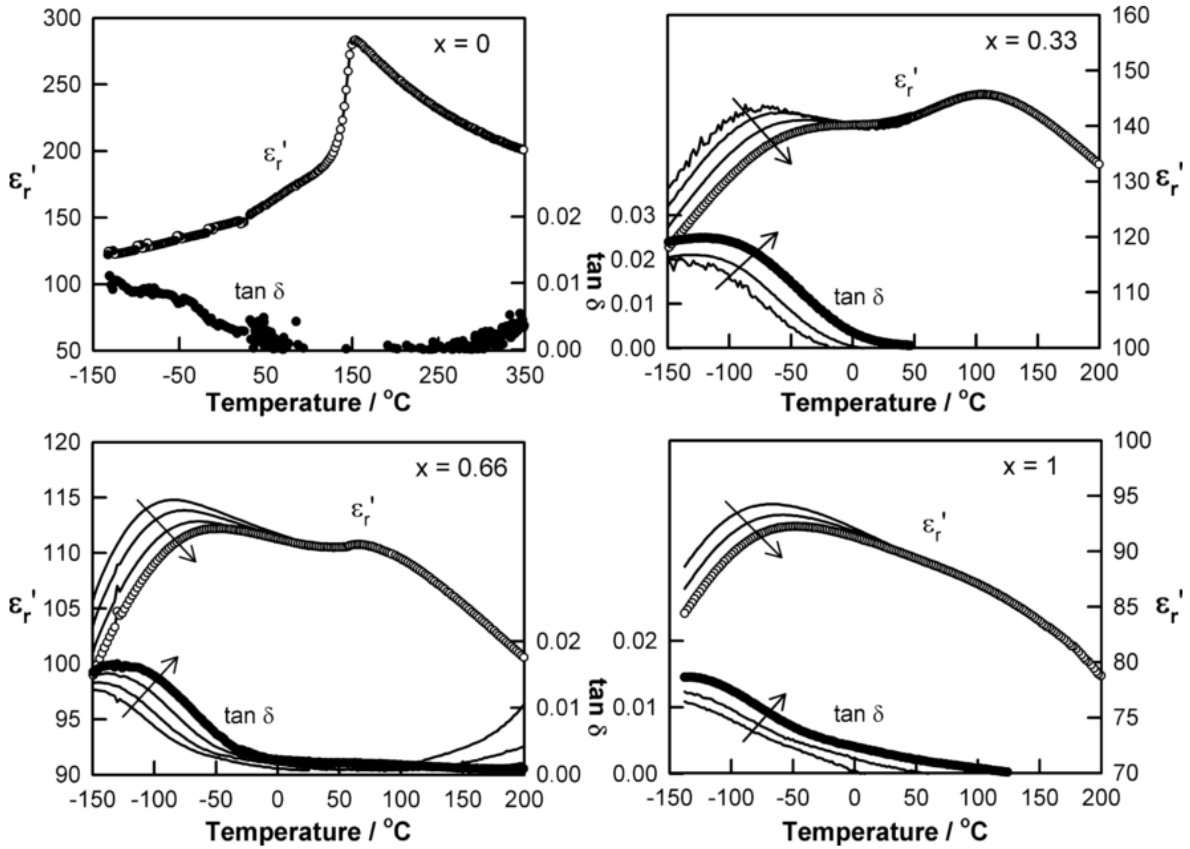


Figure 17:  $\epsilon'_r$  and  $\tan \delta$  data as a function of temperature for several compositions of  $\text{Ba}_2\text{NdTi}_{2-x}\text{Nb}_{3-x}\text{O}_{15-2x}$ . Arrows indicate the direction of increasing frequency from 1 kHz to 1 MHz.<sup>24</sup>

## 1.2. Tetragonal tungsten bronze structure

One of the most important material family in dielectrics is that of oxides and fluorides adopting the TTB structure. This structure was initially discovered with materials of composition  $\text{M}_x\text{WO}_3$  ( $\text{M}=\text{K}, \text{Na}, \dots, 0.33 \leq x \leq 0.60$ ) among which  $\text{Na}_x\text{WO}_3$  is the prototype phase. Nowadays, a large number of compositions have been related to the TTB structure, including niobates, titanates, tantalates, or tungstates. The important crystal chemical flexibility of this phase allows

tuning the dielectric properties through appropriate chemical substitutions. TTB-structured materials are an excellent example of tight structure/properties relationships.

### 1.2.1 TTB crystal chemistry

Tetragonal tungsten bronze structure is a perovskite-derived structure. It is built of corner sharing  $\text{MO}_6$  octahedra, the specific arrangement of which creates 3 different types of channels that can be totally filled, partially filled or left empty. Their general formulation can be written  $\text{A}_2\text{BC}_2\text{M}'\text{M}''_4\text{O}_{15}$  with A, B and C sites correspond to the three types of channels, and both  $\text{M}'$  and  $\text{M}''$  correspond to the two different octahedral sites.

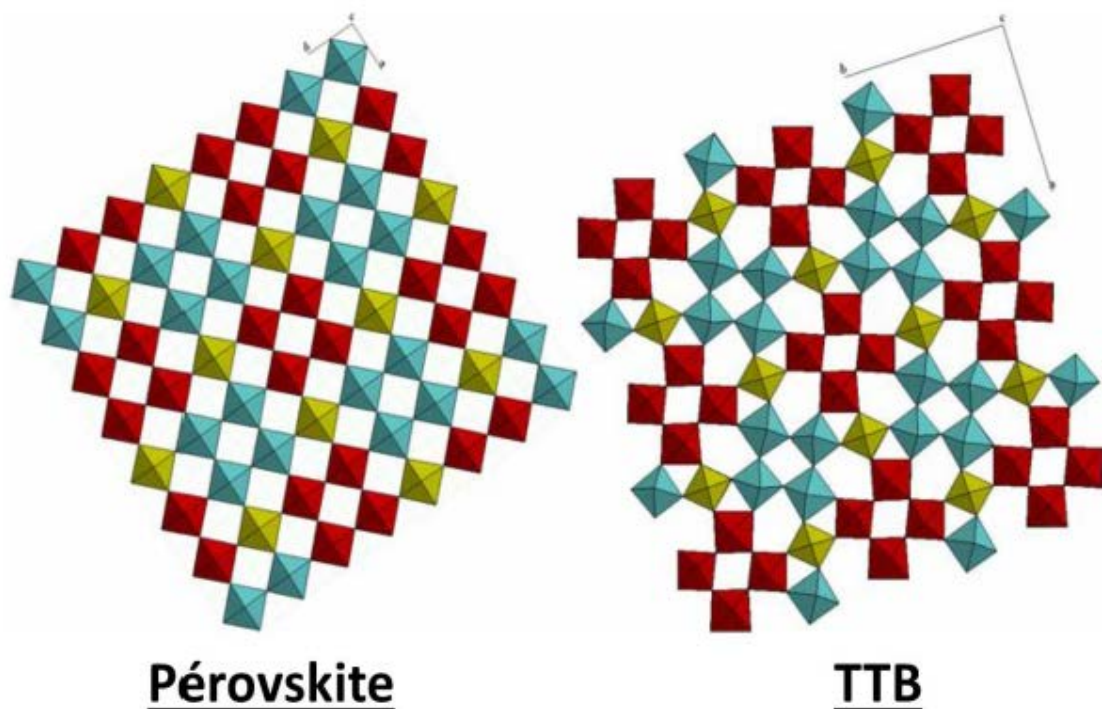


*Figure 18: Representation of perovskite and TTB structures showing the octahedron tilting and the different channels formed by such organization*

This organization creates different sites channels of different size and coordination:

- A: 15-coordinated pentagonal site (usually large alkali or alkaline earth)
- B: 12-coordinated square site (usually small alkali, alkaline earth or lanthanides)
- C: 9-coordinated triangular site (small site, usually empty or containing Li)
- $\text{M}'$ : 6-coordinated regular octahedron (yellow in fig. 18, usually transition metals)
- $\text{M}''$ : 6-coordinated distorted octahedron (usually transition metals)

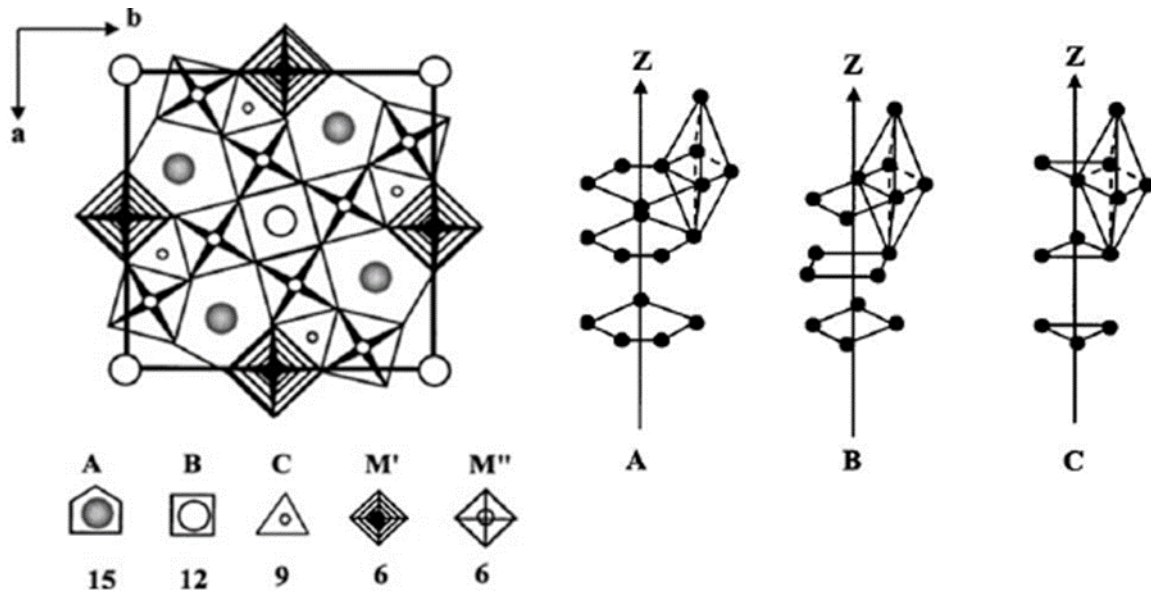


Figure 19: Schematic representation of TTB structure with different sites

With 5 cationic sites in the lattice, the number of possible compositions for a TTB structure is huge. In addition, A, B and C sites can be partially or fully occupied. The archetypal example of ferroelectric TTB material is  $\text{Ba}_2\text{NaNb}_5\text{O}_{15}$ , also called “banana”<sup>68</sup>. In this compound, A (Ba) and B (Na) sites are fully occupied and C site is left empty. Filled compounds like KLN  $\text{K}_3\text{Li}_2\text{Nb}_5\text{O}_{15}$ <sup>5</sup> (i.e.  $(\text{K}_2)(\text{K})(\text{Li}_2)(\text{Nb})(\text{Nb}_4)\text{O}_{15}$ ) can also be synthesized. In  $\text{Ba}_4\text{La}_{0.67}\text{Nb}_{10}\text{O}_{30}$ <sup>17</sup>, A site is filled, whereas B site is partially empty and C site is fully empty. The high flexibility of the TTB structure allows for various substitutions and compositional families that can be used to tune the physical properties.

TTB frequently display phase(s) transition(s) between paraelectric phase (PE) and ferroelectric phase(s) (FE). This phase transition, unlike perovskites, does not always consist in a structural modification. In the archetypal  $\text{Ba}_2\text{NaNb}_5\text{O}_{15}$  however, the loss of inversion symmetry is associated with the paraelectric ( $P4/\text{mbm}$ ,  $n^\circ 127$ ) to ferroelectric ( $P4\text{bm}$ ,  $n^\circ 100$ ) transition at 850 K. A second transition occurs at 570 K and consists in the appearance of an aperiodic structural modulation<sup>69</sup> which affects oxygen positions<sup>12</sup>, and appears strongly linked to ferroelectric properties<sup>7</sup>.

TTB structure can be described in various space groups from tetragonal  $P4/\text{mbm}$  to orthorhombic  $\text{Pb}2\text{a}$  for the most common, with unit cell parameters  $a \approx b \approx 12,5 \text{ \AA}$  and  $c \approx 4 \text{ \AA}$ . A few alternative space groups are also used to describe the TTB structure such as  $\text{Cmm}2$ ,

Bbm2 or Ima2 (this list is not exhaustive), with unit cells derived from the aforementioned one, some of them being labelled “pseudo tetragonal”. Figure 20 illustrate some of these configuration with the blue line highlighting the basic  $12,5 \times 12,5 \times 4 \text{ \AA}^3$  cell, the orange line being associated with the frequent  $a\sqrt{2} \times a\sqrt{2} \times c$  cell, the red line a  $2a\sqrt{2} \times 2a\sqrt{2} \times 2c$  cell and the black line delimiting a rarer  $3a \times 3b \times 2c$  unit cell. It is likely that all these alternative descriptions could be unified in a single structural model based on superspace formalism.

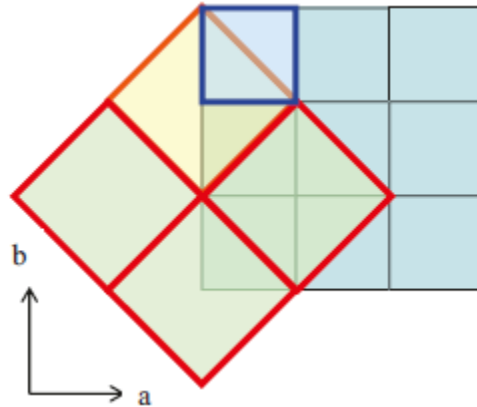


Figure 20: Various descriptions for TTB lattice

### 1.2.2 Dielectric properties

TTB materials are interesting for their dielectric properties. They can be ferroelectric<sup>9</sup> or relaxor<sup>18</sup> and even display a crossover<sup>71</sup> between ferroelectric and relaxor behavior . They can also display good piezoelectric and pyroelectric coefficients<sup>72</sup>.

In this part, we focus on the ferroelectric properties of TTB materials. For a classical ferroelectric phase, characterization is performed through capacitance/dielectric losses measurements, which gives access, knowing the geometry of the measured sample, to its relative permittivity.

Then, the result of dielectric measurements can be plotted versus temperature to assess the dielectric behavior of the sample.

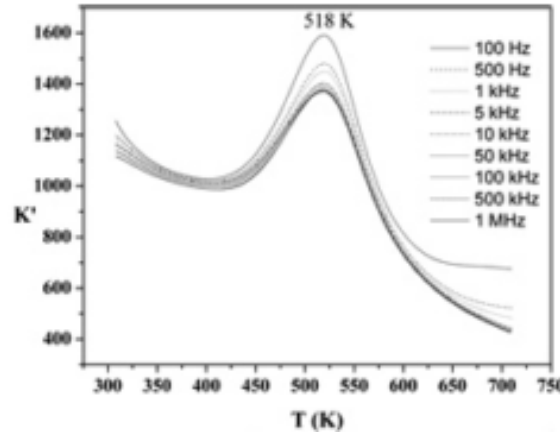


Figure 21: Real part of permittivity measurement for a SNN sample for different frequencies<sup>27</sup>

On Figure 21 is displayed a dielectric measurement performed on a TTB ceramic of composition  $\text{Sr}_2\text{NaNb}_5\text{O}_{15}$ <sup>27</sup>, in which can be seen a maximum of permittivity (here noted  $K'$ ) for a temperature of 518 K which is called Curie temperature (noted  $T_C$ ). For all the investigated frequencies, this maximum is located at the same temperature, and reveals a ferroelectric to paraelectric phase transition.

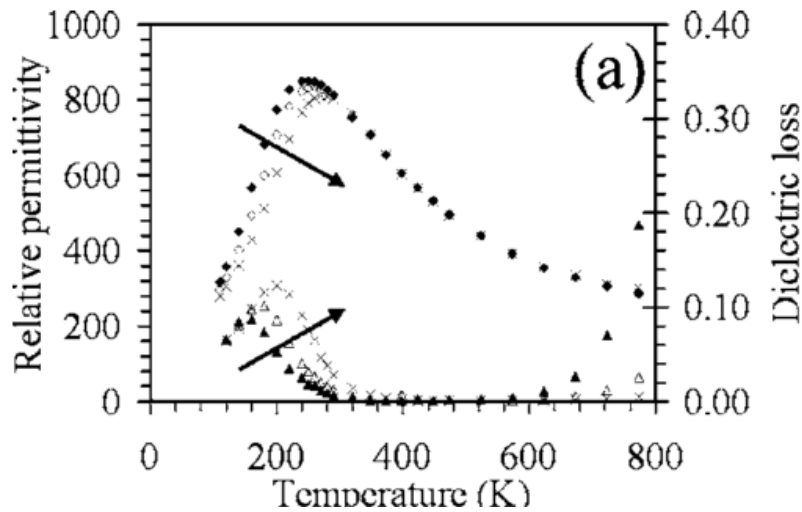


Figure 22: Dielectric measurement of  $\text{Ba}_2\text{BiTi}_2\text{Nb}_3\text{O}_{15}$  showing relaxor ferroelectric behavior<sup>14</sup>

On Figure 22 is displayed a measurement performed on  $\text{Ba}_2\text{BiTi}_2\text{Nb}_3\text{O}_{15}$ <sup>14</sup>. Both in real and imaginary parts of the permittivity, the temperature at which a maximum is reached increases with increasing frequency (represented by arrows). This is a usual observation for materials displaying a relaxor behavior. Because of the temperature-dependent maxima of permittivity,  $T_C$  cannot be determined. The dielectric transition can here be characterized by two values,

$T_m(f)$  and  $\Delta T_m(f_1, f_2)$ . Then, one can compare transition temperatures (noted  $T_m$ ) at a chosen frequency ( $f$ ), or evaluate the amplitude of the dielectric dispersion in a given frequency range, which is then given by  $\Delta T_m(f_1, f_2) = T_m(f_2) - T_m(f_1)$  ( $f_2 > f_1$ ).

Exploration of solid solutions can lead to the discovery of relaxor to ferroelectric crossovers. This behavior may be expected when the compounds delimiting the explored phase diagram exhibit relaxor and ferroelectric transitions respectively, so that intermediate compositions may exhibit both transitions. It is the case in the solid solution  $\text{Ba}_2(\text{Pr}, \text{Nd})\text{FeNb}_4\text{O}_{15}$  where the Nd compound is reported to be ferroelectric and Pr compound is reported as relaxor.

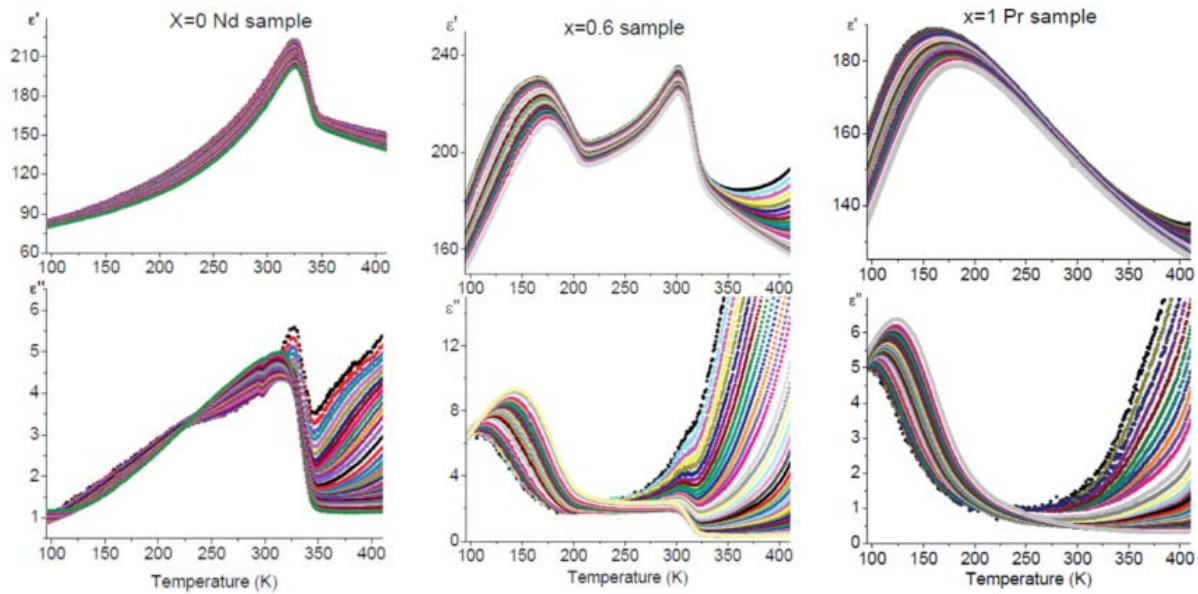


Figure 23: Dielectric measurement of  $\text{Ba}_2\text{Nd}_{1-x}\text{Pr}_x\text{FeNb}_4\text{O}_{15}$ <sup>26</sup>

Intermediate sample with  $x = 0.6$  exhibits both transitions. In these kinds of materials, characterization of the internal mechanisms appears interesting.

### 1.2.3 Particular case of $\text{Ba}_2\text{LnFeNb}_4\text{O}_{15}$ (Ln=rare earth)

The TTB family of  $\text{Ba}_2\text{LnFeNb}_4\text{O}_{15}$  (Ln = La, Pr, Nd, Sm, Eu and Gd) has been widely studied in our group. The initial goal was to look for intrinsic multiferroic properties in TTB, as such properties were briefly reported in this family<sup>73</sup>. It was finally established that that these materials consist in a mix of a ferroelectric TTB associated with ferromagnetic barium hexaferrite  $\text{BaFe}_{12}\text{O}_{19}$  and form a composite multiferroic material<sup>29</sup>. Whereas La, Pr and Gd compounds were shown to be relaxor ferroelectrics, Nd, Eu and Sm representatives display

classical ferroelectric transition. Hysteresis loops measured in the ferroelectric states are displayed on Figure 24.

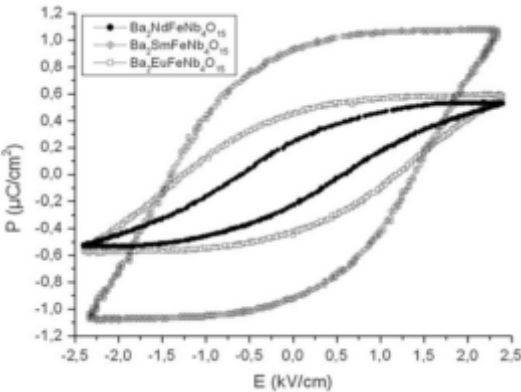


Figure 24: Hysteresis  $P(E)$  loops of Nd, Sm and Eu compounds of  $Ba_2LnFeNb_4O_{15}$ <sup>29</sup>

This measurement shows an increase of saturation polarization ( $P_s$ ) and coercive field ( $E_c$ ) inversely proportional to rare earth size. In the same time, it has been shown that the smaller the rare earth is, the lower the occupancy of the rare earth site. This way, Eu shows an occupancy of about 70 % when Pr is close to 95 % occupancy. This depletion of the rare earth is observed through the formation of a secondary phase determined to be of fergusonite type  $LnNbO_4$ . This loss of Ln and Nb in the TTB structure creates an excess of Fe and Ba that induces the formation of third phase which is the ferromagnetic barium hexaferrite.

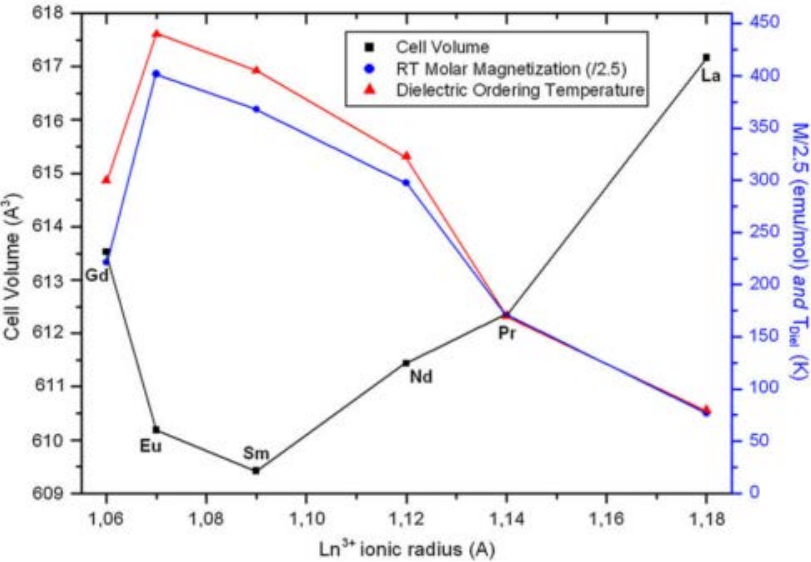


Figure 25: Influence of  $Ln^{3+}$  size on cell volume, molar magnetization and dielectric ordering temperature for  $Ba_2LnFeNb_4O_{15}$

This is confirmed through the observation of magnetization for each sample. Except for the particular case of Gd sample, magnetization increases while rare earth size decreases. In the meantime, dielectric polarization increases with the evolution of rare earth size also, which is directly linked to the ferroelectric structure and that points out the effect of cations occupying the square channel ((B) site) on dielectric properties. This behavior has also been observed in titanate, tantalate and niobate TTB materials<sup>16,17</sup>.

Cationic substitutions have been explored in  $Ba_2LnFeNb_4O_{15}$ , with A, B and M sites being substituted with other elements. What has been demonstrated is the global influence of cationic substitutions on dielectric properties, that can be described as a systematic relaxor to ferroelectric crossover for relatively small substitution rates, and then a transition to a single relaxor transition with increasing substitution. This behavior has been summarized on Figure 26 below<sup>13</sup>.

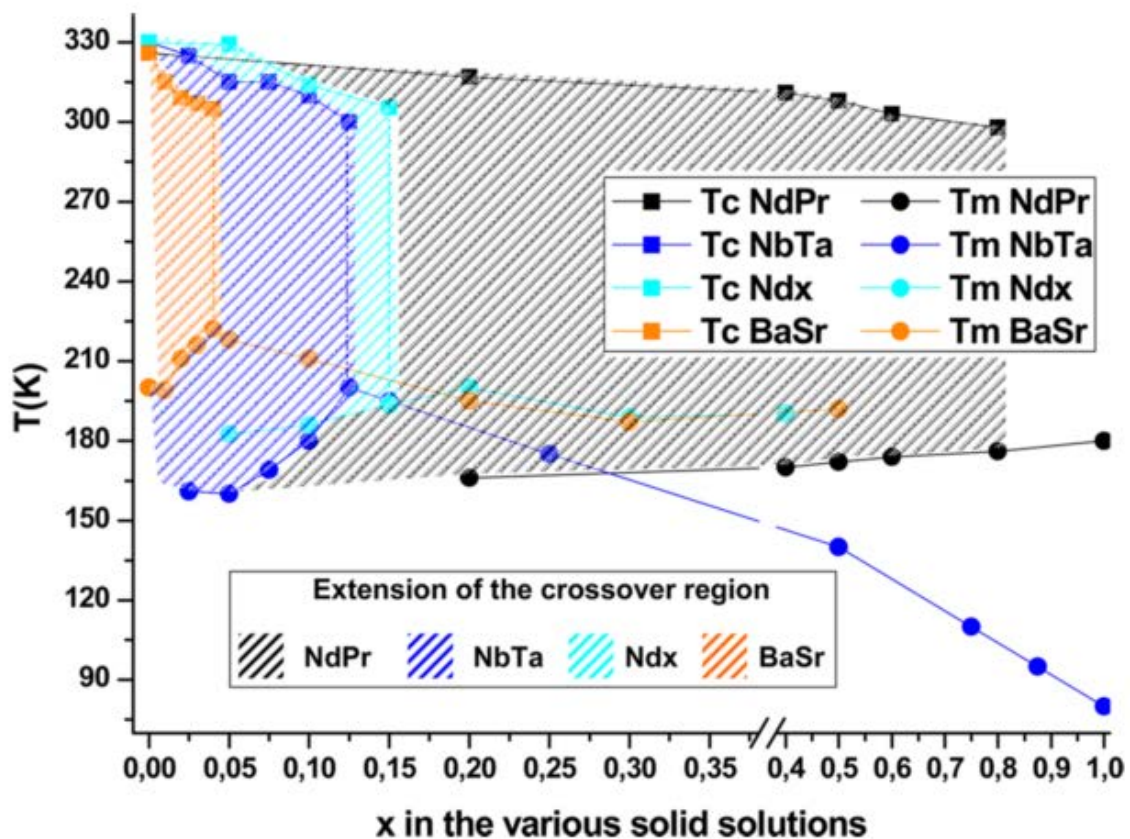


Figure 26: Dielectric phase diagram of  $(Ba,Sr)_2(Nd,Pr)Fe(Nb,Ta)_4O_{15}$  solid solutions showing the evolution of ferroelectric Curie temperatures  $T_C$  and relaxor transition temperatures  $T_m$  when increasing substitution. Shaded areas show the crossover region<sup>13</sup>

However, different substitution levels can be reached in the various solid solutions before triggering the transition from a relaxor-ferroelectric-paraelectric crossover to a single relaxor-paraelectric transition, although in a general way, all the substitutions that have been performed yielded the same qualitative result. Starting from crossover behavior in  $\text{Ba}_2\text{NdFeNb}_4\text{O}_{15}$ , substitution of Sr in A site, Pr in B site, Ta in M site, and a mixed substitution scheme involving A,B and M sites, leads to relaxor compounds<sup>13</sup>. Remarkably, with the latest substitution scheme, which can be written  $\text{Ba}_{6-2x}\text{Ln}_{2x}\text{Fe}_{2+x}\text{Nb}_{8-x}\text{O}_{30}$  (with Ln = Nd<sup>74</sup> and Eu<sup>75</sup>), the ferroelectricity disappear while the niobium content increase. Niobium clearly being a ferroelectrically active ion, this means that in the  $\text{Ba}_2\text{LnFeNb}_4\text{O}_{15}$  family the ferroelectricity is *not* due to Nb<sup>5+</sup> ions. This observation, and the global solid-state chemistry approach described above, lead to the conclusion that the cationic nature of the elements that are inserted in the material is not *directly* influencing dielectric properties. The real driving force behind ferroelectricity is the anionic framework (oxygen) which undergo modifications due to cationic substitutions, and these modifications are responsible for the change in dielectric properties. This modification is likely small and barely visible, in most cases, in classical diffraction techniques (*i.e.* X-ray and neutron powder diffraction analyzed with three dimensional structural models), for which the best structural model is frequently built in a centrosymmetric space group<sup>74</sup> that is not compatible with ferroelectric properties, for example.

However, it has been shown, as described earlier for the so-called “banana”, that periodic or aperiodic structural modulation can take place in the TTB framework, and can be described, using the superspace formalism, as commensurately or incommensurately modulated crystal structures.

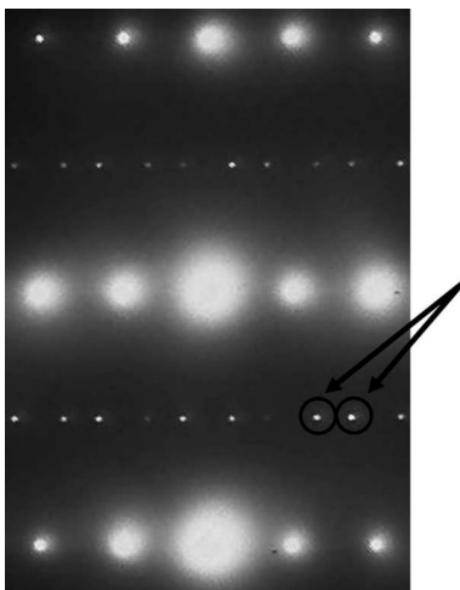


Figure 27: [114] Selected area electron diffraction pattern (SAED) of  $Ba_2LaTi_2Nb_3O_{15}$  with satellite reflections related to an incommensurate structural modulation, highlighted by arrows<sup>16</sup>

#### 1.2.4 Modulated structure of TTB

Few examples of TTB structure are known to be commensurately or incommensurately modulated. However, these structural modifications are of importance as they are generally observed at the ferroelectric  $\rightarrow$  paraelectric or relaxor  $\rightarrow$  paraelectric phase transition. In the  $Ba_2MTi_2Nb_3O_{15}$  family ( $M = La, Bi, Nd, Sm, Gd$ ), a relationship between structure modulation and dielectric properties has been established<sup>16</sup>:

- For Bi and La samples: incommensurate modulations, relaxor behavior
- For Nd, Sm and Gd samples: commensurate modulations, FE behavior

In this work, the authors did not intend to understand the role of structural modulation on dielectric properties, but they highlighted the presence of modulations oriented along [110] (with respect to the standard 12/12/4 unit cell), which were associated with a doubling of the  $c$  parameter, which usually correspond to the polar axis in the TTB matrix.

Further works on TTB superstructures have been undertaken for other compounds. A summary has been performed in order to make a link between ferroelectric properties and the nature of observed modulation (either commensurate or incommensurate)<sup>7</sup>.

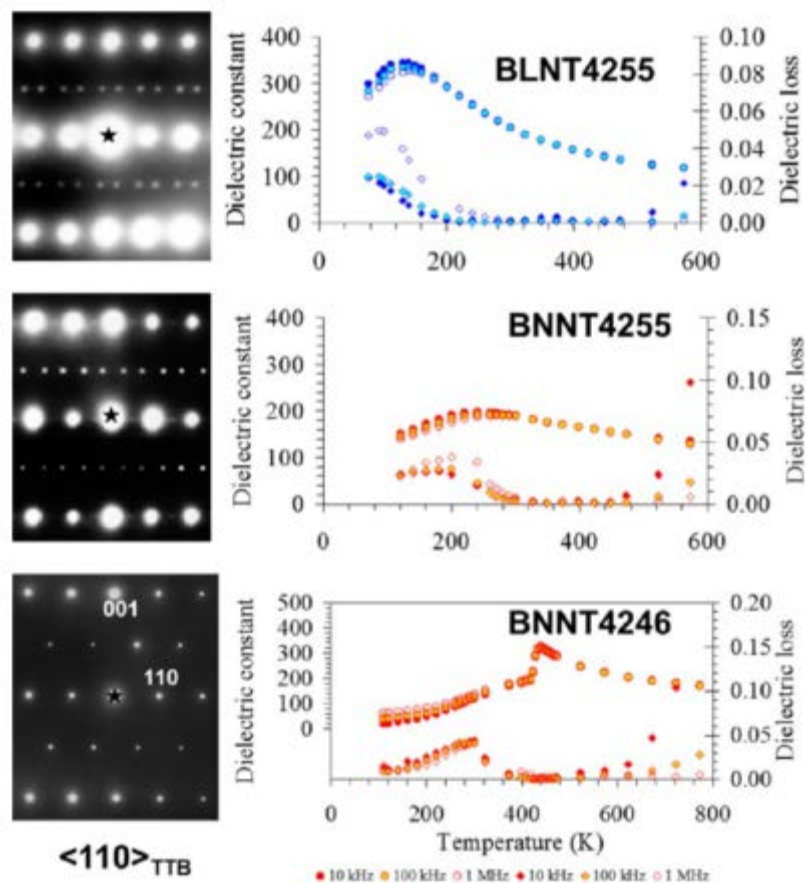


Figure 28:  $\langle 110 \rangle$  Zone Axis Diffraction Pattern (ZADP) and dielectric data as a function of temperature for  $Ba_4La_2Nb_5Ti_5O_{29}$  (BLNT4255),  $Ba_4Nd_2Nb_5Ti_5O_{29}$  (BNNT 4255) and  $Ba_4Nd_2Nb_4Ti_6O_{30}$  (BNNT4246)<sup>7</sup>

On Figure 28 above, the example of zone axis electron diffraction patterns (ZADP) along  $\langle 110 \rangle$  axis for three different TTB compositions show the presence of modulated structures. Both BLNT4255 and BNNT4255, which present one O vacancy per formula unit, present a relaxor  $\rightarrow$  paraelectric transition associated to incommensurate (IC) structure. The third example of BNNT4246 is taken to represent the case of classic ferroelectric transition and show the commensurate structure associated to it.

In a general manner, structure modulation in TTB niobates is strongly linked to the FE or R properties. In these materials, it is very difficult to characterize transitions from relaxor  $\rightarrow$  ferroelectric  $\rightarrow$  paraelectric. Pierre Heijboer demonstrated this difficulty with several members of the  $Ba_2LnFeNb_4O_{15}$  family<sup>74</sup>. For these compounds,  $P4/mbm$  is the space group which gives the best fit with both X-ray and neutron experimental powder diffraction data. This space group is used to describe the three dielectric phases: paraelectric, but also ferroelectric and relaxor phases. This centrosymmetric space group is not compatible with ferroelectric properties.

Incommensurate modulation were also observed in a further work by Pierre Heijboer<sup>74</sup> both on ceramics and single crystals.

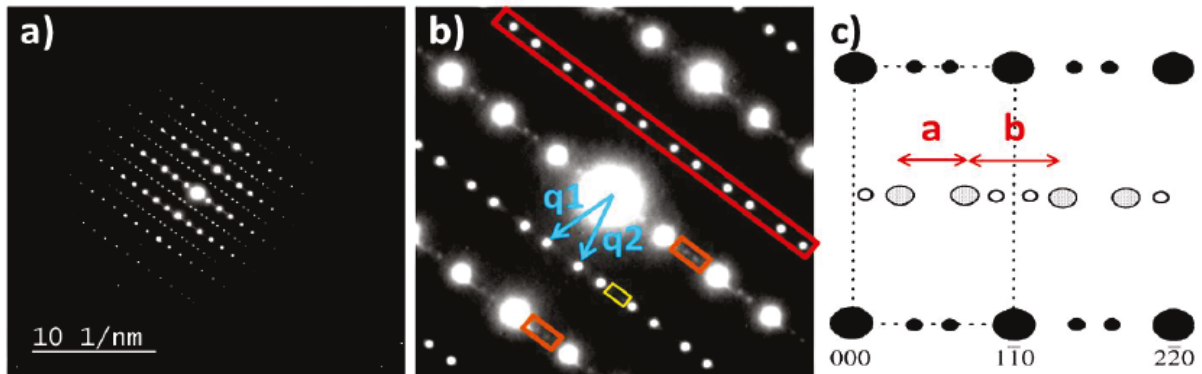


Figure 29:  $\langle 110 \rangle$  SAED on  $\text{Ba}_2\text{LaFeNb}_4\text{O}_{15}$  single crystal sample with a) and b) usign different magnification, and c) schematic representation of the diffraction spots, showing the lack of translationnal symmetry with a and b distances of different value. Red rectangle show first order satellites, orange rectangle the second order and in yellow the third order satellites

Electron diffraction allows for unambiguous detection of aperiodic satellites related to the structural modulation. Here the structure is incommensurate with two modulation vectors  $q_1$  ( $\alpha, \alpha, \frac{1}{2}$ ) and  $q_2$  ( $-\alpha, \alpha, \frac{1}{2}$ ) with  $\alpha \approx 0.3$  which define the superstructure in 3+2 dimensions. Other crystals of essentially the same composition, but different growth conditions, show commensurate modulations with  $\alpha \approx 0.25$ . Synthesis of large single crystals with good homogeneity is very difficult, but both were found to be relaxors, similarly to ceramics of the same composition, although they exhibit different phase transitions. In the end, the study of these single crystals' structure by conventional means (*i.e.* in 3D) did not bring new insight on the mechanism involved in their relaxor behavior.

Indeed, only a few examples of structure refinement using the superspace formalism are available in literature. Among them is the study by Graetsch and co-workers, of the aperiodic crystal structure of  $\text{Ca}_{0.28}\text{Ba}_{0.72}\text{Nb}_2\text{O}_6$  from single crystal X-ray diffraction<sup>12</sup>. Structure refinement was possible using supercentering  $X4bm(A,A,0)(-A,A,0)$  of the 3+2-dimensional superspace group  $P4bm(\alpha, \alpha, \frac{1}{2})(-\alpha, \alpha, \frac{1}{2})$ .

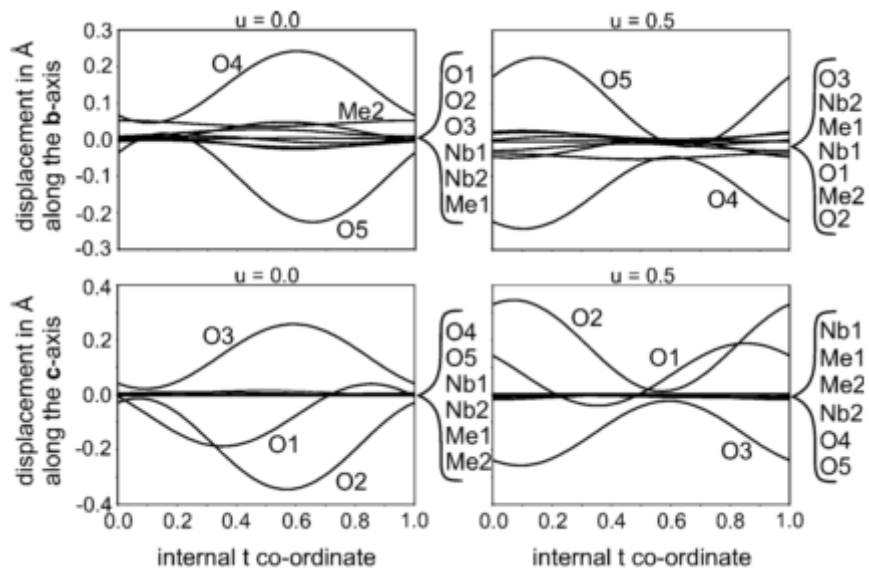


Figure 30: Cationic and anionic displacements along internal  $t$  coordinate after refinement of  $\text{Ca}_{0.28}\text{Ba}_{0.72}\text{Nb}_2\text{O}_6$ <sup>12</sup> aperiodic crystal structure

Figure 30 displays the cationic and anionic displacements from their equilibrium position (determined using conventional 3D crystallography), along the internal  $t$  coordinate (*i.e.* along one of the additional dimension in the superspace formalism). It is visible that in both ( $ab$ ) plane and along the  $c$  axis, cations essentially remain at their equilibrium position (displacements along  $b$  are rather small), whereas oxygens undergo strong displacements, in the ( $ab$ ) plane for octahedral apical oxygens O4 and O5 and along the  $c$ -axis (up to 0.3 Å) for equatorial O1, O2 and O3 oxygens. These displacements are the result of the structural modulation, which are traduced, in averaged 3D models, into atomic displacement parameters (ADP) having exaggerated component along these directions (Figure 31).

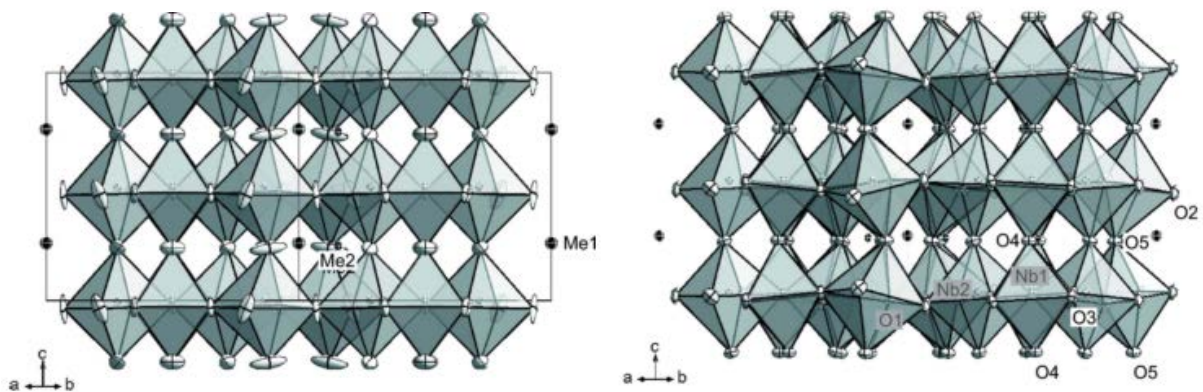


Figure 31: Representation after structure refinement in the hypothesis of (left) 3D and (right) 3+2D space group<sup>12</sup>

In comparison with these results, the refinements realized on  $\text{Ba}_2\text{LnFeNb}_4\text{O}_{15}$  ceramics by Marjorie Albino (from neutron diffraction data) highlighted a similar behavior of oxygen ADP. Apical oxygens look to be strongly displaced in (ab) plane while equatorial oxygens move along the c axis, as illustrated by figure Figure 32.

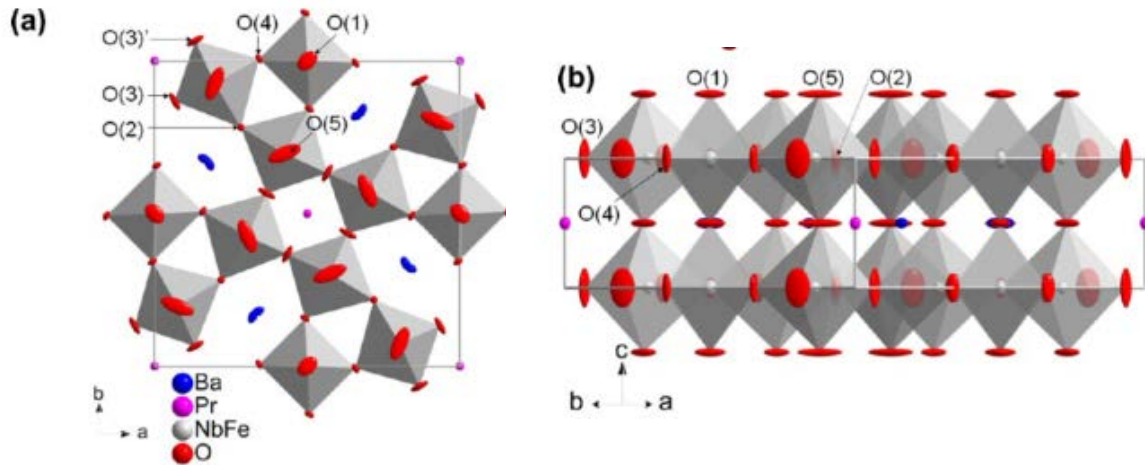


Figure 32: Representation of  $\text{Ba}_2\text{PrFeNb}_4\text{O}_{15}$  after X-ray refinement considering  $P4/mbm$  3D space group<sup>32</sup>

Finally, TTB material exhibit an original behavior, with a strong link between ferroelectric properties and structure, but structural changes are so small that they are not detected by PXRD, even in Rietveld condition, while they can trigger transitions between paraelectric, ferroelectric and relaxor behaviors.

### 1.3. Conclusion on chapter

TTB materials represent an important family of dielectric materials, especially throughout their FE properties. Their high structure flexibility allows for a wide number of compositional possibilities, which have a strong influence on physical properties. This way, it is possible to tune dielectric properties and get pure ferroelectric, relaxor ferroelectric or sometimes both behaviors. The coexistence of these behaviors still hasn't been explained and exploration of these properties would be an interesting way to understand their structural and chemical conditions of appearance.

Different lattice cells have been used to define TTB lattice, but most of all highlight the presence of transitions from periodic to aperiodic structures with the observation of satellite peaks which can either be commensurate or incommensurate. Moreover, the presence of such transitions has

been related to dielectric properties and show a strong influence of the structural modification on the nature of the dielectric anomaly (FE or R).

The exploration of TTB materials of the  $\text{Ba}_2\text{LnFeNb}_4\text{O}_{15}$  family has been performed in ceramics and single crystals. The dielectric behaviour differences between these two forms evidences the necessity to treat them separately. Moreover, the exploration of solid solutions is a powerful tool to explore structure properties relationship. Exploration of various solid solutions done *via* substitutions in pentagonal A, square B and both octahedral M sites in  $\text{Ba}_2\text{NdFeNb}_4\text{O}_{15}$  lead to the observation of a transition from pure FE to R behavior. This seems to highlight the strong role of played by the anionic framework. Therefore, it looks interesting to investigate the effects of  $\text{Li}^+$  insertion in the smallest triangular C site, which has not been explored up to date.

# Chapter 2: Study of structure and dielectric properties of Li substituted $\text{Ba}_2\text{NdFeNb}_4\text{O}_{15}$

A huge work has already been performed on  $\text{Ba}_2\text{NdFeNb}_4\text{O}_{15}$ -based TTB in our group, but still lot of questions remain. A classical approach used to explore the properties of a crystal-chemical family is to explore solid solutions in order to see the influence of substitution(s) on physical properties. In the precise case of  $\text{Ba}_2\text{NdFeNb}_4\text{O}_{15}$ , the influence of substitutions at the A, B, M' and M'' sites has been explored and globally the investigations point out the role of anionic framework on the dielectric properties<sup>13</sup>. To complete this study on cationic substitution, the influence of C site filling remains to be explored, through the insertion of  $\text{Li}^+$  ions that are small enough to be accommodated in this site. This chapter deals with the exploration of three different solid solution and their dielectric properties, in order to confirm or infirm the previous conclusion concerning the role of the anionic framework. The final part highlights some particular observations on  $\text{Ba}_2\text{NdFeNb}_4\text{O}_{15}$ , which is the parent compound in this study.

## 2.1. Synthesis of solid solutions

### 2.1.1 Choice of solid solutions

The TTB matrix is very flexible and allows a large and diversified range of possible compositions. In this work, we start from the parent compound  $\text{Ba}_2\text{NdFeNb}_4\text{O}_{15}$  and insert  $\text{Li}^+$  in C site, but when doing so, we have to adjust the cationic composition at other sites, as preservation of electroneutrality is a key point in dielectric solid solutions. Consequently, lithium insertion may not be the only reason for the modification dielectric behavior. Removing cations at other sites, or changing their relative contents for the sake of electrical compensation, can also have an influence on these properties. So, to avoid this problem, a solution is to explore solid solutions relying on different compensation schemes, and then compare the resulting behavior. If all the solid solution present the same evolution, this one can be attributed to  $\text{Li}^+$  insertion. If not, one can attempt exploration of the underlying mechanisms.

Three solid solutions have been selected in order to perform such exploration:

- $\text{Ba}_2\text{Nd}_{1-(x/3)}\text{Li}_x\text{FeNb}_4\text{O}_{15}$  (abbreviated NL) in which  $\text{Li}^+$  insertion is compensated by  $\text{Nd}^{3+}$  vacancies in the square channels (B site).
- $\text{Ba}_{2+x}\text{Nd}_{1-x}\text{Li}_x\text{FeNb}_4\text{O}_{15}$  (abbreviated BNL) in which  $\text{Li}^+$  insertion is compensated by the substitution of  $\text{Nd}^{3+}$  by  $\text{Ba}^{2+}$  in square channels (B site) without introduction of vacancies.
- $\text{Ba}_2\text{NdLi}_x\text{Fe}_{1+(x/2)}\text{Nb}_{4-(x/2)}\text{O}_{15}$  (abbreviated LFN) in which  $\text{Li}^+$  insertion is compensated by changing the  $\text{Fe}^{3+}/\text{Nb}^{5+}$  ratio in octahedral sites, with a limited impact on the TTB framework as iron and niobium have similar radii.

Through these three solid solutions, all the different sites are involved selectively and the specific contribution of  $\text{Li}^+$  insertion in triangular C sites can be evaluated. The choice of these solid solutions results from previous works on various solid solutions<sup>13,26,75,76</sup>, as well as single crystals. The influence of  $\text{Nd}^{3+}$  vacancies was studied by Marjorie Albino in single crystals<sup>32</sup>. The influence of  $\text{Nd}^{3+}$  substitution was studied by Pierre Heijboer<sup>74</sup>, and will be used as a reference in this work. As a general trend in this family of materials, rare earth accommodation at the B site is most of the time incomplete<sup>46</sup>. This observation lead to the exploration of Nd deficient ceramics of  $\text{Ba}_{6-2x}\text{Nd}_{2x}\text{Fe}_{1+x}\text{Nb}_{9-x}\text{O}_{30}$ <sup>74</sup>. Inserting  $\text{Li}^+$  in the C site can then compensate the loss of  $\text{Nd}^{3+}$  in B site and may also avoid the formation of secondary phases, for limited concentrations at the least. The accommodation of Ba at the Nd site has been demonstrated<sup>74</sup> and allows to accommodate Li while keeping the square channel fully occupied. Finally, the substitution of Nb by Fe, the radii of which are very close ( $\text{Nb}^{5+}$ : 64 pm;  $\text{Fe}^{3+}$ : 65 pm) allows for the insertion of Li without much modification of the TTB framework otherwise.

### 2.1.2 Solid state synthesis

Once the compositions have been determined, the synthesis protocol has to be precised. In TTB materials, most of the published works are based on the solid-state route. This simple technique allows for highly crystallized and pure phase in the case of TTB, and for the exploration of dielectric properties thanks to highly pure and dense ceramics. Solid state route is therefore relevant to obtain reliable samples with the desired compositions and microstructures. Sample

preparation is performed in two conventional steps, firing and sintering, with optimized thermal cycles. An important work on synthesis conditions to get a good crystallinity associated to the lowest secondary phase content has been done by Elias Castel<sup>46</sup> for  $\text{Ba}_2\text{LnFeNb}_4\text{O}_{15}$  TTBs (Ln = La, Pr, Nd, Sm, Eu). In the present work, the samples are elaborated according to the conclusions of this work. In the following the preparation of the samples is described in detail.

#### 2.1.2.1 Powder mixing

Synthesis is performed with oxides and carbonates.  $\text{BaCO}_3$ ,  $\text{Nd}_2\text{O}_3$ ,  $\text{Li}_2\text{CO}_3$ ,  $\text{Fe}_2\text{O}_3$  and  $\text{Nb}_2\text{O}_5$ , and the purest precursors among those available are used (typically above 99%). To remove hydroxyl groups resulting from hydroxylation of rare earth oxide, a preliminary treatment is performed overnight in a furnace at  $1000\text{ }^\circ\text{C}$  on Neodymium oxide. After this treatment, powders are mixed in targeted stoichiometric quantities, then are hand milled in an agate mortar for 30 min (for small contents below 4 g). This step is one of the most important of the solid-state route, and is critical to obtain a good homogeneity. After mixing the powders, these are fired.

#### 2.1.2.2 Pellet firing

After the mix of powder is obtained, they are pelletized and inserted in a furnace for the following heat treatment under air:

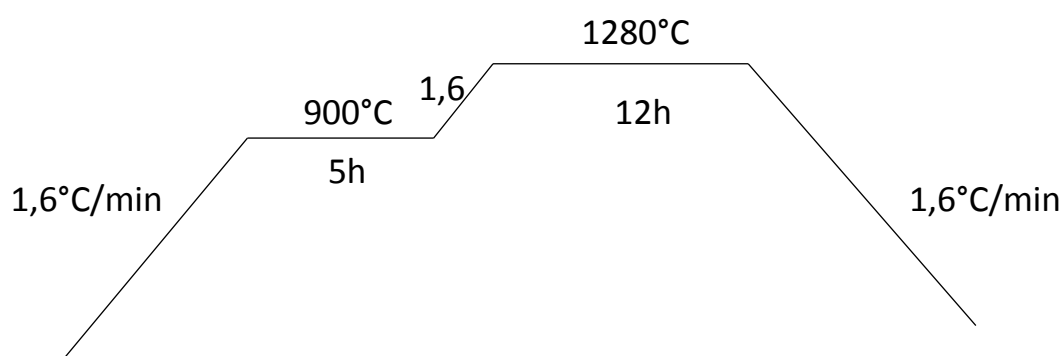


Figure 33: Schematic representation of synthesis heat treatment for TTB ceramics

A first dwell at  $900\text{ }^\circ\text{C}$  for 5h is applied for the decarbonation of  $\text{BaCO}_3$ . After this dwell, reaction takes place at  $1280\text{ }^\circ\text{C}$  for 12h, under air. After the firing, the pellets are milled in a vibrating mill for 45 min and phase purity is checked in XRD. The final step is now sintering.

### 2.1.2.3 Pellet sintering

If the powder obtained following firing has the expected composition, sintering has to be performed. In order to have a good mechanical strength of the green pellets before sintering, a sintering additive (binder) is used. Then, powders are pressed into pellets and placed in a furnace under air and undergo the following thermal cycle (Figure...).

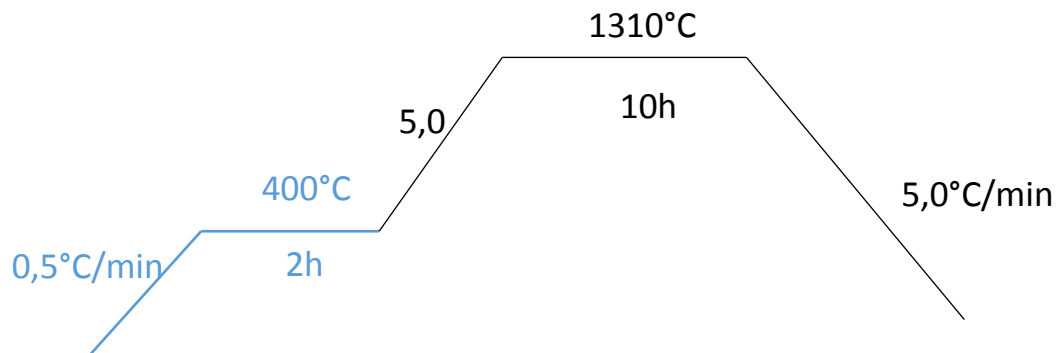


Figure 34: Schematic representation of sintering treatment of ceramics under air

After sintering, the obtained pellets can be used for characterization. Three pellets are prepared in the same conditions for each composition. All are 8 mm diameter, but one is about 2-3 mm thick and the two others are 1 mm thick. The smallest ones are dedicated to dielectric measurements and the largest one is broken and partly milled for the sake of structural and microstructural analysis.

## 2.2. Powders and pellets characterizations

Characterization of ceramics is the objective of this study, especially structural and dielectric characterizations, but before doing so, a good purity of the powder is essential before sintering, and therefore characterization of fired powders is important.

### 2.2.1 Structural characterization of fired powders

Structural characterization has been performed on fired powders after the first heat treatment using XRD.

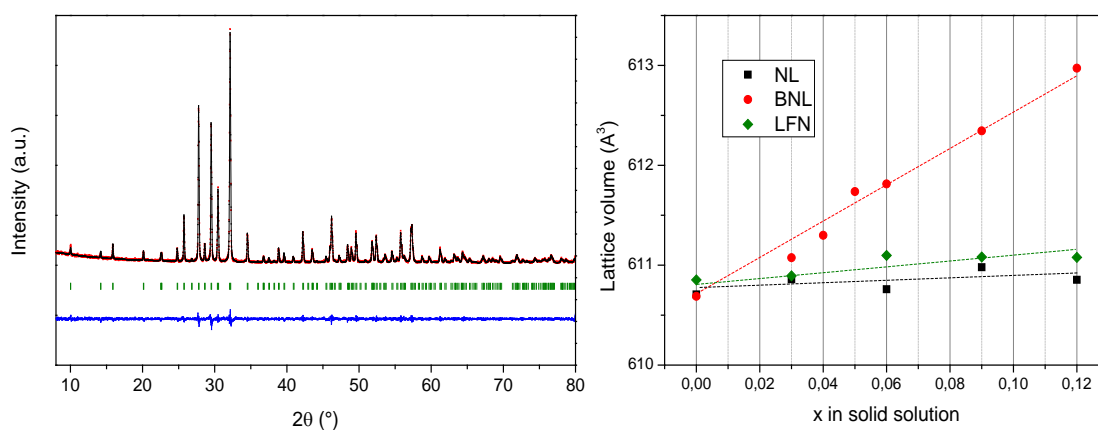


Figure 35: XRD profile refinement of  $x = 0$  for NL solid solution and lattice volume plot for the three solid solutions NL, BNL and LFN. Dotted lines are guides for the eyes

Profile refinement is performed on routine XRD patterns (the quality of which allows for such analysis) and give access to lattice parameters. With increasing  $x$  (Li content) in the various solid solutions, two different evolutions can be seen. In the NL and BNL solid solutions, no significant evolution of lattice volume is visible, whereas in the BNL solid solution, a larger evolution can be observed with a global increase of lattice volume from  $610.71(1) \text{ \AA}^3$  to  $613.03(1) \text{ \AA}^3$  when increasing Li content from  $x = 0$  to  $x = 0.12$ . This is due to the substitution scheme. In the first solid solution NL, insertion of Li is compensated by removing up to 0.04 Nd when  $x = 0.12$ , which corresponds to a formula  $\text{Ba}_2\text{Nd}_{0.96}\text{Li}_{0.12}\text{FeNb}_4\text{O}_{15}$ . In this case it means  $\text{Nd}^{3+}$  site occupation is 96 %, which is close to the limit observed for this phase in prior studies. In addition, and according to Shannon and Prewitt ionic radii<sup>77</sup>,  $\text{Li}^+$  is a very small ion and in a 8-coordinated environment, its size reaches  $0.92 \text{ \AA}$ . Its apparent size may increase a little in a 9-coordinated environment but since only 0.12 Li are added to the phase, the lattice evolution must remain very small. In LFN solution,  $\text{Li}^+$  insertion is accompanied by a substitution of  $\text{Fe}^{3+}$  for  $\text{Nb}^{5+}$  at octahedral sites, their ionic radii being  $0.645 \text{ \AA}$  and  $0.64 \text{ \AA}$  respectively. Thus, no massive lattice parameter change is expected from the substitution of  $\text{Fe}^{3+}$  for  $\text{Nb}^{5+}$ . On the opposite, in the case of BNL solution, for each  $\text{Li}^+$  that is inserted, one  $\text{Ba}^{2+}$  ion is substituted for an  $\text{Nd}^{3+}$  ion. Since the A site is fully occupied by  $\text{Ba}^{2+}$  ions, the substituted ones must be inserted at the B site, a substitution scheme that was confirmed by Pierre Heijboer in his study of the  $\text{Ba}_{6-2x}\text{Nd}_{2x}\text{Fe}_{2+x}\text{Nb}_{8-x}\text{O}_{30}$  solid solution. As  $\text{Ba}^{2+}$  ionic radius reaches  $1.61 \text{ \AA}$ , and taking into account that  $\text{Nd}^{3+}$  ionic radius is  $1.27 \text{ \AA}$  - considering 12-coordination<sup>77</sup> - the substitution of  $\text{Nd}^{3+}$  by  $\text{Ba}^{2+}$  must result in a significant lattice size increase.

Then, one can conclude that the evolution of lattice volume determined from PXRD seem to be consistent with what can be expected from crystal-chemical considerations.

After structural characterization of fired powders has been achieved, sintering is performed at 1310 °C for 10h. In the following will be presented the microstructural, physical and structural characterization of these pellets, in this order.

### 2.2.2 Pellet microstructure

As explained previously, densification of samples is an important step to be able to perform reliable measurements of intrinsic dielectric properties. After pellets are sintered, their densification is measured by measurement of thickness and diameter, then they are weighed, and relative densities calculated. All samples are dense enough for dielectric characterization, with compactness beyond 90 %, which limits the spurious contributions from porosities, especially open ones.

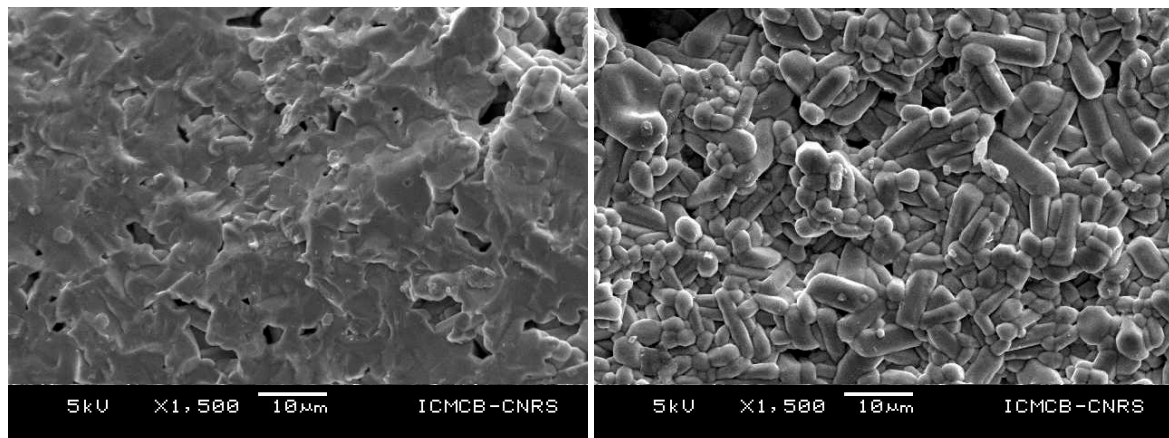
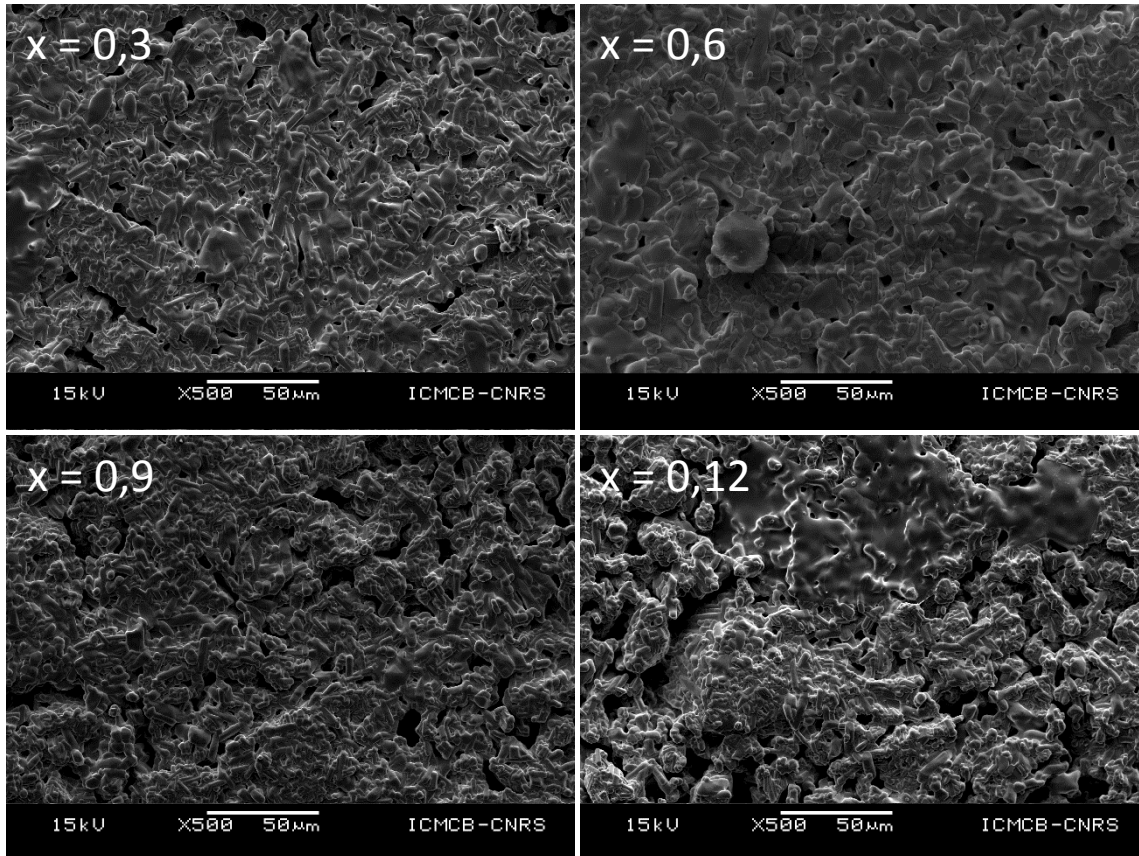


Figure 36: SEM pictures of a (left) fracture and (right) surface of a pellet with NL ( $x = 0$ ) composition

Figure 36 shows SEM pictures of surface and fracture of a pellet with  $\text{Ba}_2\text{NdFeNb}_4\text{O}_{15}$  composition. The grains are easily visible on the surface view and show two different shapes. Some of them are spherical but most them are rod-like. The fracture view shows a rather dense ceramic, with closed porosities visible, and intragranular fractures which supports a satisfying sintering.

Figure 37 shows the surfaces of samples of the NL solid solution for various Li contents ( $x = 0.3, 0.6, 0.9$  and  $0.12$ ). Compared to the microstructure of the sample without Li, all the

substituted compounds present a microstructure composed of rod-like grains and signs of partial melting. These fused zones may be related to the presence of Lithium as Li compounds<sup>78,79</sup> are known as sintering aids ( $\text{BaLiF}_3$  used for  $\text{BaTiO}_3$ <sup>80</sup>), and Li salts are also frequently used for single crystal growth<sup>81</sup>, as was the case for  $\text{Ba}_2\text{LnFeNb}_4\text{O}_{15}$  single crystals<sup>31,32</sup>.



*Figure 37: SEM pictures of pellets of NL solid solution with different Li content*

Anyway, no abnormal grain growth is observed and the liquid part in pellets remains limited to the surface, thus no influence of this microstructure on the dielectric behavior of the pellets is expected.

For the two other solid solutions the same evolution is observed and no difference with NL solution has been observed with increase of Li content. As the microstructures are comparable and can be expected to have limited and similar contribution to the pellets dielectric response, allowing for comparison of these response, dielectric measurements were performed for the three solid solutions.

### 2.2.3 Dielectric measurements

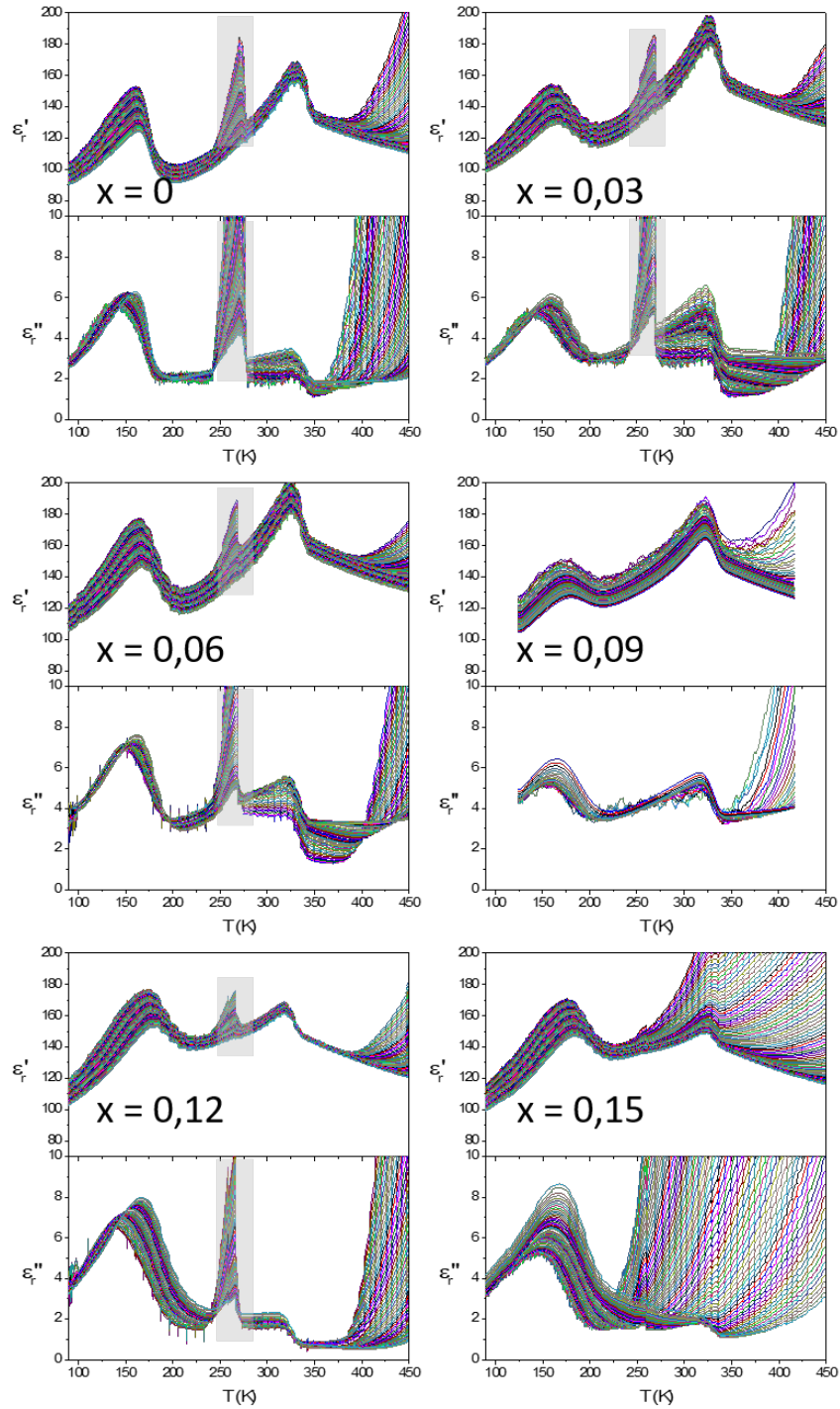


Figure 38: Permittivity measurements of NL solid solution ceramics for  $x = 0$  to  $x = 0.15$  and frequency from  $10^2$  to  $10^6$  Hz. Grayed areas indicate water contribution

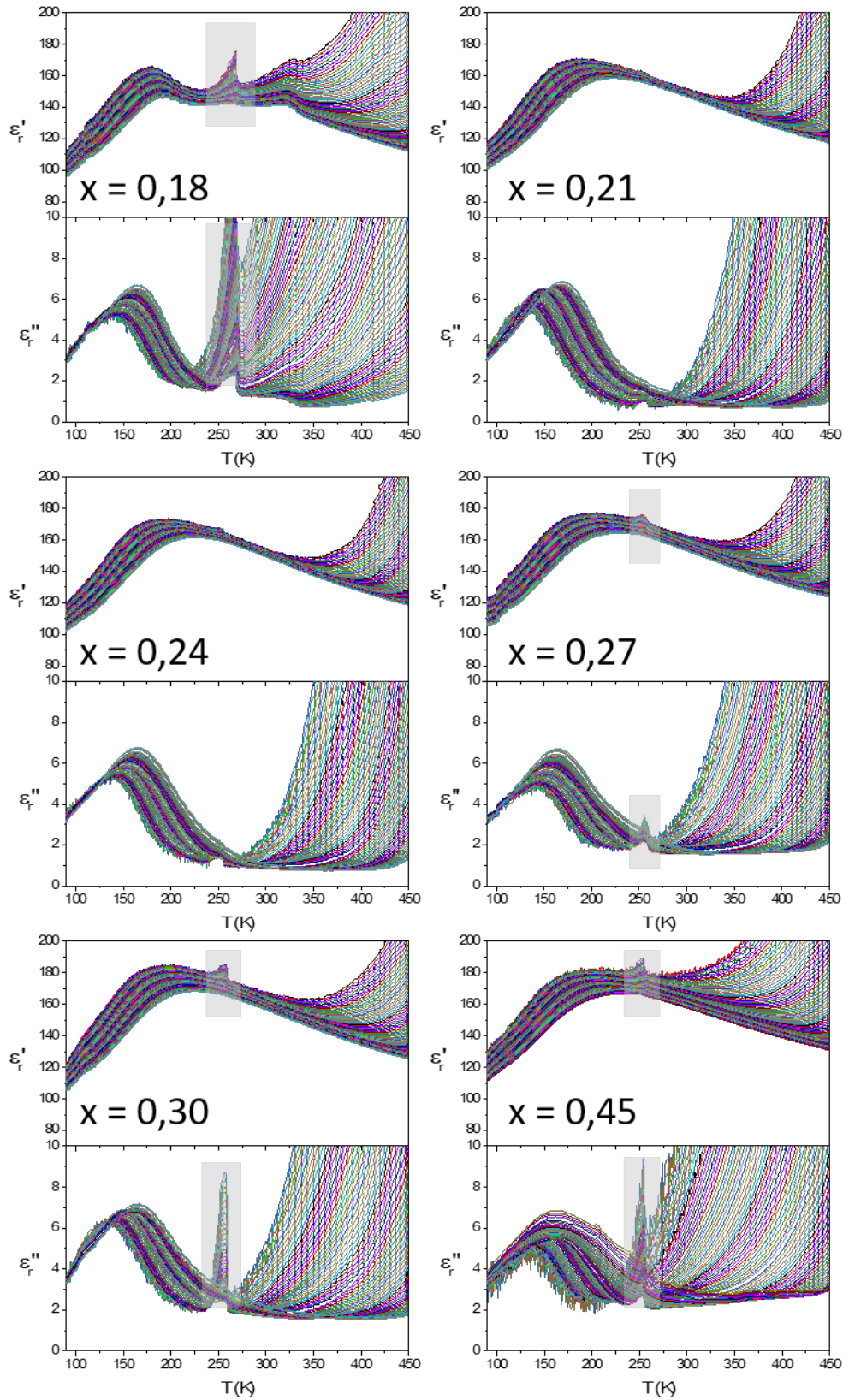


Figure 39: Permittivity measurements of NL solid solution ceramics for  $x = 0.18$  to  $x = 0.45$  and frequency from  $10^2$  to  $10^6$  Hz

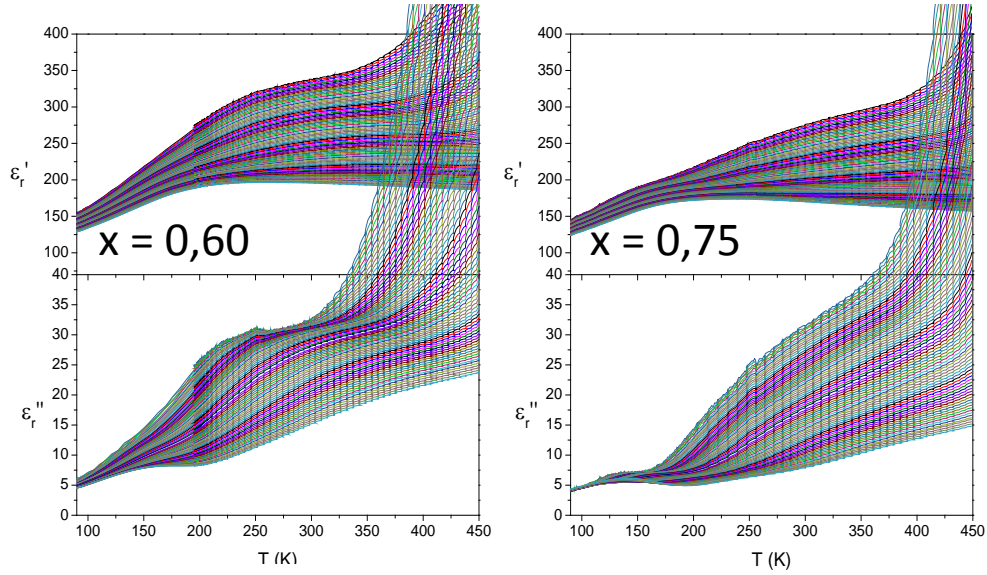


Figure 40: Permittivity measurement of NL solid solution for  $x = 0.60$  and  $x = 0.75$ , frequency from  $10^2$  to  $10^6$  Hz

For all the pellets of the three solid solutions, NL, BNL and LFN, dielectric measurements have been performed to obtain real and imaginary part of relative dielectric permittivity  $\epsilon'$  and  $\epsilon''$ .

Figure 38, Figure 39 and Figure 40 display the permittivity of NL solid solution for  $x = 0, 0.3, 0.6, 0.9, 0.12, 0.15, 0.18, 0.21, 0.24, 0.27, 0.30, 0.45, 0.60$  and  $0.75$  on heating. In some cases, residual water in the environmental setup lead to the observation of a peak, both in real and imaginary part of permittivity, in the range 250-270 K, which is not considered in the interpretation of the results. Two different kinds of response appear in these measurements. For small Li contents,  $0 \leq x \leq 0.18$ , two distinct peaks are observed. The low temperature one (around 200 K) has a maximum that is frequency dependent, whereas the second one around 330 K is frequency independent. They respectively correspond to relaxor  $\rightarrow$  ferroelectric (R) and ferroelectric  $\rightarrow$  paraelectric (FE) phase transitions and thus a relaxor to ferroelectric crossover is found in this region of the dielectric phase diagram. For larger Li contents, only R transition is observed, and this behavior is similar to that of others solid solutions derived from  $\text{Ba}_2\text{NdFeNb}_4\text{O}_{15}$ . In addition, for  $x > 0.03$ , the amplitude of the FE transition decreases with increasing Li content, while that of the R transition seems to reach a plateau. The dielectric transition temperatures  $T_C$  and  $T_m(100 \text{ kHz})$  have been extracted from these measurements and are plotted on Figure 41.

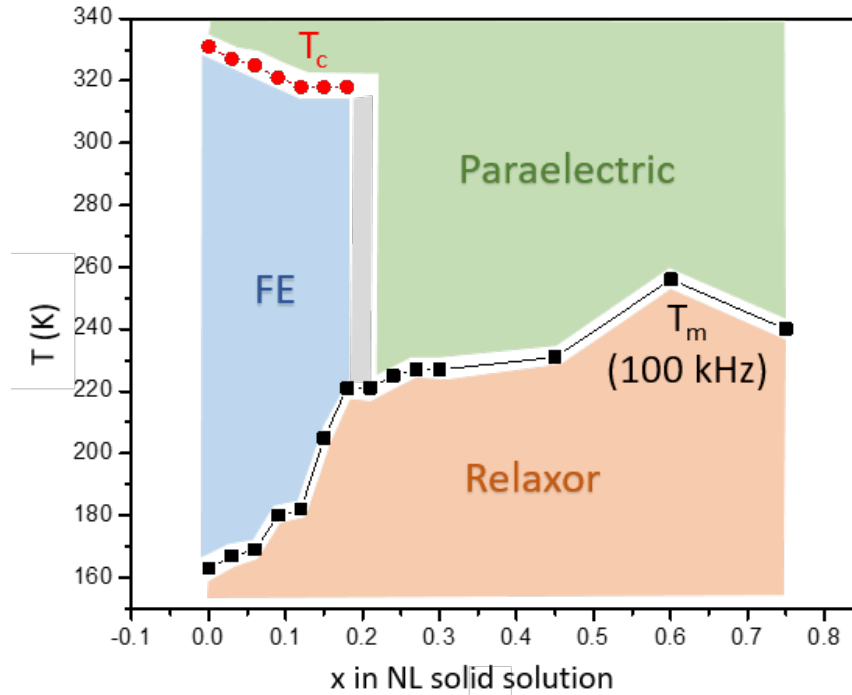


Figure 41: Dielectric phase diagram with FE Curie temperature ( $T_c$ ) and  $T_m$  at 100 kHz in NL solid solution. Grey zone is undetermined

A constant decrease of  $T_c$  from 331 to 318 K is observed between  $x = 0$  and  $x = 0.12$ , then what appears as a plateau at 318 K for  $x = 0.12$  to  $0.18$ , then no FE transition is observed for larger Li contents. The linear evolution of  $T_c$  with Li content for  $x \leq 0.12$  tends to confirm a linear evolution of the composition of ceramics, and thus the successful insertion of Li in the structure (which cannot be confirmed from structural or microstructural analysis). Stabilization of  $T_c$  between  $x = 0.12$  and  $0.18$  points out a second behavior in the evolution of this NL solid solution, which could be related to a crystal-chemical interplay between lithium insertion and the corresponding neodymium vacancies.

Three stages are visible in the evolution of  $T_m$  (100 kHz) of NL solid solution with increasing Li content. The first one for  $0 \leq x \leq 0.12$  shows a linear increase of  $T_m$  from 163 to 182 K associated to the linear decrease of  $T_c$ . The ramp of  $T_m$  versus  $x(\text{Li})$  is  $\sim 160$  K/Li in this range, while  $T_c$  decreases of about  $-110$  K/Li in the same range. The second is in the range  $0.12 \leq x \leq 0.18$ . This range corresponds to a stronger increase of  $T_m$  from 182 to 221 K, which represents about 650 K/Li, while  $T_c$  remains constant. After the ferroelectric transition vanishes, for  $x \geq 0.21$ ,  $T_m$  evolution is more limited ( $T_m$  for  $x = 0.6$  is not considered here due to perturbation by large dielectric losses) ranging from 221 to 240 K, which represents 35 K/Li.

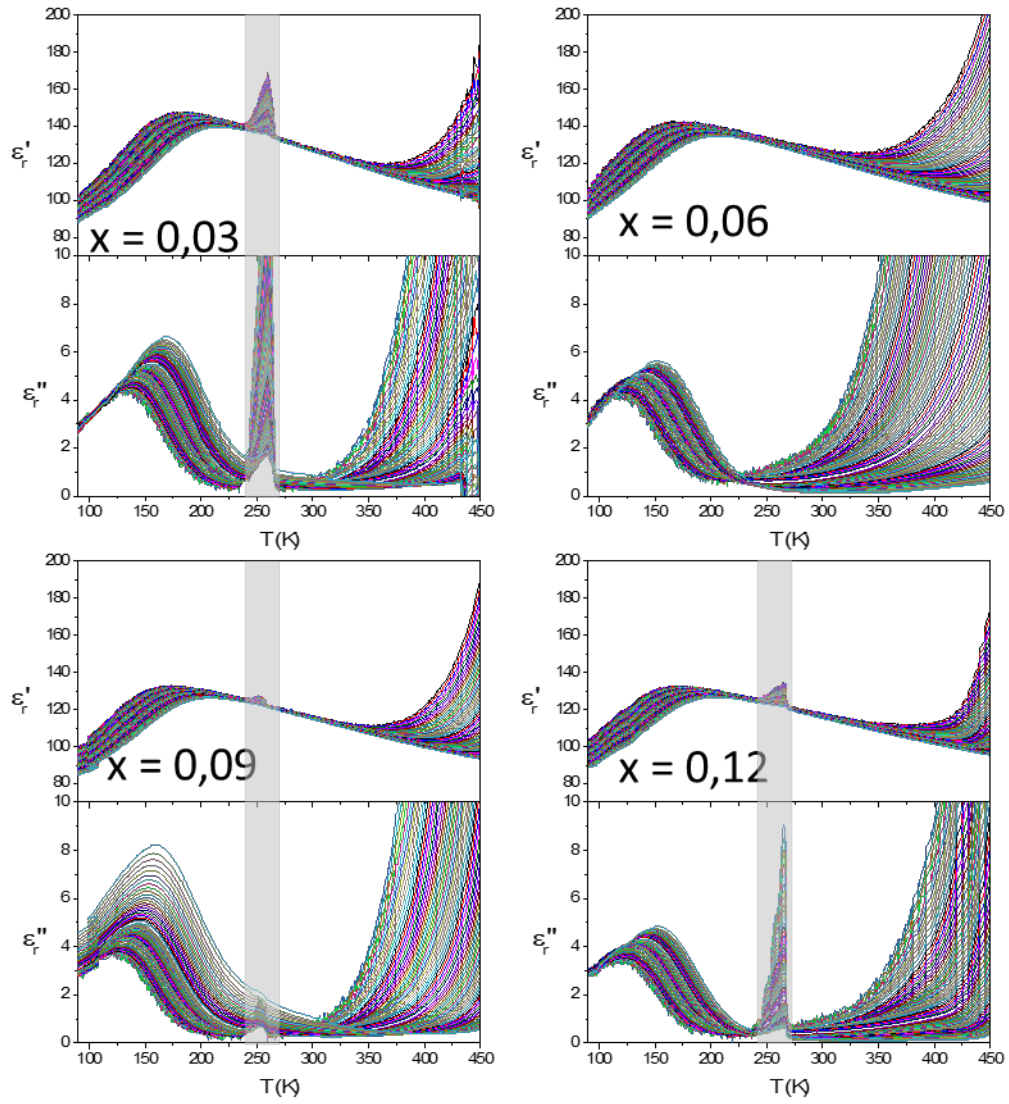


Figure 42: Permittivity measurements of BNL solid solution ceramics for  $x = 0.03$  to  $x = 0.12$

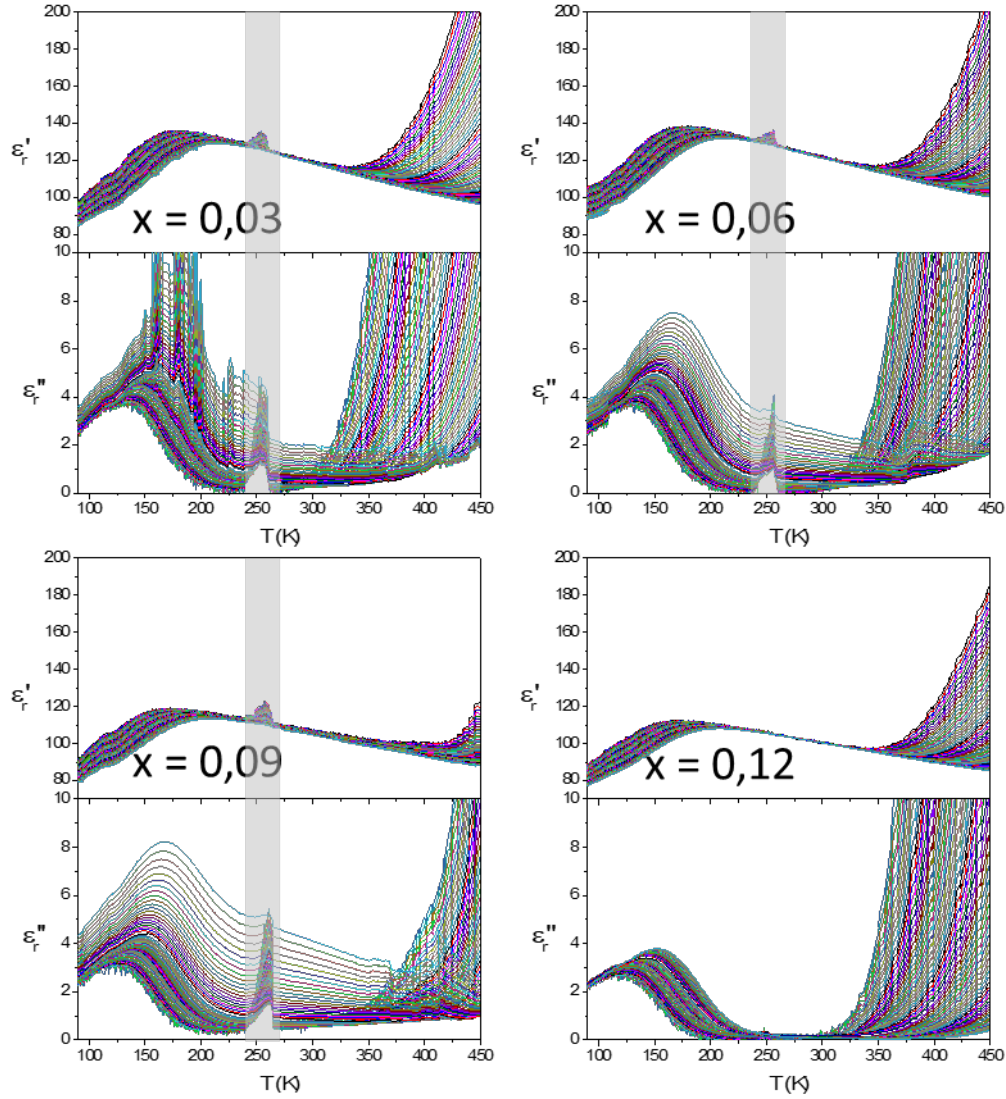


Figure 43: Permittivity measurements of LFN solid solution ceramics for  $x = 0.03$  to  $x = 0.12$

Figure 42 and Figure 43 represent the other BNL and LFN solid solutions. As observed on these measurements, insertion of Li in the phase leads to a single R transition that is observed even for the low Li contents, although these solid solutions rely on very different compensation mechanisms (Ba/Nd and Fe/Nb substitutions). However, the evolution of  $T_M$  (100 kHz), displayed on Figure 44 is different in LN and in BNL and LFN. In the case of NL, there is an increase of  $T_m$ , whereas in BNL and LFN, the single R transition is characterized by rather elevated  $T_m$  (with respect to samples with similar Li content from the NL solid solution) which are slightly decreasing with increasing Li content ( $\sim 120$  K/Li for BNL and  $\sim 90$  K/Li for LFN). It is noteworthy that throughout the whole explored range of the NL solid solution,  $T_m$  increases

albeit very slowly when  $x(\text{NL}) > 0.21$ . Thus, very different behaviors are found when Li insertion is not compensated by Nd vacancies.

Additionally, the  $x = 0$  sample correspond to  $\text{Ba}_2\text{NdFeNb}_4\text{O}_{15}$  and is the same for the three solid solutions (*i.e.* it has only been prepared once). For BNL and LFN solid solutions, no data has been collected in the range  $0 \leq x \leq 0.03$ , but one can expect a  $\text{R} \rightarrow \text{FE}$  crossover in that region for BNL and LFN, with a fast increase of  $T_m$  (dotted lines on figure...). To explore this idea, additional syntheses have been realized, but yielded unexpected behaviors for  $x = 0$ , that were further explored and will be presented in the next chapter of the present manuscript.

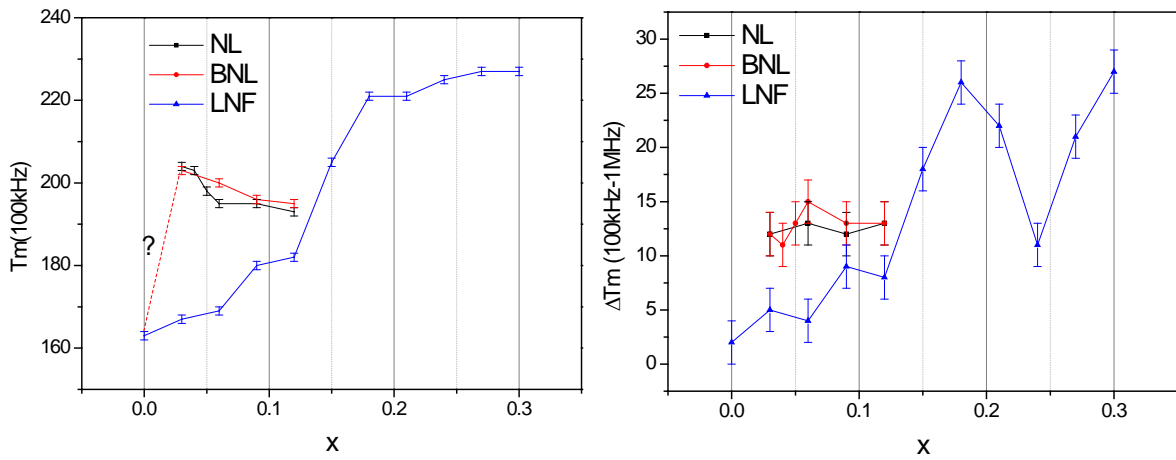


Figure 44: Evolution of  $T_m$  (100 kHz) and  $\Delta T_m(100\text{kHz}-1\text{MHz})$  in the different solid solutions

In addition,  $\Delta T_m(100\text{kHz}-1\text{MHz})$  is displayed on Figure 44 and shows here again a difference between NL and the two other solid solutions. For NL,  $\Delta T_m$  is very small at low  $x$  values (up to 0.06) it remains close to a FE behavior with limited frequency dependence of the transition temperature. However, at higher  $\text{Li}^+$  content, the relaxor effect, with a diffuse phase transition, is clearly visible. Especially from 0.12 to 0.18, there is an increase of 18 K which is quite important, and corresponds to the increase observed on  $T_m$  values, right before the transition from  $\text{R} \rightarrow \text{FE}$  region  $0 \leq x \leq 0.18$  to the R transition region  $0.21 \leq x \leq 0.75$ . One could consider that the increasing  $T_m$  is essentially due to the spreading of the relaxor effect through a larger temperature range.

It is possible to follow the evolution of  $\max(\epsilon')$  with Li content (Figure 45). In NL, the previously cited two regimes are depicted in black and green, respectively for the  $\text{R} \rightarrow \text{FE}$  crossover region  $0 \leq x \leq 0.18$  and the R transition region  $0.21 \leq x \leq 0.75$ . In the first region,  $\epsilon'$

increases from 150 to 175, then drops back to 150 at the transition to a single R phase. Then, an increase is observed up to 200 for  $x = 0.45$  and the permittivity drops back to 175 for  $x = 0.75$ , but the two last values are difficult to evaluate because of the large dielectric losses for samples with  $x > 0.45$ , as can be seen in Figure 40.

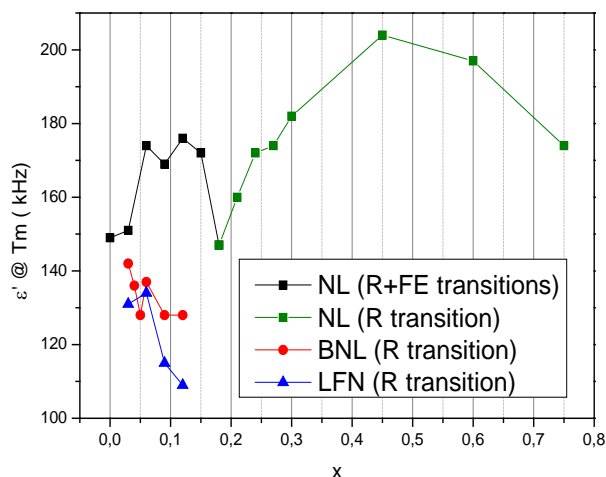


Figure 45: Evolution of  $\epsilon'$  at  $T_m$  (100 kHz) in NL, BNL and LFN solid solutions

In BNL, permittivity decreases from 140 to 130 between  $x = 0.03$  and 0.12, which is, in comparison to NL solution, a quite small variation. The suppression of ferroelectricity with a very small substitution rate is to be compared with the  $(\text{Ba,Sr})\text{NdFeNb}_4\text{O}_{15}$  solid solution in which the substitution of 5% of baryum by strontium suppress ferroelectricity. It is likely that the insertion of Ba in the square channels in the BNL solid solution has a strong influence on the dielectric properties. In the case of LFN, permittivity decreases from 135 to 110 from  $x = 0.03$  to  $x = 0.12$ , which is a small but significant evolution. This decrease is expected since Li insertion is compensated by an increase of  $\text{Fe}^{3+}/\text{Nb}^{5+}$  ratio. Since  $\text{Nb}^{5+}$  is the ferroelectrically active cation in the structure, FE interactions (and polarization) could be expected to decrease with Li content increasing. Finally, remarkably enough, in NL solid solution, neither  $\text{Li}^+$  nor  $\text{Nd}^{3+}$  are ferroelectrically active and their influence on FE transitions must lie in the geometrical modifications of the octahedral framework they induce.

As a global behavior, these three explored solid solutions exhibit a transition from a first composition with both FE and R transitions, which turns into a single R phase transition upon Li insertion. Depending on the substitution scheme, the contents of Li necessary to obtain this

transition can vary from less than 0.03 to  $\sim 0.2$  Li. On the one hand, in the BNL solid solution it is likely that the Ba/Nd substitution plays the most important role, while the similar behavior observed in the LFN solid solution suggest that here also Li insertion may not be the main parameter. On the other, this family of TTB is known for its ability to accommodate  $\text{Ln}^{3+}$  vacancies (refs 42,44, 46) while maintaining FE properties, and thus the NL solid solution likely depicts the influence of  $\text{Li}^+$  insertion in these materials. Overall, the evolution of the dielectric response in these solid solutions is rather similar to the previously explored systems involving substitutions at A, B and M sites. In this view, the present work tends to confirm the previous hypothesis on the preminent role of the anionic framework in the FE properties of this phase<sup>13</sup>. However, some questions remain about the structural origin of these behaviors and the microscopical mechanisms responsible for the transition from  $\text{R} \rightarrow \text{FE}$  to single R behavior.

#### 2.2.4 Structural characterizations

In order to characterize the structure of each sample, routine XRD patterns have been collected on both powders and pellets. Profile refinements have been performed on these samples to get access to lattice parameters and use them to decipher the dielectric measurements performed on the same samples. In order to get access to crystallographic information like atomic positions and displacements, or site occupancies, Rietveld acquisition were also performed on a few samples of the NL solid solution, which appears as the most relevant concerning the influence of Li on the dielectric properties of these TTBs.

Figure 46 shows a routine XRD pattern profile refinement of NL  $x = 0$  composition as an example. Refinement was performed in the  $P4/\text{mbm}$  space group ( $n^\circ 127$ ). This XRD pattern indicates a good crystallization of the phase and reveals the absence of a secondary phase. From this refinement, we have access to lattice parameters of the sample. This way, all the solid solution's samples were measured by XRD and their lattice parameters were determined and are displayed in Figure 47.

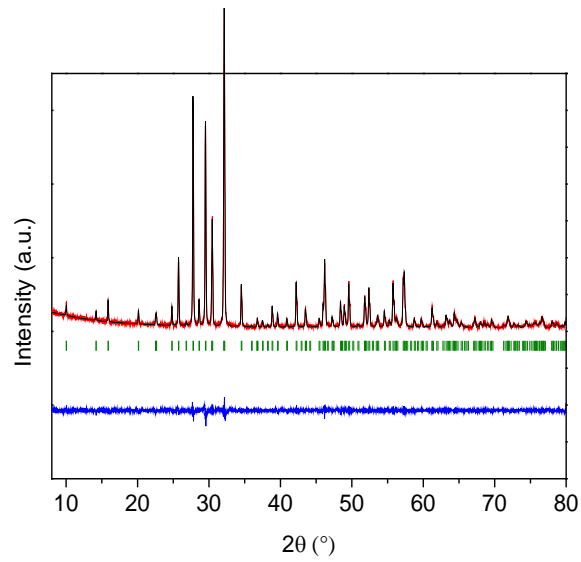


Figure 46: Routine XRD pattern refinement of NL  $x = 0$  powder

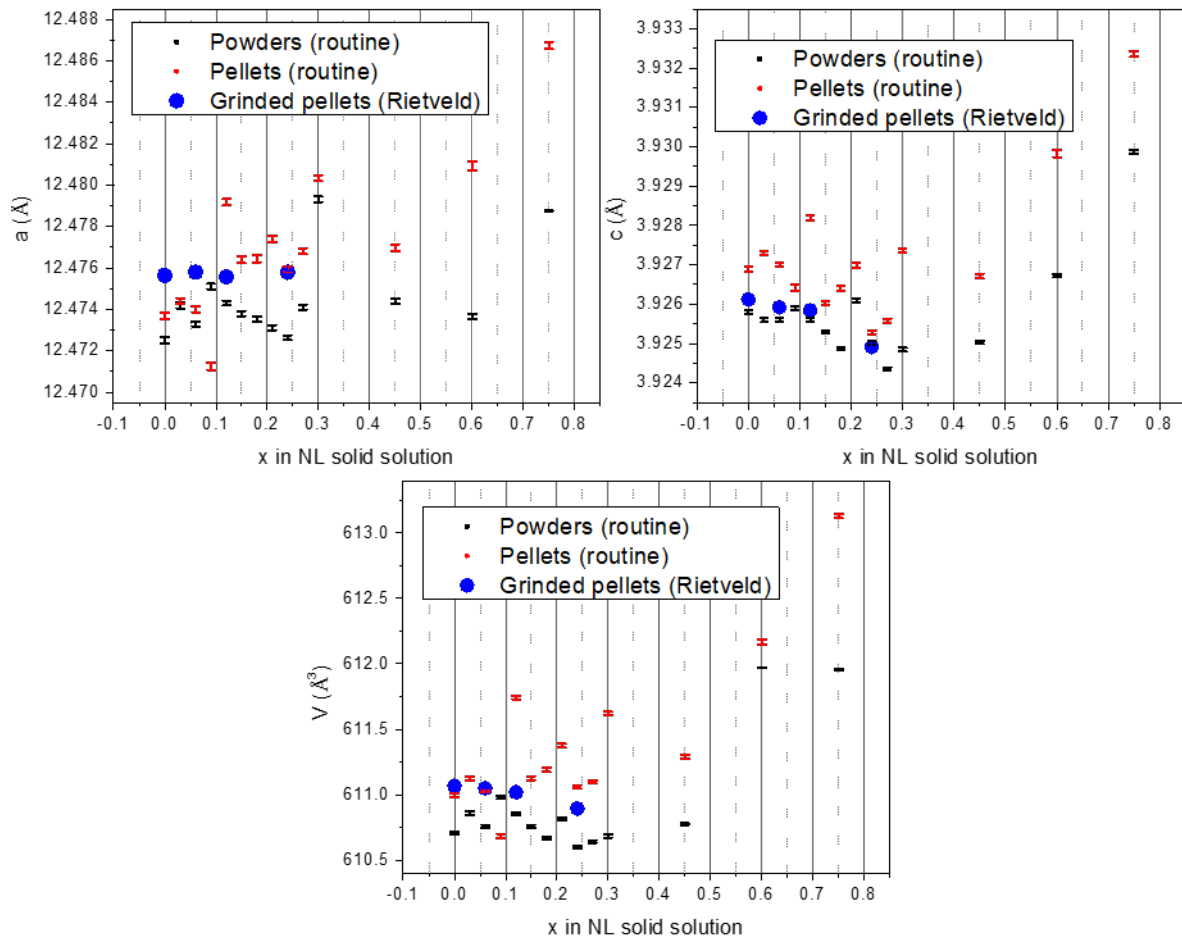


Figure 47: Refined lattice parameters (including error bars) for NL solid solution of powder and pellets. Rietveld refinements (in blue) were measured on grinded pellets

Lattice parameters of the fired powders are slightly smaller than those of the fired pellets of the same composition. The unit cell volume shows a significant increase for the largest lithium content, which also correspond to the largest amount of  $\text{Nd}^{3+}$  vacancies. Since for smallest lithium contents, the cell volume is almost stable, it is likely that the volume increase observed for the largest Li content is due to  $\text{Nd}^{3+}$  vacancies. In the R to FE crossover region, Rietveld refinements performed on grinded pellets (in blue) show a slight increase of cell parameters, as compared to powders, but confirm the stability of the cell volume. It is worth mentioning that a slight increase of the cell parameters following sintering was also detected in the previous work of E. Castel who demonstrated that a reactive sintering is taking place when using optimized elaboration conditions<sup>46</sup>. The cell parameters determined from sintered pellets show strong anomaly from the sample with  $x = 0.09$  to the sample with  $x = 0.12$ . This must result from a microstructural effect specific to pellets of these composition, as for the  $x = 0.12$  sample, the cell volumes determined from routine and Rietveld refinements are in agreement. Overall, two regimes can be distinguished concerning the evolution of the cell volume. A first regime from  $x = 0$  to  $x = 0.45$  in which the cell volume evolve from  $610.64 \text{ \AA}^3$  to  $610.98 \text{ \AA}^3$ , which is a difference of about 0,6%, *i.e.* the lattice parameters are almost constant. In the second regime, for  $x > 0.45$ , the cell parameters increase and the cell volume reaches  $612.00 \text{ \AA}^3$  for  $x = 0.75$ , which represents a variation of 2,2%.

However, in comparison with dielectric properties, no obvious link with the transition from the R-FE crossover to the pure R transition behavior can be established, as from  $x = 0$  to 0.75, the space group remains the same ( $P4/mbm$ ). Although dielectric properties are known to be strongly coupled to the crystal structure, in the NL solid solution, the structural evolution is either small or cannot be detected and described by means of conventional, 3D crystallography.

For the two other solid solutions, BNL and LFN, the same characterizations were performed and lattice parameters are presented in Figure 48 and Figure 49. Both solid solutions exhibit the same difference between lattice parameters refined on powder and pellet, with slightly larger parameters for pellets. In both BNL and LFN, the R and FE transitions are observed only for  $x = 0$ , while purely R transitions are observed for  $x > 0$ . Lattice parameters and cell volume evolve almost linearly on the whole composition range in BNL, while the cell volume as determined from powders appears stable in LFN (as expected from the substitution scheme).

This confirms the previous observations on NL solid solution and the fact that structural modification associated with different dielectric behaviors must be subtle.

To further investigate the structural modifications at the origin of dielectric anomalies observed, Rietveld refinements are particularly indicated. As discussed previously, this was performed for the NL solid solution for 4 different samples with compositions  $x = 0, 0.06, 0.12$  and  $0.24$ . The first three exhibit a relaxor to ferroelectric crossover whereas the last one is purely relaxor.

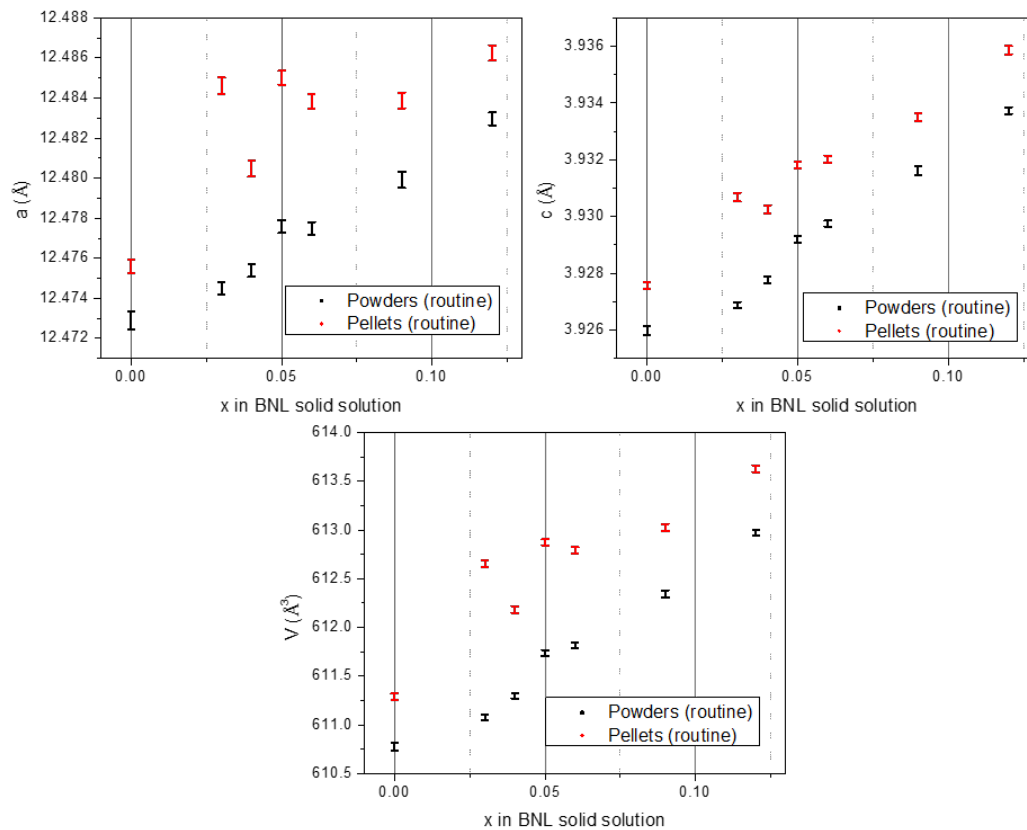


Figure 48: Refined lattice parameters for BNL solid solution of powder and pellets

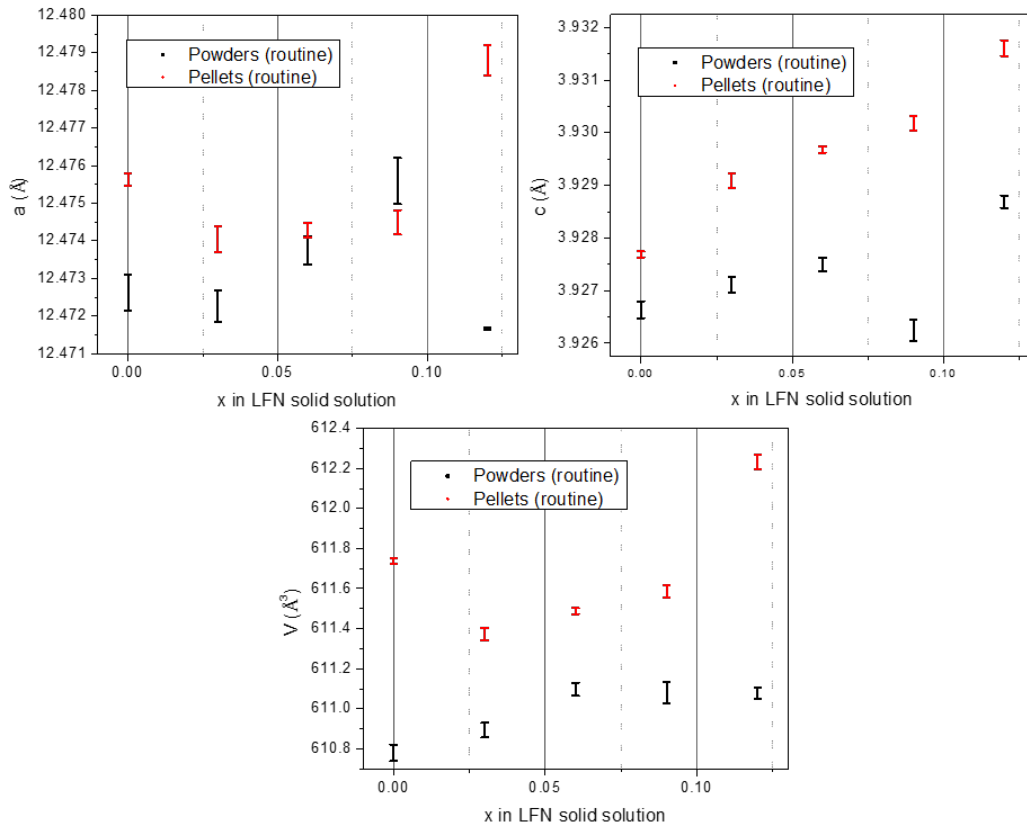


Figure 49: Refined lattice parameters for LFN solid solution of powder and pellets

In the structure refinement of the four patterns, oxygen occupancy is assumed to be maximal. Then relative occupancies of cations can be obtained from Rietveld refinement.

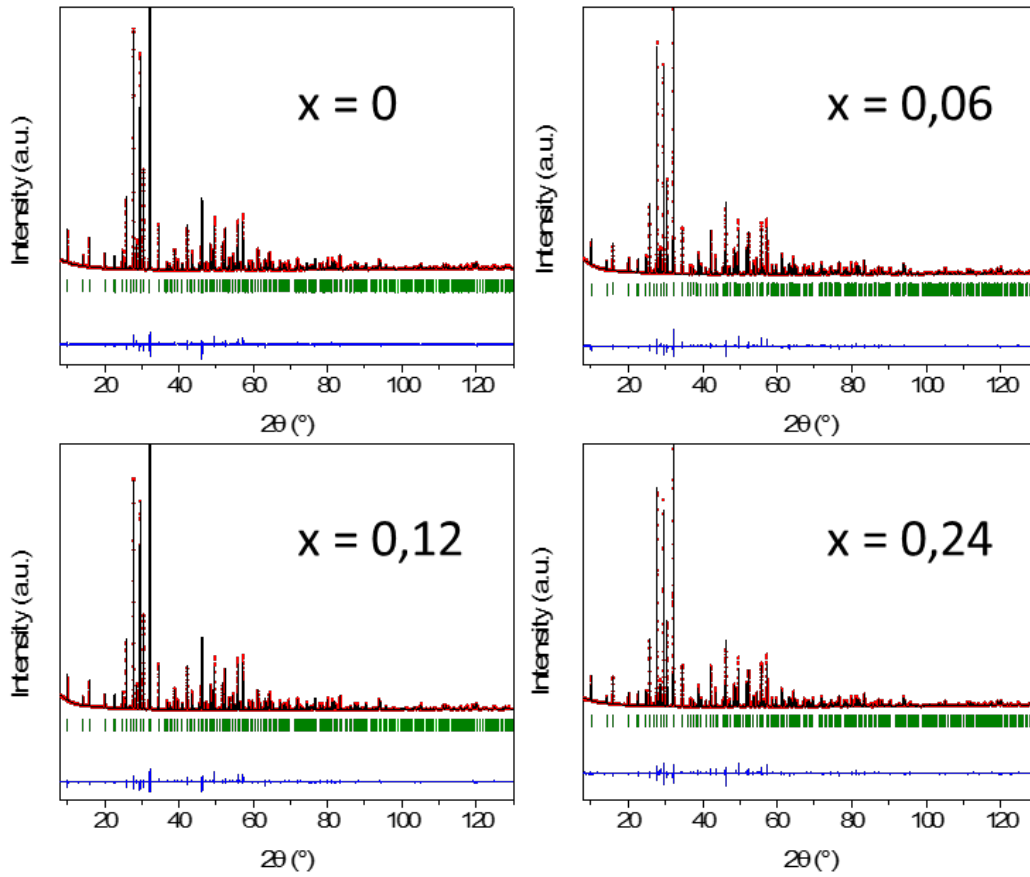


Figure 50: XRD pattern Rietveld refinements for NL solid solution with  $x$  ranging from 0 to 0.24

However,  $\text{Li}^+$  containing only 2 electrons is not detected in XRD experiment. Therefore, its quantification is very difficult to establish and is not given here. An effective approach for Li quantification would be to dissolve the material and perform ICP to determine its composition precisely. Unfortunately, we were unable to properly dissolve the material as small remaining grains were found in the liquid solution, resulting in unrealistic cationic ratio after ICP measurements. Table 1 gathers the theoretical and refined compositions of the four samples.

Table 1: Theoretical and refined compositions for samples of NL solid solution

| $x$  | Theoretical composition   | Refined composition   | Rp   | Rwp  |
|------|---|---|------|------|
| 0    | $\text{Ba}_2\text{NdFeNb}_4\text{O}_{15}$                               | $\text{Ba}_{2,02(2)}\text{Nd}_{0,98(2)}\text{Fe}_{1,02(5)}\text{Nb}_{3,98(5)}\text{O}_{15}$ | 4,21 | 5,50 |
| 0.06 | $\text{Ba}_2\text{Nd}_{0,98}\text{Li}_{0,06}\text{FeNb}_4\text{O}_{15}$ | $\text{Ba}_{2,03(2)}\text{Nd}_{0,98(1)}\text{Fe}_{0,91(4)}\text{Nb}_{4,09(4)}\text{O}_{15}$ | 3,76 | 4,90 |
| 0.12 | $\text{Ba}_2\text{Nd}_{0,96}\text{Li}_{0,12}\text{FeNb}_4\text{O}_{15}$ | $\text{Ba}_{2,01(1)}\text{Nd}_{0,96(2)}\text{Fe}_{1,10(5)}\text{Nb}_{3,90(5)}\text{O}_{15}$ | 6,13 | 7,92 |
| 0.24 | $\text{Ba}_2\text{Nd}_{0,92}\text{Li}_{0,24}\text{FeNb}_4\text{O}_{15}$ | $\text{Ba}_{2,02(2)}\text{Nd}_{0,96(2)}\text{Fe}_{0,65(6)}\text{Nb}_{4,35(6)}\text{O}_{15}$ | 3,99 | 5,27 |

In the whole range, Ba content is found to be between 2.01 and 2.03, which is consistent with the theoretical content. Refinement attempts with Ba in B site (square channels) and Nd in A site (pentagonal channels) lead to the conclusion that A site is fully filled with  $\text{Ba}^{2+}$  and B site does not contain Ba. Nd content shows a maximum of 0.98 instead of 1, which is in good agreement with the previous work of E. Castel<sup>46</sup>. Increasing the Li content leads to a diminution of  $\text{Nd}^{3+}$  content down to 0.96 for  $x = 0.12$  and 0.24. Whereas this is expected for  $x = 0.12$ , it is slightly above the expected Nd quantity for  $x = 0.24$ . This, accompanied by an off stoichiometry of Fe and Nb (0.65 and 4.35 respectively instead of 1 and 4) leads to a composition with an excess of positive electric charges, therefore unlikely to be accurate. This also suggests a release of Fe from the TTB phase, and therefore could provoke the formation of secondary phases. However, no clue of any other phase was found, neither from XRD nor from EDX. It remains to be seen if a secondary phase is present in a very small amount and remains undetectable, or if the refined composition is erroneous. It should be recalled that a spinel phase, possibly maghemite  $\gamma\text{-Fe}_2\text{O}_3$  or  $\text{Li}_{0.5}\text{Fe}_{2.5}\text{O}_4$ , was detected following crystal growth of  $\text{Ba}_2\text{LnFeNb}_4\text{O}_{15}$  TTBs in a  $\text{LiBO}_2$  flux<sup>32</sup>. From a symmetry standpoint, the structural solution does not allow a FE state, but results in rather good agreement factors ( $R_p = 3.99$  and  $R_{wp} = 5.27$ ). Although the precise chemical composition remains to be determined, this confirms again that the structural modifications responsible for dielectric properties are very small in these systems.

As previously discussed, the ferroelectrically active elements in the structure is  $\text{Nb}^{5+}$ . While it may not be the driving force for ferroelectricity, it looks interesting, nonetheless, to focus on Nb environment. Figure 51 displays octahedral site occupancy of both  $\text{Nb}^{5+}$  and  $\text{Fe}^{3+}$  in the different octahedral sites  $M'$  and  $M''$ . In every case, there is a preferential filling of Fe in site 1 ( $M'$ ) and Nb in site 2 ( $M''$ ). Since  $M'$  is the more regular octahedron, it may favor the accommodation of  $\text{Fe}^{3+}$ , while ferroelectrically active  $\text{Nb}^{5+}$  is preferentially accommodated in the more distorted  $M''$ . However, the difference is not important enough to conclude and it would be necessary to acquire higher resolution data to get more precision on the site occupancies. Moreover, it has already been shown in  $\text{Ba}_2\text{NdFe}(\text{Nb},\text{Ta})_4\text{O}_{15}$  that octahedral site occupancy refinement is not reliable using XRD for such small variation values<sup>82</sup>. Comparison of Nb/Fe ratio between the different samples show a small increase for  $x = 0.24$  sample, which is a pure relaxor. Because the initial precursors were mixed in Nb/Fe ratio of 4, it is surprising to obtain an off stoichiometry of Nb/Fe with no visible secondary phase containing Fe. It seems

also unlikely that the Nb excess detected in the octahedral site could be explained by the accommodation of Li in these sites, as  $\text{Li}^+$  is more than 30 times lighter than  $\text{Nb}^{5+}$  with respect to XRD scattering and its presence at these sites would likely affect the refinement.

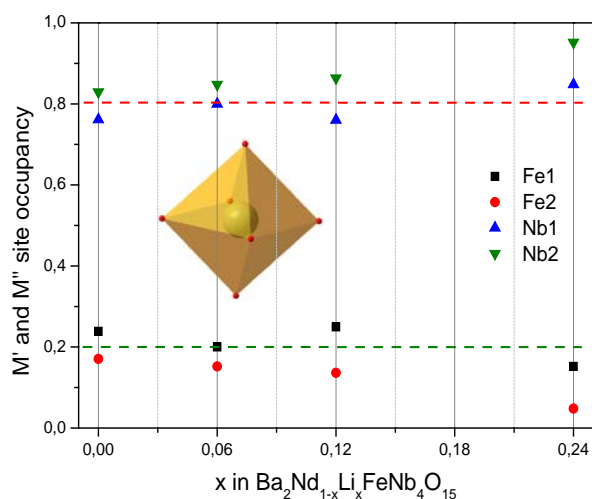


Figure 51: Site occupancy of octahedrons in NL solid solution for  $x = 0, 0.06, 0.12$  and  $0.24$

Moreover, no drastic change of relative occupancies can be related to the dielectric transition between  $x = 0.12$  and  $0.24$ . Further analysis of Nb environment parameters are displayed on Figure 53. They concern both Nb-O distances and angles, in comparison with  $x = 0$  sample of the NL solid solution, and in both cases, the maximum variation reaches 1 to 1,5%.

Angles reveal a similar behavior, *i.e.* no major difference is observed at the transition from  $0 < x < 0.12$  to  $x = 0.24$ . A slight increase of octahedral distortion is observed, but which is of limited significance, because of the limited sensitivity of XRD towards oxygen. Further study through neutron diffraction could highlight some differences between these samples.

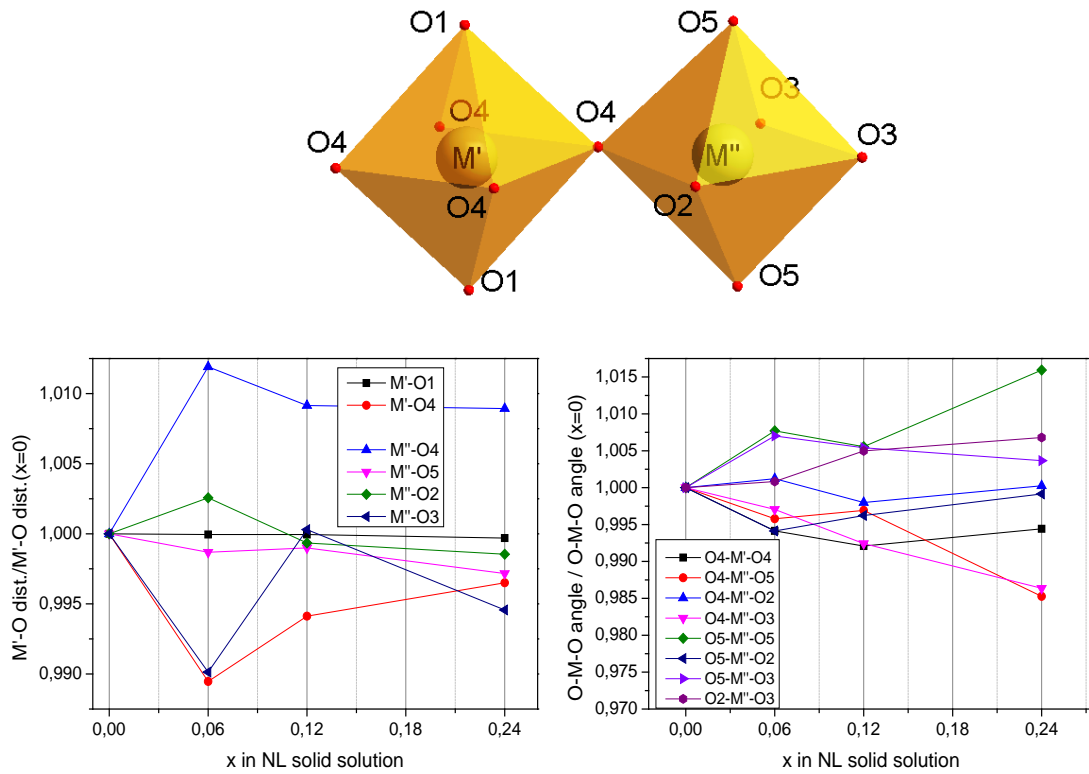


Figure 52: Relative distances and angles of  $x = 0.06$  to  $0.24$  compared to  $x = 0$  sample in NL solid solution

XRD technique is a powerful technique to determine crystal structure of crystalline materials. However, some very small crystallographic evolutions are barely detected with such technique, especially when light elements such as oxygen or lithium are involved. Thus, the variations of dielectric properties, which must be related to some crystalline difference, originate from very subtle crystallographic evolutions. Considering both the previous conclusions on other solid solutions<sup>13</sup> and the present study it appears clear that the anionic framework, and likely its aperiodic modulations, play an important role in the emergence of FE properties in  $\text{Ba}_2\text{NdFeNb}_4\text{O}_{15}$ .

## 2.3. Conclusion

Synthesis of three solid solutions has been successfully achieved through solid state route. The high crystallinity and the absence of secondary phase has been evidenced using XRD technique. Whereas the BNL solid solution shows a constant linear increase of lattice parameters consistent with the insertion of large  $\text{Ba}^{2+}$  ions in the lattice, the influence of cationic modifications in the two other solid solutions result in constant values of lattice cell parameters. These results suggest a good accommodation of Ba for BNL solid solution and the absence of evolution for LFN and NL solid solutions confirm the expected trends, thus is a clue of the good insertion of Li in the phase.

Dielectric measurements have been performed and all lead to the observation of the same evolution from samples with low Li content exhibiting both R and FE transitions, to samples with high Li content exhibiting pure R phase. In NL solution, the transition from one to another has been particularly identified for x between 0.18 to 0.21.

In order to identify the structural origin of the two different dielectric properties observed, Rietveld refinements have been performed on samples of NL solid solution in both regimes (R/FE and R). The presence of Li being almost undetectable through XRD technique, especially for low quantities, the only visible difference is the modification of the rest of the structure. This observation lead to the conclusion that no obvious difference can be highlighted from these data, and suggests, in agreement with both literature and previous works, the strong influence of oxygen framework on dielectric properties.

During this study, the observation of unexpected dielectric responses on  $x = 0$  samples lead to the questioning on the sensitivity of the phase to synthesis procedure and the influence of various synthesis steps on these properties. This will be developed in the following chapter.

# Chapter 3: Influence of elaboration conditions on $\text{Ba}_2\text{NdFeNb}_4\text{O}_{15}$ dielectric properties

In the previous section have been presented three solid solutions derived from  $\text{Ba}_2\text{NdFeNb}_4\text{O}_{15}$ . This central composition has been known for years in the group but still harbors some questions. During the exploration of solid solutions, synthesis of this parent composition has been performed many times and resulted in different dielectric behaviors. This has been known for few years. E. Castel first defined it as ferroelectric<sup>46</sup> phase, before additional investigation related to the study of the  $\text{Ba}_2(\text{Pr},\text{Nd})\text{FeNb}_4\text{O}_{15}$ <sup>26</sup> solid solution revealed a relaxor to ferroelectric crossover. Later, single crystal of this compound were grown and revealed a purely relaxor behavior induced by  $\text{Nd}^{3+}$  vacancies<sup>32</sup>.

This chapter aims at exploring  $\text{Ba}_2\text{NdFeNb}_4\text{O}_{15}$  elaboration parameters in order to determine which of the three responses (purely ferroelectric, purely relaxor or R to FE crossover) corresponds to the intrinsic dielectric response of this phase, and what are the associated synthesis conditions that allow obtaining one of these three dielectric behavior on purpose.

The significant contribution of Tom Delage, during his master internship, to synthesis and characterizations allowed to obtain an important amount of data allowing this investigation.

## 3.1. Multiple dielectric behaviors for a single phase

As described previously, different dielectric behaviors have been observed for the same composition. Through the exploration of solid solutions, the synthesis of  $\text{Ba}_2\text{NdFeNb}_4\text{O}_{15}$  has been performed many times and lead to different dielectric responses. Figure 54 shows three different ceramic samples of the same composition with totally different dielectric responses.

In the previous works on  $\text{Ba}_2\text{LnFeNb}_4\text{O}_{15}$  materials, such as for a lot of research focused on TTB materials, the main approach has been to explore solid solution, to identify crystal chemical parameters of the original dielectric behaviors encountered. In such approach, chemical composition modification induces crystallographic evolution, which can influence the properties. It becomes complicated to identify whether the evolution of physical properties is

due to the chemical substitution or to some crystallographic modification. In the case of Li-based solid solutions, an evolution from R to FE crossover to purely relaxor behavior is observed, but identifying the specific role of Li insertion remains complicated. In the present case, the possibility for a single phase to exhibit different dielectric responses offers a great opportunity to investigate the crystallographic origin of the physical properties, without compositional modification. But to this aim, these different dielectric behaviors must be obtained in reproducible and controlled conditions.

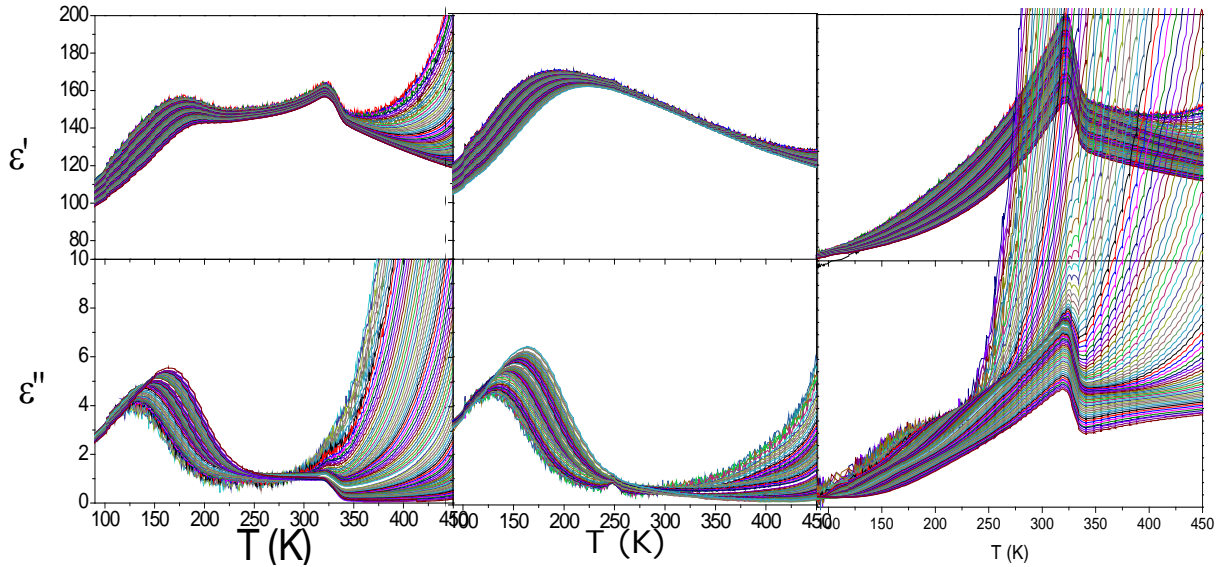


Figure 53: Dielectric measurements of different  $Ba_2NdFeNb_4O_{15}$  ceramics

To realize this identification, 34 samples of the same  $Ba_2NdFeNb_4O_{15}$  composition have been synthesized. In these samples were measured the following dielectric behaviour:

- 1 pure ferroelectric (FE)
- 11 pure relaxor (R)
- 22 crossover relaxor-ferroelectric (RF)

Through these examples, various parameters have been tuned (temperature, sintering time, double heat treatment, powder milling and grinding) and lead to identification of conditions allowing for the stabilization of relaxor or R to FE crossover behavior. In the case of purely ferroelectric behaviour, only a single sample has been obtained, and that does not allow identification of conditions that can lead to its observation. While the ferroelectric behaviour

will be briefly discussed in the next section, the main part of this chapter focuses on the R and R to FE crossover responses.

## 3.2. Synthesis parameters, post treatments of ceramics

In the previous chapter, the  $x = 0$  sample,  $\text{Ba}_2\text{NdFeNb}_4\text{O}_{15}$ , has been defined as RF and was elaborated under the particular conditions that will be determined in the present chapter. In this part, the different parameters that will be investigated are firing and sintering time, type of powder milling and associated experimental conditions, multiple firing steps, but also post-synthesis thermal treatments.

### 3.2.1 Two step-firing

The synthesis process consists of a milling step, followed by a firing step in which the mix of carbonates and oxides reacts to form the targeted phase. In a previous work, the presence of impurities has been evidenced for some firing conditions, with the possible formation of two main phases,  $\text{NdNbO}_4$  and  $\text{BaFe}_{12}\text{O}_{19}$ <sup>76</sup>. The formation of a perovskite phase,  $\text{Ba}(\text{Nb,Fe})\text{O}_3$  has also been occasionally observed.

Figure 54 displays the XRD patterns of two powders made in the same conditions (1280 °C / 12h) after hand milling of precursor powders during 30 min in an agate mortar by two different experimenters (called #A1 and #B1). Sample represented by the black line contains a perovskite phase whereas the one represented in red is composed of pure TTB phase only. After synthesis, these two powders were sintered into pellets (#A1p and B1p) in the same conditions (1310 °C / 10h). During sintering, the formation of TTB phase is complete and results in two comparable XRD patterns for both samples. No remaining perovskite phase is detected. On the same figure are presented the dielectric measurements of these samples. The first one (#A1p) on the left shows a pure relaxor to paraelectric phase transition while the second one (#B1p) presents a clear R (around 150K) to FE (at 330K) crossover. The peak in the middle temperature range corresponds to residual water in the measurement cell. These two different samples then exhibit different dielectric responses although they have the same composition. The amount of

each precursor is the same in both cases, milling, firing and sintering have been performed in the same way. However, they exhibit different properties.

Solid solution relying on every type of cationic site (and some combination thereof) were investigated in the  $(\text{Ba,Sr})_2\text{Ln}(\text{Fe,Nb,Ta})_5\text{O}_{15}$  ( $\text{Ln} = \text{Pr, Nd, Sm, Eu}$ ) systems and lead to the same conclusion. The transition from a RF to purely R is systematically observed with any kind of substitution tested. Looking at the level of cationic substitution needed to transit from RF crossover to pure R is somehow interesting in comparison with the present results. In the aforementioned solid solutions, R behavior is observed for Ba substituted by Sr above 5 %, Nb substituted by Ta above 12 % and Nd by Pr above 15 %<sup>13</sup>. However, in the present case R behavior and RF crossover are observed for identical compositions, and while an eventual departure from the nominal composition may originate from weighting error, it is unlikely to reach a few percent. Thus the difference must arise from a difference in the crystallographic arrangement.

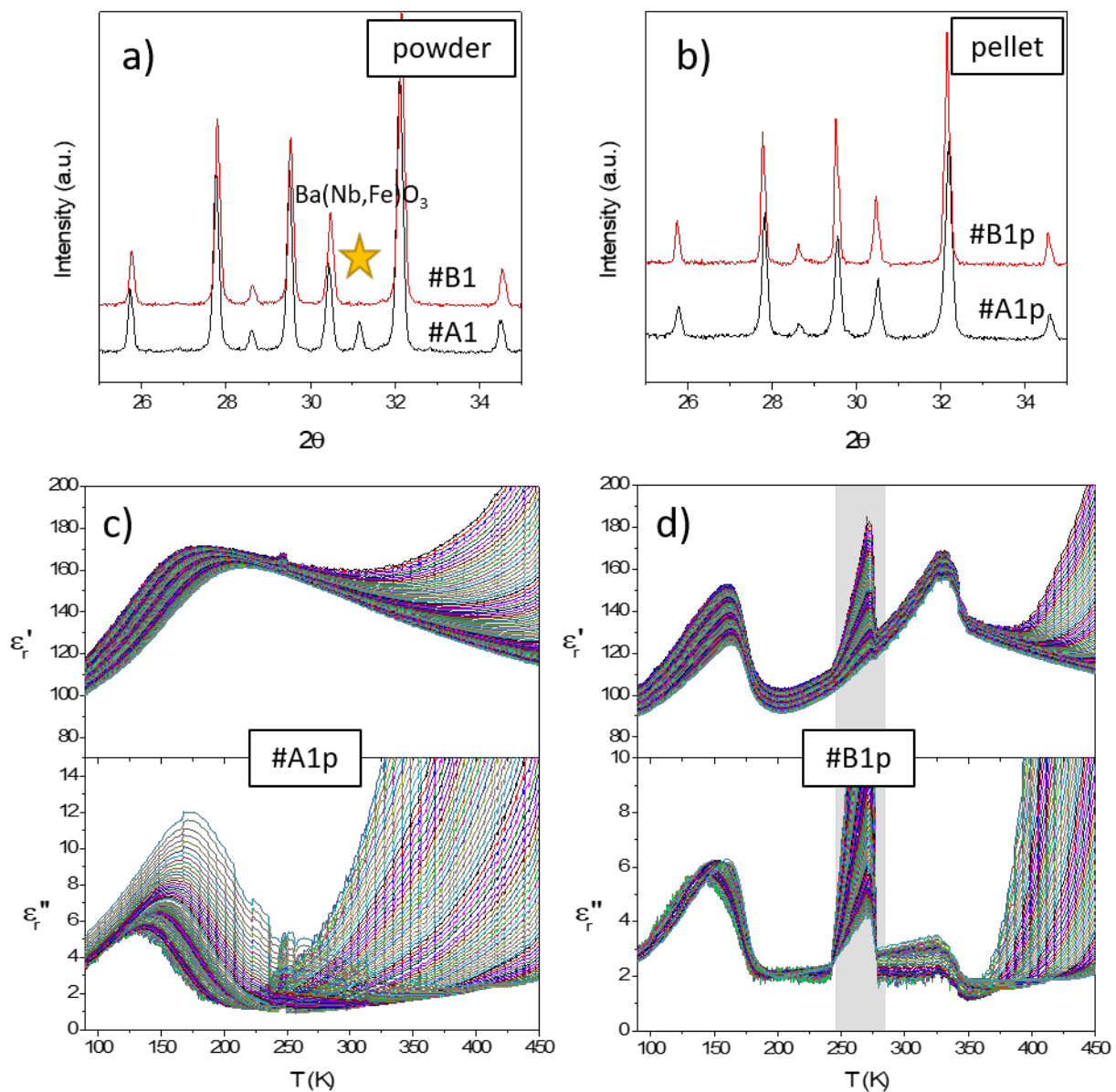


Figure 54: XRD patterns of two - #A1 and #B1- (a) powders and (b) pellets made in the same conditions (yellow star represents perovskite phase) and dielectric measurement of (c) #A1p and (d) #B1p

In order to further investigate these two powders, two step firing has been performed on both samples. To this end, the fired powders, which XRD pattern are presented on Figure 54 a), have been fired a second time (#A2 and #B2) in the same conditions (1280 °C / 12h). Sintering has then been performed on these two-step fired (TSF) powders to obtain pellets (#A2p and #B2p).

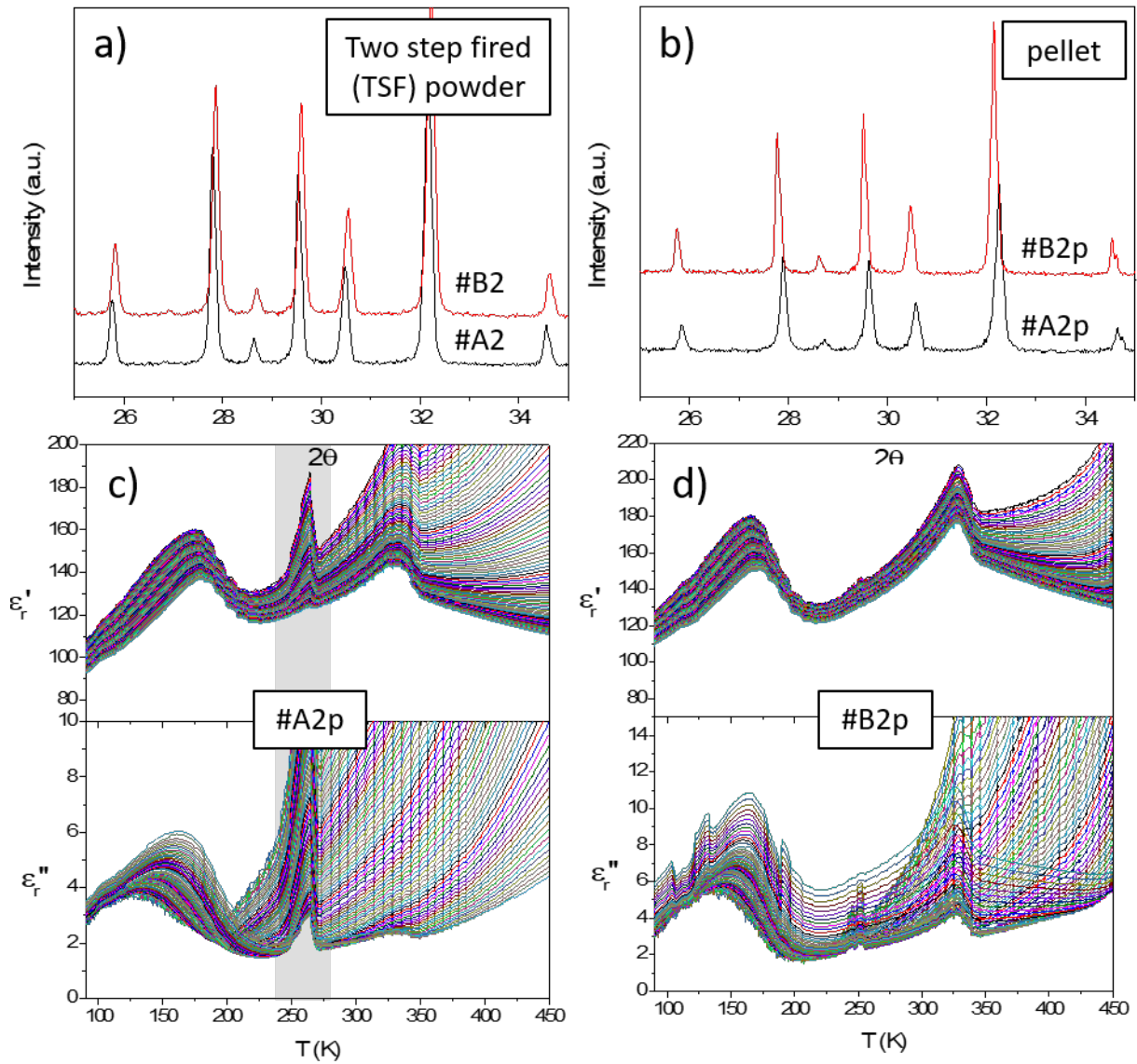


Figure 55: XRD patterns of #A2 and #B2 (a) two-step fired (TSF) powders and (b) sintered pellets, plus dielectric measurement of (c) #A2p and (d) #B2p

Figure 55 displays the XRD patterns of TSF powders and sintered pellets for the two different samples. In both cases, TTB phase is pure after the second firing and remains pure after sintering. No perovskite phase is observed. The resulting pellets exhibit the same dielectric behavior (RF). It is remarkable that after a single firing step, the two samples have different dielectric responses (R and RF), while after a second firing, a unique behavior is found (RF). The crossover behavior appears as more stable than pure R for  $\text{Ba}_2\text{NdFeNb}_4\text{O}_{15}$  since successive firing leads to this response. Profile refinements have been performed on these XRD patterns to evaluate the cell parameters, and results are presented in Table 2 below.

Table 2: Refined lattice parameters of powders and pellets

| Sample # | Dielectric transition | a (Å)       | c (Å)      | V (Å <sup>3</sup> ) | $\chi^2$ |
|----------|-----------------------|-------------|------------|---------------------|----------|
| #A1      | -                     | 12,4725 (1) | 3,9258 (1) | 610,71 (1)          | 2.03     |
| #B2      | -                     | 12,4774 (2) | 3,9294 (1) | 611,75 (1)          | 2.41     |
| #A2      | -                     | 12,4745 (4) | 3,9258 (1) | 610,91 (3)          | 1.83     |
| #B2      | -                     | 12,4751 (3) | 3,9260 (1) | 610,99 (3)          | 2.09     |
| #A1p     | R                     | 12,4753 (4) | 3,9286 (1) | 611,42 (3)          | 1.92     |
| #B1p     | RF                    | 12,4737 (2) | 3,9269 (1) | 611,00 (2)          | 1.77     |
| #A2p     | RF                    | 12,4815 (6) | 3,9279 (2) | 611,92 (5)          | 1.98     |
| #B2p     | RF                    | 12,4738 (3) | 3,9271 (1) | 611,05 (3)          | 1.65     |

Refined lattice parameters for powders, two-step fired powders and corresponding pellets display very small difference. Especially, between #A1p and #B1p which were fired once before sintering, and which exhibit different dielectric responses, the cell volume difference is smaller than the one observed for ceramics obtained through TSF (#A2p and #B2p). Thus, no lattice size difference can explain the origin of these different dielectric behaviors. This shows once again that the difference must lie in subtle crystallographic modifications, and their investigation requires a specific strategy.

A third sample, called #C1, has been prepared in different precursor mixing conditions. Planetary milling in agate mortar with a rotation speed of 200 rpm for 1h has been performed to mix the precursors instead of a hand milling. The resulting powder was fired (#C1) and sintered (#C1p) using the same conditions as for the previous examples (1280 °C/12h and 1310 °C/10h, resp.). The XRD pattern (Figure 56) reveals the presence of TTB phase after the first treatment, accompanied by the presence of perovskite phase BaFe<sub>0,5</sub>Nb<sub>0,5</sub>O<sub>3</sub>. This phase is no longer present after sintering and the pellet exhibits a pure FE transition. Dielectric properties of this sample (#C1p) have been measured and a single FE transition observed (Figure 56a) and c)). The initial powder #C1 was then used for a second firing (#C2) and sintered (#C2p) in the same conditions as previously, to observe the influence of the second firing. Results are displayed on Figure 56 b) and d). After a second firing, the XRD pattern of #C2 (Figure 56 b) shows a pure TTB phase with no perovskite remaining. The final pellet sintered after two firings (#C2p) shows a R to FE crossover.

In the previous case, the presence of perovskite lead to a pure R response. Here, in presence of the same perovskite, dielectric behavior is the opposite, a pure FE transition. A possible explanation for that could be that the non-observation of this phase in the XRD pattern does not mean its total absence. If perovskite is present in the material, one can expect a deficit of Ba, Fe and Nb in TTB main phase, that will have an impact on the TTB phase.

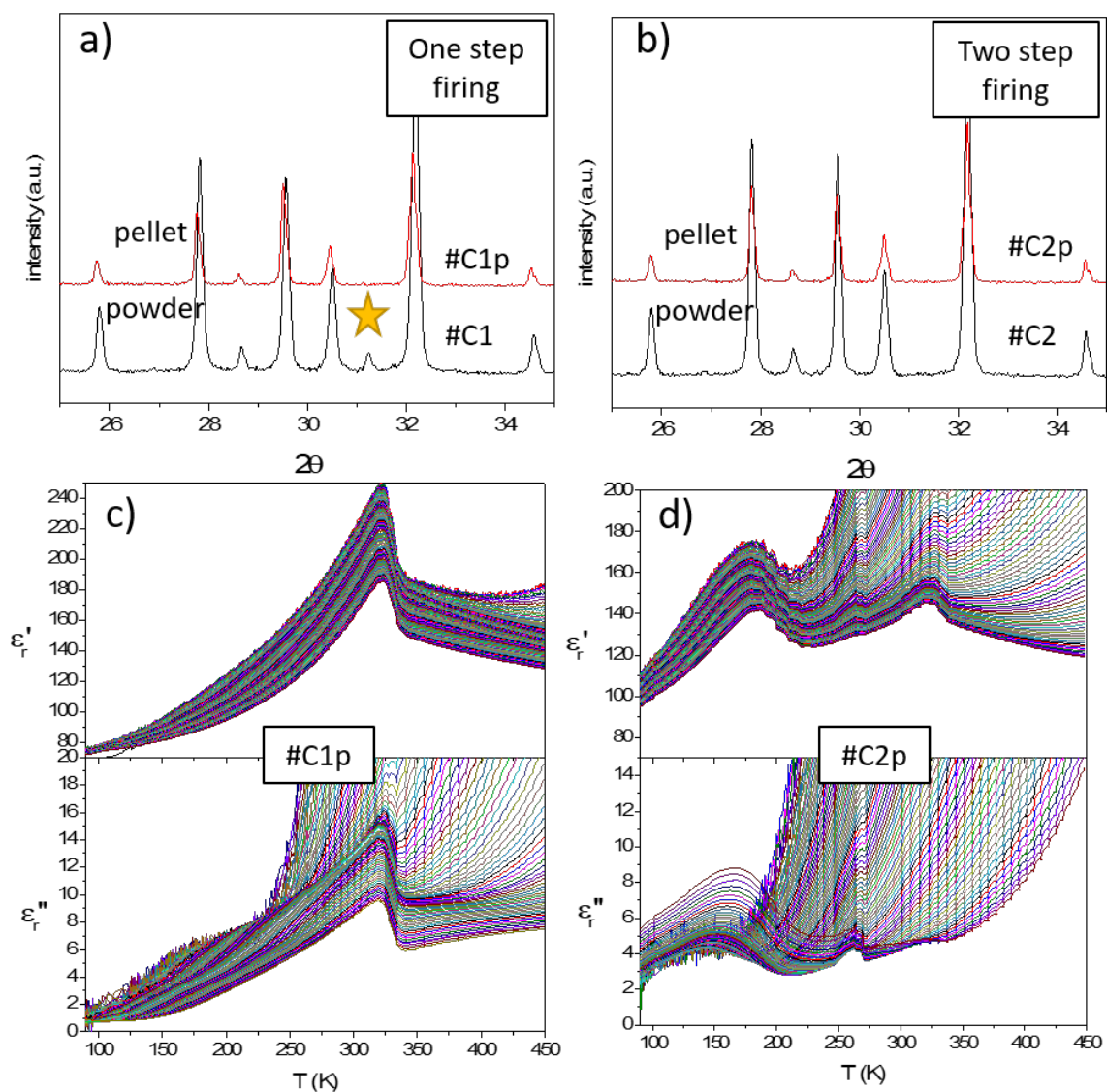


Figure 56: XRD patterns of (a) one-step and (b) two-step fired powders and pellets, and dielectric measurement of pellet corresponding to the (c) one-step fired and (d) two-step fired powders

Among impurities formed during the synthesis of TTB,  $\text{BaFe}_{12}\text{O}_{19}$  and fergusonite-type  $\text{NdNbO}_4$  have already been reported in previous works<sup>46,74,82</sup>, without much effect on the dielectric properties. Thus, observation of the perovskite phase reveals an off-stoichiometry of the main TTB phase that could result, depending on local and global stoichiometries, in

different physical properties. A second firing applied to the powder helps with the obtaining of homogenous composition and structure by enhancing solid state diffusion.

### 3.2.2 Sintering time and post-sintering heat treatment

Exploring multiple step firing has been performed through the comparison of one and two step firing. Increasing the firing time with that second step is a possibility to complete the homogenization of composition and structure through solid state diffusion. Other possibilities include the increase of sintering time. Classical sintering in the present work is 10h long at 1310°C. Sintering of 60h were used to evaluate this parameter effect on physical properties.

SEM pictures are displayed on Figure 57 showing the microstructure of two different pellets surfaces. In the first one (represented on Figure 57 a) and b)), sintered 10h at 1310 °C, some porosity remains, and elongated rods of about 5  $\mu\text{m}$  long can be seen at the surface. The second pellet has been prepared from the same initial fired powder but sintered with a dwell time of 60h, and its microstructure is slightly different. Less porosity remains than in the first case, probably thanks to the extra sintering time that allows for solid state diffusion. The grains are slightly longer than after 10h sintering, reaching about 8-10  $\mu\text{m}$ . The most interesting evolution of the microstructure with extra dwell time is the formation of very large zones with an apparent liquid phase that seems to have formed during sintering and solidified on cooling. However, this microstructure seems to have a limited impact on the physical properties since the dielectric response of this pellet is very close to that of the 10h sintered pellet (Figure 58). However, even if no qualitative impact on the nature of transitions is observed, a difference in the amplitude of the dielectric anomalies at the R and F transitions is clear. Indeed, a smaller permittivity is measured when a longer sintering dwell is used. This synthesis procedure, *i.e.* producing two samples with the same firing but two different dwell times (10 and 60h), has been reproduced to confirm the present observations. Dielectric measurements also displayed two RF behaviors, but the intensity was more important for the sample sintered 60h than the one sintered 10h. This observation, associated to the dielectric measurements presented on Figure 58, points out the possibility that these intensity variations are associated to microstructural modifications. More generally, we can confirm that an increase of sintering dwell time from 10h to 60h is associated with the conservation of the RF crossover behavior.

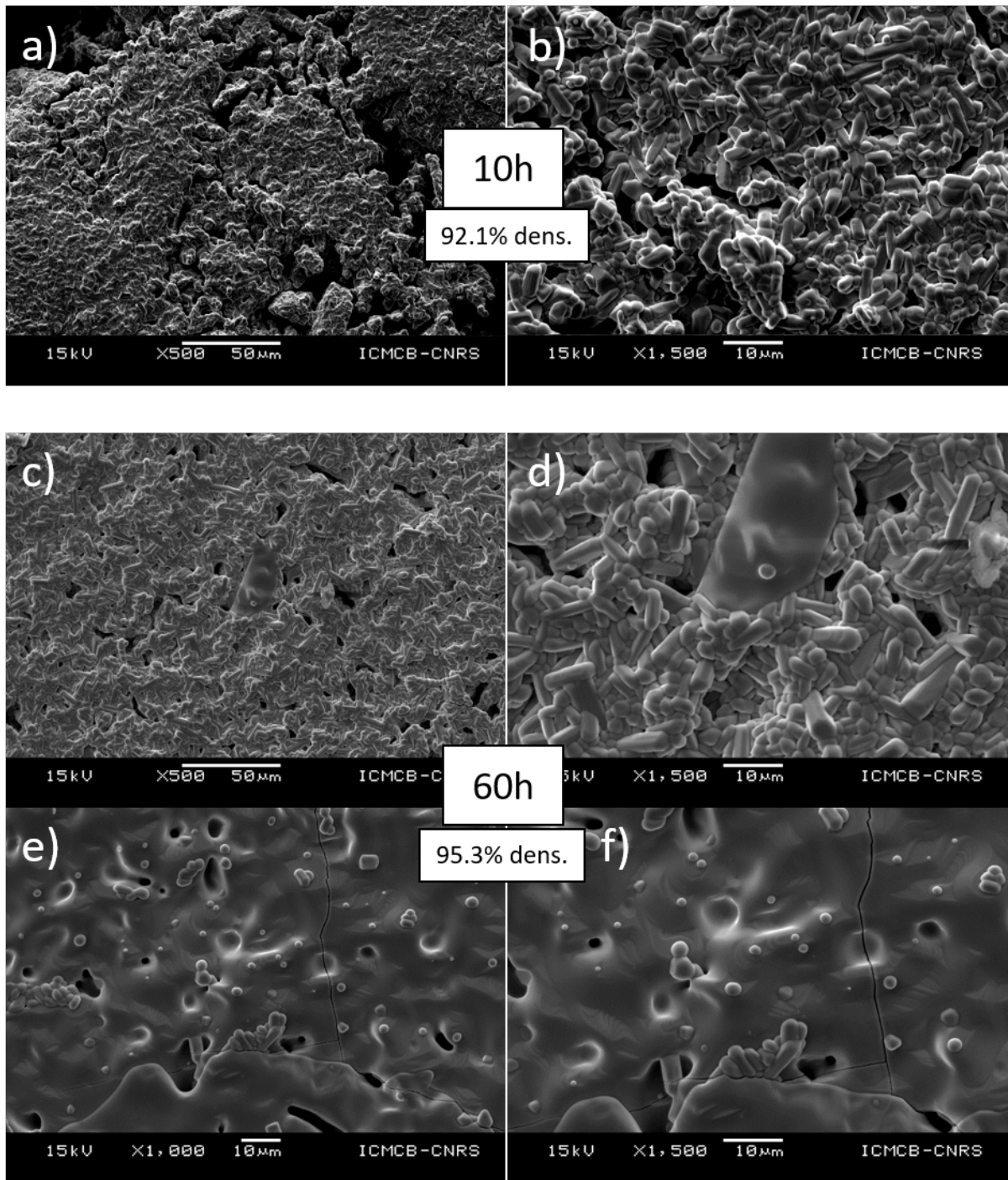


Figure 57: SEM pictures of surface of two different pellets sintered from the same initial powder during (a-b) 10h and (c-f) 60h

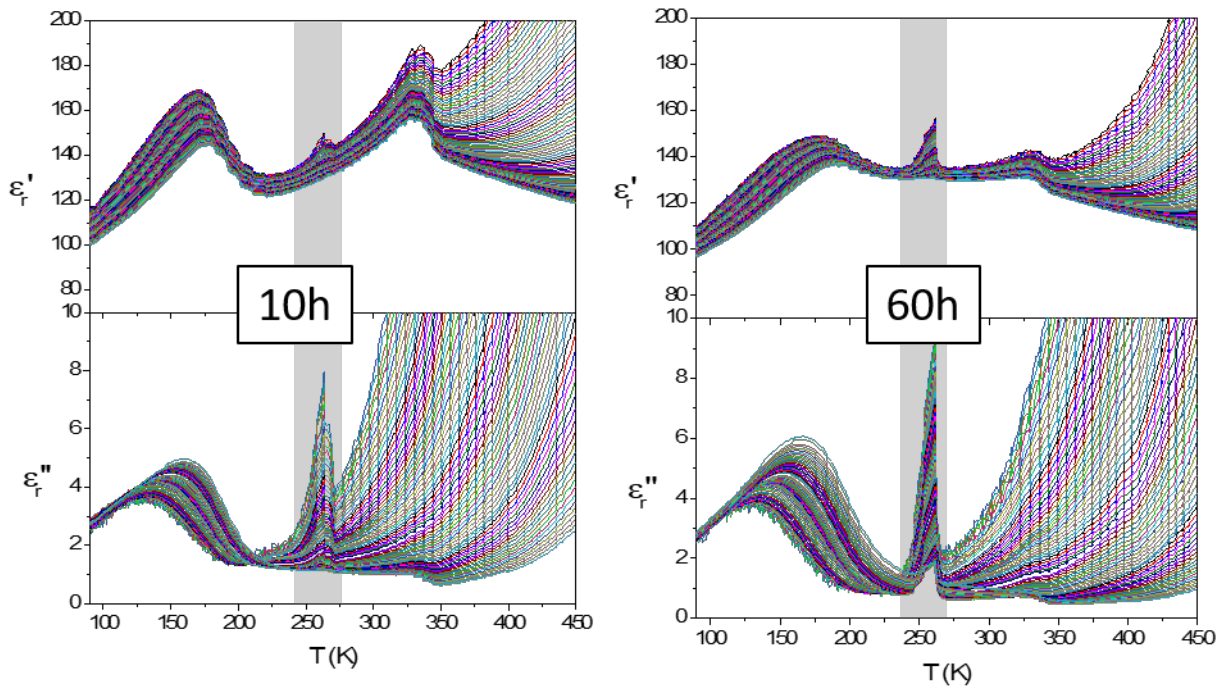


Figure 58: Dielectric measurements of two pellets of the same composition sintered 10h and 60h respectively

In the case of a R sample, the same experiment has been performed on #A1p6 sample, *i.e.* sintering during 60h has been performed (#A1p6) and observation of microstructure lead to the same conclusion as in the previous case. Increasing sintering time promotes appearance of liquid phase during sintering and is visible on the surface of the pellets.

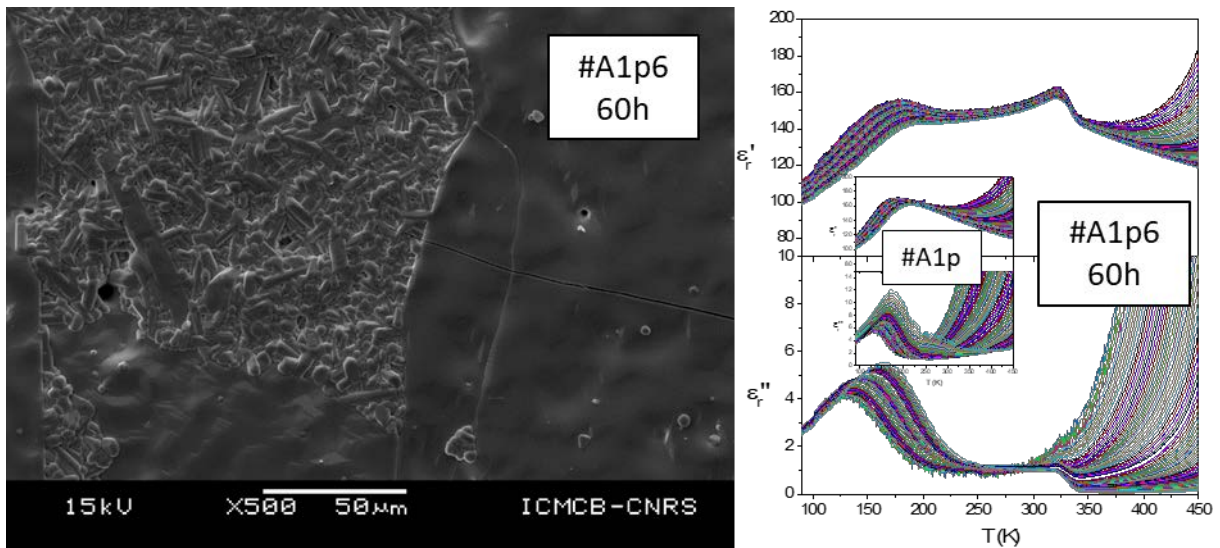


Figure 59: SEM picture and dielectric measurement of #A1p6 pellet sintered 60h, inset reminds of relaxor behavior of #A1p

Figure 59 shows a SEM picture of the surface of the pellet. The corresponding dielectric measurement is presented on the right side of the figure. It is clear that the extension of sintering time to 60h provokes the transition to RF behavior with two distinct transitions.

In both cases, R and RF samples, increasing sintering time from 10 to 60h leads to RF behavior. This result, in addition to the previous ones on two-step firing, confirm the intrinsic dielectric nature of the present  $\text{Ba}_2\text{NdFeNb}_4\text{O}_{15}$  phase which is characterized by a relaxor to ferroelectric crossover.

### 3.2.3 Post annealing treatment

In a previous work, M. Albino explored the effect of such annealing on single crystals of  $\text{Ba}_2\text{NdFeNb}_4\text{O}_{15}$  grown by the flux method<sup>30-32</sup>. These crystals, with relaxor properties, exhibited large dielectric losses which were diminished after a treatment at 900 °C for 10h under oxygen flux, indicating that these losses were at least partially related to oxygen vacancies. If this oxidizing treatment was useful to reduce dielectric losses, R behavior was stable after firing and no FE transition was observed. The same treatment is applied in the present case to ceramics with both R and RF behavior to measure its impact on dielectric properties. In the present work, only R and RF samples are treated because of the small quantities of FE powders and pellets.

Oxidizing treatment of 10h at 900 °C under oxygen flux has been performed on different pellets after sintering for both RF (#D1p) and R (#A1p) samples. The R sample is the same as previously presented, while RF sample is second sample synthesized in the same conditions as #B1. Results are displayed on Figure 60 and show in both R and RF initial pellets, a transition to a RF behavior after oxidizing treatment.

As previously observed through TSF and longer sintering times, oxidizing treatment provokes the transition from a R behavior to RF behavior. Again, the confirmation is here that RF is the intrinsic response of the phase, whereas pure R correspond to some kind of “transition” state, which is obtained before a homogeneous, RF state is reached.

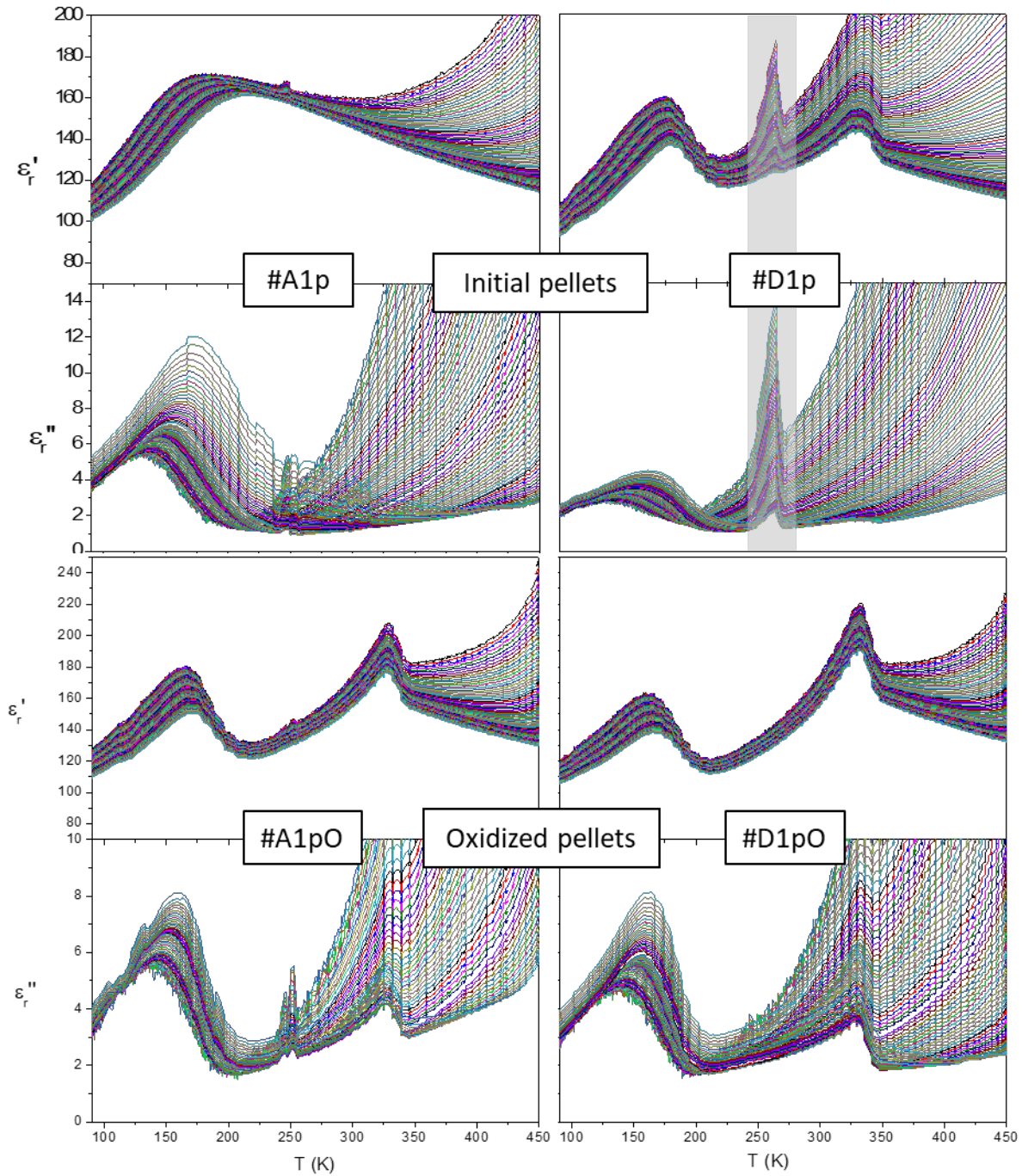


Figure 60: Dielectric measurements of pellets pellets before (#A1p and #D1p) and after oxidizing treatment at 900°C/10h (#A1pO and #D1pO)

### 3.2.4 Persistence of perovskite phase

A particular case has been observed for 60h sintering and oxidizing heat treatment. In that case, the sample (named #E1) has been once fired and sintered, and a perovskite phase was present after synthesis. The surprising result was that a sintering was not able to remove this perovskite

phase, contrary to what was observed for other samples prepared in similar conditions. Therefore, the sintered pellet exhibits a pure relaxor behavior. Oxidizing treatment has also been performed on the pellet sintered 10h after a single firing step. Here again, perovskite is present and a single relaxor to paraelectric transition is measured. Moreover, a long sintering of 60h has been applied to the fired powder and lead to the same result. This is different from all the previous observations and remains up to now unexplained. The results are summarized in Figure 61.

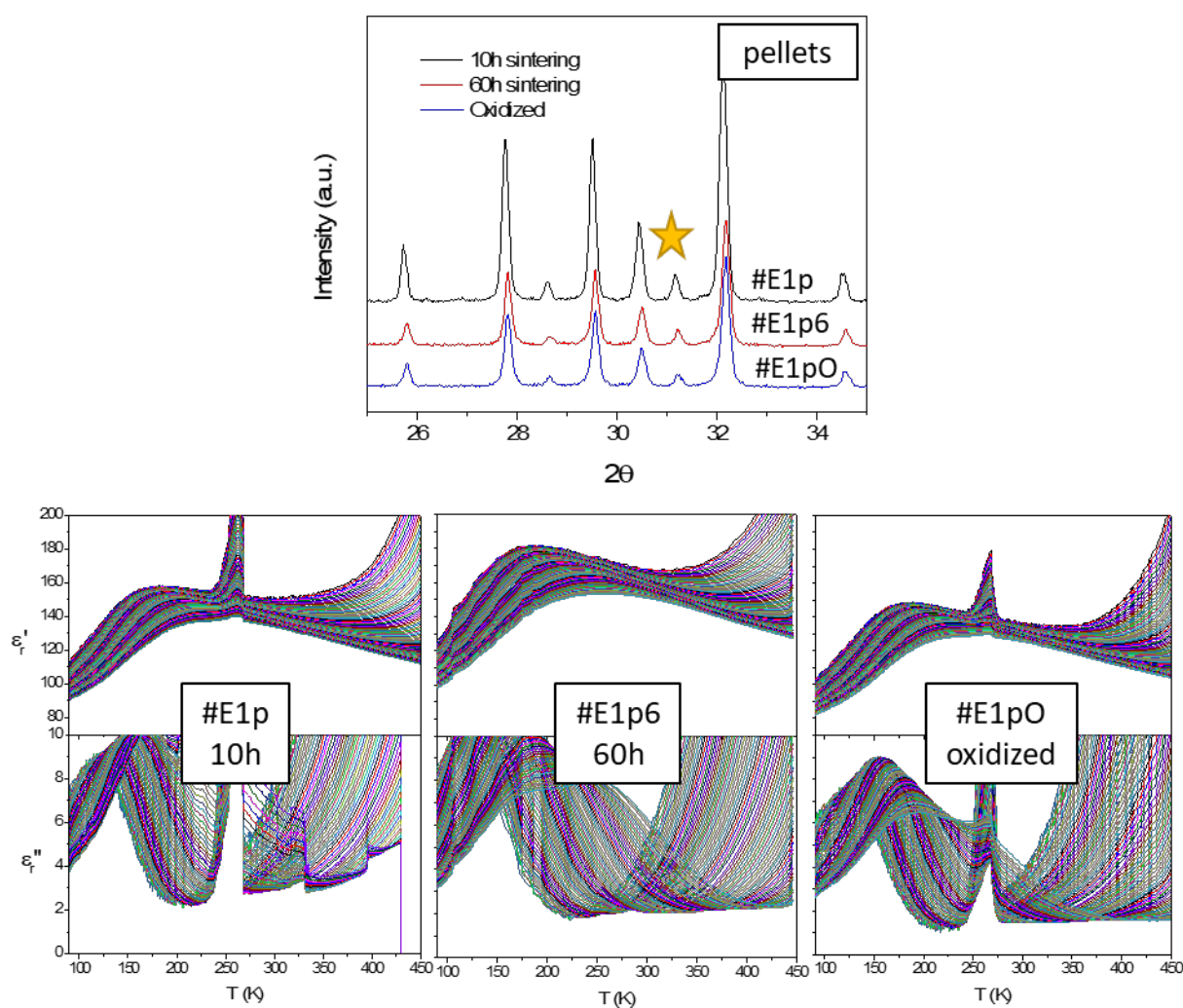


Figure 61: XRD patterns of pellets after 10h sintering, 60h sintering and after oxidizing treatment. Perovskite is always present on each sample, represented by a yellow star. Dielectric measurements of each pellet are displayed on the bottom

However, applying TSF on the sample, and then sintering it for 10h (#E2p) lead to the observation of RF transition. Moreover, both 10h (#E2p) and 60h (#E2p6) sintering display a

RF behavior. In both cases, the XRD measurements also confirm the absence of perovskite phase in the TSF powder and the resulting pellets (#E2, #E2p and #E2p6) (see Figure 62).

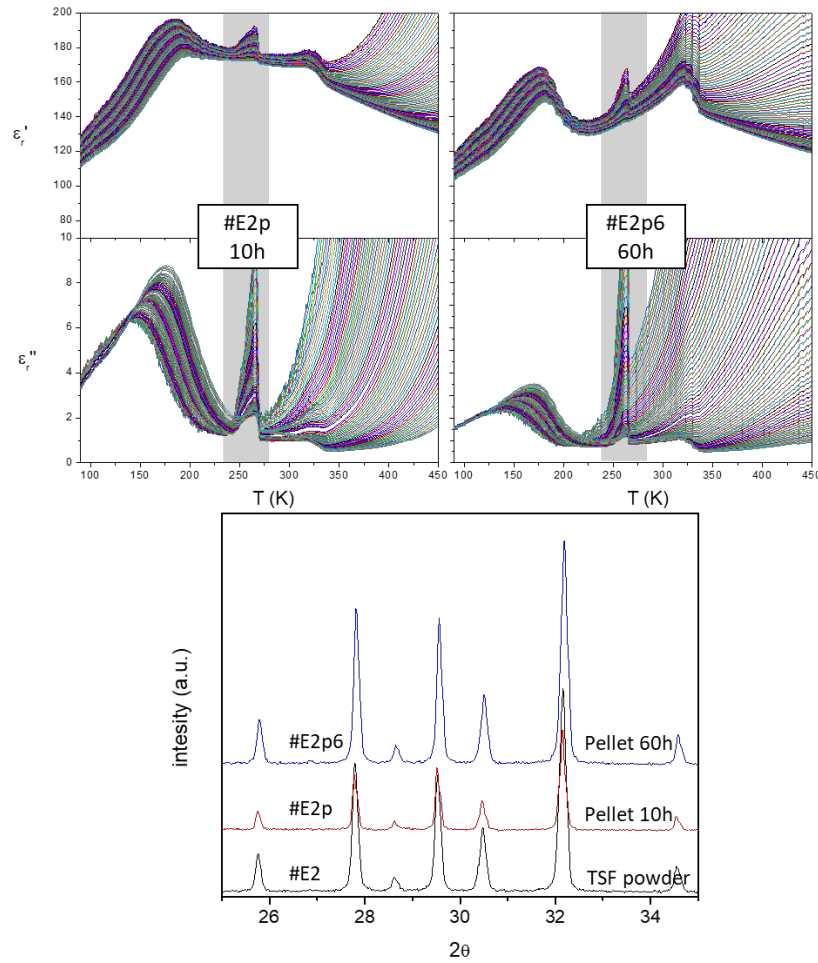


Figure 62: Dielectric measurements and XRD patterns of #E2 pellets after 10h (#E2p) and 60h (#E2p6) sintering time

The stoichiometric  $\text{Ba}(\text{Fe}_{0.5}\text{Nb}_{0.5})\text{O}_3$  perovskite phase must be very stable due to its stoichiometry, and therefore may be stabilized in a wide range of temperatures, which also partially correspond to the stability temperature domain of the TTB phase. Thus, it is possible that heat treatment is inefficient in trying to remove that perovskite phase and isolate the TTB one. However, using a TSF seems to be an efficient way in doing so, and further sintering preserve the phase purity of the TTB phase. This also points out the strong impact of the initial presence of the perovskite on dielectric properties of pellets. On this last point, it is noteworthy that in this phase the Fe/Nb ratio is 1/1, while it is 1/4 in the TTB phase, which also has an ability to accommodate Ba vacancies without much influence on dielectric properties. Thus, a

possible explanation of the influence of this secondary phase could be that it favors the formation of oxygen vacancies, to compensate for the Nb deficiency induced by its formation.

The presence of this phase in the very first step of the synthesis claims for the importance of focusing on the initial milling step before the first firing is performed.

### 3.2.5 Precursor milling

The last parameter explored is the milling step. This step is the first of the synthesis process and can be achieved through different ways. In the present work, it was either the classical hand milling in an agate mortar during 30 min, or planetary milling. The latter offers the advantage of a better control of the final result through tunable milling time and speed, but also scalable quantities of powders and the presence of a liquid phase (usually ethanol). In the present work, the reduction of particle size is not investigated, but could be an interesting future complement to the present study.

Different milling time and speeds were explored, and powders quantities were kept constant, consisting in a mix of  $\text{BaCO}_3$ ,  $\text{Fe}_2\text{O}_3$ ,  $\text{Nd}_2\text{O}_3$  and  $\text{Nb}_2\text{O}_5$  in such quantities that the final powder would result in 4 g of  $\text{Ba}_2\text{NdFeNb}_4\text{O}_{15}$ . Milling was performed with the mixed powders and 20 mL of ethanol to prevent aggregation of powders at the bottom of the jars and ease heat absorption.

*Table 3: Milling conditions of time and speed for planetary milling and sample codes*

|         | 0,5h | 1h  | 1,5h |
|---------|------|-----|------|
| 400 rpm | n/a  | 410 | n/a  |
| 500 rpm | 505  | 510 | 515  |
| 600 rpm | n/a  | 610 | n/a  |

In Table 3 are summarized the samples codes and the associated milling conditions. Further treatment is the same for each sample, with a first firing at 1280 °C/12h and a sintering at 1310 °C/10h. Fired powders are crushed in a mortar with an agate ball, put on a vibrating plate for 45 min before sintering.

The resulting pellets underwent dielectric characterization and three different responses were observed, one being slightly different of the responses previously observed. These three types of responses are represented in Figure 63 and summarized in Table 4.

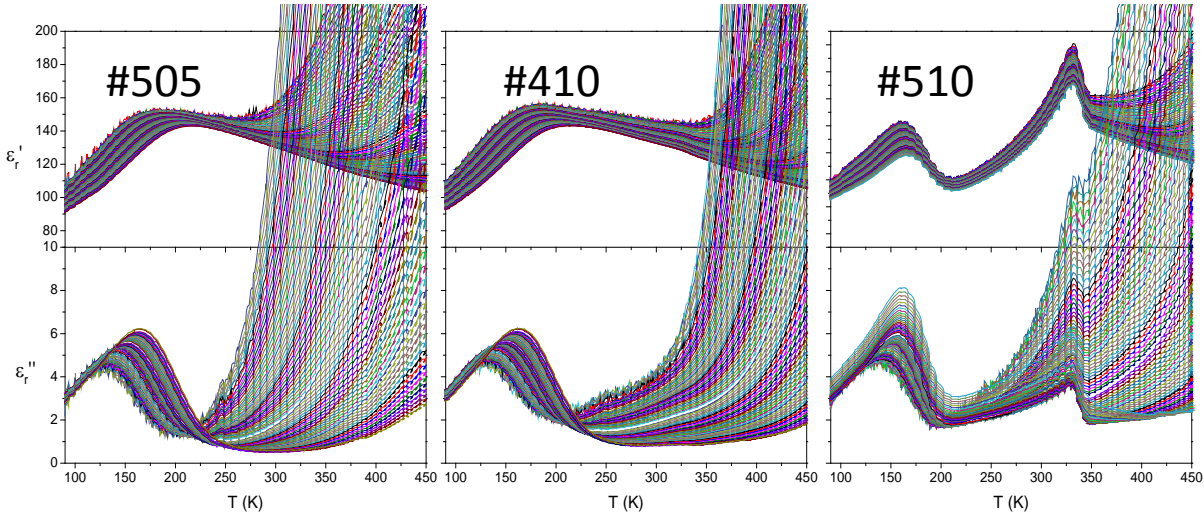


Figure 63: Different types of dielectric responses observed

Table 4: Dielectric transition types measured on pellets

|         | 0,5h | 1h   | 1,5h |
|---------|------|------|------|
| 400 rpm | n/a  | R(f) | n/a  |
| 500 rpm | R    | RF   | RF   |
| 600 rpm | n/a  | RF   | n/a  |

R: relaxor ; RF: Relaxor and ferroelectric ; (f): weak ferroelectric

In this table, three different behavior are presented. For higher speed and milling times, a RF crossover behavior is observed, whereas for short milling time (0.5h, 500 rpm) R state is observed. A particular case for sample milled 1h at 400 rpm where the FE transition (see Figure 63) is very small in amplitude.

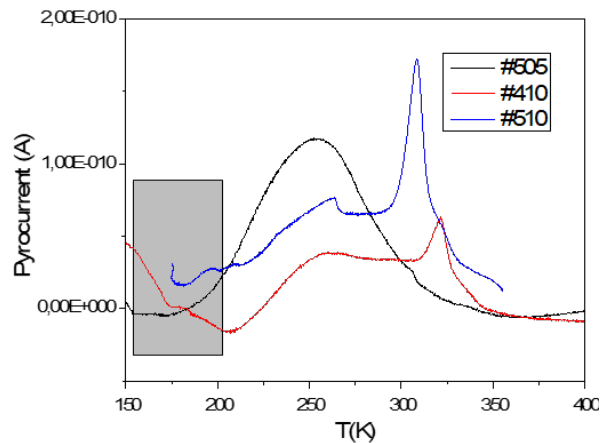


Figure 64: Pyrocurrent measurement performed at 4K/min, after poling under  $5 \text{ kV.cm}^{-1}$  down to 100K, of samples #505, #410 and #410, grey zone represents non-linear thermal ramp responsible for a non-zero pyrocurrent

In order to confirm the ferroelectric transition in sample #410, pyrocurrent measurements (4 K/min) were performed on pellets after poling under  $5 \text{ kV.cm}^{-1}$  while cooling from 350 K to 100 K. Figure 64 displays the results for samples #410, #510 and #505, the two latter being used as references.

These results show for #505 a single broad peak centered at 250 K which is due to the presence of a relaxor to paraelectric phase transition. In the case of sample #510, two peaks are observed. The first one is located at around 260 K and corresponds to the relaxor phase transition, while a second peak at 320 K corresponds to the FE→PE phase transition. This latter peak is more intense and sharper than the one associated to the R transition. For sample #410, two peaks are also observed and correspond to the same type of transition as that observed for sample #510. The temperatures, size and shape are slightly different but the presence of the high temperature sharper peak does not suffer any doubt and is a clear proof of a FE state in the sample.

Two different behaviors arise from these measurements, R and RF. A "purely FE" sample has not been obtained using the explored conditions, and up to now, no conditions have been clearly identified to reliably isolate such kind of sample. However, it has been once obtained for slower milling speeds (200 rpm) and further work could lead to the determination of specific conditions to obtain this behavior again. For the moment, what is displayed in these results are different dielectric responses depending on the milling conditions. R sample has been obtained for the shortest milling time, and the slowest milling conditions gave rise to RF sample with a weak FE transition. These results point out the effect of milling on the final dielectric properties of  $\text{Ba}_2\text{NdFeNb}_4\text{O}_{15}$  TTB. The RF crossover has been evidenced as the intrinsic response of the

phase and is obtained for longer and faster (i.e. more energetic) milling. This must result from a better homogenization of precursors, in terms of mixture as well as chemical reactivity, which results in a better homogenization of the final crystal structure. For less energetic milling conditions, the distribution and/or reactivity of precursors may remain inhomogeneous, which results in poorer crystallization of the target phase, and dielectric properties different from the intrinsic behaviour of the target phase.

This work highlighted the different dielectric responses observed for  $\text{Ba}_2\text{NdFeNb}_4\text{O}_{15}$ . From these three responses, it is clear that the RF crossover is the intrinsic response of the phase. Through different treatments, like two-step firing, longer sintering or oxidizing treatments, the intrinsic RF behavior has been recovered from purely R ceramics (FE ceramics could not be tested). The milling has been highlighted as a key step which determines the final properties of the pellet, allowing to select a R or RF response. This is promising for the exploration of structural modification at the origin of these dielectric responses, and will be the object of the following part.

### **3.3. Structural comparison of samples with different dielectric properties**

#### **3.3.1 Rietveld XRD refinement**

Since it is now possible to reproducibly prepare samples of identical composition and different dielectric behavior, it is tempting to explore the subtle structural differences that could explain these different dielectric behaviors. For this study, a powder has been synthesized through precursor milling at 500 rpm for 0.5h and firing at 1280 °C for 12h. A part of this powder has been sintered at 1310 °C for 10h and the second part of the powder underwent a second firing in the same conditions, followed by a same sintering in the same conditions. Two pellets of each kind (R and RF) are obtained with densities of 96 (R) and 98 % (RF) respectively. For each couple of R and RF pellets, the first one is metalized and used for dielectric measurement, while the second one is crushed to obtain a fine powder through 20  $\mu\text{m}$  sieving. Rietveld refinement have been performed on both samples to access structural information. Dielectric measurements and XRD pattern refinements are displayed on Figure 65.

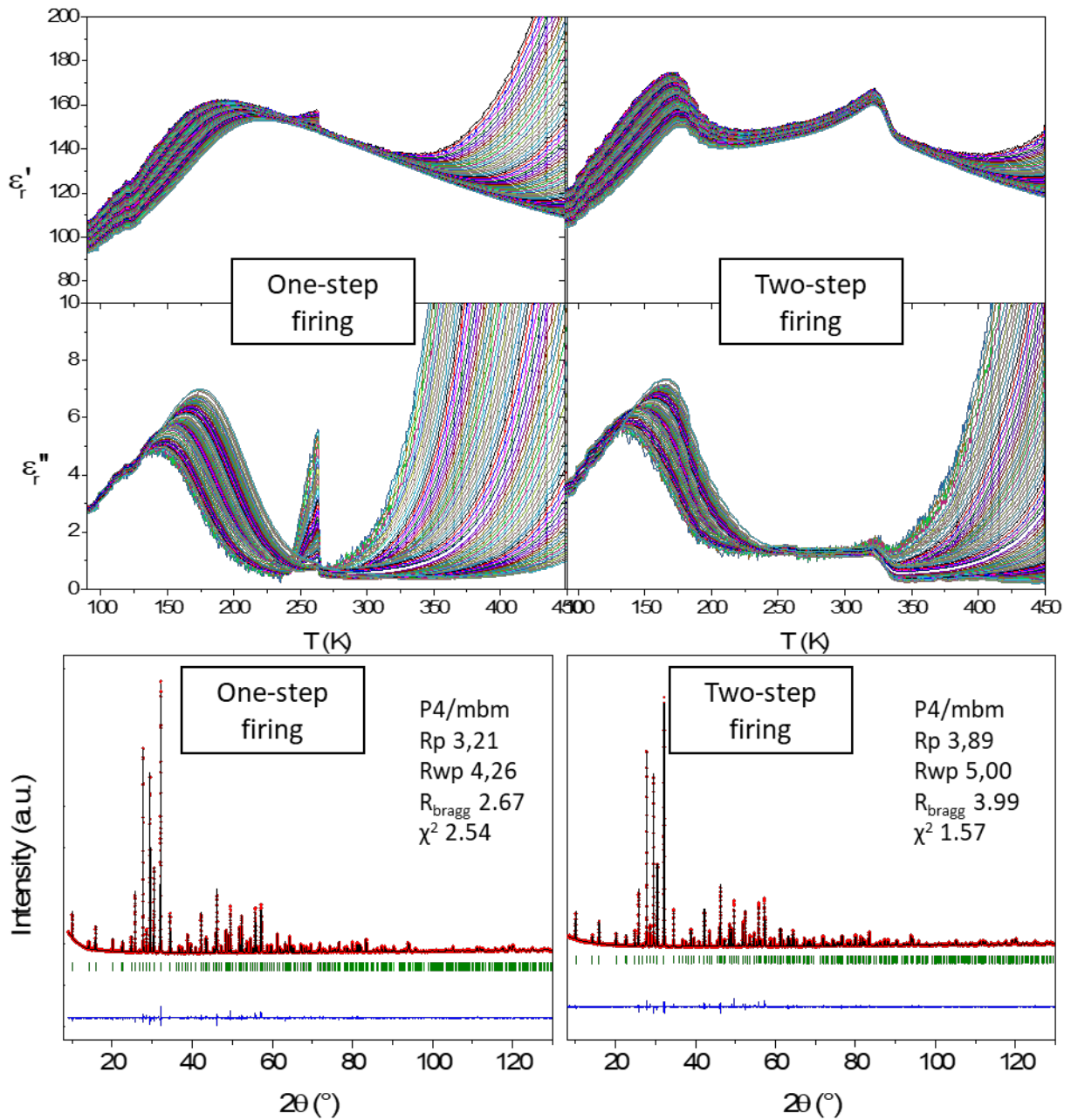


Figure 65: Dielectric measurement and Rietveld refinements performed on pellets after (left) one-step and (right) two-step sintering

Dielectric measurements show the two different responses expected, R and RF. The corresponding refinements are represented below and show a good fit (Rp and Rwp,  $R_{\text{Bragg}}$  and  $\chi^2 \leq 5.00$ ).

Table 5: Lattice parameters of relaxor and crossover sample

|           | <b>a (Å)</b> | <b>c (Å)</b> | <b>v (Å<sup>3</sup>)</b> |
|-----------|--------------|--------------|--------------------------|
| Crossover | 12.47430 (3) | 3.92691 (1)  | 611.060 (2)              |
| Relaxor   | 12.47439 (2) | 3.92697 (1)  | 611.078 (2)              |
| Deviaton  | 0.00072%     | 0.0015%      | 0.0029%                  |

Table 6: Refined atomic positions, displacement and site occupancies. for the crossover and the relaxor samples

|    | <b>x</b>     | <b>y</b>     | <b>z</b>     | <b>B<sub>iso</sub> (Å<sup>2</sup>)</b> | <b>Occ.</b> |           |
|----|--------------|--------------|--------------|--|-------------|-----------|
| RF | Ba           | 0.31956 (2)  | 0.83890 (2)  | 0.5                                    | 0.412 (4)   | 100.7 (2) |
|    | Nd           | 0            | 0            | 0.5                                    | 0.456 (4)   | 97.6 (2)  |
|    | Fe1          | 0            | 0.5          | 0                                      | 0.629 (8)   | 22.6 (4)  |
|    | Nb1          | 0            | 0.5          | 0                                      | 0.629 (8)   | 77.4 (4)  |
|    | Fe2          | 0.21420 (1)  | 0.07433 (1)  | 0                                      | 0.005 (3)   | 28.3 (5)  |
|    | Nb2          | 0.21420 (1)  | 0.07433 (1)  | 0                                      | 0.005 (3)   | 71.7 (5)  |
|    | O1           | 0            | 0.5          | 0.5                                    | 3.09 (5)    | -         |
|    | O2           | 0.21841 (6)  | 0.71841 (6)  | 0                                      | 0.49 (3)    | -         |
|    | O3           | 0.06411 (9)  | 0.13356 (8)  | 0                                      | 3.53 (3)    | -         |
|    | O4           | 0.15726 (7)  | 0.49383 (6)  | 0                                      | 0.51 (2)    | -         |
| R  | O5           | 0.19577 (7)  | 0.07472 (9)  | 0.5                                    | 3.70 (3)    | -         |
|    | Ba           | 0.31944 (11) | 0.83899 (11) | 0.5                                    | 0.266 (26)  | 99.9 (1)  |
|    | Nd           | 0            | 0            | 0.5                                    | 0.404 (26)  | 97.3 (2)  |
|    | Fe1          | 0            | 0.5          | 0                                      | 0.412 (44)  | 21.7 (3)  |
|    | Nb1          | 0            | 0.5          | 0                                      | 0.412 (44)  | 78.3 (3)  |
|    | Fe2          | 0.21427 (6)  | 0.07433 (7)  | 0                                      | -0.123 (19) | 28.3 (5)  |
|    | Nb2          | 0.21427 (6)  | 0.07433 (7)  | 0                                      | -0.123 (19) | 71.7 (5)  |
|    | O1           | 0            | 0.5          | 0.5                                    | 1.81 (27)   | -         |
|    | O2           | 0.21809 (35) | 0.71809 (35) | 0                                      | 0.01 (16)   | -         |
|    | O3           | 0.06358 (52) | 0.13305 (44) | 0                                      | 2.92 (17)   | -         |
| O4 | 0.15913 (45) | 0.49454 (34) | 0            | 0.66 (12)                              | -           |           |
| O5 | 0.19412 (43) | 0.07604 (51) | 0.5          | 3.27 (15)                              | -           |           |

From the refined parameters, Table 5 gives the lattice parameters and Table 6 the atomic positions, displacements and site occupancies. Oxygen occupancies are assumed to be 100 %. Lattice parameters can be considered identical, with a volume difference below 0.003 %. Concerning atomic positions, they coincide in both samples with a maximum difference below

0.002 Å. In terms of site occupancies, the maximum difference does not even reach 1 %. Considering those points, no crystallographic difference separates those two samples which seem to be totally identical from a structural standpoint. Concerning M'' sites, they both exhibit problematic values of their isotropic atomic displacement parameters. In RF case, they are extremely small and in the R case they are negative (which is physically impossible). At the same time, oxygen displacement parameters  $B_{\text{iso}}$  are completely inhomogeneous (ranging from 0.01 to more than 3.5 Å<sup>2</sup>). Both M'' site anomaly and inhomogeneous O displacements are basically equivalent from one sample to another. If they appear physically impossible, it is due to the applied structural model. This results from the fact that the selected space group, *P4/mbm*, is an averaged, three-dimensional structural solution, but is not the real solution. Actually, P. Heijboer showed the presence of 3+2D superstructure in this phase<sup>74</sup>, and it is the reason why *P4/mbm* is considered as an “average” solution. To attempt at bringing further insight concerning the structural mechanisms at play in these TTB, electron diffraction experiments were conducted, and are reported in the following.

### 3.3.2 Electron diffraction

This part has been achieved in collaboration with F. Weill (Placamat) and P. Boullay (CRISMAT-Caen). This part concerns preliminary results obtained during the redaction of the present manuscript and therefore do not aim at solving the question of the aperiodic structure. Experimental results presented here will need further analysis. However, the presentation of these preliminary results remains interesting in the framework of the present study.

Structure determination can be achieved with two different types of samples: powder and single crystal. Powder diffraction techniques are XRD, neutron diffraction and electron diffraction. While diffraction from single crystal allows isolating single Bragg reflections and aperiodic satellites, it generally requires the growth of the single crystals, which can be challenging. As for powder techniques, their resolution is usually poorer when compared to single crystal diffraction techniques, but they are more accessible with respect to sample preparation, and are not subject to twinning issues. Here, we demonstrated the irrelevancy of powder XRD to determine the structural mechanism behind the dielectric behaviours of TTB samples. Previous works on TTB phases of Ba<sub>2</sub>NdFeNb<sub>4</sub>O<sub>15</sub> and related solid solutions shew the same result with neutron powder diffraction<sup>13</sup>. Then, the use of single crystals is a great solution since it is

possible to access way more structural details in comparison with powder diffraction. Single crystal diffraction can be performed using neutrons, X-rays and electrons. In the case of neutrons and X-ray, large single crystals are needed and are sometimes impossible to obtain. In the case of TTB materials with  $\text{Ba}_2\text{LnFeNb}_4\text{O}_{15}$  ( $\text{Ln} = \text{La}, \text{Pr}, \text{Nd}, \text{Eu}, \text{Sm}$ ), single crystals were grown and characterized<sup>46,74,82</sup>. In every case, single crystals show a pure relaxor to paraelectric phase transition. This makes a direct comparison with ceramic difficult (or even impossible for RF samples). In the case of electron diffraction, it is possible to perform single crystal diffraction on crystals with small size of a few hundreds of nanometers.

Basically, the advantage of electron diffraction is that it offers easy access to small single crystal diffraction, but with the risk of finding twinning.

The observation of selected area electron diffraction (SAED) patterns using TEM has been performed at room temperature on RF sample. Figure 64 displays SAED where (001) and (210) plan families are visible.

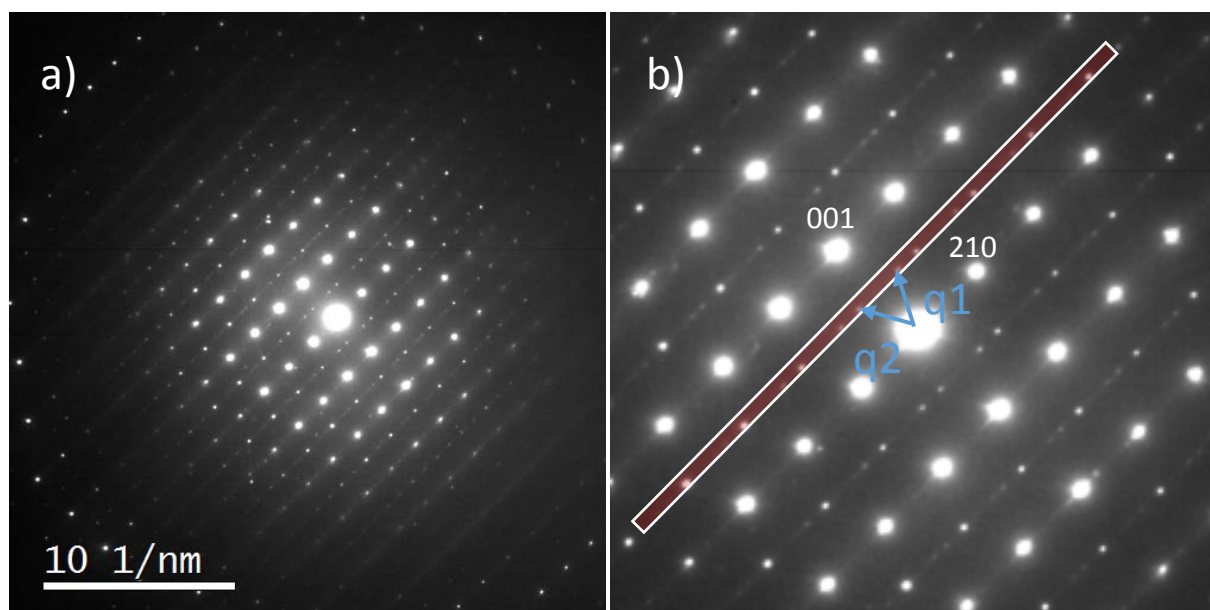


Figure 66: SAED pattern along  $\langle \bar{1}20 \rangle$  of RF sample showing two modulation vectors  $q_1$  ( $\alpha; \alpha; 1/2$ ) and  $q_2$  ( $\alpha; -\alpha; 1/2$ ). Red box shows an incommensurate satellite line

SAED pattern along  $\langle \bar{1}20 \rangle$  shows the result for an oriented single crystal. Two plan families are indexed, (001) and (210). These spots define the tetragonal lattice and diffractions peaks having decimal h, k or l values are forbidden. On this pattern are visible families of plan parallel

to (210) planes but having  $l = 0.5$ . This suggests the existence of a superstructure with larger lattice parameters. Modulation vectors are identified and defined as  $q_1 = \alpha.a^* + \alpha.b^* + 0.5.c^*$  and  $q_2 = -\alpha.a^* + \alpha.b^* + 0.5.c^*$  with  $\alpha \approx 0.3$ . Whereas a doubling of  $c$  parameter can define the  $c_{\text{super}}/c$ , no integer multiplication of lattice parameters  $a$  and  $b$  can encompass these satellites. The phase is thus defined as aperiodically (or incommensurately) modulated.

Classically, electron diffraction (ED) focuses on qualitative analyses of diffraction patterns for space group determination, satellite observation and modulation vector determination. In recent years, techniques have been developed to achieve structure refinement from electron diffraction data, through the development of precession electron diffraction (PED)<sup>83</sup> and electron diffraction tomography (EDT)<sup>84,85</sup> methods, structure determination became possible. Another difficulty in refining ED patterns is that the kinematical approach, usually valid for X-ray and neutron diffraction, is no longer valid for electron diffraction and the use of dynamical diffraction theory is needed<sup>86</sup>. The use of EDT associated to PED and dynamical diffraction theory led to the development of precession electron diffraction tomography (PEDT)<sup>87</sup> which allowed structure determination of  $\text{Ni}_2\text{Si}$ ,  $\text{PrVO}_3$ , kaolinite, orthopyroxene and mayenite<sup>88</sup>. Further development even allowed determination of hydrogen positions in crystalline macromolecules<sup>89</sup>.

PEDT is also used to determine superstructures, including aperiodic modulation. Aurivillius phases of  $\text{ABi}_7\text{Nb}_5\text{O}_{24}$  ( $A = \text{Sr, Ba, Pb}$ ) compositions have been determined to be (3 + 1)D modulated structures and comparison with neutron diffraction pattern refinement gave similar results<sup>90</sup>. This example of aperiodic modulation of Aurivillius phases shows the possibility to explore in more detail the structure of TTB materials, and eventually their structural modulation. Exploring the structure of both R and RF samples could give a direct access to the structural differences between both samples, and the structural origin of both behaviors. In addition, it is possible to follow the evolution of superstructure satellites versus temperature, and then have access to the structural differences between the different phases (relaxor, ferroelectric and paraelectric).

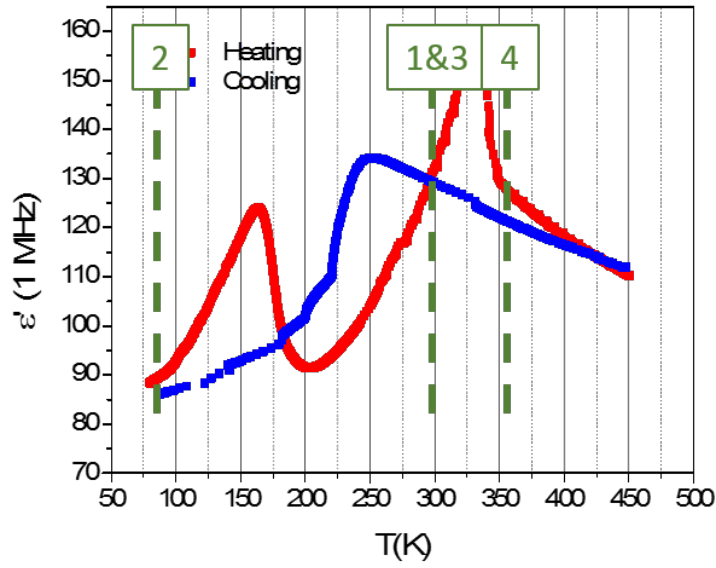


Figure 67: Dielectric measurements performed both on heating and cooling on a RF sample. Four different PEDT measurements have been performed at temperatures ranging from 1 to 4, in this chronological order

In this section, preliminary results are presented on a RF sample, with data acquisitions for various temperatures. As explained in the first chapter of the present manuscript, TTB materials of the  $\text{Ba}_2\text{NdFeNb}_4\text{O}_{15}$  family exhibit different dielectric behavior on heating and cooling. After heating in the PE temperature range and cooling down to ambient, the phase remains PE. Then it becomes FE below room temperature, and then R at low temperature and the two transitions (R, FE) are again observed on heating. Therefore, diffraction measurement has been performed in order from 1 to 4 as presented on Figure 65.

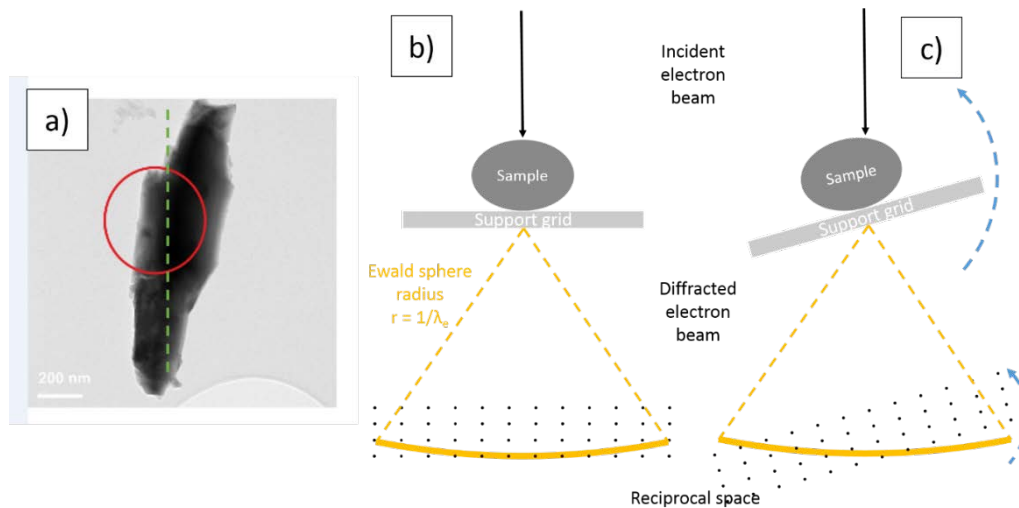


Figure 68: Representation of PEDT experiment in TEM with (a) picture of a single crystal (scale 200 nm) used for diffraction experiment, red circle represents incident beam size and green dashed line represents rotation axis. Schematic representation of diffracted beam observation for a crystal (a) before and (b) after rotation

The experimental procedure is represented on Figure 68. It consists in recording diffraction patterns on a small part of single crystal (red circle on the figure) first in a random angle and then the next patterns are obtained by tilting the sample around a rotation axis (green dashed line) at various angles. From this data collection, lots of patterns are obtain and can be used to reconstruct reciprocal space in 3 dimensions.

Once reconstruction has been performed, it is possible to represent the reciprocal lattice as displayed on Figure 69. Each red dot represents a measurement on a pattern. By slowly tilting the sample, each reciprocal reflexion (h,k,l) is obtained on several patterns. Each of these are represented here by a single red dot. The average position of a set of dots is used to determine the position of the reflexion. Here is represented a NL sample a low temperature (95 K) in the relaxor state. The represented black box corresponds to the reciprocal tetragonal cell used for X-ray refinement, and therefore fits with the hypothesis of  $P4/mbm$  space group. However, extra-reflexions are observed in the center of the cell. This means some satellite peaks are present, showing a structure modulation defined by a vector  $q \approx 0.5a^* + 0.5b^* + 0.5c^*$  which defines a commensurately modulated structure.

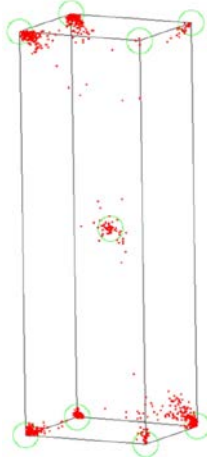


Figure 69: Reciprocal lattice cell of BaNdFeNb4O15 at 95 K

Superstructure evolution with temperature has been followed for 3 different temperatures on the same crystal, as scheduled. Results are displayed on Figure 68. First, what is confirmed is that if we exclude satellite peaks, the phase remains tetragonal all over the explored temperature range. Second, the only evolution in the reciprocal space concerns the satellite peak. First, at room temperature in the initial PE state, two satellites are observed at  $0.5c^*$ . Their associated vectors are  $q_1 \approx \alpha.a^* + \alpha.b^* + 0.5.c^*$  and  $q_2 \approx -\alpha.a^* + \alpha b^* + 0.5.c^*$  with  $\alpha \approx 0.29$ . Because  $\alpha$  has a real value, this structural modulation is incommensurate. When the temperature is decreased down to 95 K in the relaxor phase, both these satellites merge in a single satellite at the center of the reciprocal lattice and the modulation becomes commensurate. A single, commensurate modulation vector remains which is approximately  $q \approx 0.5a^* + 0.5b^* + 0.5c^*$ , as previously mentioned. This commensurate state is preserved when temperature is increased back to room temperature in the FE state. The hysteretic behavior of this satellite (incommensurate at room temperature on cooling and commensurate on heating) is likely related to the hysteretic behavior of the ferroelectric transition reported in previous works<sup>46,74,82</sup>. At high temperature (90 °C – 360 K) in the PE state, the crystal structure is incommensurately modulated, similarly to the first measurement at room temperature in the PE state. Therefore, the commensurate modulation is associated with polarized R and FE states, whereas the PE state is associated with an incommensurate structural modulation. The incommensurate satellites in the PE state show an evolution of their intensity with time. When standing at 90 °C for few tens of minutes, the satellite remains stable (in the center of the reciprocal cell), and progressively evolves into a diffuse peak after approximately an hour, which finally splits into

two different peaks. Moreover, the satellites' intensities also decrease with time, and after a few hours, become difficult to observe. An explanation to this observation can invoke the actual temperature in TEM which is actually difficult to measure precisely. Considering 90 °C (360 K) for diffraction experiment and comparing with FE→PE transition at 330 K, there are only 30 K difference between both values. Temperature controller in TEM is not directly in contact with the sample, so it is possible that the sample is right at the transition temperature while diffraction is performed, which results in the observation of the evolution of satellites' position. Unfortunately, the sample holder that can explore low temperatures (below ambient temperature, which is a range necessary to this study) is limited to 90 °C, which seems to be close to the FE transition of our sample. It would be interesting now to perform satellite observation in SAED at higher temperature to survey the evolution of the satellites, and check if they totally disappear. This would mean the high temperature PE phase would actually crystallize in  $P4/mbm$  space group, and that the behavior observed in the present study should be ascribed to the FE to PE transition. It is worth mentioning that these results are reproducible as the same experiment has been performed on a second crystal at the different temperatures tested and observations are similar. Because electron diffraction of an isolated crystal is localized, it would be interesting to perform the same experiment on many crystals to confirm whether all behave the same way, or whether there are different structural evolutions from one crystal to the other, within a polycrystalline otherwise considered homogeneous.

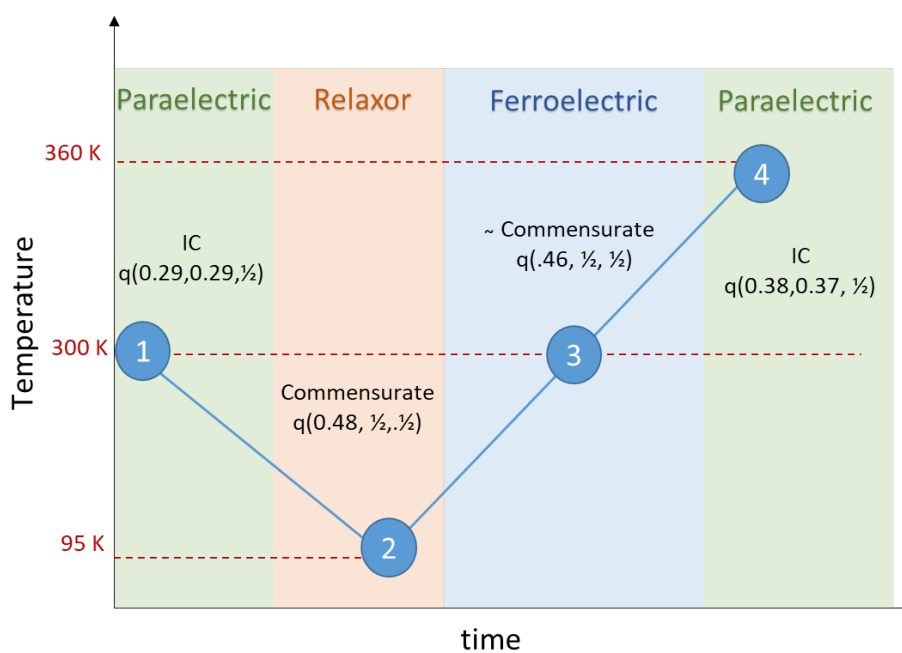
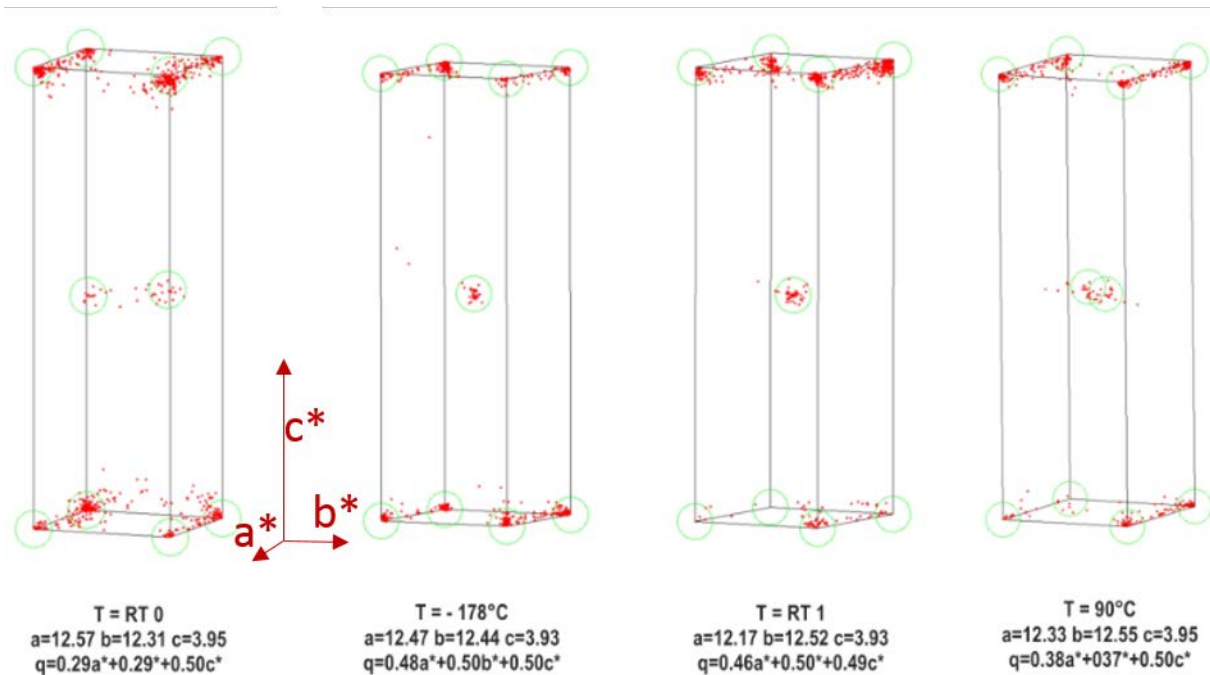


Figure 70: Evolution of modulation vector versus temperature at room temperature PE phase, then  $-178^\circ C$  (95 K) R phase, back to room temperature FE phase and final high temperature  $90^\circ C$  (363 K), associated to a sketch representing the evolution of satellite peaks with temperature

Some clarification is necessary concerning the experimental values of  $\alpha$  parameter on Figure 70. It is actually determined from the observation of about 50 patterns taken at different angles on a single crystal (Figure 68). However, from one pattern to another, there might be a slight shift of peaks (due to the geometry and the position of the crystal), then the precision of the

position of a peak is determined statistically by a comparison of the multiple patterns on which this peak appears. Thus, for weakly intense peaks, such as satellites, the uncertainty level is higher than for intense peaks. In the present case, satellite position is determined without structural considerations. Because  $q$  is defined as  $(\alpha, \alpha, 1/2)$ , the observation of experimental  $q(0.48, 1/2, 1/2)$  at 95 K is physically impossible. However, this is due to the uncertainty on peak position. Here, we assume  $q$  is  $(1/2, 1/2, 1/2)$ , thus the structure is considered commensurate.

Complete analysis of data has not been possible yet and structural refinement are still ongoing. However, preliminary results were deemed significant enough to be presented at this point, although they are not definitive.

Considering the easier case of commensurate modulation (*i.e.*  $T=95\text{K}$ ), a three-dimensional space group can be used to define the structure. In the present case, lattice refinement leads to the description of the structure in a slightly orthorhombic  $Icmc$  space group with cell parameters  $a = 17.652 \text{ \AA}$   $b = 17.592 \text{ \AA}$   $c = 7.870 \text{ \AA}$ . This orthorhombic space group is in opposition with the previous observation on this phase, which is always described in a tetragonal space group. However, electron diffraction is not appropriate to precisely determine lattice parameters. Thus, considering  $a/b = 1.0034$ , we would better consider the phase as tetragonal, resulting from a rotation of  $45^\circ$  of the initial tetragonal cell with cell parameters  $a^{Imcm} = \sqrt{2} \cdot a^{TTB}$ ,  $b^{Imcm} = \sqrt{2} \cdot b^{TTB}$  and  $c^{Imcm} = 2c^{TTB}$ . Basic refinement has been performed on dataset assuming kinematical diffraction. This method allows a rough definition of atomic parameters (position).

Table 7: Atomic positions, Wyckoff sites and associated symmetry obtained from preliminary kinematical PEDT refinement

| Position | x       | y       | z       | Wyckoff site | Symmetry |
|----------|---------|---------|---------|--------------|----------|
| Ba1      | 0.579   | 0.24    | 0       | 8h           | m..      |
| Ba2      | 0.25    | 0.079   | 0.5     | 4e           | mm2      |
| Ba3      | 0.25    | 0.079   | 0       | 4e           | mm2      |
| Nd1      | 0.5     | 0       | 0       | 4a           | 2/m..    |
| Nd2      | 0.5     | 0       | 0.5     | 4b           | 2/m..    |
| M'1      | 0.643   | 0.431   | 0.247   | 16j          | 1        |
| M'2      | 0.431   | 0.143   | -0.248  | 16j          | 1        |
| M''1     | 0.75    | 0.25    | 0.25    | 4d           | .2/m.    |
| M''2     | 0.25    | 0.25    | -0.25   | 4c           | .2/m.    |
| O1       | 0.327   | 0.169   | -0.226  | 16j          | 1        |
| O2       | 0.47307 | 0.25    | 0.25    | 8g           | .2.      |
| O3       | 0.75    | 0.03205 | 0.22874 | 8i           | .m.      |
| O4       | 0.66505 | 0.32572 | 0.21509 | 16j          | 1        |
| O5       | 0.53367 | 0.39657 | 0.19641 | 16j          | 1        |
| O6       | 0.04378 | 0.13084 | 0       | 8h           | m..      |
| O7       | 0.62423 | 0.07536 | 0       | 8h           | m..      |
| O8       | 0.0756  | 0.37366 | 0       | 8h           | m..      |
| O9       | 0.25    | 0.26414 | 0       | 4e           | mm2      |
| O10      | 0.07402 | 0.03224 | 0.24464 | 16j          | 1        |
| O11      | 0.63778 | 0.46404 | 0       | 8h           | m..      |
| O12      | 0.75    | 0.2492  | 0       | 4e           | mm2      |

Atomic positions are summarized in Table 7 and represented in Figure 71, along with the structural model refined from XRD data. Atomic position differences are visible between both refinements. The difference is visible for the Nd site at the center of the cell which is more distorted in the low temperature phase, confirming the major role of  $\text{Ln}^{3+}$  accommodation in the crystal chemistry of these TTBs<sup>13,29,32</sup>. Among the various differences, the most important change concerns the oxygen positions.

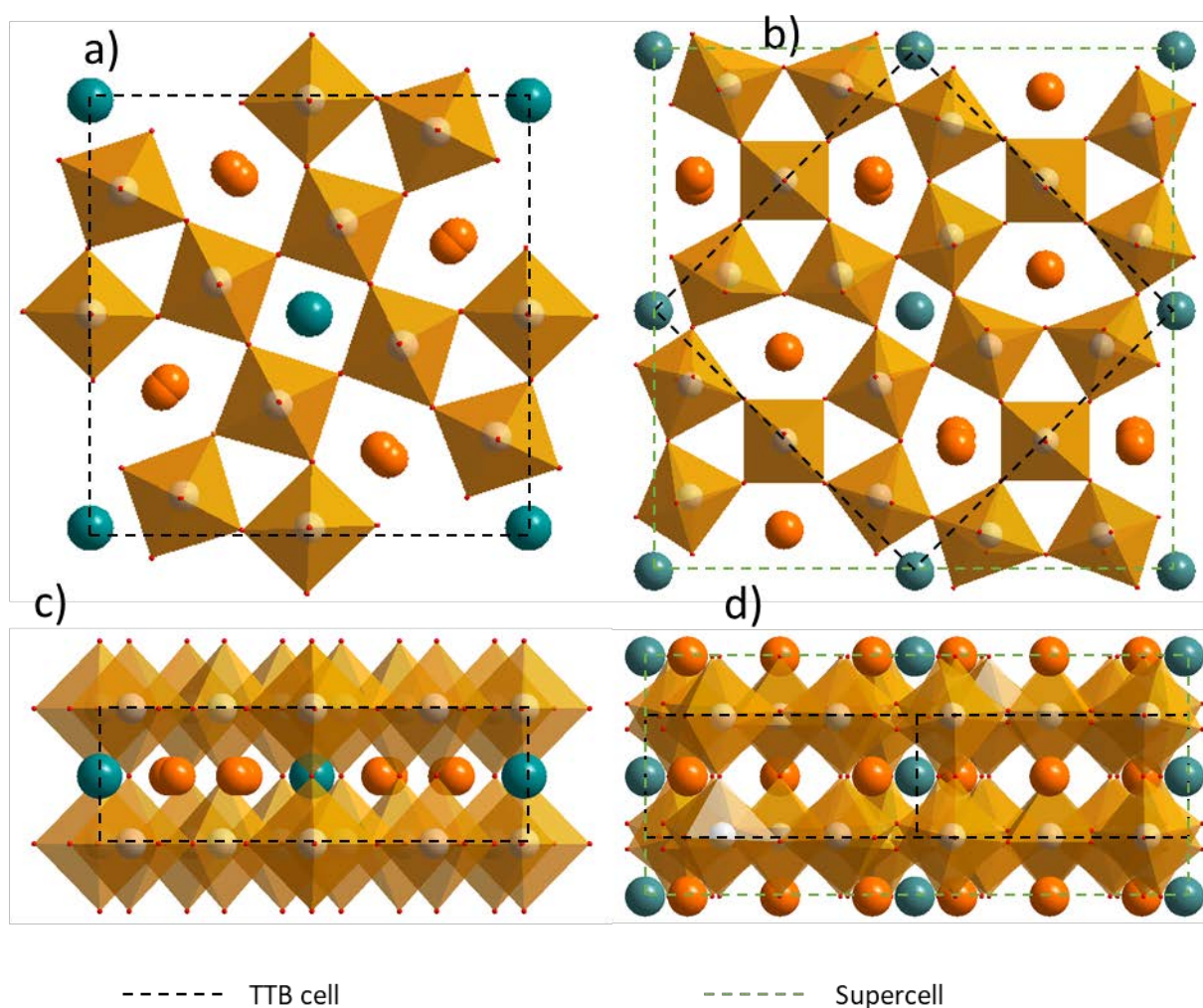


Figure 71: Representation of lattice refined in (a & c) XRD and (b & d) PEDT in two different orientations, (a & b) along (001) and (c & d) along (100). TTb initial lattice and supercell are represented in dashed lines

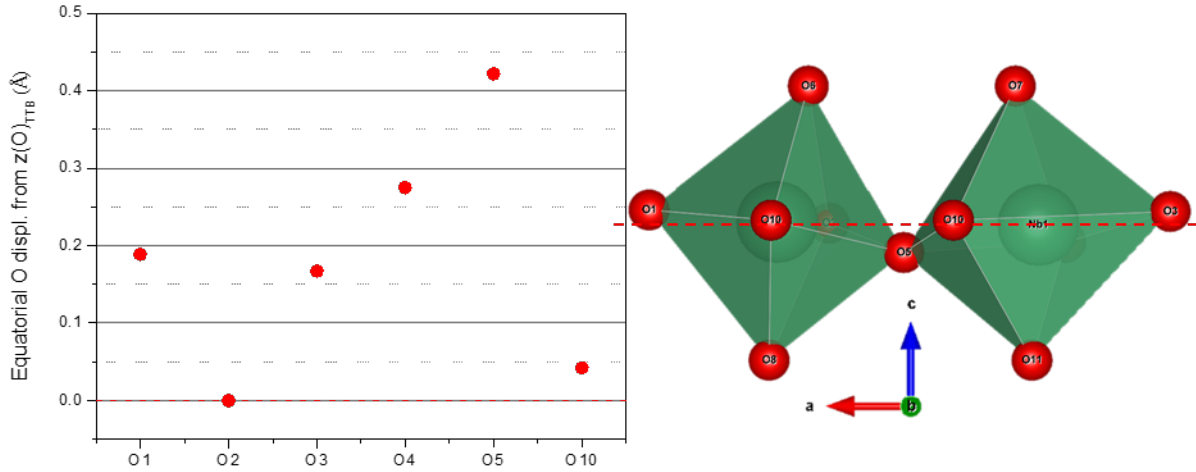


Figure 72: *z* coordinate displacement of equatorial oxygens from their position in room temperature XRD refined TTB structure. Red dashed lines represent the *z* coordinate of equatorial oxygens in the room temperature XRD refined structure and representation of both  $M''$  sites along *b* axis

In average 3D  $P4/mbm$  space group, equatorial oxygens are considered to lie in the (002) plane. Considering the *c* axis doubling in the superstructure cell, they would lie in the (004) plane, with  $z = 0.25$ . However, as displayed in Figure 72, the *z* coordinate of equatorial oxygens are almost all (except for O2) off centered, and this off centering even reaches  $0.42 \text{ \AA}$  for O5. This results in a strong distortion of  $M''$  (Nb-Fe) site. This must be the explanation for the strong oxygen displacements parameters observed in Rietveld refinement of XRD patterns previously presented in Table 6, page 97. At the same time, apical oxygens are off centered in *ab* plane from the position they hold in room temperature TTB structure.

This highlights the role of aperiodic modulations on the anionic framework of the TTB structure, and therefore will be useful to propose a structural explanation to the dielectric properties of  $\text{Ba}_2\text{NdFeNb}_4\text{O}_{15}$ , following further analysis and complimentary experiments. The precise determination of oxygens and FE element  $\text{Nb}^{5+}$  will help determine the orientation of polarization.

As for the commensurate phase, it was possible to propose an alternative space group to fit the incommensurately modulated structure in PE state. This space group has been defined so that the structure can be described with a single modulation vector  $q(0.5, 0, \gamma)$  with  $\gamma \approx 0.46$ , and can be approximated with 3D space group  $Ammm$  with cell parameters  $a^{Ammm} = c^{TTB}$ ,  $b^{Ammm} \approx$

$\sqrt{2} \cdot b^{\text{TTB}}$  and  $c^{\text{Ammm}} \approx \sqrt{2} \cdot a^{\text{TTB}}$ , slightly orthorhombic with  $b/c = 1.011$ . Here also, tetragonality has to be considered, according to the small difference between  $b$  and  $c$  parameters.

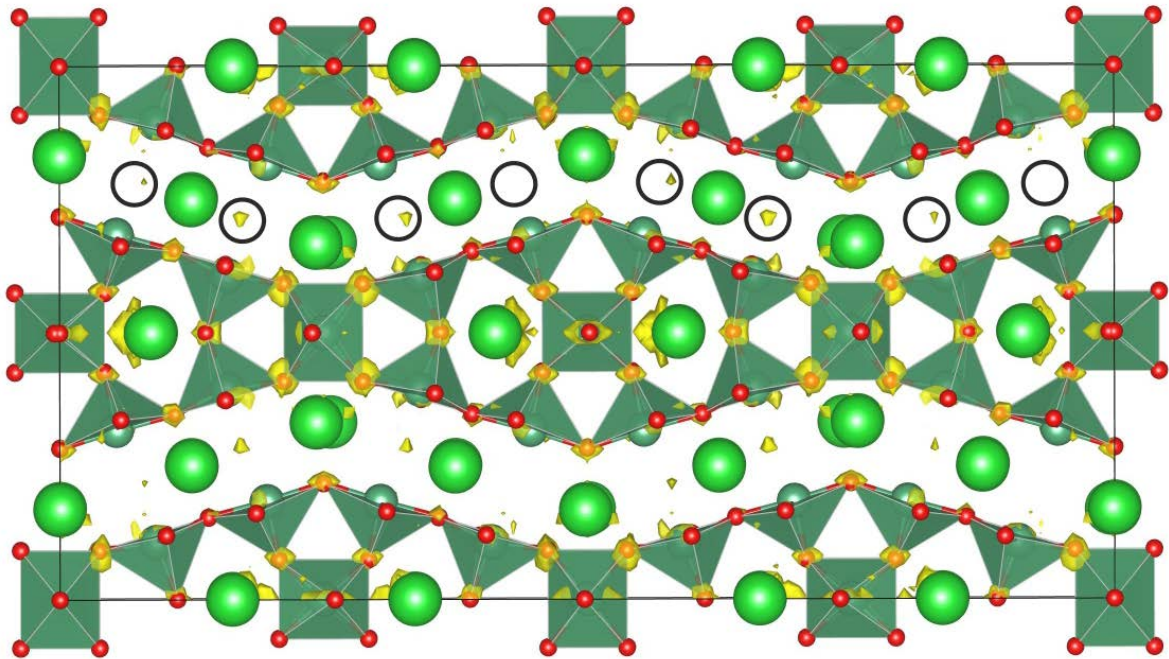


Figure 73: Projection along (100) incommensurate phase  $Ammm(0.5,0,0.46)000$  of  $Ba_2NdFeNb_4O_{15}$  at room temperature

Figure 73 represents incommensurate lattice of  $Ba_2NdFeNb_4O_{15}$  at room temperature after PEDT refinement in kinematical mode.  $Ba^{2+}$  and  $Nd^{3+}$  are displayed in the same color and yellow zones represent electron density. This representation is not the actual result of refinement but is an approximation of it. Further refinement work is needed to obtain the actual structural solution. However, there are some information that can be obtained from this first structure representation. One oxygen position is missing and represented by black circle to show hypothetical position since first runs of refinement did not recognize immediately this position, probably due to structural model. Interpretation of the present results is difficult because they consist in preliminary refinements. However, the observation of a structural evolution with temperature affecting specifically the satellite peaks and reproducing the thermal hysteresis observed for the FE transition, is promising. Indeed, it is the first clear observation of a structural modification with temperature in the  $Ba_2NdFeNb_4O_{15}$  system that relates to the dielectric properties, and confirms the conclusion drawn from conventional studies that the driving force of these properties lies in the anionic framework and emerges from an aperiodic

degree of freedom<sup>13</sup>. Transitions from commensurate to incommensurate phases in TTB systems have already been observed in other structures and their link with dielectric properties also been evidenced. However various relationships are reported, with incommensurate phases associated to PE, FE or R phases, and the same for commensurate phases associated to R and FE states. This work is a confirmation of these hypothesis and an indictment to further explore the aperiodic crystal chemistry of TTBs. In the present case, no full description of both commensurate and incommensurate phases is given but the use of PEDT technique allows such achievement. This could be a great asset to explore slight structural changes like in the present case, where classical X-ray and neutron diffraction pattern refinements give no answer to the question of the structure/property link. Further refinement must be able to define precise atomic positions and displacements, which can then be used to explain the origin of dielectric properties of  $\text{Ba}_2\text{NdFeNb}_4\text{O}_{15}$ . In addition, the exploration of differences between relaxor and FE states in terms of structure has to be performed to identify these differences. Measurements on pure R sample of  $\text{Ba}_2\text{NdFeNb}_4\text{O}_{15}$  would also be useful to understand the structural differences between R and RF samples.

## Part conclusion

As shown in the present examples, TTB materials can exhibit complex properties and structures, and they are therefore of great interest. Exploring solid solutions allowed the confirmation of the important role played by the anionic framework on the dielectric properties of the phase. Ranging from a crossover state to relaxor state, Li substituted samples show an interesting properties evolution that has been followed with structural analyses. Moreover, the observation of these different behavior has been shown to be linked to no crystallographic change from powder X-ray diffraction point of view, which is very surprising.

Tuning the synthesis parameters of the parent phase  $\text{Ba}_2\text{NdFeNb}_4\text{O}_{15}$  lead to the observation of the same variety of dielectric responses as in the solid solutions. This very surprising result becomes a great asset in the research of structure/property relationship. After identifying the strong influence of milling conditions on the resulting properties, without any structural or compositional associated difference, further heat treatments have been performed and crossover response has been determined to be the intrinsic response.

However, no difference was observed in PXRD refinement that could explain the different dielectric behavior, neither the phase transitions from PE to FE or R states. The use of recently developed electron diffraction technique, called precession electron diffraction tomography (PEDT) allowed the observation of satellite peaks in the assumed 3D structure, therefore pointing the presence of a modulated structure. Following this modulation when tuning temperature lead to the observation of transition from commensurate to incommensurate phases. The link between these transitions with the appearance of FE and R phases has not been confirmed since these results are still preliminary, but provide a promising way to explore these materials, in order to understand the structural mechanisms responsible for their dielectric properties.



**Part 2: Ferroic, multiferroic  
and magnetoelectric  
prospective search using  
Spark Plasma Sintering (SPS)**

During the past decades, the development of electronic devices has been exponential. They are omnipresent in every-day life, with many different applications such as telecommunication, storage, calculation, localization, medical imaging, and many other uses. The need of increasing speed, storage density, or even reducing processing costs and reduce the environmental impact of these materials, from their production to their destruction, through their use, represents a huge stake nowadays. Since 2000, a renewed interest has been focused on multiferroic (MF) and magnetoelectric (ME) materials<sup>91-94</sup> for wide applications as multifunctional devices<sup>95-100</sup>. The lack of interest prior to this period was mainly due to the difficulty to obtain such materials that combine self-excluding properties (electric and magnetic ordering), and the development of models, especially by Hill<sup>91,92</sup>, brought a better understanding of these properties and the available solutions to obtain such properties<sup>94,101-104</sup>. However, no ideal material has yet been identified as perfect candidate and many researches are still focused on the development of new phases or the investigation of properties in existing materials in order to find materials with ferroelectric (FE) and ferromagnetic (FM) ordering and/or magnetoelectric (ME) coupling at room temperature. Nowadays, the current researches are focused on the prospection of phases with these properties so as to understand the underlying mechanisms leading to such properties, which could give the key elements leading to the ideal phases.

The object of the present work is to explore potential materials encompassing these needs, *i.e.* to possess (multi)ferroic properties, and/or ME. Because of their ease of production, most of the researches focus on ceramic materials. Since electrical measurements of dense samples are necessary to characterize the FE properties, a sintering step is necessary during the process to obtain measurable samples. This step usually requires high temperature (typically above 700 °C), thus becomes limiting for phases having low decomposition temperature or exhibiting irreversible phase transition before sintering temperature (considering the low temperature phase is the more interesting for properties purpose, MF or ME in the present case). These materials will be referred to as “fragile” in the following.

Based on crystal chemical aspects, candidate materials will be chosen among fragile materials for which electrical properties remain unexplored, and densification will be performed using spark plasma sintering (SPS) technique under high pressures (between 300 and 600 MPa) and low temperatures, aiming to obtain dense samples to perform electrical characterization.

To reach that objective, the main step we will develop will be sintering ceramics with low decomposition temperature ( $< 700\text{ }^{\circ}\text{C}$ ). Therefore, a major objective of the present work is to use the SPS in unusual operating conditions and demonstrate its efficiency and potentialities.

Thus, a first description of the physical properties of MF and ME materials will be given, highlighting the criteria that will be necessary to determine our candidate phases. Then, sintering mechanisms and some techniques will be presented in order to justify the use of SPS. Finally, the experimental results will be developed and discussed, focusing on the sintering results and possible mechanisms encountered in the different materials explored.

# Chapter 1: A state of the art, from multiferroic and magnetoelectric materials to low temperature sintering

## 1.1. Definition, classification of (multi)ferroic and magnetoelectric materials

### 1.1.1 Definition

The discoveries of ferromagnetism and ferroelectricity are responsible for a great interest in both research and industry, which lead to the development of wide range of functional materials. These are strongly present in daily life, widely used, for computer hard disks, power transformers, sensors (for ferromagnets), as actuators, sensors, capacitors, and in nonvolatile computer memory for ferroelectric materials. As it can be seen on Figure 74 representing the number of publications per year containing the term ferroelectricity and ferromagnetism, these two topics are present in a large number of publications every year and show the current interest both in research and industry. More recently, multiferroicity and magnetoelectricity have attracted lot of attention because of their high potential for applications. Combining both these ferroic orders, or even showing a coupling between both magnetic and electric properties, *i.e.* being able to reverse a magnetization (polarization) with the application of an electric field (magnetic field) paves the way for new generations of electronic components and new concepts in computer architecture with smart, compact and energy-efficient devices. An example of antiferromagnetic magnetoelectric random access memory (AF-MERAM) has been developed based on this scheme<sup>98</sup>.

The term “ferroic” which encompasses ferroelectric (FE), ferromagnetic (FM) and ferroelastic has been defined by Aizu<sup>2</sup>: “A crystal is provisionally referred to as being “ferroic” when it has two or more orientation states in the absence of magnetic field, electric field, and

*mechanical stress and can shift from one to another of these states by means of a magnetic field, an electric field, a mechanical stress, or a combination of these.*

Multiferroicity (MF) and magnetoelectric (ME) effect were first predicted by Pierre Curie as early as in 1894, when he identified the structural origin of both electrical and magnetic properties<sup>105</sup>. He described the possibility for some symmetries to allow electric polarization and magnetization in materials crystallized in adapted symmetry groups. This work was followed, six decades later, by a prediction, made by Landau and Lifshitz in 1956, of the possible appearance of a linear magnetoelectric coupling in crystals<sup>106</sup>, that was developed by Dzyaloshinsky 3 years later with the prediction of a magnetoelectric coupling in  $\text{Cr}_2\text{O}_3$ <sup>107</sup>. This prediction was immediately confirmed by Astrov<sup>108</sup> and Rado et al.<sup>109</sup> experimentally.

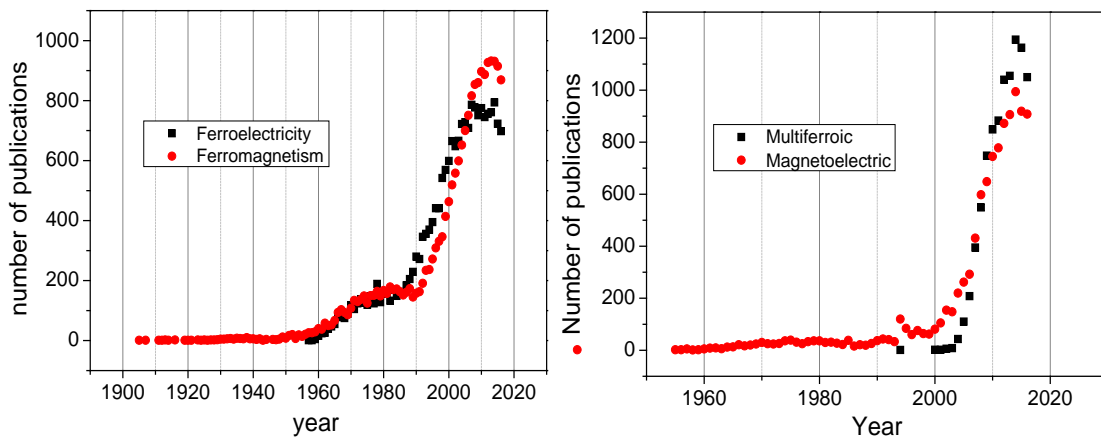


Figure 74: Number of publication for both fields of "ferroelectricity" and "ferromagnetism" (left) and multiferroic and "magnetoelectric" (right) materials over the years [source: SciFinder]

This first discovery is then quickly followed in 1966 by the publication by Ascher & al.<sup>110</sup> of the first multiferroic magnetoelectric material,  $\text{Ni}_3\text{B}_7\text{O}_{13}\text{I}$ . In their publication, they define this material as "ferromagnetoelectric". The proof is made that a single phase can exhibit both ferroelectricity and ferromagnetism (actually weak ferromagnetism in this example). The currently used term of "multi-ferroic" was introduced in 1994 by Hans Schmid<sup>111</sup>. His definition encompasses the three known ferroic orders, *i.e.* ferroelectric, ferromagnetic, and ferroelastic<sup>1</sup>. Nowadays, most of the interest is focused on ferroelectric and ferromagnetic, often neglecting the elastic ordering. Nevertheless, ferroelastic ordering, combined with electric or magnetic ordering, represent a big part of research and have important applications. These are

<sup>1</sup> In this manuscript we will not consider the case of ferrotoridic order<sup>236</sup>

electrostrictive and magnetostrictive materials that combine elastic and ferroic properties in a material, used as pressure sensors, sonar equipment, medical imaging, optical adjustment, actuators, or even microelectronic mechanical systems (MEMS).

A usual shortcut is often taken from MF to ME. It appears that a definition of magnetoelectricity is required. In a single phased material, a direct ME coupling, noted  $ME_H$ , corresponds to the modification of polarization induced by the application of an external magnetic field. In the opposite, the reverse ME effect is noted  $ME_E$  and corresponds to the modification of magnetization of a material under an applied electric field. Considering a direct magnetoelectric coupling and a linear magnetoelectric coupling  $ME_H$ , polarization becomes<sup>112</sup>:

$$P = \alpha H \quad (16)$$

with P the polarization in  $C.cm^{-2}$ , H the applied magnetic field in Oe and  $\alpha$  the second rank magnetoelectric tensor expressed in  $s.m^{-1}$ . To adapt this to experimental samples geometries and measurement setups, a pseudo-coefficient has been introduced and is called magnetoelectric potential coefficient, noted  $\alpha_E$ , expressed as:

$$\alpha_E = \frac{\delta_P}{\delta_H} \times \frac{1}{\epsilon_0 \epsilon_r} = \frac{\delta_E}{\delta_H} \quad (17)$$

with  $\epsilon_0$  and  $\epsilon_r$  the dielectric permittivity of vacuum and the relative permittivity of the material. This coefficient is expressed in  $V.cm^{-1}.Oe^{-1}$  has become the main used coefficient among people working on magnetoelectricity.

The opportunity to tune electric polarization through application of magnetic field, and *vice-versa*, is very promising for computer applications and data storage. As depicted on Figure 2, it allows tuning a ferroic order using external fields of different nature. The difficulty appears at this point: how to design materials in which polarization is coupled to (and controlled with) magnetic field and magnetization via electric field?

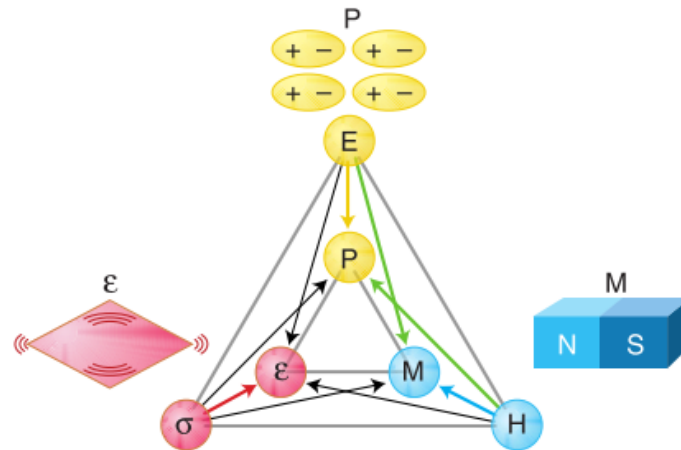


Figure 75: Phase control in ferroics and multiferroics<sup>94</sup>. The three ferroic orders can be controlled by their corresponding external field, but also by another type of external field, and giving rise to piezoelectric, piezomagnetic and magnetoelectric couplings

After the first discoveries of multiferroic magnetoelectric materials, interest in magnetoelectricity decreased. The main reasons for that are a scarcity of candidates after the first discoveries, plus a technical complexity in the characterization experiments of such properties, combined with a lack of available market for potential applications. In a recent work published in 2000, Nicola Spaldin explains “*Why are there so few magnetic ferroelectric?*”<sup>113</sup>, completed in 2002 with a second paper, “*Why is there any magnetic ferroelectric?*”<sup>92</sup>. This work highlights the mismatch between the prerequisite for a ferromagnetic and a ferroelectric phase to coexist. In perovskites, known as the most important ferroelectric family, ferroelectricity arises from the off-centering of B site cation (Ti in BaTiO<sub>3</sub> for instance) leading to the emergence of a local dipolar moment. Long range ordering of these B site cationic off-centerings along the material leads to ferroelectric polarization. The required condition for the possibility of a cationic off-centering is the d<sup>0</sup> electronic configuration. Cations with d orbitals partly filled exhibit a first order Jahn-Teller distortion leading to the symmetric deformation of the surrounding anionic octahedron which stabilizes the central position for the B-site cation, preventing the appearance of dipoles and the emergence of ferroelectricity. In the case of a d<sup>0</sup> cation, first order Jahn-Teller distortion becomes zero, and the second order term becomes dominant. Its contribution, in opposite to the first order term, is non symmetric and can provoke an off-centering of the d<sup>0</sup> cation<sup>114</sup>. As opposed to FE, a FM material requires unpaired electrons on its d shell for a magnetic moment to emerge. Consequently, it appears complicated to have both properties in a single phase material. The scarcity of materials belonging to the MF family,

defined as combination of two among the three ferroelectric, ferromagnetic and ferroelastic orders, lead to a relaxation of this definition.

In the present manuscript, we will focus on FM and FE properties, and will use the term MF to describe the combination of these two properties, without considering elastic ordering and properties. As depicted on Figure 76 below, a first definition of MF was proposed as being the combination of FE and FM properties in one phase. Now, it is commonly accepted to call “multiferroic” a material with magnetic and polar ordering, due to the aforementioned relaxation. This new definition includes materials with ferroic, but also anti-ferroic ordering (anti-parallel arrangement of dipoles or spins).

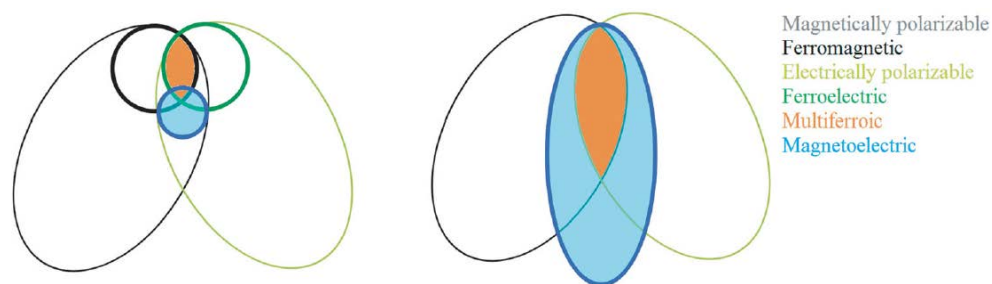


Figure 76: A schematic landscape of multiferroic and magnetoelectric materials<sup>100</sup>. First representation (left) proposed by Eerenstein & al.<sup>115</sup> defines multiferroic materials only as being in the same time both ferroelectric and ferromagnetic. The second representation (right) proposed by Dong & al.<sup>100</sup> enlarges multiferroics to both electrically and magnetically polarizable materials (including antiferromagnetic and antiferroelectric orderings)

In order to complete this new definition, a classification of single phased multiferroic materials has been proposed by Khomskii in two groups<sup>116</sup> that will be defined in the following sections

### 1.1.2 Classification of multiferroics

To define possible ways to obtain a single phased MF, one has to combine both FE and FM in the same time. This where the difficulty resides. To overcome the apparent contradictions between the parameters needed to obtain FE and the one for FM, different strategies have been developed. Khomskii proposed a way to classify them according to the origin of FE<sup>116</sup> and the following part is largely inspired from his work. Microscopic origin of magnetism is basically the same in all magnets: localized electrons, mostly in partially *d* and *f* shells of transition metal and rare-earth ions, which have a corresponding localized spin, or magnetic moment. Exchange interactions between these localized moments lead to magnetic order. Because FE can emerge

from different microscopic sources, this one is used to define MF. Resulting from that, two different groups emerge.

#### 1.1.2.1 Type I multiferroics

Type I MF are materials in which FE and FM have two different microscopic sources that appear largely independent from one another. In these materials, FE and FM usually appear at high temperature, in many cases above room temperature, and spontaneous polarization  $P$  is often rather large (of order of  $10 - 100 \mu\text{C}/\text{cm}^2$ ). Unfortunately, the independence of FE and FM results in rather weak coupling between both. Examples are  $\text{BiFeO}_3$  ( $T_{\text{FE}} \sim 1100 \text{ K}$ ,  $T_{\text{N}} = 643 \text{ K}$ ,  $P \sim 90 \mu\text{C}/\text{cm}^2$ ) and  $\text{YMnO}_3$  ( $T_{\text{FE}} \sim 914 \text{ K}$ ,  $T_{\text{N}} = 76 \text{ K}$ ,  $P \sim 6 \mu\text{C}/\text{cm}^2$ ). Four major groups can be highlighted to describe type I MFs although other subclasses could be presented.

- *Independent systems*

Since FE and FM necessitate different conditions to arise in a same phase, the simplest idea to obtain both at the same time can be to synthesize multiferroics with two independent structural units functioning separately for ferroelectricity and magnetism. One of the well-known examples are borates, such as  $\text{GdFe}_3(\text{BO}_3)_4$ , in which  $\text{BO}_3$  groups are ferroelectrically active and  $\text{Fe}^{3+}$  bear magnetism<sup>117</sup>, or in  $\text{Ni}_3\text{B}_7\text{O}_{13}\text{I}$  which was one of the first multiferroic magnetoelectric phase to be discovered<sup>118</sup>. These materials are not perovskites, which is the most known structure in ferroelectric materials with  $\text{BaTiO}_3$  (BT) which exhibits the highest permittivity<sup>119</sup>. It is normal that attempts on perovskites materials were lead in order to mix  $d^0$  with  $d^n$  cations in a single structure. An example of that is  $\text{PbFe}_{0.5}\text{Nb}_{0.5}\text{O}_3$  (PFN) with  $\text{Nb}^{5+}$  as a ferroelectrically active cation and  $\text{Fe}^{3+}$  bearing magnetism<sup>120</sup>. Other perovskite of  $\text{AB}'_{1-x}\text{B}''_x\text{O}_3$  were tested as multiferroic magnetoelectric such as  $\text{PbFe}_{0.5}\text{Ta}_{0.5}\text{O}_3$  (PFT)<sup>121</sup> and  $\text{PbFe}_{0.67}\text{W}_{0.33}\text{O}_3$  (PFW)<sup>122</sup> but their magnetoelectric couplings remain rather weak.

- *Lone pair ferroelectric*

This phenomenon can occur in different crystal structure types but the two main examples are perovskite based materials:  $\text{BiFeO}_3$  and  $\text{BiMnO}_3$ . This technique consists in the insertion of a non  $d^0$  ferroelectrically active cation with lone pair electrons. In this case, cations like  $\text{Bi}^{3+}$  or

$\text{Pb}^{2+}$  can be used. All these ions possess  $6s^2$  outer electrons. These outer electrons can have a stereochemical activity<sup>123</sup> which can induce a ferroelectric polarization such as the ferroelectric  $\text{TlGaSe}_2$ <sup>124</sup> which is ferroelectric due to the stereochemical activity of the  $\text{Tl}^+$   $6s^2$  lone pair. Magnetoelectric coupling has also been evidenced in the piezoelectric ferrimagnetic  $\text{Cu}_2\text{SeO}_4$ <sup>125</sup>. In the particular case of perovskites, to engineer a lone pair ferroelectric phase, it is possible to use both A and B sites of  $\text{ABO}_3$  as ferroelectrically and magnetically active. Usually, FE and FM properties of perovskites come from the B site cation. The presence of A site cation mainly results in a mechanical strain on the lattice and tunes the resulting property. It is the case of  $(\text{Ba},\text{Sr})\text{TiO}_3$  which is ferroelectric, but in which Ba replacement by Sr results in a decrease of Curie temperature ( $T_C$ )<sup>126</sup>. In lone pair ferroelectrics, A site is filled with a ferroelectrically active cation, and B site contains a magnetic  $d^n$  cation. This is the case of the well-known multiferroic families of  $\text{BiMO}_3$  (M being  $d^n$  transition metal). This way, both perovskite sites are active and materials with high ordering temperatures can be obtained (for  $\text{BiFeO}_3$ ,  $T_{\text{FE}} = 1100 \text{ K}$ ,  $T_{\text{N}} = 643 \text{ K}$ <sup>127</sup> and  $P = 60 \mu\text{C}/\text{cm}^2$ ), while  $\text{BiMnO}_3$  is the only example of a purely FE and FM multiferroic. Here also, different sources for magnetism and FE result in a weak coupling but magnetoelectric couplings can be observed above room temperature in  $\text{BiFeO}_3$ <sup>128</sup>.

- *Charge ordering*

The third possibility is to have ferroelectricity coming from charge ordering (CO). This happens when ions with mixed valences are introduced and the charges order in the material. In these materials, ferroelectricity does not arise from classical cationic-anionic dipole. Figure 77A represents a neutral chain with no polarization. Figure 77B represents a linear chain of charges with equivalent distances but inequivalent charges resulting in a global unpolarized macroscopic chain like  $\text{NaCl}$  with  $\text{Na}^+$  and  $\text{Cl}^-$ . In Figure 77C, charges are equivalent but sites ordering is bond centered, with short and long distances. Both (B) and (D) cannot be ferroelectric. Figure 77D represents the combination of bond centering and charge ordering which results in a macroscopic polarization with two inequivalent dipolar moment in opposite direction. This results in a global FE polarization<sup>129</sup>.

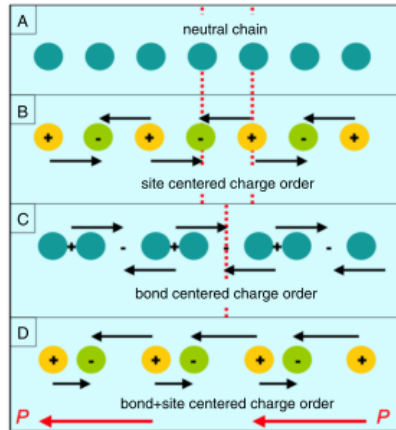


Figure 77: Representation of charge ordered polarization with (A) neutral one-dimensional chain (B) site-centered charge ordering, (C) bond-centered charge ordering and (D) linear combination of these two that is ferroelectric. Arrows indicate polarization, which is in total 0 in (B) and (C) but develop a macroscopic moment indicated by the red arrows in (D). Red dotted lines represent mirror planes of the system<sup>129</sup>

In the archetype example of charge ordering ferroelectric,  $\text{LuFe}_2\text{O}_4$ <sup>130</sup>, iron is present as a mix of half  $\text{Fe}^{2+}$  and half  $\text{Fe}^{3+}$ . Ferroelectricity is driven by the CO of the different  $\text{Fe}^{2+}$  considered as negative charge (one more electron) and  $\text{Fe}^{3+}$  considered as the positive charge (containing one less electron). It has been shown that charges can order in the lattice, which results in the formation of a superstructure observed in resonant X-ray scattering (RXRD) which originated from the presence of  $\text{Fe}^{2+/3+}$  ordering<sup>130</sup>. In CO systems, polarization can be quite elevated in the polarization range of classical ferroelectrics. In the case of  $\text{LuFe}_2\text{O}_4$ , polarization reaches about  $25 \mu\text{C}/\text{cm}^2$ . In addition, strong magneto-dielectric coupling was found in  $\text{LuFe}_2\text{O}_4$ .

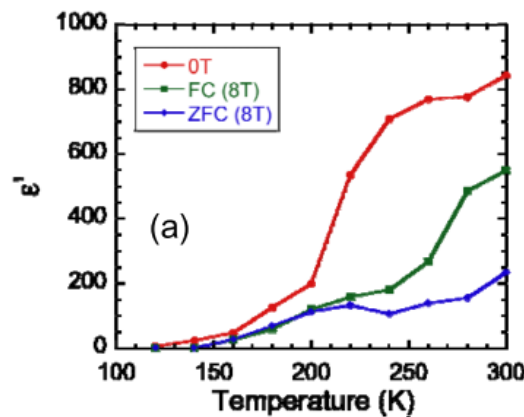


Figure 78: Dielectric measurements of  $\text{LuFe}_2\text{O}_4$  single crystal performed at 10 kHz under different magnetic fields with both magnetic field and electric field along  $c$  axis

- Geometric ferroelectric

Another possibility in type I multiferroic to generate ferroelectricity is to explore “geometric ferroelectricity”. In this case, like in  $\text{YMnO}_3$  ( $T_C(\text{FE}) = 950 \text{ K}$  and  $T_N(\text{AFM}) = 77 \text{ K}$ )<sup>102</sup>, ferroelectricity is caused by the tilting of the practically rigid  $[\text{MnO}_5]^{5-}$  block. As displayed on Figure 79, at the FE  $T_C$  occurs this buckling. Mn ions position remains the same as in paraelectric phase and a c-axis displacement of Y and O atoms is observed. DOS calculations present no rehybridization of ions and the polarization only arises from the geometric displacement of these ions. Note that opposite displacement of Y and O ions, with some moving up along c and some moving down, tends to partly compensate the dipole moment generated by the buckling, resulting in a weak polarization of  $5.5 \mu\text{C}/\text{cm}^2$ <sup>131</sup>.

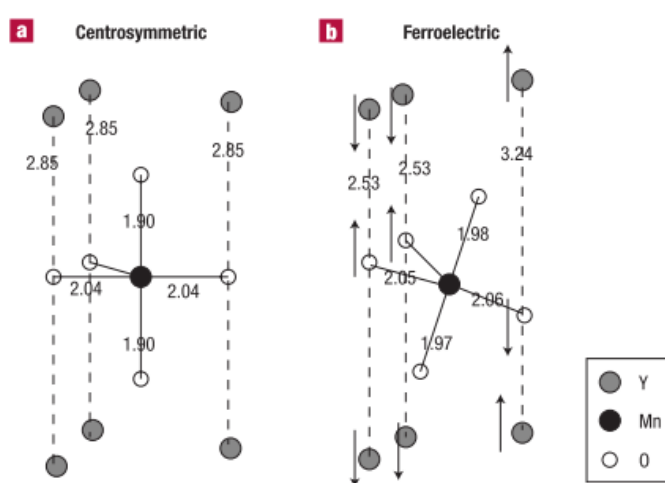


Figure 79: Schematic of  $\text{MnO}_5$  polyhedron with Y layer above and below. Calculated atomic positions in (a) centrosymmetric phase and (b) non-centrosymmetric ferroelectric phase. Numbers correspond to bond lengths and arrows to direction of ions displacements compared to the centrosymmetric configuration<sup>102</sup>

Overall, these mechanisms in which ferroelectricity is independent of the magnetic ordering allow for multiferroics with different electric and magnetic ordering temperatures. These materials exhibit good polarization and magnetization, that could be useful for high density memories, but magnetoelectric coupling is quite weak, due to the separated origin of both properties. However, a second type of multiferroic material exists.

#### 1.1.2.2 Type 2 multiferroic

There is a second family of multiferroics, in which ferroelectricity is induced by a specific magnetic ordering in the material and gives rise to the so called “improper ferroelectrics”. Both ordering will appear at the same (or close) temperature and while the magnetically induced

polarization is usually small, the resulting magnetoelectric coupling can be of large amplitude. A lot of recent work has been focused on these new type of materials, which attract a high interest. The well-known  $\text{TbMnO}_3$  highlighted by Kimura *et al.*<sup>132</sup> and the similar  $\text{TbMn}_2\text{O}_5$  by Cheong *et al.*<sup>133</sup> are good examples of this effect.

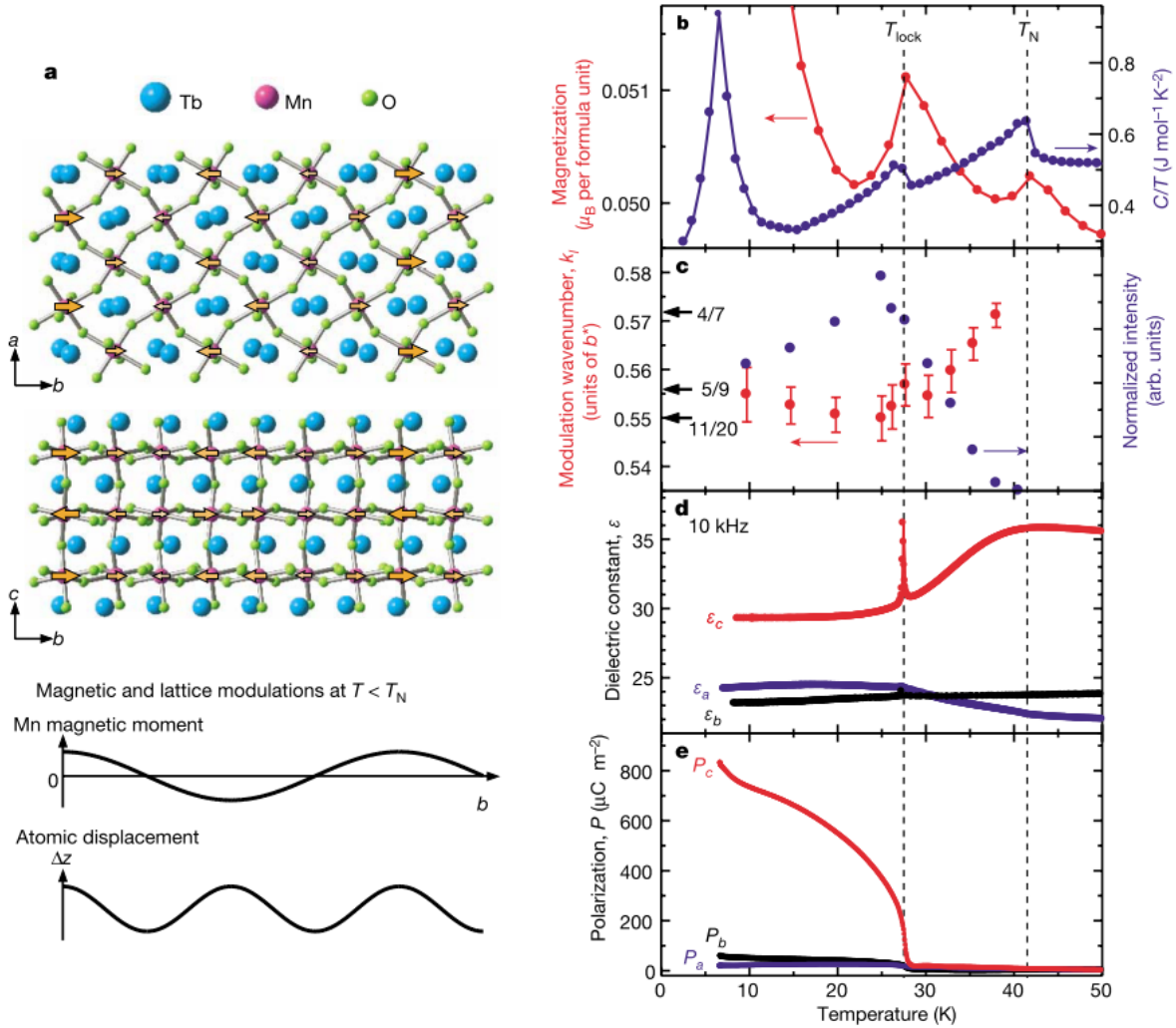


Figure 80: (a) Rough sketches of crystal structure at room temperature (top) and spatial variation along the  $b$  axis of Mn magnetic moment and atomic displacement ( $\Delta z/c$ ) below  $T_N$  (lower). Orange arrows denote Mn magnetic moments below  $T_N$ . Temperature profiles of (b) magnetization and specific heat divided by temperature  $C/T$ , (c) modulation waveform evolution with temperature and its intensity, (d) dielectric constant and (e) electric polarization along the principal axes of  $\text{TbMnO}_3$  single crystals<sup>132</sup>

The magnetic structure of  $\text{TbMnO}_3$  consists in the sinusoidal AF ordering of  $\text{Mn}^{3+}$  moments below  $T_N = 41$  K with a wave vector  $q = (0, k_s, 1)$  in the  $Pbnm$  orthorhombic cell (Figure 80). The wavenumber  $k_s$  is incommensurate ( $\approx 0.295$ ) at  $T_N$  and decreases with decreasing temperature, becoming nearly constant ( $\approx 0.28$ ) below 30 K. At  $T_{\text{lock}}$ , a dielectric transition is

observed along *c* direction and in the same time, polarization becomes positive along this same direction. This one reaches a maximum value of about  $8 \times 10^{-4} \text{ C/m}^2$ . Kimura *et al.* also claim that reversing external electric field results in the reversal of polarization, which confirms the ferroelectric nature of the transition. The polarization obtained in this case is close to the polarization observed in the same type of improper ferroelectrics, such as  $\text{Rb}_2\text{ZnCl}_4$  with a polarization of  $1,2 \times 10^{-3} \text{ C/m}^2$  at  $153 \text{ K}$ <sup>134</sup> or even  $\text{K}_2\text{SeO}_4$  with  $5.6 \times 10^{-4} \text{ C/m}^2$  at  $77 \text{ K}$ <sup>134</sup>. In opposite, proper ferroelectric such as  $\text{BaTiO}_3$  exhibits much stronger spontaneous polarization of  $2.6 \times 10^{-2} \text{ C/m}^2$ <sup>135</sup>.

Among these improper ferroelectric materials,  $\text{RMnO}_3$  ( $\text{R} = \text{Tb, Dy, Eu}_{1-x}\text{Y}_x$ ) were the first reported. These materials crystallizing in perovskite structure exhibit a layered AFM organization (A-type), such as the one encountered in  $\text{LaMnO}_3$  (Figure 81 a). In this case, two types of in plane interactions coexist ( $J_1$  and  $J_2$ ), among which  $J_1$  dominates the global response. For smaller cations in the A-site of the perovskite (such as Tb or Dy), the structure turns into orthorhombic cell. In that case, Mn-O-Mn angle distortion increases and the AFM interaction  $J_2$  starts to compete with the FM  $J_1$ . This creates in a spin frustration resulting in a long-period incommensurately modulated magnetic structure<sup>132</sup>. Between  $T_C(\text{FE})$  and  $T_N(\text{AFM})$ , the structure exhibits a collinear AFM structure (represented on Figure 81 b). When temperatures goes below  $T_C$ , the magnetic vector turns into a bc-plane cycloidal spin order which is well observed on  $(\text{Tb,Dy})\text{MnO}_3$  (Figure 81 c), and confirmed by neutron diffraction data (Figure 81 d), and results in the appearance of a spontaneous polarization along the *c* direction. Because this polarization is induced by the presence of a specific spin ordering, its direction along the *c* axis can be reversed by the application of an external magnetic field. This results in a strong magnetoelectric coupling.

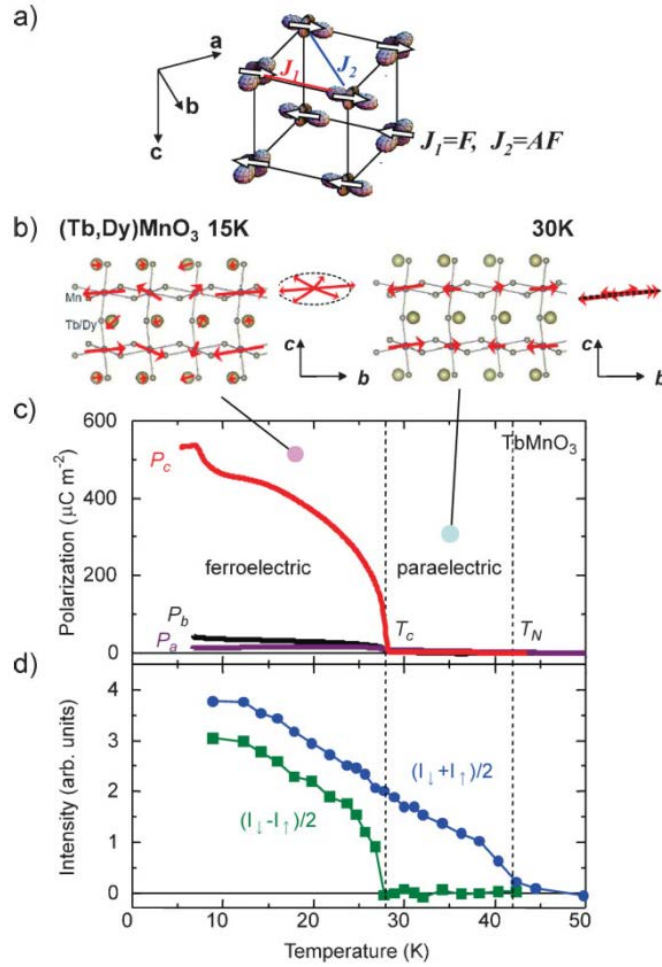


Figure 81: (a) Schematic representation of spin-orbital ordered state of  $\text{LaMnO}_3$ . (b) Solved magnetic structure on Mn sites in the paraelectric antiferromagnetic phase ( $T_c < T < T_N$ ;  $T_N$  = Neel temperature) and the ferroelectric antiferromagnetic phase ( $T < T_c$ ) for  $(\text{Tb, Dy})\text{MnO}_3$  ( $q_m = 1/3$ ). (c) Temperature profiles of the electric polarization along the a-, b-, and c-axes of  $\text{TbMnO}_3$ . (d) Corresponding temperature dependence of the polarized neutron scattering intensity at the scattering vector  $Q = (4, +q_m, l)$ .  $I_{\uparrow}$  and  $I_{\downarrow}$  indicate the scattering intensities for the neutron spin parallel and antiparallel to  $Q$ , respectively<sup>132</sup>.

A similar behavior occurs in  $\text{TbMn}_2\text{O}_5$ . The first paper about  $\text{TbMnO}_3$  showed that a magnetic field can strongly influence the electric polarization: *e.g.*, in  $\text{TbMnO}_3$  the polarization rotates (or “flops”) by 90 degrees when a critical magnetic field is applied along a certain direction. In  $\text{TbMn}_2\text{O}_5$  the influence of an external field is even stronger: the polarization changes sign with field, and a field alternating between +1.5 and -1.5 Tesla leads to corresponding oscillations in the polarization<sup>136</sup>. In  $\text{DyMnO}_3$ , a magnetic-field-induced polarization flop phenomenon was found, leading to a gigantic magnetocapacitive effect with a change of dielectric constant up to  $\epsilon(H)/\epsilon(0) \sim 500\%$  (see Figure 82 below), also due to the small values of  $\epsilon(0)$  for this kind of materials.

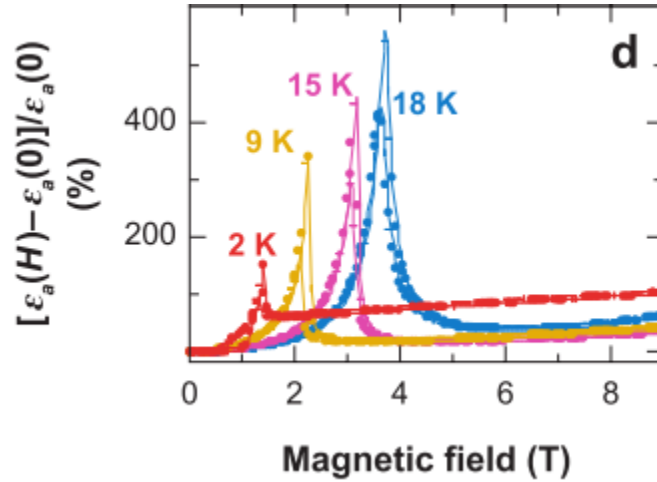


Figure 82: Dielectric constant along a axis at selected temperatures in DyMnO3. Magnetic fields applied along the b axis.<sup>136</sup>

This phenomenon is not restricted to cycloidal spin arrangements and a recent review of Tokura and Seki<sup>137</sup> exhibit the different possibilities that can lead to the emergence of ferroelectric polarization in screw, cycloidal, or conical spin arrangements in magnetic materials. Examples such as CoCr<sub>2</sub>O<sub>4</sub><sup>138</sup>, Ba<sub>2</sub>Mg<sub>2</sub>Fe<sub>12</sub>O<sub>22</sub> (BMFO)<sup>139</sup> or ACrO<sub>2</sub> (Cu, Ag, Li, Na)<sup>140</sup> are good recent examples of the possibility to design multiferroic materials with complex magnetic arrangements resulting in possible ferroelectric polarization.

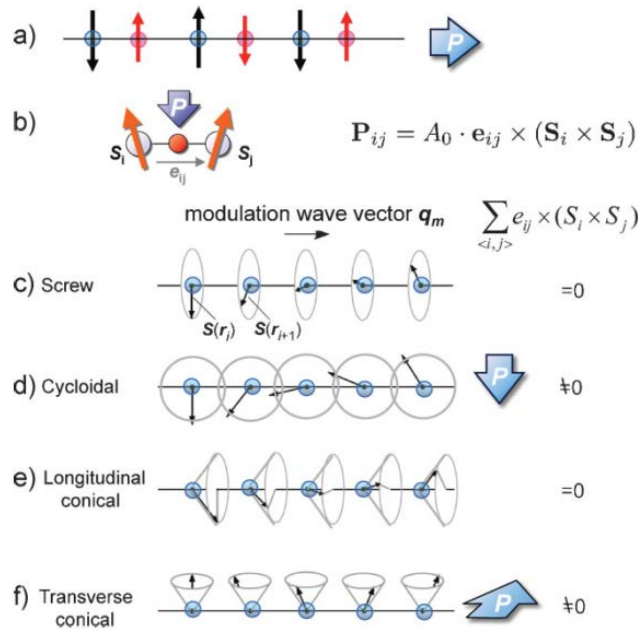


Figure 83: Inversion symmetry breaking by (a) collinear and (b) noncollinear magnetic order and possible polarization direction. (c–f) Schematic illustrations of types of spiral magnetic structures on a 1D array of magnetic moments  $S(r)$ . They include (c) proper-screw, (d) cycloidal, (e) longitudinal-conical, and (f) transverse-conical magnetic structure.<sup>137</sup>

In such materials, the strong magnetoelectric coupling appears to be appealing for interesting applications, but there is another issue with them. Up to now, most materials highlighted present ordering temperatures in temperature range of few tens of Kelvin, well below the boiling point of nitrogen. However, recent results obtained on  $\text{Ba}_{0.5}\text{Sr}_{1.5}\text{Zn}_2\text{Fe}_{12}\text{O}_{22}$  with ferroelectric polarization close to RT are very promising. The current efforts in such materials is likely to be pursued since they represent one of the most promising solution to reach room temperature magnetoelectric materials.

In parallel, and to overpass the drawbacks and difficulties of such materials, other type of materials have been developed, consisting in a mix of both ferromagnetic and ferroelectric phases in composite material.

### 1.1.3 Composite multiferroics

As discussed previously, the existence of a third ferroic order is of great importance. Up to now we only discussed the possibility of developing single phase materials. To overcome the difficulty of engineering single phased devices, the idea of designing room temperature ferromagnetic and ferroelectric composite materials emerged. The principle is to create a magnetoelectric coupling *via* the elastic properties of electrostrictive and magnetostrictive materials. It is in 1972, with the work of Van Suchtelen, that the first ME composite design is proposed<sup>141</sup>. If the idea looks simple, the realization is more complicated. The principle is to use magnetostrictive  $\text{CoFe}_2\text{O}_4$  material (*i.e.* there is a coupling between elastic and magnetic properties), and to closely bond this phase to a piezoelectric (*i.e.* mechanical deformation induces polarization and *vice versa*),  $\text{BaTiO}_3$ . When the magnetic field is applied, the magnetostrictive phase is mechanically deformed and creates a stress on the piezoelectric phase through elastic interactions mediated by the composite's interfaces. This mechanical stress then induces polarization in the piezoelectric phase, resulting in an indirect magnetoelectric coupling. Therefore, none of the two phases displays magnetoelectric coupling but the combination of piezoelectric and magnetostrictive effects result in a magnetoelectric coupling in the composite material. In this example, the ME coupling reached  $130 \text{ mV}\cdot\text{cm}^{-1}\cdot\text{Oe}^{-1}$ , about a hundred times that of  $\text{Cr}_2\text{O}_3$ <sup>142</sup>, which possesses the highest magnetoelectric coupling known in single phased materials. During the 90's, materials processing development brought an increase of interest in such composites and the development of thin films, soft chemistry and

sintering techniques helped increasing the quality of MF/ME composites. Nowadays, nanostructured materials attract a large part of the research effort with the possibility to design (0-3), (2-2) or (1-3) nano-composite materials (the annotation “(n-n)” represents the dimensions of both materials in the composite, for example a (1-3) composite is composed of 1D wires embedded in a 3D matrix<sup>143</sup>). The development of such materials lead to coupling up to  $1800 \text{ mV cm}^{-1} \text{ Oe}^{-1}$  using (2-2) composite of FeCoSiB/AlN<sup>144</sup>. The key point in these cases is the synthesis process of the heterostructure. If the first examples of composite multiferroic magnetoelectric materials were (0-3), it is due to the ease of synthesizing them. This way, a mix of BaTiO<sub>3</sub> and CoFe<sub>2</sub>O<sub>4</sub> gave rise to a ME coupling of  $50 \text{ mV.cm}^{-1}.\text{Oe}^{-1}$ . The development of depositions techniques for thin film production allowed to obtain successive multilayers (2-2) was a very important step in the development of multiferroic composites. This way, coupling of more than  $10,000 \text{ mV.cm}^{-1}.\text{Oe}^{-1}$  have been obtained in multilayered materials, such as FeCoSiB/AlN<sup>144</sup>. Nowadays, the development of nanostructured materials and synthesis techniques pushes the current trend to materials in (1-3) architecture. This form develops the highest surface area between magnetostrictive and piezoelectric materials and therefore increases the resulting magnetoelectric coefficient of the final material. It also presents the advantage of reducing the clamping effect of the substrate. In (2-2) materials, the magnetoelectric material has to be deposited on a substrate, and the mismatch between the structure size of the deposited phase with the substrate result in mechanical constraints which therefore reduce the piezoelectric or magnetostrictive effect<sup>145</sup>. This particular (1-3) shaping is of high complexity and requires challenging synthesis route developments<sup>146</sup>. This shaping still presents a limited amount of results since techniques are now being developed and the shaping induces complicated experimental coupling measurements, because of the absence of substrate (necessary to reduce the clamping effect). This technique, in development, looks to be a promising way to reach high coupling at room temperature.

As discussed in this brief overview of the different strategies to prepare multiferroic and/or magnetoelectric materials, two main ways are possible. The single-phase method is based on complex crystal chemistry issues, showing up to now limited results in terms of useful devices, either because of the small couplings or because of too low operating temperatures. In parallel, composite route helps avoiding these issues and leads to operating materials at room temperature with high couplings by the association of both magnetostrictive and piezoelectric

phases. However, their synthesis complexity and cost makes it difficult to transfer into industrial production. The recent works on type II multiferroics show a diversification of magnetoelectric phases. This points out the interest of prospective search of new phases or in existing phases but up to date not characterized because of processing issues.

#### 1.1.4 Sintering, an opportunity for the investigation of dielectric properties through ceramics

Among the issues when trying to explore new multiferroic materials, the last, but not least is the shaping of materials. In the case of polycrystalline materials, different forms can be explored. The first one, and more accessible one is the powder form. In the case of electrical measurement of a sample, it is necessary to apply separated electrodes on the sample and therefore a dense form is necessary to perform such measurement. Moreover, electrical responses are both affected by the intrinsic response of the sample and its microstructure. In order to access the purely intrinsic contribution, it is necessary to minimize microstructure's contribution and therefore to minimize the porosity. While it is rather impossible to explore electrical properties of powders, preparing a ceramic of rather high density can be difficult to achieve. The ideal possibility is to explore electric properties on single crystals, in which microstructural defects are almost absent. This form allows for a quality crystallographic information, reliable intrinsic responses for dielectric measurements and allows oriented measurements. The problem of this form is the synthesis. It takes actually long time to develop the appropriate synthesis techniques dedicated to one composition and structure. Moreover, measurement require complex sample preparation, such as orientation or cutting and polishing steps. In a primary prospective approach, single crystals are therefore not well suited. An easier possibility is to use the solid and highly dense polycrystalline form, meaning a sintered form of initial powders. This is the most common dense form, due to the ease of preparation. The fast preparation of dense ceramics (usually few hours to days) compared to the preparation of the same amount of single crystals (few days to months) makes them very useful and represent the largest part of the current ceramic materials used in daily life. In addition, most of the time, application do not need particular crystalline orientation. Another interesting possibility is to explore thin films for electrical properties, which present other advantages such as the possibility to obtain chemical gradients, mechanical stresses, high aspect ratio

(surface/thickness) but their production is usually performed from physical deposition methods (PVD, PLD, magnetron sputtering) which needs a first densification step of a target with the desired composition, and then appears more a complementary than a substitutive tool for ceramics. Other techniques like chemical vapor deposition (CVD, MBE, ALD) can be used but here again, the synthesis of such films is quite long to develop and to control, especially the development of specific chemical precursors.

Considering these aspects, the decision to explore materials in polycrystalline form appeared quite obvious, combining faster, easier and cheaper synthesis. In that case, one of the biggest issue is the last preparation step, sintering. To measure dielectric properties, or even to perform a magnetoelectric coupling measurement, one needs a high densification level to avoid extrinsic contribution in the electric response and/or proper application of an electric field. As discussed in the previous part, densification can have a big impact on the dielectric properties and can lead to increased losses or even change the dielectric behavior of the material. Thus it is very important to reach high density to get reliable dielectric measurements. Taking this into account, Jaffari et al.<sup>147</sup> noticed the influence of sintering temperature on the dielectric properties of  $\text{Ba}_{0.4}\text{Sr}_{0.6}\text{TiO}_3$ .

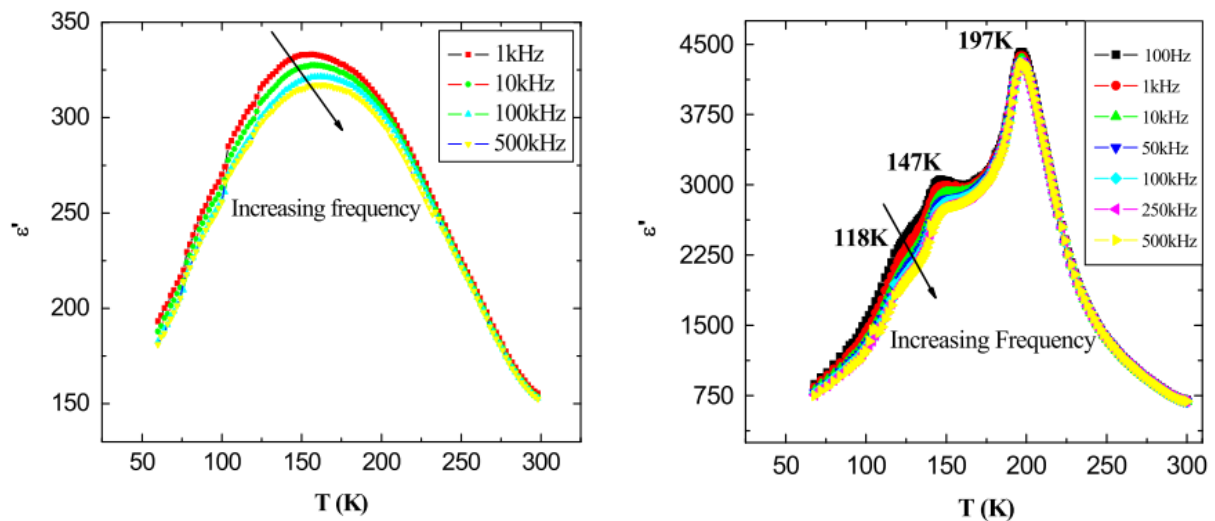


Figure 84: Real part of permittivity of two  $\text{Ba}_{0.4}\text{Sr}_{0.6}\text{TiO}_3$  ceramics sintered at (left) 1000 °C and (right) 1400 °C<sup>147</sup>

Densification is a key step that should not be disregarded, but that is not trivial. Sintering is usually performed beyond 800 °C. In this temperature range, many materials or phases cannot be stabilized and then the exploration of their electrical properties appears impossible in a

ceramic form. There is then a need to develop sintering techniques at lower temperatures to widen the scope of functional polycrystalline materials.

## **1.2. Sintering techniques and how to reduce the sintering temperatures**

As discussed previously, densification is a key in the preparation of ceramics to obtain reliable electrical measurements, especially for dielectrics. Anyway, this aspect of material processing is often depreciated and considered as an obstacle to overcome in order to obtain the desired form and properties. It can be more than that. Sintering is a tool, and when it is well understood and controlled, it can be used to design and tune final properties.

Historically, sintering has been performed for ages, using high temperatures to make the first ceramic materials in human history. This method has been long used and still today, most of the ceramic materials are produced using such route. Anyway, recent interest, both in research and industry, lead to the emergence of new techniques and understanding of more developed and more complex sintering mechanisms. With a wide range of techniques, such as hot pressing, isostatic, controlled rate, multi-step, microwave, solvothermal or even electric field and current assisted sintering techniques, the scope of techniques is large and it is important to fully understand pros and cons of each one in order to choose the one designed for some purpose. Material processing and design attracts more and more interest nowadays with the emergence and new techniques of which 3D printing can be a good example.

In the present study, the objective is to first identify materials with possible (multi)ferroic and/or magnetoelectric properties. Among the various possibilities, the aim has been set to explore properties in materials that have not been electrically characterized because of their low temperature decomposition

Before any discussion about sintering techniques, the term “sintering” has to be defined and well understood. Once the definition will be set and delimited, natural (or classical) sintering will be discussed, in order to understand the available tools and their impacts on sintering. These bases will then bring to the discussion about the different techniques available nowadays and their scope of use, which will lead us to explain the choice of Spark Plasma Sintering for the present purpose.

### 1.2.1 Definition

Sintering of materials is defined as the change of shape from powdered to densified polycrystalline material under the action of temperature. This consolidation comes from the formation of chemical bonds between separated grains. If there is a fusion in the process, this one must remain localized to keep the overall shape of the material. When the powder is heated at high temperature, sintering occurs and leads to diminution of reactive surface and often hinders powder's reactivity (in the case of a catalyst for instance). Before sintering, material can be shaped in different forms, but we will focus here on the formation of pellets made through uniaxial applied pressure using a die. The so called resulting "green" body is then densified during heating treatment. This step also has a second objective, which consists in the rearrangement of grains under the application of pressure and that will minimize the presence of macropores that cannot be removed after. Technologically, a difference is done between natural sintering without mechanical pressure and pressure assisted sintering, in which the pressure is applied on the sample (uniaxial or isostatic pressure) during processing to help the sintering of materials that are difficult to sinter or to access very high densification level. From a physicochemical point of view, different events can happen leading to sintering:

- Solid state sintering, during which every part remains solid. Densification results from shape modification of the grains. This can be done for single or multiple phases. Additives can be used but remain solid and help sintering process. This process is mainly used for technical ceramics for which grain boundaries must remain pure to preserve material properties.
- Vitrification, corresponding to the formation of a large part of liquid phase during the heat treatment. This phase can then fill the pores and lead to fully dense material. This process is used for "traditional" ceramics such as porcelain. The formation of a liquid part must come from the reaction between constituents, or melting of one of the phases. This leads to polyphased materials.
- Liquid phase sintering, in which case the liquid is just in the necessary amount to promote particle's rearrangement, make liquid bridges between grains and put them into contact. This type of sintering also leads to polyphased materials, and the effect on the properties depend both on the chemical nature and the amount of the liquid phase.

- Reactive sintering. In the general case, the material obtained after sintering has the same composition as the initial powder, and is called “non-reactive” sintering. In some cases, the initial green material is made of different phases that can eventually react during the process to make a new phase. The reaction leading to the new phase can then help the sintering of the phase and help reduce the sintering temperature compared to the sintering of the isolated material.

Focusing on solid state sintering, different steps have been identified during sintering, mainly separated in three different regimes. As shown on Figure 85, these three steps can be highlighted by plotting relative density versus sintering time. After compacting the green body, materials usually reach a densification ratio between 0.5 and 0.6 (densification ratio noted  $\lambda$  and corresponds to the ratio of  $d/d_{th}$ , with  $d$  the actual density of the material and  $d_{th}$  the theoretical density of a defect free single crystal). This starting value of  $\lambda$  is determined by the level of the first rearrangement induced by the application of pressure. Considering a constant temperature applied on the material (above the sintering temperature of the phase), we can notice the increase of relative density happening quite fast. This first step corresponds to the neck formation, bridging each grain to its neighbors. At this moment, the reduction of surface is important and a first increase of density is observed. The major part of the sintering occurs during the second step when all the evolution of microstructure leads to the closing of open porosity. When only closed porosity remains,  $\lambda \approx 0.92$ , the last sintering step takes place but the evolution of the microstructure gets slower. This closed porosity is difficult to totally remove, and the application of pressure is often needed to reach densities of  $\lambda > 0.99$ , in the case of transparent ceramics for instance.

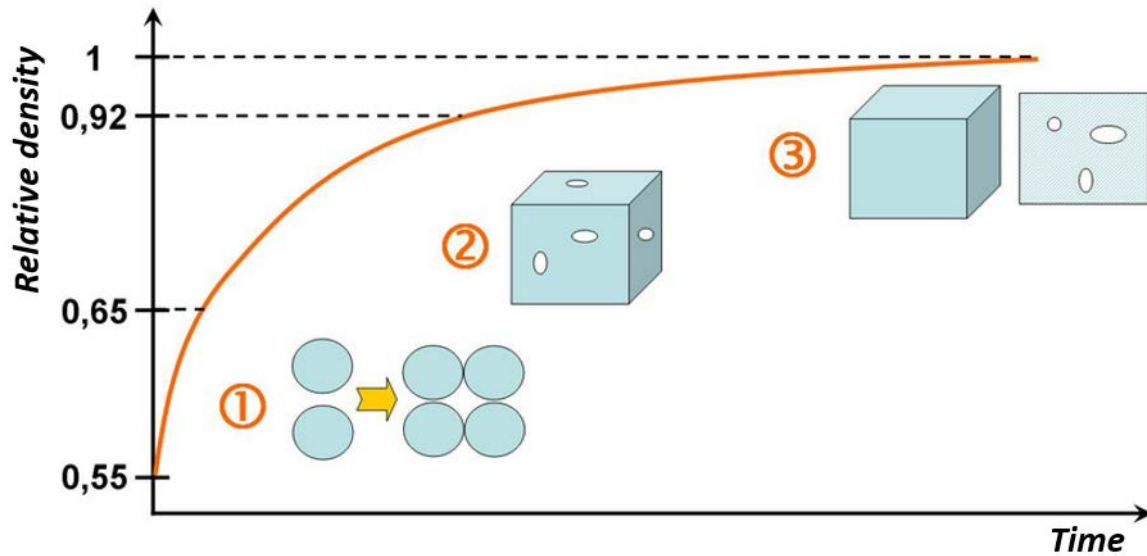


Figure 85: Relative density and microstructure evolution during densification steps <sup>148</sup>

In competition with this phenomenon, there is a second effect occurring when the sample is heated up. This phenomenon, which can be problematic, is the grain coarsening. This results in the increase of mean grain size and if this happens too soon in the densification process, can hinder densification by creating large, closed porosities that can prevent any further densification.

Depending on the targeted application, different densities and chemical purities can be achieved. Some applications such as bioceramics, and particularly hydroxyapatite that represent an important stake in bone replacement<sup>149</sup>, require sometimes ~ 20-30% porosity, when in the same time transparent ceramics necessitate density close to 100%<sup>150</sup>. To achieve an adapted densification of the different materials, various sintering techniques have been developed and represents an important stake.

## 1.2.2 Sintering techniques of ceramics

### 1.2.2.1 Solid state sintering

The oldest sintering technique, used for millenniums, is called “conventional”, “traditional” or pressureless sintering<sup>151,152</sup>. Even after the development of new techniques, the oldest method is still widely used nowadays. The main reason for that is the simplicity and the versatility of

its use. Solid state sintering simply consists of the heating of a green body (pre-pressed sample). The possibilities of this technique are quite wide, and represent up to now the most used and known technique.

#### 1.2.2.1.1 *Origin of solid state sintering*

Sintering, such as any other physicochemical process, needs to satisfy two different aspects, the first one being thermodynamics and the second one being kinetics. We will briefly describe both aspects to explain the origin of solid state sintering in ceramics.

##### 1.2.2.1.1.1 Thermodynamic approach

The thermodynamical origin of sintering has to be found in the presence of interfaces that can be created between solid and gas. For a solid, there are two possibilities which are the formation of solid-solid or solid-gas interfaces. The creation of interface induces surface tensions noted  $\gamma_{ss}$  (solid-solid) and  $\gamma_{sg}$  (solid-gas). Typical values of  $\gamma_{ss}$  is about 10 times lower than  $\gamma_{sg}$  for a given material in air, which makes the solid-solid interface less energetic. This is the reason for the evolution from dispersed powder to dense material. In order to decrease these solid-gas interfaces, two ways are possible:

- Ostwald ripening – Reduction of solid-gas interface is achieved by the reduction of the number of particles. In this case, the small particle merge with the bigger and are finally absorbed inside the bigger particles, which reduces the number of grains and participate in the increase of mean particle size <sup>153</sup>.
- Grain sintering – Solid-gas interfaces are removed with the creation of chemical bonds between grains, making solid-solid interfaces. The creation of these bonds leads to the effective densification of the final material and is the targeted sintering process.

The resulting grain boundaries that are formed still represent an excess of energy that can be lowered after their migration, promoting the growth of the grains. To reach maximum density, two ways are possible. Either the grains can first merge and grow further, either they can grow and finally merge and densify. The second way is less probable because of the kinetic of sintering. As it will be discussed later, the bigger the size of the grains, the slower the sintering occurs. Both mechanisms, densification and growth, are in competition during sintering and the objective is to favor densification while avoiding grain growth.

#### 1.2.2.1.1.2 Kinetic approach

The second effect to consider for the explanation of sintering is the kinetic of the process. In fact, for a given material, the kinetic of grain growth and grain merging can be different according to the situation. Considering an infinite solid or a flat interface, pressure inside this solid is constant and can be noted  $P_0$ . In the case of solid grains with finite size, the curvature of the surface creates a supplementary pressure on the surface of the grain that can be expressed:

$$P_i = P_0 + \frac{2\gamma_{sg}}{r} \quad (18)$$

$P_i$  is the effective pressure inside the grain,  $\gamma_{sg}$  is the solid-gas interfacial tension and  $r$  is the grain radius size. The pressure is bigger for grains than for a flat surface, and the smaller the grains get, the more this pressure increases. For copper grains of  $0.1 \mu\text{m}$ , the extra pressure in the grains compared to a flat surface of copper,  $P_i - P_0$  has been calculated to be  $28 \text{ MPa}$ <sup>148</sup>. It works the same way with pores, just by adding a negative value on the radius of the pore, but induces a pressure release. Values of  $\gamma_{sg}$  vary with temperature, atmosphere, and humidity. A sample composed of small grains and small pores will then exhibit high pressures at the surfaces that will increase the resulting interfacial tension, and then lead to the increase of sintering kinetics. Big grains will be difficult to sinter since their surfaces will be closer to flat surfaces and the energetic gain will be reduced, resulting in a slow sintering process that can even favor the grain growth instead of the densification of the body.

Another kinetic effect of sintering is the mass transport. Different ways can be followed for the matter to diffuse. First possibility is to go through the gas phase (sublimation of solid) which, as in the case of interfacial tension, is increased with the curvature of the grain. Other possible ways are solid state diffusion on surface, inside bulk, or at grain boundaries. The mechanism of matter diffusion is also important and can result in different microstructures. This one can originate from grain surface or grain boundaries. If the matter comes from surfaces, the final result consists mainly in linked grains through the formation of bridges.

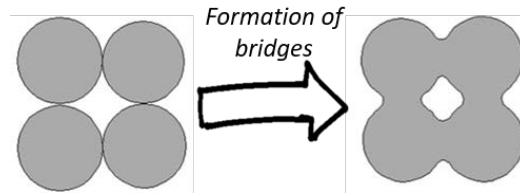


Figure 86: Sketch representing the formation of bridges between particles under the action of temperature

Surface diffusion mechanism results in the consolidation of the bridge without shrinkage, whereas in the case of matter coming from grain boundaries, diffusion of matter will allow narrowing of the intergrain volumes and an actual shrinkage will occur. Surface diffusion processes result in consolidation of the material and bulk diffusion results in sintering. Both mechanisms are thermally activated but their evolution with temperature is different. It has been shown for  $\text{Ca}_{10}(\text{PO}_4)_6(\text{OH})_2$  (hydroxylapatite) that between 600 and 850 °C, there is a reduction of surface area without densification, due to the mass transport at the surfaces of grains, and above 850 °C, this reduction of surface area is accompanied by densification<sup>154</sup>. It is important to overpass the bulk mass diffusion temperature to achieve densification, because the grain growth, which is responsible for surface area decrease, can promote merging of porosities that will finally be locked within the bulk of the ceramic, even after long heating treatment.

#### 1.2.2.1.2 Effect of experimental conditions

Depending on the experimental conditions, sintering will be effective or not. These experimental conditions are of different natures, ranging from the preparation of the powders, through the synthesis conditions and the milling, to the sintering treatment (atmosphere, temperature cycles, pressure), and can also include the use of additives.

### 1.2.2.1.2.1 Powder preparation

Before any sintering is performed, it is important to fully characterize the powder that is used. It starts with the synthesis route, which has an influence on the reactivity of the powder during heat treatment. Bousquet & *al.*<sup>155</sup> prepared  $\text{Al}_2\text{O}_3$  using supercritical synthesis in two different media. A first one using  $\text{H}_2\text{O}$  and ethanol, and a second one using  $\text{CO}_2$  and ethanol. The first

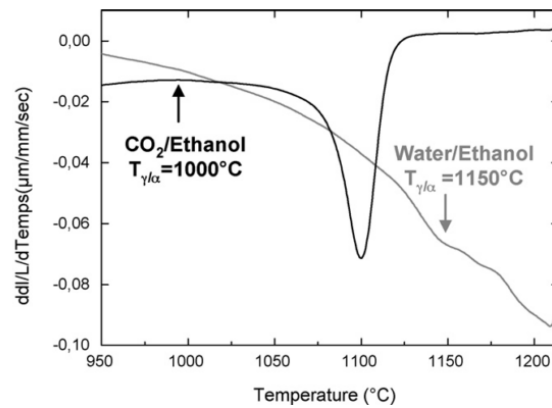


Figure 87: Time derivative of shrinkage for  $\text{Al}_2\text{O}_3$  powders prepared by supercritical fluid synthesis in  $\text{CO}_2/\text{ethanol}$  and  $\text{water}/\text{ethanol}$ <sup>155</sup>

route lead to  $\text{AlO}(\text{OH})$  phase, whereas the second one lead to amorphous alumina. During sintering treatment, it is visible on Figure 87 that shrinkage occurs at different temperatures, depending on the type of synthesis. After sintering, both samples present the  $\alpha$ -alumina form and the shrinkage actually occurred after the phase transition  $\gamma \rightarrow \alpha$  is reached. The preparation clearly has an important influence on the reactivity of the powder, on its structural transition and on its sintering behavior.

Another way to control reactivity through preparation of the initial powder is breaking aggregates. In fact, in some synthesis routes, agglomerates can be formed when powder is dried or calcined during synthesis.

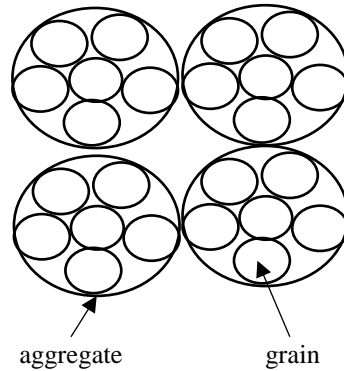


Figure 88: Representation of agglomerated powder <sup>154</sup>

The formation of such aggregates will prevent rearrangement of grains during the first moments of sintering, and then only micro porosities will be removed inside the agglomerates, while the macro porosities between agglomerates will be retained.

Final preparation step is the milling of the powder. Milling can be a tool to break aggregates that have been formed during or after synthesis, but is also be able to break grain into smaller ones. This way, as discussed previously, surface areas are increased, grain curvatures are more important and porosities size will also be smaller, thus sintering kinetic is enhanced.

#### 1.2.2.1.2.2 Sintering protocol

Obviously, the sintering protocol has an importance in the process, and there are different tools to reach an effective sintering. The first parameters to tune to control sintering are obviously temperature and time. Since the objective is to reach high densification without grain growth, and since both are thermally activated, one must consider the temperature range in which the materials will be more efficiently densified. When activation energy of crystal growth is lower than the one of densification (in most cases considering ceramics) one must sinter at high temperatures to favor fast densification and limit as much as possible grain growth. In the opposite case, it is necessary to find the temperature range in which it is possible to densify fast enough without activating growth. In some cases, gas release is observed during heating step. It is necessary to use slow temperature ramps to avoid too fast sintering and maintain a free path for gas evacuation, ultimately by multiplying the dwells.

Another element to take into consideration is the atmosphere in which is performed the sintering. This one can have two different impacts. It can affect mechanically, through the application of pressure that can promote or hinder sintering, or it can also have a chemical impact through reaction with the solid. Gas must be soluble into the solid so that the maximum density can be reached. This is the reason why alumina is better sintered in oxygen than in air, because nitrogen from the air has high difficulty to diffuse inside the solid<sup>156</sup> and then remains inside pores that will be impossible to remove further. For the same reason, working under low pressures, or even better, under vacuum, is then a good asset that helps removing the remaining porosities at the final steps of sintering. The problem with vacuum or low pressure is that they can affect the chemistry of the solid, and in the case of ceramic, oxygen deficient solids are common when vacuum is used. A compromise has to be found between both. The nature of the gas must correspond to the stability of the solid. Oxides are more stable in oxygen, nitrides in nitrogen and carbonates in CO<sub>2</sub> for instance. But sometimes it can be interesting to sinter oxides in partially reductive atmosphere to induce oxygen vacancies that can enhance oxygen diffusion through the solid<sup>156</sup>. This can be useful when oxygen is the slowest diffusing element in the solid, and determines the sintering kinetics.

Whether it is not always necessary, pressure can be an efficient tool for materials that are difficult to sinter. Usually, it helps reducing both sintering temperatures and times, favoring densification instead of grain growth. Two main effects are observed, the first one is that pressure helps compacting grains with one another, and also promote grain rearrangement through sliding during heating treatment. Different specific techniques have been developed using pressure assisted sintering, and some will be described in the following.

#### 1.2.2.2 Pressure assisted sintering

As mentioned above, pressure can be an efficient tool to both lower the sintering temperatures and times. Different techniques make use of pressure but also combine pressure with other effects like microwave heating, or electric current assisted heating. Three techniques will be briefly explained and a focus will be made on Spark Plasma Sintering technique since it is of great interest in the present work.

#### 1.2.2.2.1 Hot pressing

The conception of a hot pressing is basically realized when combining a uniaxial press with a furnace. This system is usually used under inert atmospheres or under vacuum, but also some can be used under oxidizing atmosphere if the heating elements are not made of graphite. Powder is inserted inside a die with two pistons that are used to apply the pressure and the resistance are used to heat the die. This system is limited to around 20 °C/min temperature heating ramp and usually for small diameters (10 to 20 mm). Many works have been published in 1950's and 1960's on hot pressing of ceramics aiming to determine the mechanisms explaining the observed macroscopic densification<sup>157-162</sup>. With this technique, densification is realized through plastic deformation (called *plastic-flow*) and grain rearrangement.

Since plastic deformation is the major driving effect for densification in this technique, the main use has been developed for metals and alloys sintering. Few ceramics are sintered using hot pressing but it is mainly restricted to UHTCs (Ultra High Temperature Ceramics) that are used in high temperature refractory mechanical application<sup>163-165</sup>, dedicated to aerospace uses (TiB<sub>2</sub>, ZrB<sub>2</sub>, SiC, ZrC).

Some variations of the uniaxial hot-pressing technique have then been developed. HIP (Hot Isostatic Pressing) is one of the more important. In HIP, pressure and temperature are mediated through a gas around the sample that has to be encapsulated in a glass or metal container, that has the desired shape and should be able to shrink with sintering going on. HIP can be performed directly on sample if this one has no open porosity. It is then used to fully densify pre-sintered materials to a very high densification, near 99%, which makes *post-HIP* an interesting tool to densify transparent ceramics<sup>166</sup>. This technique is used at high temperatures, usually above 1000 °C, and pressures around 100 MPa<sup>167</sup>. HIP is well adapted to very high densification levels and this way can be used has a complementary tool to other techniques (post-HIP).

#### 1.2.2.2.2 Microwave sintering

Microwaves have been long used for material synthesis, and since two decades for the sintering of materials. The interests of microwaves in sintering are the fast thermal ramps, fast reduction in cycle times resulting in large energy savings, selective and volumetric heating providing fine microstructures, and leads to improved mechanical properties<sup>168</sup>.

In the case of microwave heating, electromagnetic energy is converted into thermal energy through the interaction between the incident wave and the material. This way, all material don't present the same behavior for the same incoming energy. Specific operating conditions have to be determined for each new phase. An advantage of the technique is that, since heating is achieved through the penetration of an incident electromagnetic wave, all the sample can be heated uniformly, so there is no thermal conductivity mechanism involved. Heating is instantaneous and rapid, depending on the considered material.

Microwave sintering presents nice advantages and lead to some interesting results in ceramic sintering ( $\text{Al}_2\text{O}_3$ ,  $\text{ZrO}_2$ ,  $\text{ZnO}$ , PZT, ...) <sup>168</sup> with for instance 98% density for  $\text{Al}_2\text{O}_3$  at 1400 °C with no hold time <sup>169</sup>. The same density is obtained under conventional sintering for a treatment of 2h at 1600 °C with a substantial grain growth, which makes 200 °C difference for the same densification, plus drastic time reduction and limited grain growth. Moreover, microwave sintering allows an important decrease of sintering dwell times, and then gives access to fully densified materials which can possess a controlled nanostructuration.

However, microwave sintering is for the moment mainly used at high temperatures (>800 °C) and remains only applied to few types of ceramics due to its complex mechanisms, which requires good absorbing properties in the relevant frequency range for example.

### 1.2.2.2.3 Spark Plasma Sintering (SPS)

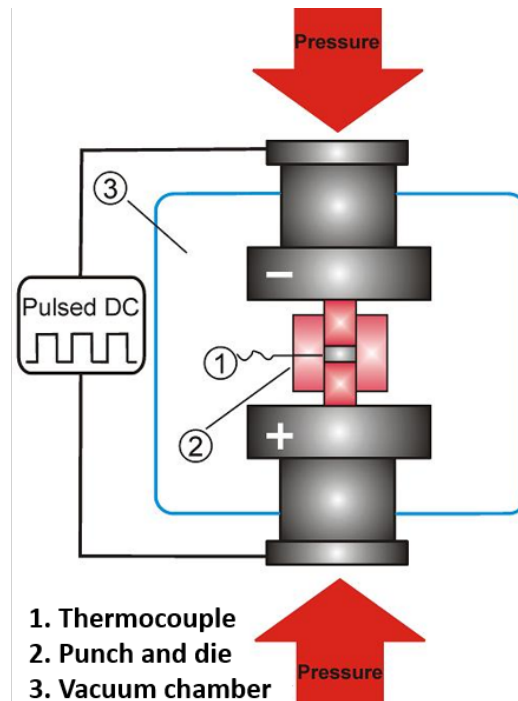


Figure 89: Schematic representation of a SPS apparatus

This technique has been mostly developed in Japan during the 1960's<sup>170</sup> and the initial objective was to create a plasma by the application of an electric discharge in a sample under pressure, in order to sinter refractory ceramics and metals. Basically, the SPS system is based on the hot-pressing principle, with the use of a press, and in most case sintering is performed under vacuum in a graphite die. Temperatures up to 2000 °C can be reached using such technique and pressures of few MPa to around 600 MPa can be applied, even if some setups allow the application of pressures of about 1 GPa. Unfortunately, it is impossible to apply these extreme conditions of temperature and pressure simultaneously. Graphite dies allow for a high temperature use but are limited in pressure at about 100 MPa and dies like WC:Co can exceptionnaly reach 1 GPa but are limited in temperature at around 600 °C. Current development of new dies widen the range of experimental conditions accessible (double wall graphite<sup>171</sup>, SiC<sup>172</sup>). As for the sintering atmosphere, vacuum is usual but can be replaced by argon, nitrogen or Ar/H<sub>2</sub>. In some conditions, oxygen can be used, but it forbids the use of graphite dies (due to combustion, obviously), and for metallic dies, can be complicated by oxidation issues. The specificity of this technique comes from the heating mechanism, as an intense electric current should go through the die and induce a temperature increase by Joule

effect. However, depending on the electrical conductivity of the sintered sample, the current path can change<sup>173</sup>. Although SPS has been largely used and proved to be highly efficient in reducing the sintering temperatures<sup>174</sup>, holding times, and reaching high densification for ceramics<sup>175</sup>, metals and alloys<sup>176</sup>, and even refractory materials like WC<sup>177</sup>, there is still debate on the origin of the actual mechanism and the related operating parameters that make this technique different from others.

Some consider that the generation of a plasma – when the electric discharge is effective – is responsible for the sintering of materials, at least in the initial stage of sintering, and then has less influence as the porosity decreases<sup>178</sup>. Munir & *al.* propose, since no evidence of a plasma was presented, to attribute the effect of sintering to the presence of an electric field that activates the diffusion<sup>174</sup>. Whatever the origin of SPS efficiency, it has been compared to hot pressing for the sintering of alumina, and the final density is higher for SPS than for HP, for the same experimental conditions<sup>179</sup>.

Lets remind that in the present study, the aim is to reach high densification levels while working on low temperature decomposition materials. It remains important to identify whether sintering techniques can provide this lowering of sintering temperatures.

Important sintering temperature lowering has already been achieved for some materials in SPS, and some interesting results have been obtained for instance on ZnO ceramics<sup>180</sup>. This work

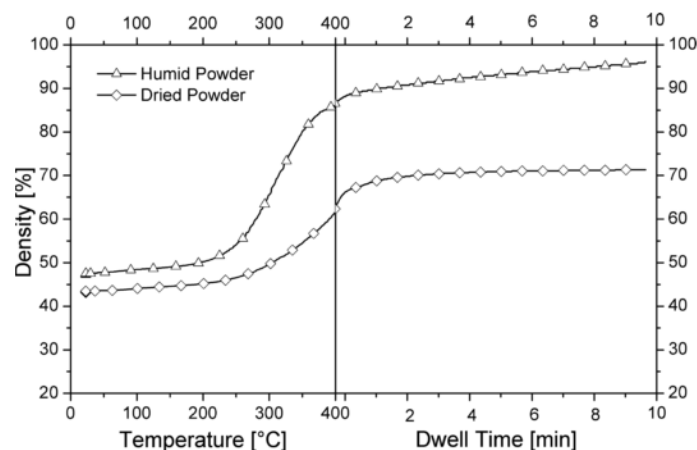


Figure 90: Comparison of densification of humid and dry ZnO powders at a heating rate of 100 °C/min<sup>180</sup>

shows (Figure 17) the possibility to sinter ZnO nano-powders at 400 °C for 10 min with a density of 97% under 50 MPa. The authors discuss the importance of using high heating ramps (> 100°/min), which is one of the advantages of the technique<sup>181</sup>.

Another important effect of sintering conditions in this work is the hydration level of the powder. As shown on Figure 90, densification of humid powder when reaching the dwell at 400 °C for ZnO powders is almost 25% higher than dry powder. Even during the dwell time, densification is over for the dry powder after a few minutes, whereas the humid powder's density increases all the dwell time long and seems not to be over after 10 min. Decreasing the sintering temperatures down to a range where liquid water can be present highlights its important role in the sintering mechanisms at low temperature.

In another work, Massoni *& al.*<sup>182</sup> densified carbonates at low temperatures, from 270 to 670 °C. The authors particularly aim at highlighting the impact of using high thermal ramp (up to 200 °C/min) on both the sintering efficiency and the water release. In their examples, water is still present in the powders after synthesis in small amounts (< 5 %) and must correspond to adsorbed water. They don't aim to point out the effect of water on sintering, but the previous example of adsorbed water influence on ZnO sintering, even with water contents of 1.6wt.% clearly suggests the importance of considering its presence in the case of carbonates. However, this last work also points the fact that heating ramps of 200 °C/min lead to the sudden release of water in the case of barytocalcite ( $\text{BaCa}(\text{CO}_3)_2$ ) that implied the breaking of the final pellets. It is also noteworthy that in this study most of the final pellets are not pure due to partial decomposition of the target carbonate. One has to find a compromise between the increase of heating ramps that lead to high densification, but taking care of the gas release speed in order to preserve the chemical cohesion and mechanical strength of the pellet.

Nowadays, SPS is as a versatile technique that already proved its sintering efficiency for many material families. Through its high tunability and operating parameter control, it shows a good adaptability to various conditions such as wide temperature and pressure ranges, plus various possible atmospheres. It is also possible to tune the pulse sequence to control the thermal cycle.

Lowering the sintering temperatures appears to be possible in SPS but these sintering temperature ranges almost unexplored (< 400 °C) are very promising and need deeper characterization in order to understand the underlying mechanisms and possibilities. For example, the suspicion of liquid  $\text{NaNO}_2$  presence during  $\text{BaCa}(\text{CO}_3)_2$  sintering<sup>182</sup>, could influence the mechanisms. Water and more generally gas release are likely to play a role when sintering in these temperature ranges, and in the following a specific attention will be paid to that.

### 1.2.2.3 Liquid phase sintering

Although sintering is thermally activated and can be reached in a solid-state way, other sintering techniques were developed using a liquid phase in the process. This method has long been explored in the case of refractory materials, thus at high temperature, but is scarcely used, if at all, for low temperature sintering.

#### 1.2.2.3.1 Sintering mechanisms

Liquid phase sintering consists in a mix of phases including a solid and a liquid, or two solids with one that liquefies during the sintering process. In any case, the liquid phase must remain the minor phase. In liquid phase sintering, the solid-gas interfaces are replaced by solid-liquid interfaces. This way, surface tension  $\gamma_{sg}$  (surface tension solid-gas) are replaced by  $\gamma_{sl}$  and  $\gamma_{sv}$  (solid-liquid and solid-vapor surface tensions). In liquid phase sintering, three main parameters are:

- Solubility of the solid in the liquid
- Wettability of the liquid on the solid
- Diffusion of dissolved solid in the liquid

The reason why liquid phase sintering can be achieved faster than solid state sintering resides in the fact that diffusion speed of matter in liquid is higher than classical solid state diffusion of elements<sup>183,184</sup>. Moreover, since the solid phase is surrounded by the liquid phase, diffusion of species can be more efficient at lower temperatures than for a solid. The objective is then to reach the melting point of one of the present phases in order to start the sintering process. For example, sintering of lead zirconate titanate (PZT) is usually achieved at 1250 °C in solid state sintering. Using a 5 wt.% mix of Cu<sub>2</sub>O-PbO with an eutectic point at 680 °C as a sintering aid helps lowering the temperatures down to 800 °C<sup>185</sup>. Sintering at such temperature helped preserving the sub-micrometer size of the grains in this case, while allowing densification above the reference sample obtained from solid state sintering at 1250 °C.

Concerning the mechanisms, liquid phase sintering basically decomposes in three steps:

- Rearrangement of the powder
- Dissolution-precipitation

- Final densification

The first step of liquid phase sintering is the rearrangement of grains. This occurs as soon as the liquid is present. Under the application of a pressure, capillary forces allow the liquid to flow between the grains and fill the porosities. In this case,  $\gamma_{sl}$  must be small, so that the wettability is favored and rearrangement enhanced.

Once the rearrangement is over, dissolution-precipitation step becomes dominant. At this stage, the solid phase is partially dissolved in the liquid phase at a rate inversely proportional to the grain size. It means that small grains will dissolve faster because of the surface tension created by the curvature of the grains (described previously in the solid state sintering mechanisms). The higher solubility of the small grains creates a chemical gradient in the liquid, leading to diffusion in direction of the bigger grains, and then provokes Ostwald ripening. In the same time, the curvature of the grains creates a local pressure gradient between the grain contact zone and the porosities. At the contact zone, the pressure is slightly higher and then an increase of chemical potential promotes dissolution. In the same time, the low pressure zone favors

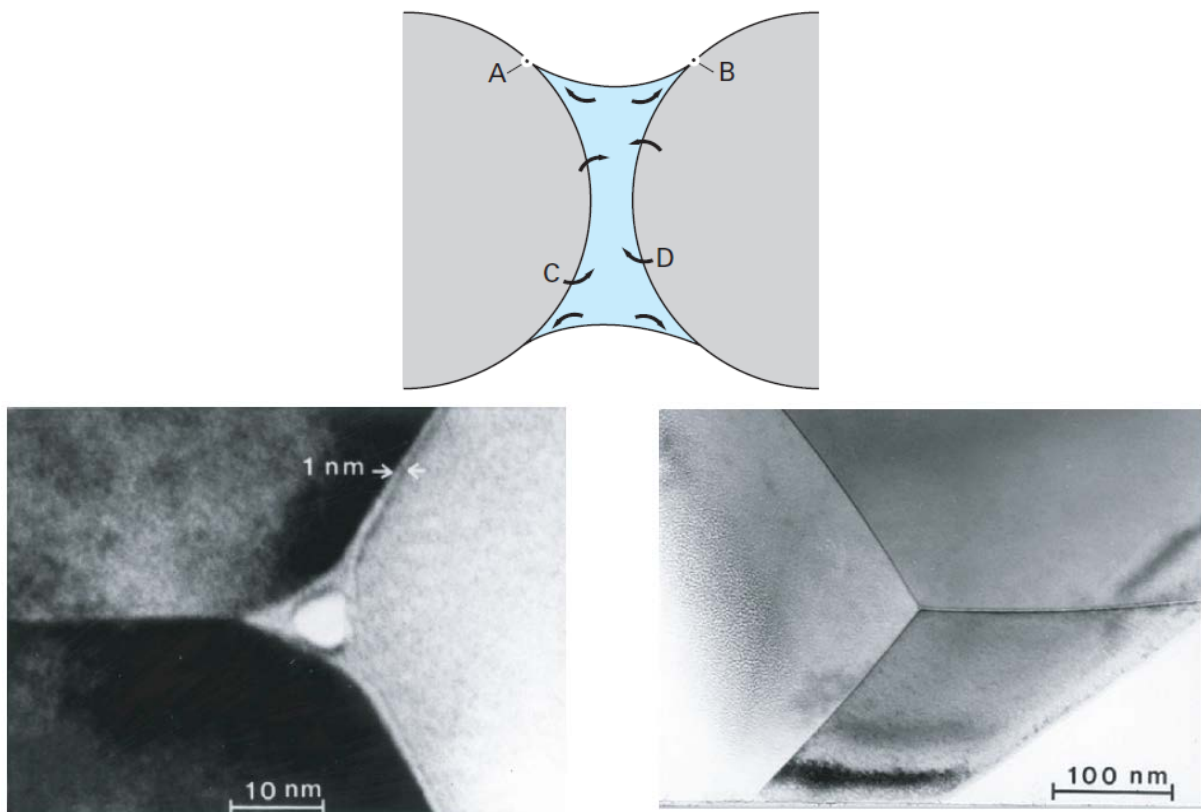


Figure 91: (top) representation of the chemical transfers occurring at a liquid bridge between two grains, and (bottom)  $BaTiO_3$  sintering with addition of 2 wt.% LiF after (left) 10 min and (right) 90 min <sup>237</sup>

precipitation process. This way, both grain shape evolution and porosity reduction occur and cause densification.

The final stage of liquid phase sintering is called the final densification and actually corresponds to the equivalent of solid state sintering. In the solid-solid contacts, diffusion is active but remains a minor effect compared to the liquid phase diffusion. With the decrease of solid-liquid interfaces with sintering going on, solid-solid interfaces become the main part of interfaces and solid state sintering becomes the major diffusion process. The same porosity collapsing effect can then happen if there are some trapped gases, and grain growth can occur if dwell time is too long.

The larger the liquid phase content, the more the liquid phase sintering process will dominate over the solid state one, but the secondary phase used to create liquid phase will remain present at the end, which can be a problem for the properties. With a lower liquid content, dwell times will have to be increased to guarantee an effective diffusion. Here also, a compromise has to be found in the phase contents.

#### 1.2.2.3.2 Solvothermal/hydrothermal hot pressing

Based on the liquid phase sintering principles, another technique was developed and proposed by Yanagisawa & *al.* in 1986 designed to sinter ceramics using water and called Hot Hydrothermal Pressing (HHP)<sup>186</sup>. The objective is to use water as the liquid part for the sintering, which makes a temperature limit for the process at maximum 375 °C (pressure about

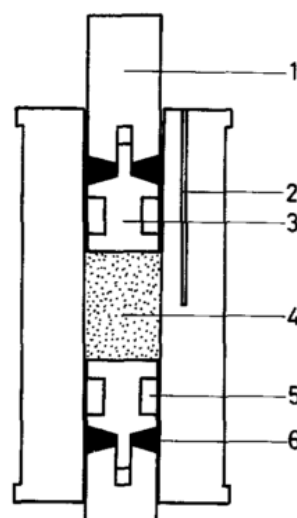


Figure 92: Autoclave for hydrothermal hot-pressing: 1, push rod; 2, well for thermocouple; 3, piston; 4, sample; 5, space for water retreat; 6, gland packing (Teflon)<sup>186</sup>

200 MPa is applied) in order not to overcome the critical point of water (in a critical state, water becomes apolar, no dissolution of ionic species can be achieved). This system is displayed on Figure 92 and its interest lies in the space for water retreat. In this system, water is first used as liquid media for diffusion, but at the end of the treatment, it is evacuated so that the sample remains pure and dry. Using such technique, it was possible to slightly sinter titania<sup>187</sup>, calcium carbonate<sup>188</sup>, hydroxyapatite<sup>189</sup> and silica<sup>190</sup> down to 350 °C under pressures of 200 MPa.

These results clearly highlighted the possibility to sinter refractory ceramics at much lower temperatures than with other sintering techniques and paved the way for the development of a new technique based on the same process, named Cold Sintering Process.

### 1.2.2.3.3 Cold Sintering Process (CSP)

Proposed by Randall's group in 2016, the Cold Sintering Process (CSP) is based on liquid state sintering, as described previously, slightly derived from the HHP system proposed by Yanagisawa. The main difference is the absence of Teflon gasket (as displayed on Figure 93),

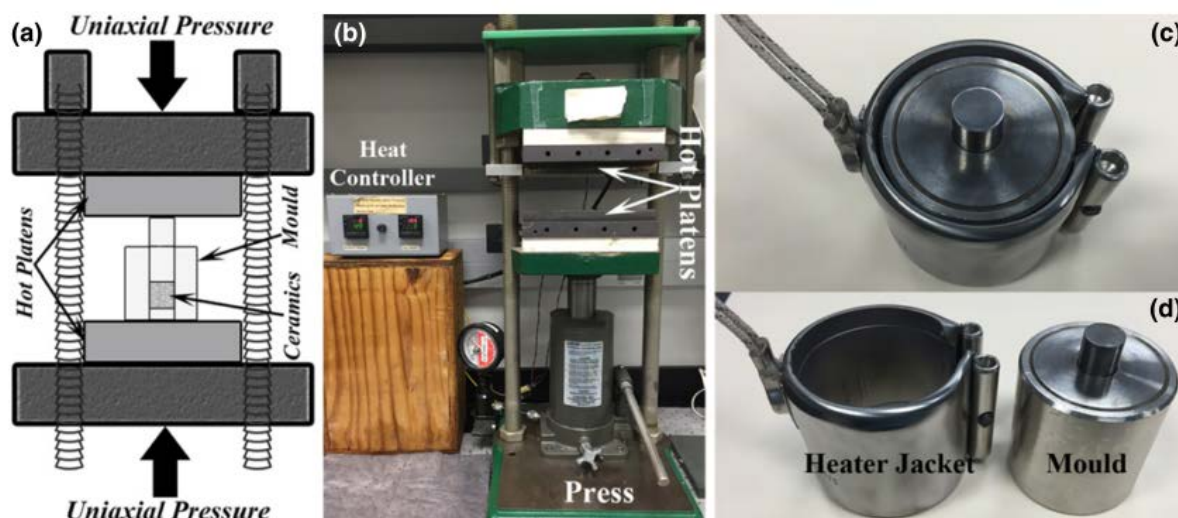


Figure 93: (a) schematic illustration, and (b) photograph, of the experimental setup for Cold Sintering Process. (c)-(d) The photographs of the die and heater jacket<sup>191</sup>

making it possible for water to exit the system during sintering. This way, water is evaporated and the final pellet is dry. This technique, even very recent, already lead to high densities > 90 % after sintering in limited dwell times (20 to 30 min) at temperatures below 200 °C for more than 50 different compounds such as MoO<sub>3</sub>, MgO, V<sub>2</sub>O<sub>5</sub>, Al<sub>2</sub>O<sub>3</sub>, or ZnO for instance<sup>191</sup>. This system proved efficient densification of ceramics, but remains limited in some cases. Actually, the mechanisms of densification have been detailed in a recent paper<sup>192</sup> and are

explained through the dissolution-precipitation process. The key step here is the dissolution, because for complex compositions (multiple cations), the dissolution can either be congruent, in which case the dissolved liquid contains a stoichiometric mix of cations that will further precipitate with the desired stoichiometry, or be incongruent. In the latter case, the cations will dissolve separately and result in a solid with passivated surface and inappropriate composition<sup>192,193</sup>. It is the case of BaTiO<sub>3</sub> in which the poor Ti<sup>4+</sup> solubility compared to Ba<sup>2+</sup> results in a core shell system made of Ti-rich cores and Ba-rich shell, thus inducing a chemical inhomogeneity.

CSP is a very interesting technique that demonstrated the possibility to reach high densities and lower the sintering temperatures, but in the case of incongruent dissolution, is not adapted to preserve the composition of the phase during sintering.

### 1.2.3 Conclusion on sintering

Sintering is based on complex mechanisms, with the influence of many factors ranging from the powders characteristics such as grain size, hydration level or surface chemistry, to operating conditions which encompass the temperature and time, but also can be assisted with pressure, electric current or microwaves, and the atmosphere which also plays an important role. Liquid sintering techniques operate through different mechanisms than solid state sintering, and can be useful to lower the sintering temperature, especially for highly refractory materials. Different sintering techniques have been presented with their pros and cons in order to choose the more adapted one for the present purpose, which is the sintering of fragile materials, and therefore the need to lower the sintering temperatures. SPS sintering has been selected for this work as a good candidate to perform such lowering thanks to the presence of pressure, controlled atmosphere and electric current. Previous studies have shown the possibility to achieve such sintering temperature lowering and seems to confirm the choice of this technique.

## 1.3. Experimental approach

According to the previously explained situation, the work will be divided in three steps. The first one will consist, on crystal chemical basis allowing the occurrence of ME and MF properties, to determine a few candidate materials among fragile materials. Then, the main part

will concern sintering results and observations. This will aim to characterize the initial powders prior to sintering in order to determine their decomposition temperature and, in some cases, phase transitions, and after that sintering behavior and the possible mechanisms involved will be discussed. A particular objective within this part is to develop a proof of concept for the possibility to use SPS for low temperature sintering, typically below 400 °C. Finally, pellets will be characterized to confirm the preservation of their properties, such as magnetic properties and their structure, and electrical measurement will be performed to confirm or infirm their ME or MF properties.

# Chapter 2: Spark Plasma Sintering of fragile ferroic materials at low temperature

As detailed in the previous section, the main objective of the present work is to explore the use of Spark Plasma Sintering (SPS) technique as a prospective tool. Ceramics with both high density and phase purity are very convenient to explore the physical properties of new or promising compounds (ferroic properties, but particularly ferroelectric properties in the present work). The prospective aspect of this work resides in the nature of selected materials. As discussed previously, ferroelectric properties characterization necessitates highly dense materials, usually ceramics > 90-95 % density, single crystals or thin films. However, elaboration of single-crystals or thin films is time-consuming and requires elaborated technical environments that are not suited for an exploratory work. Moreover, many materials may decompose or undergo phase transition before any sintering occurs. However, among these materials, potential candidates for interesting properties can be found, but because of their limited stability, they have not yet been obtained in a dense form, nor their properties investigated. Exploring the properties of these “fragile” materials through physical measurements requires dense pellets that must be sintered beforehand. In this chapter, we will explore the potential of SPS to reach that first goal.

An objective definition for “low temperature sintering” can hardly be established, since it strongly depends on the context and the period. For instance, in 2015, low temperature in the case of dielectric materials was considered as being below 900 °C and ultra-low sintering temperature below 650 °C<sup>194</sup>. One year later, Guo & *al.* define ultralow temperatures as below 400 °C<sup>192</sup>. They also point out the huge efforts that have recently been achieved in reducing sintering temperatures through the development of new sintering techniques such as Spark Plasma Sintering, but also point out the fact they still remain “well above 400 °C”. It would be interesting to investigate SPS efficiency at very low temperatures (below 400 °C). Four different materials will be presented following the same description scheme. Synthesis will first be described, followed by structural and microstructural characterization of powders, before the

actual sintering step can be detailed and discussed. Final characterization of pellets will be presented to confirm phase purity, magnetic property preservation after sintering, then dielectric and magnetocapacitance measurements will be discussed. In order to understand sintering mechanisms, and due to the presence of water in some phases, the final part of this chapter will be devoted to the results of a comparative study SPS and hydrothermal sintering applied to a structurally hydrated material -  $\text{MnSO}_4 \cdot \text{H}_2\text{O}$ . The opportunities emerging from this proof of concept study will be discussed in the conclusion of this chapter.

To present the current work, synthesis required many attempts before obtaining any pure powder. That has been possible thanks to the important contributions of Anna Sangregorio and Iñaki Cornu during master internship.

## 2.1. Candidate materials selection

Ferroc properties are strongly related to crystal structure and composition of materials. The selection of materials with, potentially, ferroc properties, has to be focused on crystal chemical framework allowing or favoring these properties. In that case, and as described by Hill *et al.*<sup>91</sup>, few conditions have to be filled:

- $d^n$  cation to hold magnetization
- polarizable elements ( $d^0$  ions, lone pair ions...) or groups
- no inversion symmetry in the lattice

These conditions are designed in the purpose of obtaining materials with potential ferroc properties. However, further conditions have to be considered while selecting candidate materials:

- Mineral resources being depletable, elements that are abundant in the earth crust should be favored, as long as they do not belong to the Critical Raw Materials list<sup>1</sup>
- Complex ions ( $\text{NH}_4^+$ ,  $\text{SO}_4^{2-}$ ,  $\text{CO}_3^{2-}$ ...) could allow for multifunctional materials, as for example ammonium sulfate is ferroelectric below 223 K<sup>195</sup>. Moreover most salts encompassing these species are water-soluble, thus bearing promises of easier retreatment, or even recyclability

- The dielectric properties of many fluorides and halides, hardly densified through conventional methods, could be readily and easily explored through the use of SPS
- The dielectric properties of allotropic varieties which stability does not allow for conventional sintering could also be explored

Once the choice a candidate phase is achieved, it becomes interesting to explore whether the selected phase actually possesses interesting physical properties. Unlike electrical properties, magnetic property measurement can be achieved on samples of any design (crystal, powder, films, ceramics or glass). Although our aim is to measure dielectric and magnetic properties of ceramics, it is already possible to perform magnetic measurements on powders so as to know whether the selected phase is magnetically ordered. The selection of phases then focuses on magnetically ordered materials, preferably ferromagnetic but also antiferromagnetic.

Among the variety of candidate materials, a few ones attracted a particular attention. The first material that was selected is  $\text{NH}_4\text{FeP}_2\text{O}_7$ . It belongs to the  $\text{A}^{\text{I}}\text{M}^{\text{III}}\text{P}_2\text{O}_7$  diphosphate group with trivalent cation. Three structural types are reported in these phases:  $\text{NaFeP}_2\text{O}_7$ -I type (low temperature form),  $\text{NaFeP}_2\text{O}_7$ -II type (high temperature form), which are not isotypic but crystallize in the same space group  $\text{P2}_1/\text{c}$ , and  $\text{LiFeP}_2\text{O}_7$ <sup>196–198</sup>. Anyway, all the structures can be described as an alternated succession of  $[\text{M}^{\text{III}}\text{O}_6]^{9-}$  octahedra and of  $[\text{P}_2\text{O}_7]^{4-}$  layers sharing corners with octahedral groups. The main differences lies in the conformation of  $\text{P}_2\text{O}_7$  groups, influenced by the  $\text{A}^{\text{I}}$  cation's size that determine the structural type of the host matrix<sup>196</sup>.  $\text{A}^{\text{I}}\text{FeP}_2\text{O}_7$  ( $\text{A}^{\text{I}} = \text{Li}, \text{Na}, \text{K}, \text{Cs}$  and  $\text{Ag}$ ) are known to be antiferromagnetic<sup>199</sup>, but  $\text{NH}_4^+$  compound has only been reported for its synthesis and structural characterization<sup>197,200</sup>. Moreover, isostructural  $\text{KCrP}_2\text{O}_7$  is known as a potentially magnetoelectric<sup>201</sup>. Thanks to ammonium groups,  $\text{NH}_4\text{FeP}_2\text{O}_7$  could possibly present interesting ferroelectric polarization, such as in  $\text{NH}_4\text{CuCl}_3$  which was recently shown to exhibit weak ferroelectricity<sup>202</sup> attributed to the presence of  $\text{NH}_4^+$  groups.

The second material we got interested in is antiferromagnetic,  $\text{MnSO}_4$ . This follows previous research lead on the similar  $\text{MnWO}_4$  and its Mo substituted compounds showing ferroelectric transitions at 13 K<sup>203,204</sup>. Such as in the case of  $\text{MnWO}_4$ ,  $\text{MnSO}_4$  magnetic structure is a cycloidal spiral arrangement in which ferromagnetic sheets (001) are coupled antiparallel<sup>205</sup>. This results in an antiferromagnetic phase below  $T_{\text{N}} = 16 \text{ K}$ <sup>206</sup>. Because of this spiral

antiferromagnetic arrangement, inversion symmetry is broken and polarization can occur. This material, which presents a potential interest because of its physical properties became the major contribution to the exploration of sintering behavior and will represent a large part of the present chapter.

The following two materials are from the same compositional family but crystallize in different space groups and have different structural features. These compounds are  $A_2Cu(CO_3)_2$  with  $A = Na$  and  $K$ . The first compound we were interested in is the  $K$ -containing phase, with a non-centrosymmetric space group  $Fdd2$  at room temperature and a ferromagnetic phase below  $T_C = 6\text{ K}^{207,208}$ . This compound, with a non-centrosymmetric structure at room temperature, a small electronic asymmetry<sup>209</sup> around  $Cu^{2+}$  ions and a ferromagnetic phase transition, appears to be an interesting candidate as multiferroic material. Its parent compound with  $Na^+$  ions is also presented in this work. After exploring  $K_2Cu(CO_3)_2$  compound, our aim was to explore solid solutions in  $A_2Cu(CO_3)_2$  with  $A = Na, K$  and  $NH_4$ . The ammonium compound is not described in the literature and synthesis attempts quickly lead to the conclusion that it is possible to obtain it using the same synthesis route as the one used for  $Na$  and  $K$  compounds. However, surprising results were obtained with this phase, that will be detailed separately. Although the  $K$ -based compound is reported as a 3 dimensional arrangement of  $CuO_4$  planes bonded to  $CO_3$  groups at  $90^\circ$  angle,  $Na$  compound consists of a layered arrangement with ferromagnetic interactions between layers below  $T_C = 5.6\text{ K}^{210}$ . Carbonate groups present an asymmetric arrangement with different  $C-O$  distances, resulting in small dipolar moment that could possibly be polarized.

In order to know whether these materials possess the expected properties, and especially to investigate their dielectric properties, they must be obtained in a dense form, through sintering, and their thermal behavior has to be explored beforehand to evaluate the temperature range suitable for their sintering.

## 2.2. Experimental Spark Plasma Sintering setup

Now we have identified the materials we are interested in, the objective is to densify them to obtain ceramics with relative densities  $> 90\%$ , to be able to measure dielectric properties with negligible extrinsic contributions. Sintering processes usually require high temperature

(typically  $> 700\text{ }^{\circ}\text{C}$ ). In the present work we focus on materials displaying a lack of stability which can be due to a low melting point, an irreversible phase transition, or even a thermal decomposition occurring at low temperature. We will refer to them as “fragile” materials or phases. For such materials, reaching temperatures in the typical range required for sintering is impossible, due to the phase transitions (such as anatase to rutile occurring between 500 and  $600\text{ }^{\circ}\text{C}^{211}$ ) or even the total decomposition of the material occurring at temperatures below sintering. In the present work, the four target phases decompose in air at temperatures ranging from 160 to  $680\text{ }^{\circ}\text{C}$  and no sintering can be achieved using conventional sintering techniques (that of  $\text{MnSO}_4$ , which decomposes at  $680^{\circ}\text{C}$ , was attempted at  $670^{\circ}\text{C}$  without success). In order to perform sintering we explored the SPS technique, using it in a low temperature range ( $\leq 400\text{ }^{\circ}\text{C}$ ) to preserve these fragile phases. Because our aim is to perform sintering at low temperatures to preserve the phase, use of pressure and electric current are expected to compensate the lack of thermal energy needed to trigger sintering mechanisms. Figure 94 displays the available operating conditions for the SPS set-up at our disposal. Graphite dies are used for high temperatures, and are limited in applicable pressure to the range 40-100 MPa. Therefore it appears of limited interest in the present work, and will be occasionally used for preliminary sintering attempts.

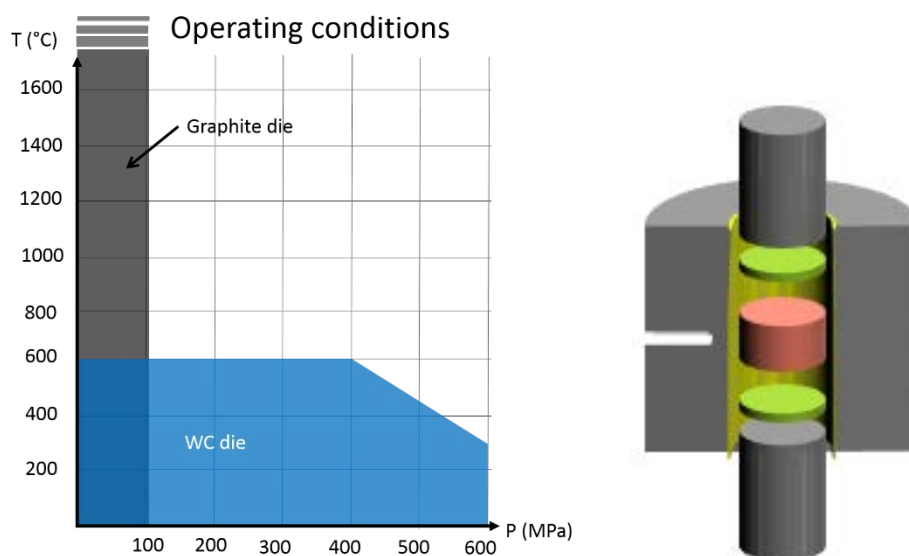


Figure 94: (left) Operating conditions in SPS available in the lab and (right) schematic representation of a WC:Co die setup: die and pistons in grey, protective sheets (green) and powder (red); space for thermocouple is represented on the left in white

However, Co-doped WC dies are able to handle larger pressures but are limited to a lower temperature range ( $< 600\text{ }^{\circ}\text{C}$ ). These operating temperatures correspond to the stability domains

of our materials, and therefore define the range of experimental conditions we can investigate. These WC:Co dies can support pressures up to 600 MPa at 300 °C, the maximum pressure decreasing as the temperature increases. At 600 °C, a maximum pressure of 400 MPa can be applied. The setup also requires the presence of protective sheets between the powder and the die. It is usually composed of graphite, but we also dispose of Mo and Ta sheets that can be used in order to avoid reactivity between the precursor powder and graphite sheets. In the present work, all the experiments were performed under vacuum, with a starting pressure of 10 Pa ( $10^{-5}$  atm,  $7.5 \times 10^{-2}$  Torr), with dwell times ranging from 5 to 60 min. Thermal ramp was kept constant at 30 °C/min for  $\text{NH}_4\text{FeP}_2\text{O}_7$ ,  $\text{K}_2\text{Cu}(\text{CO}_3)_2$  and  $\text{Na}_2\text{Cu}(\text{CO}_3)_2$ . In the case of  $\text{MnSO}_4$ , a 50 °C/min ramp was used. Below 300 °C, it becomes difficult to accurately control the temperature if the ramp is too steep. A temperature overshoot is often observed, that a 30 °C/min thermal ramp prevents. In the case of  $\text{MnSO}_4$ , temperatures up to 550 °C were explored and 50 °C/min was a good compromise to optimize both experimental time and thermal control.

Protective sheets were placed between the powder and could be of two different natures. In the case of  $\text{MnSO}_4$ , graphite sheets have been used, but in the other cases, reactions with powder makes the use of graphite sheets impossible. For that reason, Ta sheets were used to replace graphite ones.

### 2.3. $\text{NH}_4\text{FeP}_2\text{O}_7$

The first phase we are interested in is a pyrophosphate phase belonging to the  $\text{AFeP}_2\text{O}_7$  family (with  $A = \text{Li, Na, K, Cs, Ag}$ ). The ammonium containing compound of this family has only been reported few times and its characterizations is essentially limited to its structure. No magnetic measurements were published and the crystal structure is determined at room temperature. The presence of antiferromagnetic transitions in this family added to the presence of  $\text{NH}_4^+$  groups that could potentially be responsible for a small polarization, giving rise to multiferroicity<sup>202</sup>, makes this phase an interesting candidate in the present work. Moreover, a related isotype compound,  $\text{K}_2\text{CrP}_2\text{O}_7$ , has been shown to have a symmetry compatible with the existence of magnetoelectric coupling<sup>201</sup>.

### 2.3.1 Structure

$\text{NH}_4\text{FeP}_2\text{O}_7$  crystallizes in a monoclinic space group  $P2_1/c$ <sup>197</sup>. All  $\text{A}^I\text{FeP}_2\text{O}_7$  ( $\text{A}^I = \text{Li}, \text{Na}, \text{K}, \text{Cs}$  and  $\text{Ag}$ ) structures may be described as an alternating succession of  $\text{FeO}_6$  octahedra and pyrophosphate  $\text{P}_2\text{O}_7$  groups made of di-tetrahedral layers (where tetrahedra share corners with octahedra). The structure of  $\text{NH}_4\text{FeP}_2\text{O}_7$  is I-type. The host lattice form cages resulting from intersecting tunnels where  $[\text{NH}_4]^+$  ions are located. Two sorts of tunnels are in fact observed: wide tunnels running along the  $[001]$  direction containing  $\text{A}^I$  cation and distorted hexagonal ones running along the  $[110]$  direction (Figure 95).

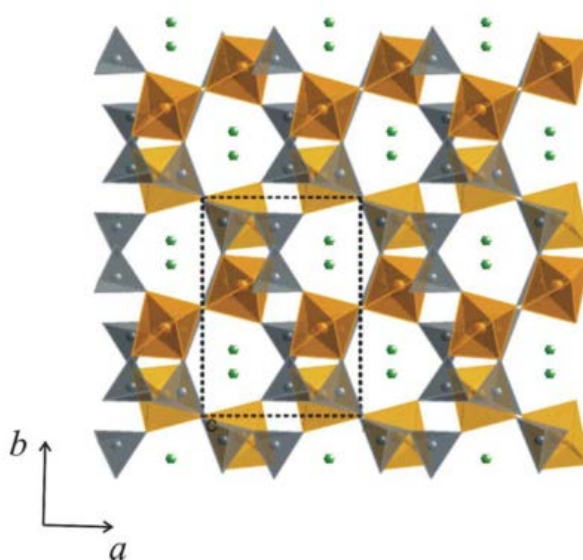


Figure 95: Representation of  $\text{NH}_4\text{FeP}_2\text{O}_7$  structure along  $(001)$  direction<sup>197</sup>. Dotted lines represent one unit cell

### 2.3.2 Synthesis

The synthesis of  $\text{NH}_4\text{FeP}_2\text{O}_7$  is performed from the heat treatment of a green pellet constituted of a mix of both  $(\text{NH}_4)_2\text{HPO}_4$  and  $\text{Fe}_2\text{O}_3$ . The latter is obtained from the heat treatment of  $\text{Fe}(\text{NO}_3)_3 \cdot 9\text{H}_2\text{O}$ , as commercial  $\text{Fe}_2\text{O}_3$  presents a poor reactivity and its use results in an important amount of non-reacted  $\text{Fe}_2\text{O}_3$ . The two powders are mixed (agate mortar) and pelletized, then they are fired in a furnace at  $200^\circ\text{C}$  for 24h. Sealed nitrogen environment, as well as nitrogen flux, were used to perform the synthesis, but resulted in a high content of remaining iron oxide, and sometimes promoted the formation of other phosphates as secondary phases. Using a sealed vacuum atmosphere allowed to obtain the higher ratio of  $\text{NH}_4\text{FeP}_2\text{O}_7$  over  $\text{Fe}_2\text{O}_3$ . When a stoichiometric ratio of  $(\text{NH}_4)_2\text{HPO}_4$  and iron oxide is used, there is an

important part of remaining iron oxide, due to the volatilization of ammonium phosphate. Adding an excess of  $(\text{NH}_4)_2\text{HPO}_4$  allows to compensate this volatilization, up to a point where other phases appear. The best compromise was found to be a 20 wt.% excess of  $(\text{NH}_4)_2\text{HPO}_4$ , although traces of  $\text{Fe}_2\text{O}_3$  are still visible on the Rietveld XRD pattern of the product (Figure 96 a and b). However, previous work from literature seems to confirm the difficulty to fully separate  $\text{NH}_4\text{FeP}_2\text{O}_7$  phase from  $\text{Fe}_2\text{O}_3$ <sup>197</sup>.

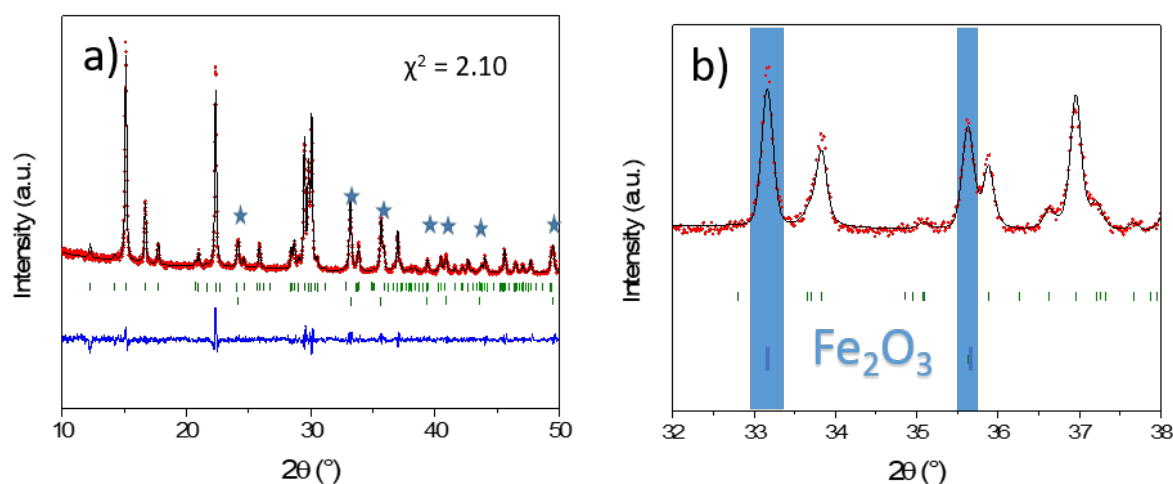


Figure 96: Profile refinement of XRD pattern of  $\text{NH}_4\text{FeP}_2\text{O}_7$  including remaining  $\text{Fe}_2\text{O}_3$  (a) zoom out and (b) zoom on two  $\text{Fe}_2\text{O}_3$  visible peaks

Synthesis times, temperature and atmospheres, but also stoichiometric ratio of powders and nature of the iron oxide (commercial  $\text{Fe}_2\text{O}_3$  or annealed  $\text{Fe}(\text{NO}_3)_3 \cdot 9\text{H}_2\text{O}$ ) have been tuned to obtain the purest  $\text{NH}_4\text{FeP}_2\text{O}_7$  powder. Although remaining  $\text{Fe}_2\text{O}_3$  has been limited, no completely pure sample has been obtained and the rest of the study has then been performed using the sample exhibiting the present XRD pattern (Figure 96).

### 2.3.3 Powder characterization

Once the synthesis has been performed, the obtained powder has to be characterized before sintering is achieved. In the present case, thermal, structural and magnetic characterizations have been performed.

As presented on Figure 96, profile refinement has been performed on XRD pattern, considering the presence of both  $\text{NH}_4\text{FeP}_2\text{O}_7$  and  $\text{Fe}_2\text{O}_3$ . The obtained lattice parameters for  $\text{NH}_4\text{FeP}_2\text{O}_7$  are summarized in Table 1 below:

Table 8: Refined lattice parameters of  $\text{NH}_4\text{FeP}_2\text{O}_7$  powder compared to literature values<sup>197</sup>

|                                  | <b>a (Å)</b> | <b>b (Å)</b> | <b>c (Å)</b> | <b>β (°)</b> |
|----------------------------------|--------------|--------------|--------------|--------------|
| <b>Refinement</b>                | 7.5197(4)    | 10.0023(5)   | 8.2759(5)    | 105.856(6)   |
| <b>Literature</b> <sup>197</sup> | 7.5219(2)    | 10.0018(3)   | 8.2729(3)    | 105.887(3)   |

For powder refinement,  $\chi^2 = 2.10$

According to the excellent agreement between refined lattice parameters and literature values, one can assume the crystallization of  $\text{NH}_4\text{FeP}_2\text{O}_7$  was effective during synthesis treatment. The presence of  $\text{Fe}_2\text{O}_3$  is confirmed, but no other phase is present. Yet, one can notice on the refinement residuals for both peaks at  $2\theta = 15$  and  $22^\circ$ , there is an important misfit. Since it is a profile refinement, intensity of peaks shouldn't be affected by the refined lattice parameters, and therefore this misfit likely results from a microstructural anisotropy of crystallites, thus affecting peaks width. These two peaks correspond to (110) and (002) directions. According to the present refinement result, (110) is broader than calculated, whereas (002) peak is thinner. This can be explained with a preferential crystal growth. Nevertheless, this does not affect the lattice parameters which are almost identical to those reported in the literature.

TGA measurement under air has been performed on the powder to determine its decomposition temperature (see Figure 97). Three main peaks are visible on DTG up to  $600^\circ\text{C}$ . Whereas mass loss is not complete at the maximum temperature of the analysis ( $600^\circ\text{C}$ ), from post annealing XRD data, it has been determined that decomposition starts during the first mass loss starting at  $170^\circ\text{C}$ . This value is then retained to characterize the thermal stability of the material in air for the determination of sintering temperature. No visible hydration of the material is detected from TGA and coupled mass spectroscopy, thus if present, water must be limited to traces.

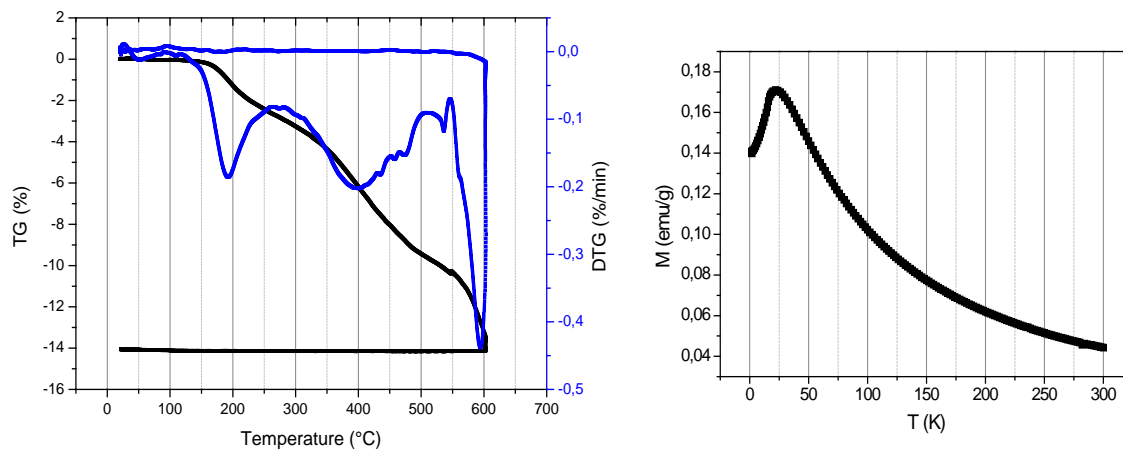


Figure 97: TGA under air and SQUID measurement of  $\text{NH}_4\text{FeP}_2\text{O}_7$  powder

As presented earlier,  $\text{NH}_4\text{FeP}_2\text{O}_7$  belongs to the  $\text{AFeP}_2\text{O}_7$  series exhibiting antiferromagnetic transitions around  $20 \text{ K}^{212}$ . Magnetic measurements (coll. Pr. C. Payen, IMN, Nantes) have been performed on powder of  $\text{NH}_4\text{FeP}_2\text{O}_7$  (see Figure 97). In that case, the antiferromagnetic transition, not documented in the literature occurs at  $T_N = 23 \text{ K}$  and Weiss temperature has been determined as  $\theta = -52 \text{ K}$ , confirming the presence of antiferromagnetic interactions.

Now the characterization of the powder has been achieved, it becomes possible to perform sintering in SPS in order to obtain dense sample that will be characterized and compared to the present powder to check phase purity and magnetic properties preservation.

## 2.3.4 Sintering

### 2.3.4.1 Sintering conditions and pellet characterization

Sintering has been performed on  $\text{NH}_4\text{FeP}_2\text{O}_7$  powder using the SPS setup described previously. Sintering has been performed at different temperatures but pressure and sintering dwell time has been kept constant over the various samples to 300 MPa and 10 min respectively (see Table 2).

Following these sintering conditions, pellets have been obtained in all cases and could be be geometrically measured to determine size and weight in order to determine their relative density. Since  $\text{Fe}_2\text{O}_3/\text{NH}_4\text{FeP}_2\text{O}_7$  ratio hasn't been determined, calculations have been performed considering pure  $\text{NH}_4\text{FeP}_2\text{O}_7$  pellets. Therefore, relative density is slightly

overestimated. ( $\text{Fe}_2\text{O}_3$ :  $5.04 \text{ g/cm}^{-3}$  vs.  $\text{NH}_4\text{FeP}_2\text{O}_7$ :  $2.75 \text{ g/cm}^{-3}$ ). For instance, when sample #3, with hypothetical 5wt.% of  $\text{Fe}_2\text{O}_3$ , the density would actually be 94.3% dense instead of 98.0.

Table 9: Sintering conditions and relative densities measured on  $\text{NH}_4\text{FeP}_2\text{O}_7$  pellets

| Sample | Sintering temperature ( $^{\circ}\text{C}$ ) | Sintering pressure (MPa) | Dwell time (min) | Relative density (%)* |
|--------|--|--------------------------|------------------|-----------------------|
| #1     | 200  |                          |                  | 94.1                  |
| #2     | 250  | 300                      | 10               | 95.6                  |
| #3     | 300  |                          |                  | 98.0                  |

\*: relative density is calculated from pure  $\text{NH}_4\text{FeP}_2\text{O}_7$  density data, whereas it has been shown the presence of  $\text{Fe}_2\text{O}_3$  impurities in the synthesized powders

Microstructural characterization has been performed through SEM observation of fractured pellets and are displayed on Figure 98.

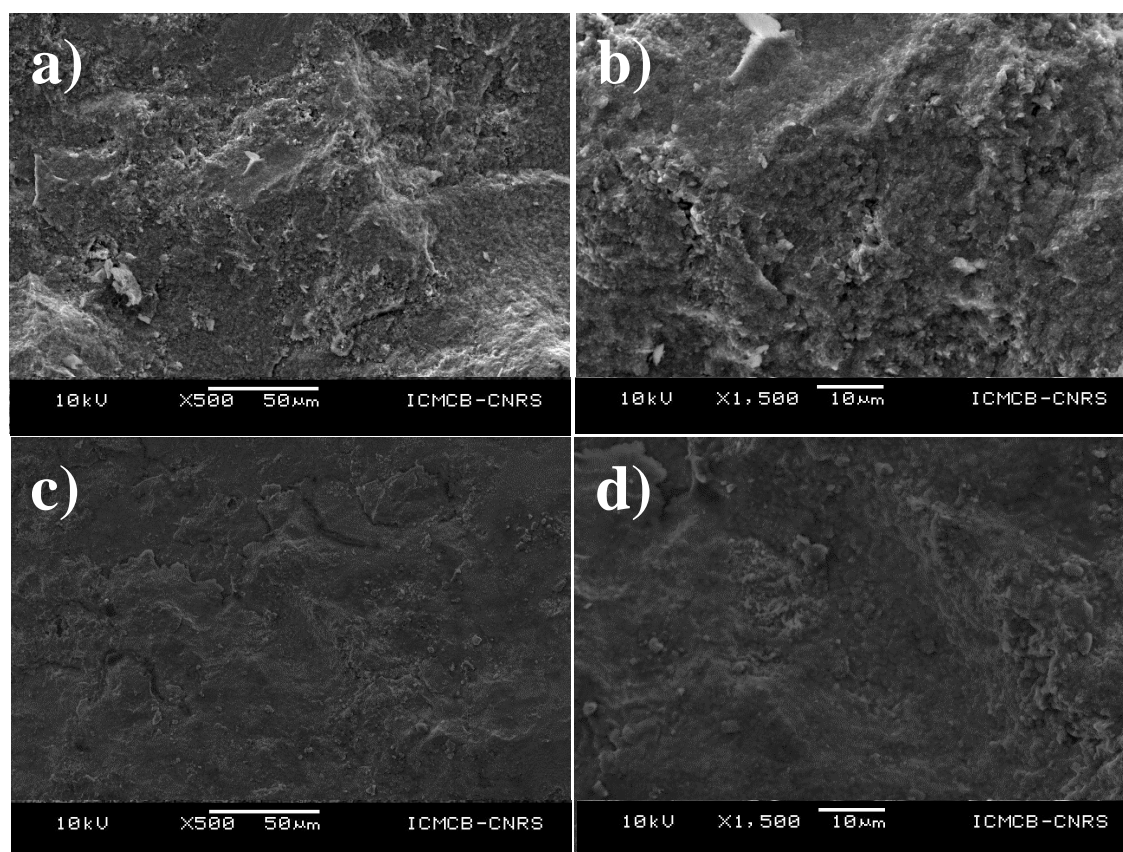


Figure 98: SEM pictures of two  $\text{NH}_4\text{FeP}_2\text{O}_7$  pellets sintered at (a-b)  $200^{\circ}\text{C}$  and (c-d)  $300^{\circ}\text{C}$

Observation of these fractures confirms a high-density level which confirms the relative density values presented in Table 2. Although a precise density cannot be provided, microstructure presents no visible porosity and a high packing level. Moreover, small grain size is observed with grains of submicrometer sizes.

Pellets structures have been characterized through refinement of XRD data. These ones have been refined in order to obtain lattice parameters for each sample. Refined patterns are presented on Figure 99 and refined parameters summarized in Table 3.

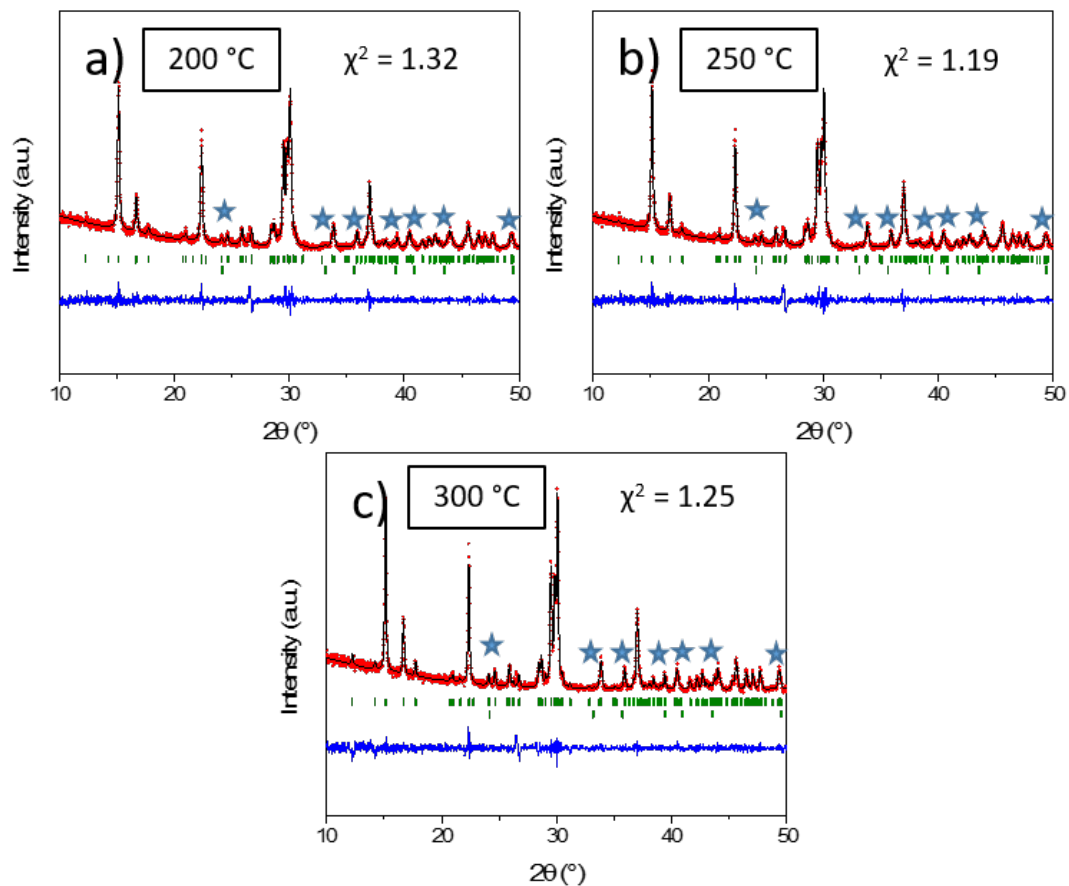


Figure 99: XRD pattern refinements of pellets sintered in SPS at (a) 200 °C, (b) 250 °C and (c) 300 °C. Blue stars represent the positions of Bragg reflections of hematite

From XRD patterns refinement, it can be noticed that various sample exhibit no phase transition to another phase.  $\text{NH}_4\text{FeP}_2\text{O}_7$  is preserved and no additional phase appears. The amount of hematite remains relatively constant. From these refinements, lattice parameters have been extracted and comparison with powder sample show no noticeable evolution of the any of the

lattice parameters. This shows that phase purity is well preserved during SPS treatment, for temperatures ranging from 200 to 300 °C.

Table 10: Refined lattice parameters of  $\text{NH}_4\text{FeP}_2\text{O}_7$  pellets sintered in SPS

| Sample        | Sintering temperature (°C) | a (Å)     | b (Å)      | c (Å)     | $\beta$ (Å) |
|---------------|----------------------------|-----------|------------|-----------|-------------|
| #1            | 200                        | 7.5175(3) | 10.0065(3) | 8.2738(3) | 105.895(3)  |
| #2            | 250                        | 7.5180(2) | 10.0055(3) | 8.2780(2) | 105.901(3)  |
| #3            | 300                        | 7.5176(2) | 10.0043(2) | 8.2729(2) | 105.900(3)  |
| <b>Powder</b> | -                          | 7.5197(4) | 10.0023(5) | 8.2759(5) | 105.856(6)  |

According to the previous results, *i.e.* pellets phase purity, microstructures and relative densities, it can be concluded that sintering of  $\text{NH}_4\text{FeP}_2\text{O}_7$  was successfully performed through Spark Plasma Sintering, which proved highly efficient at quite low temperature. Moreover, operating sintering temperature (up to 300°C), with respect to phase decomposition temperature (170°C), are surprising and promising.

#### 2.3.4.2 Phase stabilization in SPS environment

In the present case, sintering has successfully been performed for  $\text{NH}_4\text{FeP}_2\text{O}_7$  for temperatures ranging from 200 to 300 °C. After TGA measurement, decomposition of  $\text{NH}_4\text{FeP}_2\text{O}_7$  in air has been determined to be 170 °C, which is 30 °C below the lowest sintering temperature presented. However, synthesis of the phase is performed under primary vacuum at 210 °C. This means the phase stability is increased in this environment. During SPS treatment, the environment also consists in vacuum (10 Pa). For this reason, it seems normal to observe a stability increase above 170 °C. However, synthesis attempts at temperatures above 210 °C all lead to the formation of secondary phases, and 210 °C has been determined as the highest synthesis temperature that could be used to keep the phase pure. In the present case, sintering is performed at temperatures up to 300 °C, which is 90 °C above the synthesis temperature under vacuum. Although the synthesis setup used does not allow pressure measurement, and therefore no comparison with SPS chamber pressure, it is notable to observe such stabilization in SPS conditions. Moreover, no sintering attempts have been achieved at higher temperature that

could be useful to determine the actual maximum stability temperature of  $\text{NH}_4\text{FeP}_2\text{O}_7$  in SPS conditions. In addition, it could be interesting to perform TGA in the same environmental conditions as during sintering. No other example in literature has been found of such sintering beyond the stability domain of a phase, and therefore this observation is an interesting and promising result, pointing out an important asset of the SPS setup.

### 2.3.5 Physical properties

Highly dense ceramics have been obtained with preservation of the initial phase content. Microstructure observation of the different pellets shows a low level of porosity, which is necessary to perform reliable dielectric measurement. Magnetic measurement have also been performed on a pellet to confirm the preservation of magnetic behavior.

#### 2.3.5.1 Magnetic measurements

Zero field cooling measurement has been performed in SQUID under 1000 Oe to confirm the preservation of the antiferromagnetic transition observed on powder. Magnetic measurement has been performed on a part of fractured pellet sintered at 200 °C and is displayed on Figure 100.

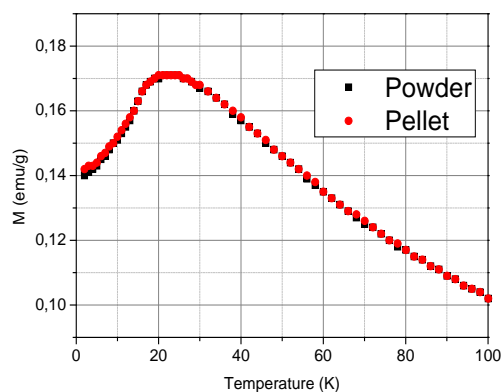


Figure 100: ZFC measurement under 1000 Oe of both sintered pellet and initial powder of  $\text{NH}_4\text{FeP}_2\text{O}_7$

The very nice superposition of both powder and pellet measurement shows the preservation of magnetic properties after sintering. Antiferromagnetic transition is observed for both samples at  $T_N = 23$  K, and confirms the XRD refinement results showing a good phase preservation, and

therefore showing the low evolution of both structural and magnetic properties through sintering.

#### 2.3.5.2 Dielectric measurements

Dielectric measurements have been performed on the pellet sintered at 250 °C both on cooling and heating between room temperature and 2 K. Scanning frequencies from 100 Hz to 1 MHz have been applied, and results displayed on Figure 101 correspond to a frequency of 300 kHz. Measurement has been performed with and without magnetic field. Both capacitance and dielectric losses measurements versus temperature are presented. Capacitance dependence on magnetic field has also been measured by scanning magnetic field from -9 to 9 T at 2 K.

Global decrease of capacitance is observed from 200 to 2 K. No obvious anomaly is visible on this plot. However, in the case of losses, a broad peak is observed between 100 and 150 K. These losses are very small, with  $\tan\delta$  below 0.003, which demonstrates the high resistivity of the material and the high quality of the sintered pellet. Above 200 K, losses become important and the increase of capacitance is concomitant with these. No particular effect is observed when a 9T magnetic field is applied, both capacitance and losses are similar under 0 and 9 T. On the right side of the figure is presented C(H) plot at 2 K. The noise level is close to the amplitude of the signal evolution ( $< 1$  fF) and no firm conclusion can be extracted from this measurement with respect to an eventual magnetoelectric coupling.

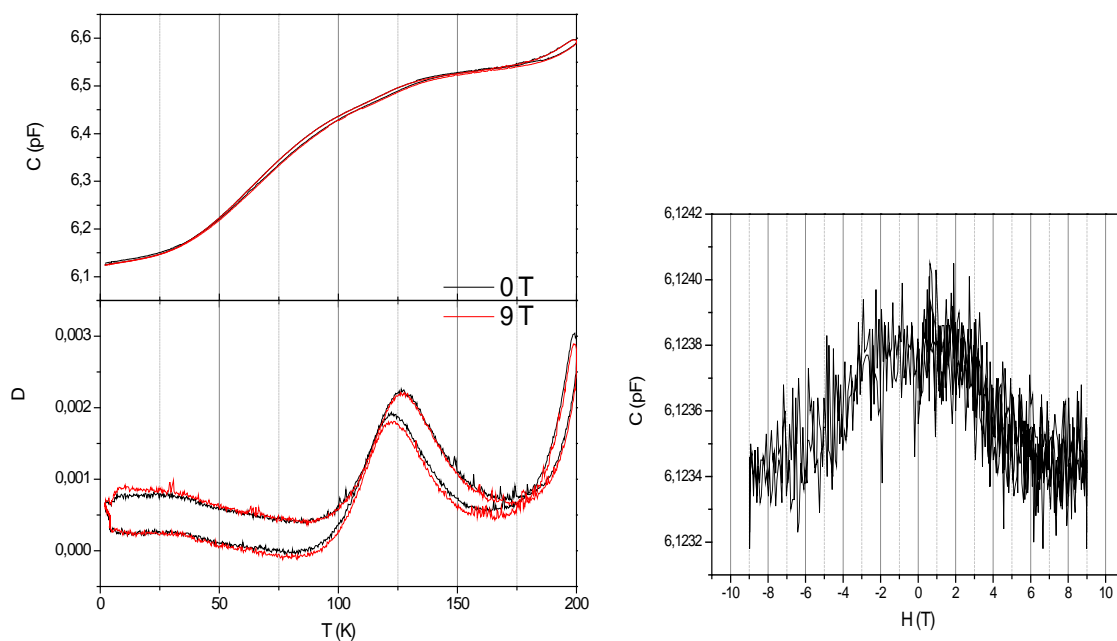


Figure 101: PPMS measurements of  $\text{NH}_4\text{FeP}_2\text{O}_7$  pellet sintered in SPS, capacitance and dielectric losses are measured at 300 kHz and  $C(H)$  measurement is performed at 2 K

### 2.3.6 Conclusion on $\text{NH}_4\text{FeP}_2\text{O}_7$

Synthesis of  $\text{NH}_4\text{FeP}_2\text{O}_7$  has been achieved through solid state route, and even though the determination of synthesis conditions required many adjustments before the best ones could be identified, the phase was finally obtained with a good crystallization, and lattice parameters that fit with the literature data. Although residual hematite  $\text{Fe}_2\text{O}_3$  couldn't be totally removed from the powder, it remains at a low quantity. Thermal stability in air has been determined as 170 °C, which is lower than the actual synthesis temperature, performed under vacuum. Sintering has been successful with high densities above 90 % of the theoretical density of  $\text{NH}_4\text{FeP}_2\text{O}_7$ , with dense microstructures showing very low porosity level and small grain sizes. Surprisingly, sintering temperatures from 200, and up to 300 °C, could be used with no apparent decomposition of the phase, and very short dwell time (10 min) was sufficient to achieve sintering. This could be confirmed with pellet characterization showing almost perfect lattice parameters preservation, but also a perfect preservation of magnetic properties between the powder and the pellet. Finally, the high density of the pellets allowed dielectric measurement showing losses below 0.003, thus confirming the high microstructure quality. If dielectric losses show a wide peak ranging from 100 to 150 °C associated with a decrease of capacitance, no

ferroelectric anomaly has been identified and the capacitance show no dependence to magnetic field.

As a major observation, this example confirmed the possibility to sinter ceramics in SPS at temperatures down to 200 °C with high density level. Moreover, it also shows the possibility to stabilize  $\text{NH}_4\text{FeP}_2\text{O}_7$  at temperature near and above its decomposition temperature observed during thermal analysis under air and synthesis under vacuum. Starting from that, it appears interesting to confirm these results through the sintering of other material families. In the next section, two carbonate materials will be presented, from synthesis to characterization, and obviously detailing SPS sintering.

## 2.4. $\text{A}_2\text{Cu}(\text{CO}_3)_2$ (A = K, Na)

Two other materials have been selected from carbonate families. Initially, the main interest was focused on the potassium containing compound,  $\text{K}_2\text{Cu}(\text{CO}_3)_2$ , which crystallizes in a non-centrosymmetric *Fdd2* space group and presents a ferromagnetic phase transition at  $T_C = 6.6 \text{ K}^{207}$ . We finally got interested in other compounds belonging to the same family. Thus,  $\text{Na}_2\text{Cu}(\text{CO}_3)_2$ , exhibiting antiferromagnetic transition at  $T_N = 5.6 \text{ K}$  but crystallizing in a different monoclinic *P2<sub>1</sub>/a* space group<sup>213-215</sup>, appeared as a good candidate in the present work..

### 2.4.1 Structure and properties

#### 2.4.1.1 $\text{K}_2\text{Cu}(\text{CO}_3)_2$

$\text{K}_2\text{Cu}(\text{CO}_3)_2$  structure has been determined by single crystal X-ray diffraction and crystalizes in an orthorhombic space group *Fdd2*<sup>208</sup>. It consists in square planar coordinated copper atoms bridged to carbonate groups. These square planes make a 83° angle with coordinated carbonate groups and result in a three dimensional “polymeric” framework in which K atoms are embedded. Carbonate groups are made of two bridging O and a third one doubly bonded to C, which therefore has a shorter bond length with C atom. The asymmetry of carbonate groups could induce a polarization, even if it must remain of small amplitude. Another fact is the presence of asymmetric electronic density around Cu. In fact, electron density is much higher

on top of the square plane than at the bottom<sup>209</sup>. This could also result in an enhanced polarizability.

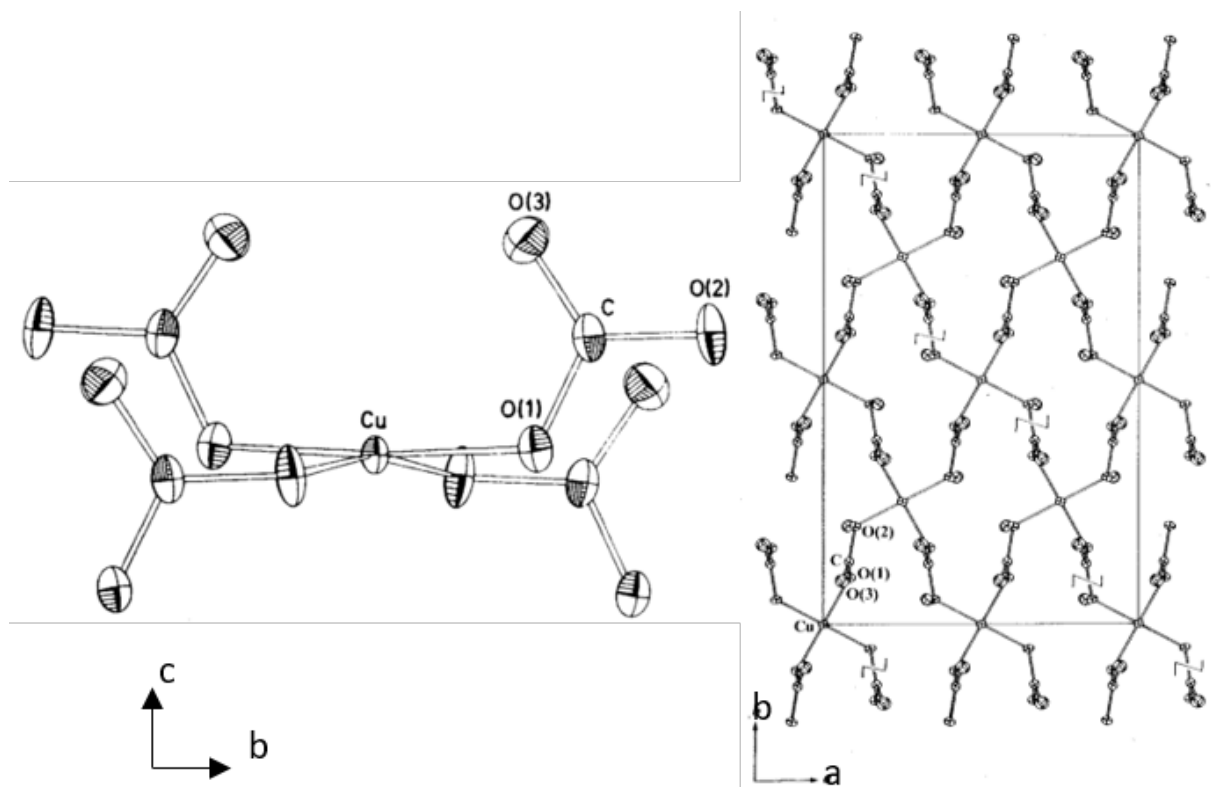


Figure 102: ORTEP drawing of  $K_2Cu(CO_3)_2$  structure along  $a$  axis showing Cu environment. Ellipsoids represent 30 % probability level

ferromagnetic interactions are present in this phase below 6.6 K, and this could be due to the nearly  $90^\circ$  angle between Cu square planes and carbonate groups.

### 2.4.1.2 $\text{Na}_2\text{Cu}(\text{CO}_3)_2$

Whereas very close in composition,  $\text{Na}_2\text{Cu}(\text{CO}_3)_2$  crystallizes in a different space group than  $\text{K}_2\text{Cu}(\text{CO}_3)_2$ , probably due to the smaller ionic radius of  $\text{Na}^+$  (XXX) as compared to that of  $\text{K}^+$  (XXX). It is of lower symmetry and crystallizes in a monoclinic space group  $P2_1/a$ <sup>213</sup>.

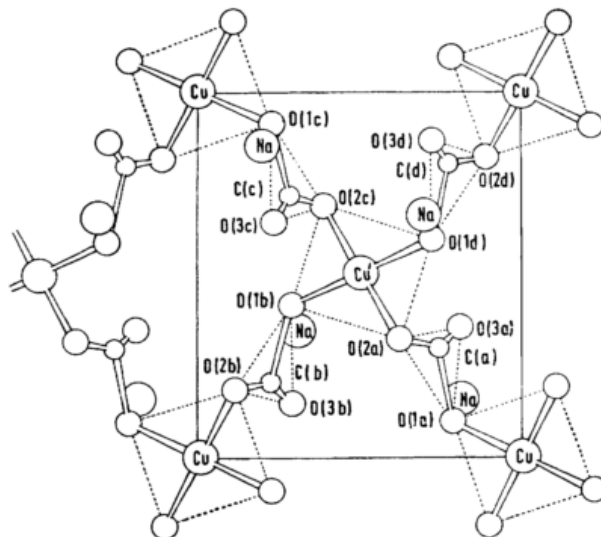


Figure 103: Representation of  $\text{Na}_2\text{Cu}(\text{CO}_3)_2$  structure viewed along the (001) axis

This structure consists, as in the previous case, of square planar  $[\text{CuO}_4]$  groups surrounded by carbonate groups. Whereas the  $[\text{CuO}_4]$  are not coplanar with carbonate groups, their arrangement consists of a bi-dimensional network in the  $ab$  plane, forming layers which are separated by Na atoms. This phase possesses complex magnetic arrangement<sup>210,214,216</sup> with the presence of intralayer ferromagnetic interactions and interlayer weak antiferromagnetic interactions. Moreover, this weak antiferromagnetism is highly affected by external magnetic field and a spin flop transition is observed above  $0.1 \text{ T}$ <sup>210</sup>.

## 2.4.2 Synthesis

### 2.4.2.1 $\text{K}_2\text{Cu}(\text{CO}_3)_2$

Synthesis information in the literature is one and a half century old. Deville<sup>217</sup> got interested in mixing metallic carbonates with alkaline carbonates in 1856, and this seems to be the first reference of  $\text{K}_2\text{Cu}(\text{CO}_3)_2$  synthesis. His work was taken over by Reynolds in 1898<sup>218</sup>, then by

Pickering<sup>219</sup> in 1911 and Applebey<sup>220</sup> in 1918. Since then, all the paper refer to the synthesis presented in these four first works.

According to these papers, the synthesis is performed in aqueous media and consists in the coprecipitation of two salts: potassium carbonate  $K_2CO_3$  and copper acetate  $Cu(CH_3COO)_2$ . A saturated solution of  $K_2CO_3$  is prepared, then copper acetate is added to the solution in adequate proportions. The key points here are both to have a good stoichiometry (*“the amount of cupric acetate solution to be added is found by trial; if too much is added, precipitation of basic carbonate occurs; if too little, there is no crystallization”*<sup>220</sup>), and second to have the density of the  $K_2CO_3$  saturated solution in the right range, so as to obtain the desired compound. In fact, in 1911, Pickering describes all the possible compounds that can be obtained depending on these synthesis parameters<sup>219</sup>. Later on, Reynolds<sup>218</sup> did propose an alternative synthesis route through grinding both the powder of copper acetate and the saturated solution of  $K_2CO_3$  in a mortar, and then to filter it to isolate the liquid part from the solid part. He apparently did manage to obtain small crystals mixed in a large quantity of  $K_2CO_3$  crystals. It was then possible to manually isolate crystals of  $K_2Cu(CO_3)_2$  thanks to their dark blue color. Unfortunately, this method is not adapted to the preparation of powder dedicated to sintering experiment and we finally developed another way to quickly obtain large quantities of powders with high purity.

Based on Reynold's method, we prepared mix saturated solution of different specific gravities (i.e. density) with  $K_2CO_3$  in different stoichiometries. After filtering the liquid part of this mix, it was let to evaporate for a couple of weeks. The color evolution from light to intense dark blue was easily visible, and after the water was almost completely evaporated and the powder looked dried, it was laid on a filter paper to absorb the residual  $K_2CO_3$  saturated solution. When no filter paper is used,  $K_2CO_3$  is in a large excess and is the major phase visible on XRD. Since it is also highly hygroscopic, it absorbs water and turns back to a viscous state in a few hours, forbidding further manipulation. After letting the powder overnight on a filter paper, it seems the  $K_2CO_3$  solution (or the product of  $K_2CO_3$  crystals hydration) is drained in the paper, whereas the target  $K_2Cu(CO_3)_2$  remains pure and dry on top. The remaining drawback is the evaporating time it takes to obtain the target phase. Yet, even if takes time to be completed, we did not get any clue of a possible limitation on the synthesized quantities. We did produce few grams (around 3-4 g) in a single batch, and it seems that upscaling must be possible.

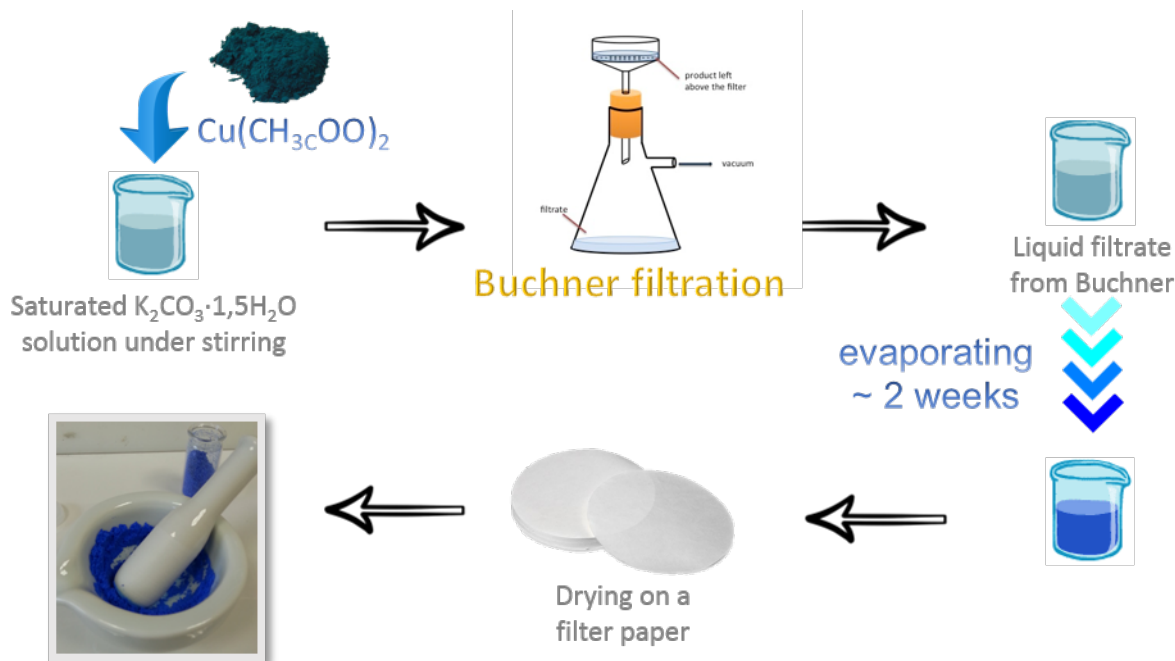


Figure 104: Schematic representation of the synthesis process of  $K_2Cu(CO_3)_2$  powder

After the synthesis was successfully achieved, the characterization of dried powder could be done before sintering.

#### 2.4.2.2 $Na_2Cu(CO_3)_2 \cdot 3H_2O$

Na containing compound has been also described in the aforementioned literature<sup>217–220</sup>. However, its synthesis is slightly different from the previous K containing compound, since it is a two-step synthesis passing by an intermediate hydrated phase  $Na_2Cu(CO_3)_2 \cdot 3H_2O$ <sup>220</sup>.

Synthesis of this phase was also described in the aforementioned works of Deville<sup>221</sup> and Applebey<sup>220</sup>. The reaction principles are the same as in the case of K containing compound, aiming to have alkaline carbonate reacting with copper acetate, but the experimental process is slightly different. Moreover, a big difference is here that synthesis leads to the formation of a tri-hydrated compound:  $Na_2Cu(CO_3)_2 \cdot 3H_2O$ . This one has to be “*digested for 24 h in saturated boiling aqueous sodium carbonate-bicarbonate solution, giving rise to small elongated royal blue insoluble single crystals of the anhydrous salt of maximum size 0.10 x 0.06 mm. They are contaminated with an insoluble white substance but their high density enabled rapid physical separation.*”<sup>213</sup> The intermediate hydrated phase is a mineral named chalconatronite that is also formed during corrosion of copper, and has attracted attention because of its widespread

occurrence in museums and industrial installations<sup>215</sup>, and is also ferromagnetic below 2.5 K<sup>215</sup>. Following the synthesis proposed by this method does not allow the production of a sufficient quantity of powder (obtained from grinded crystals) to perform multiple SPS experiments (each SPS experiment requires about 300 mg of powder for 10 x 1 mm cylindrical pellets).

The first objective has been to obtain large quantities of hydrated  $\text{Na}_2\text{Cu}(\text{CO}_3)_2 \cdot 3\text{H}_2\text{O}$  phase. This has been performed by slightly modifying methods proposed by Applebey and Deville (see Figure 105). In the present case, a solution of copper acetate is added to a saturated solution of  $\text{Na}_2\text{CO}_3$ , without any stirring. After few hours, homogenization of the solution occurs and it turns to a deep blue color. About a week after, the solution becomes lighter and contains solid part. A Buchner system is used to filtrate the solution. The solid part is retained and further water removed using filter paper. After 24h on the filter, small crystals of few hundreds of micro meters are obtained.

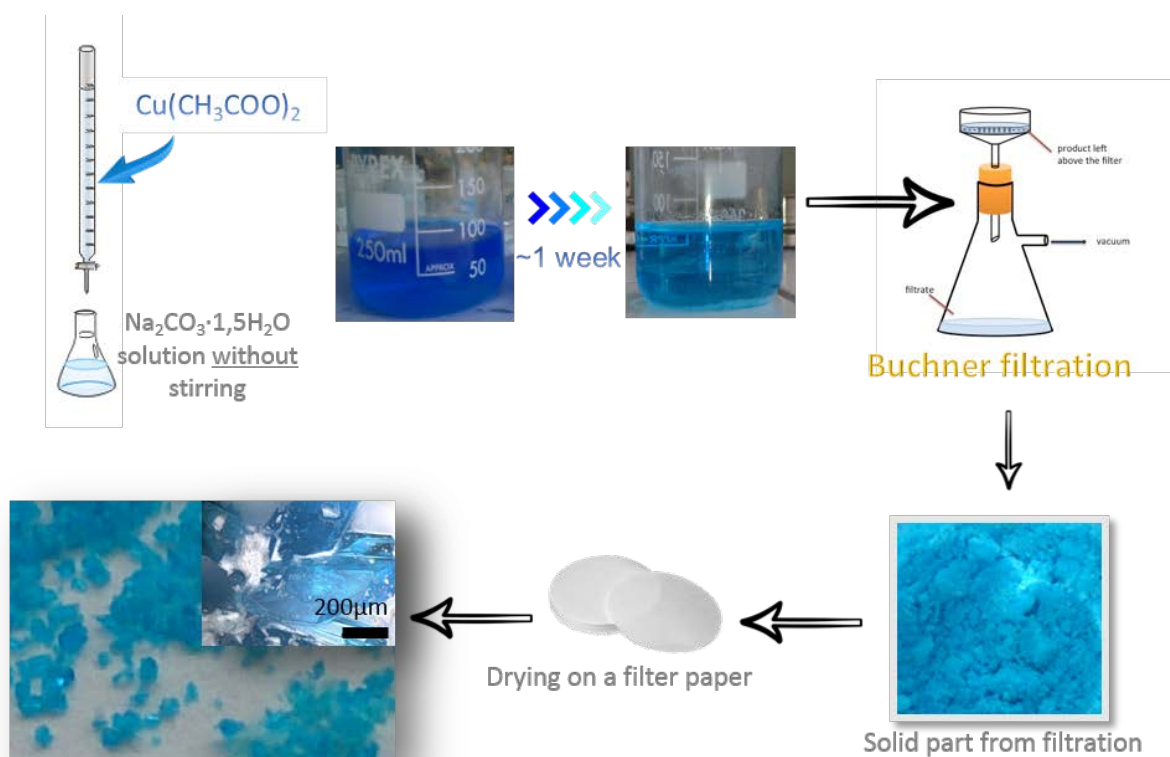


Figure 105: Schematic representation of the synthesis of  $\text{Na}_2\text{Cu}(\text{CO}_3)_2 \cdot 3\text{H}_2\text{O}$

In this synthesis process, the solid part is used to obtain the final  $\text{Na}_2\text{Cu}(\text{CO}_3)_2 \cdot 3\text{H}_2\text{O}$  crystals. However, the liquid part can be reused to perform new synthesis, just by adding new copper

acetate solution and do the same cycle again. In this process, the synthesis takes some time too, and here also, the quantities can be large. In the last experiments, quantities up to more than 5 g of powder have been obtained.

The second objective during this synthesis has been to obtain the anhydrous phase from the hydrated phase. Previous papers report, as described previously, a liquid synthesis route to get  $\text{Na}_2\text{Cu}(\text{CO}_3)_2$  from  $\text{Na}_2\text{Cu}(\text{CO}_3)_2 \cdot 3\text{H}_2\text{O}$ . However, they also report the necessity to manually extract small crystals of the desired composition among white phase forming at the same time. This step can take a lot of time and in the present work, high quantities of powders are necessary. According to that, attempts have been made to dehydrate the synthesized powder using heat treatment. To do so, TGA measurement has previously been performed on the powder to determine the temperature range in which dehydration should be performed.

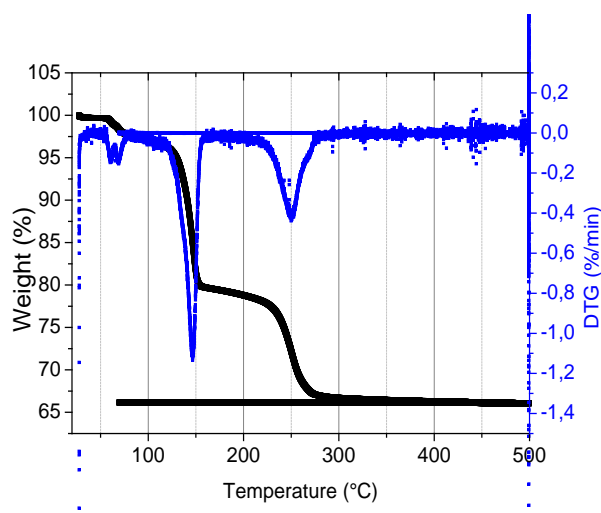


Figure 106: TGA measurement performed on  $\text{Na}_2\text{Cu}(\text{CO}_3)_2 \cdot 3\text{H}_2\text{O}$  under air

From TGA measurement under air presented on Figure 106, three mass losses are observed on the sample. The first occurs between 50 and 70 °C and corresponds to a mass loss of 3 %wt. This has been attributed to physisorbed water remaining in the powder. The presence of this water in the powder is expected since drying is only performed on a filter paper. Following mass loss occurs between 120 and 160 °C, corresponding to additional 18 %wt. According to the stoichiometry of the phase,  $\text{Na}_2\text{Cu}(\text{CO}_3)_2 \cdot 3\text{H}_2\text{O}$ , the water mass should exactly be 18 %wt. Therefore, it appears that firing the powder above this temperature must lead to the pure anhydrous phase. The last mass loss occurs between 220 and 275 °C and loss of 13 %wt. This is attributed to the decomposition of the phase, and XRD measurement on the powder after

TGA measurement confirms the absence of copper carbonate phase. It is composed of both  $\text{Na}_2\text{CO}_3$  and  $\text{CuO}$ , and thus the decomposition process is probably the following:

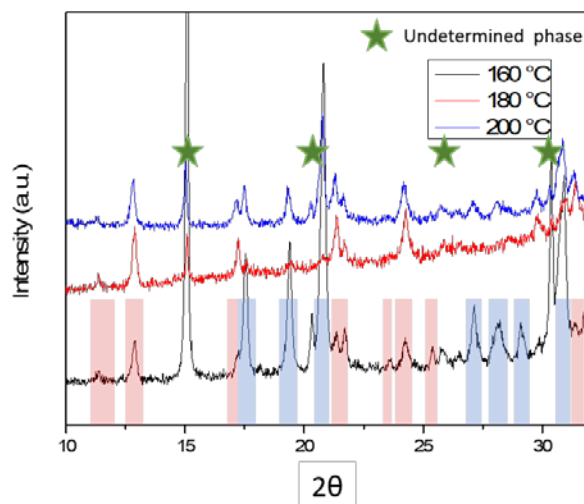


Figure 107: XRD patterns of powders of  $\text{Na}_2\text{Cu}(\text{CO}_3)_2 \cdot 3\text{H}_2\text{O}$  composition fired at various temperatures from 160 to 200 °C. Red parts represent the anhydrous phase peak positions and blue part represents the hydrated phase peak positions

Various firing temperature have been applied to hydrated powders from 160 to 200 °C (see Figure 107). The observation of XRD patterns of the various samples show that it seems impossible to totally remove the hydrated phase, and the crystallization of the anhydrous phase is accompanied by the appearance of another phase, marked with green stars on the figure, that fits with a  $\text{NaOH} \cdot \text{H}_2\text{O}$  phase. It is surprising to observe the presence of such phase without other Cu containing phase, but the high noise level which increases above 30 ° is a clue of the presence of an important part of amorphous phase. The conclusion of these attempts is that it looks impossible to isolate the pure anhydrous phase by thermal treatment, which is consistent with the fact that all previous work on that phase refer to the liquid synthesis route discussed previously. In the following part, we will focus on the hydrated phase and use it for sintering, aiming to operate *in-situ* dehydration.

## 2.4.3 Powder characterization

Once both potassium and sodium containing compositions have been synthesized, small crystals are obtained and can be crushed to be characterized. In the present part are presented the characterizations performed on both powders

### 2.4.3.1 Structural characterization (XRD)

Refined powder XRD pattern of crushed crystals is displayed on Figure 108 for the two carbonates. Both these refinements confirm the phase purity of the obtained powder. In the case of  $\text{Na}_2\text{Cu}(\text{CO}_3)_2 \cdot 3\text{H}_2\text{O}$ , the refinement has been performed with introducing Al as a second phase, which is a contribution from the XRD sample holder. These two refinements confirm the effectiveness of synthesis routes developed for both powders.

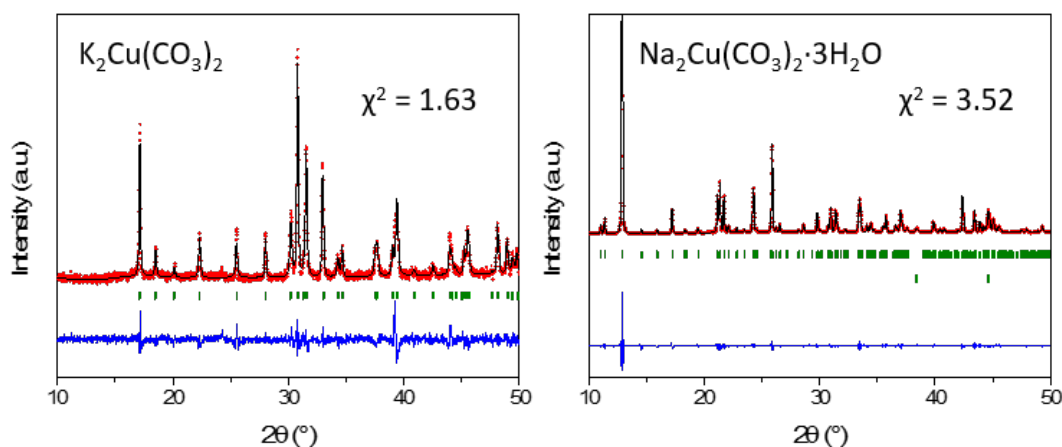


Figure 108: Refined powder XRD patterns of  $\text{K}_2\text{Cu}(\text{CO}_3)_2$  and  $\text{Na}_2\text{Cu}(\text{CO}_3)_2 \cdot 3\text{H}_2\text{O}$ . In the case  $\text{Na}_2\text{Cu}(\text{CO}_3)_2 \cdot 3\text{H}_2\text{O}$ , the Al sample holder has been included in the refinement

Lattice parameters have been extracted from refinements and are summarized in Table 4.

Comparison of lattice parameters for both anhydrous  $\text{K}_2\text{Cu}(\text{CO}_3)_2$  and hydrated  $\text{Na}_2\text{Cu}(\text{CO}_3)_2 \cdot 3\text{H}_2\text{O}$  with literature values show a very good match. Thus these refinements confirm the quality of the powders, their phase purity and good crystallization. Added to the absence of additional phases, this makes the two phases very pure. In the case of  $\text{Na}_2\text{Cu}(\text{CO}_3)_2 \cdot 3\text{H}_2\text{O}$ , an important misfit between experimental and simulated diffraction patterns is observed for (002) peak. This must result from crystallites anisotropy, but does not affect the global crystallization of the phase.

Table 11: Refined and literature values of lattice parameters for both carbonates  $K_2Cu(CO_3)_2$  and hydrated  $Na_2Cu(CO_3)_2 \cdot 3H_2O$

| Sample  | a (Å)      | b (Å)      | c (Å)      | $\beta$ (Å) |
|---|------------|------------|------------|-------------|
| <b><math>K_2Cu(CO_3)_2</math><br/>Powder (<i>Fdd2</i>)</b>                            | 11.4215(3) | 17.6555(5) | 6.1502(2)  | 90          |
| $K_2Cu(CO_3)_2$<br>Literature ( <i>Fdd2</i> ) <sup>208</sup>                          | 11.425(3)  | 17.658(4)  | 6.154(2)   | 90          |
| <b><math>Na_2Cu(CO_3)_2 \cdot 3H_2O</math><br/>powder (<i>P2<sub>1</sub>/n</i>)</b>   | 9.6933(1)  | 6.0953(1)  | 13.7895(1) | 91.915(1)   |
| $Na_2Cu(CO_3)_2 \cdot 3H_2O$<br>literature ( <i>P2<sub>1</sub>/n</i> ) <sup>222</sup> | 9.696(2)   | 6.101(2)   | 13.779(3)  | 91.83(2)    |

#### 2.4.3.2 Thermal analysis (TGA)

TGA analysis has already been presented for the hydrated sodium compound since it was a key characterization for the synthesis. We will now focus on  $K_2Cu(CO_3)_2$  thermal analysis through TGA coupled to a mass spectrometer (Figure 109).

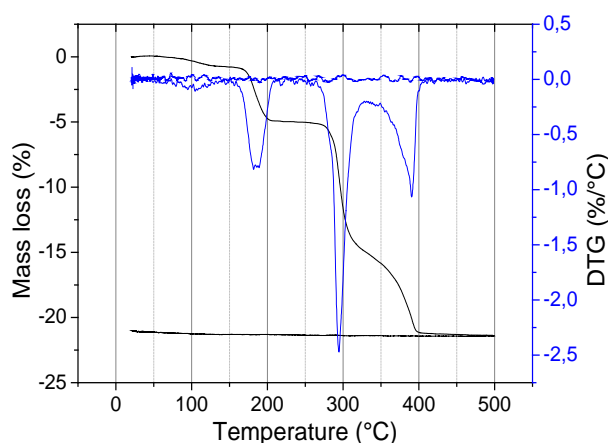


Figure 109: TGA analysis performed on  $K_2Cu(CO_3)_2$  powder under air

TGA measurement (Figure 109) shows three mass losses. The first one occurs between 160 and 210 °C and is represents 5 % wt. loss. This first loss is attributed to dehydration of the phase which must contain remaining water from synthesis, since the phase is dried on a simple filter paper. Decomposition occurs in two steps visible through the two mass losses ranging from 270 to 320 °C and from 350 to 400 °C after which the mass loss reached 22 %. Decomposition temperature is determined as 270 °C under air for this phase, according to TGA measurement.

### 2.4.3.3 Magnetic measurement (SQUID)

Magnetic measurement has been performed on synthesized  $\text{K}_2\text{Cu}(\text{CO}_3)_2$  powder to compare them with information available in literature. The inverse magnetic susceptibility is plotted on Figure 110 and is typical of a ferromagnetic transition. Curie temperature  $T_C = 6.6$  K such as reported<sup>208</sup> and Weiss temperature  $\theta = 13$  K confirms the existence of ferromagnetic interactions in the phase. These results are in good agreement with previously reported results and confirm the phase purity of potassium copper carbonate. Unfortunately, magnetic measurement of  $\text{Na}_2\text{Cu}(\text{CO}_3)_2 \cdot 3\text{H}_2\text{O}$  could not be performed before the redaction of this manuscript, due to the limited availability of the measurement setup, and therefore will not be reported here.

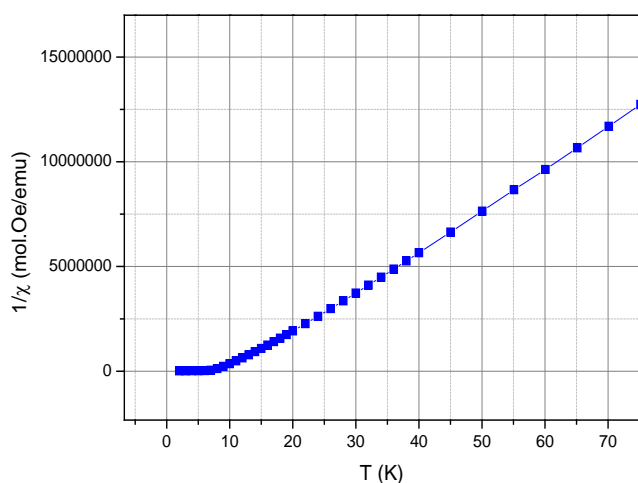


Figure 110: ZFC measurement of  $\text{K}_2\text{Cu}(\text{CO}_3)_2$  powder under 1 kOe performed in SQUID

Since both synthesis lead to pure powders, it looks interesting try sintering experiments. In this case however, one of the phase is a hydrated phase which crystallizes in a different space group than the targeted phase. It is therefore interesting to see both the influence of water during sintering, but also to see the influence of SPS environment on dehydration.

### 2.4.4 Sintering

Both powders, after synthesis, gave small crystals. In order to obtain a good density after sintering, but also to have a better powder to powder contact, but also to operate in reproducible

conditions, it is necessary to crush these crystals. This has been performed through vibrating milling in an agate mortar for 45 min for both compositions. Then, the obtained powders could be used for sintering

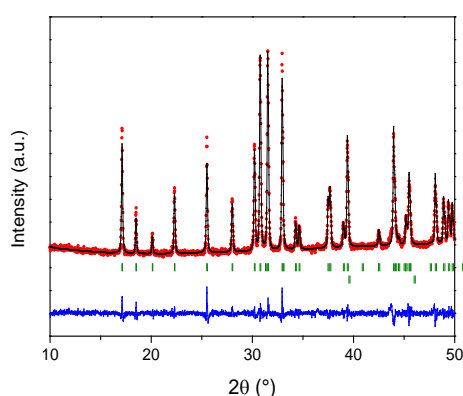
#### 2.4.4.1 Sintering conditions and pellet characterization

Various sintering conditions have been tested for both powders. The most interesting are listed in Table 5. As it can be seen, both compositions gave rise to dense pellets that could be measured geometrically. However, before any comment on these results can be made, it is important to confirm both phase purity and to observe microstructures.

Table 12: Sintering conditions and relative densities of  $K_2Cu(CO_3)_2$  and  $Na_2Cu(CO_3)_2$  pellets

| Sample | Sintering temperature (°C) | Sintering pressure (MPa) | Dwell time (min) | Relative density (%) |
|--------|----------------------------|--------------------------|------------------|----------------------|
| K #1   | 300                        |                          |                  | 94.1                 |
| K #2   | 350                        | 600                      | 10               | 95.6                 |
| Na #1  | 200                        |                          |                  | 96.8                 |
| Na #2  | 250                        | 600                      | 10               | 97.4                 |
| Na #3  | 300                        |                          |                  | 97.7                 |

##### 2.4.4.1.1 $K_2Cu(CO_3)_2$



|       | pellet     | powder     |
|-------|------------|------------|
| a (Å) | 11,4238(2) | 11.4215(3) |
| b (Å) | 17,6519(2) | 17.6555(5) |
| c (Å) | 6,1526(1)  | 6.1502(2)  |

Figure 111: Refined XRD pattern of  $K_2Cu(CO_3)_2$  pellet associated with refined lattice parameters

Refinement has been performed on XRD pattern of a pellet sintered at 350 °C and refined parameters compared with previously presented powders values Figure 111.

According to XRD data, there is a very good preservation of phase purity and crystallization of  $K_2Cu(CO_3)_2$  sample, even after sintering at 350 °C. Microstructure has also been observed on a fracture in SEM and is presented for the same pellet on Figure 112. The absence of visible porosity, and the highly dense microstructure observed in these pictures confirm the high density measured geometrically (above 94 %) on the pellet and presented in Table 5.

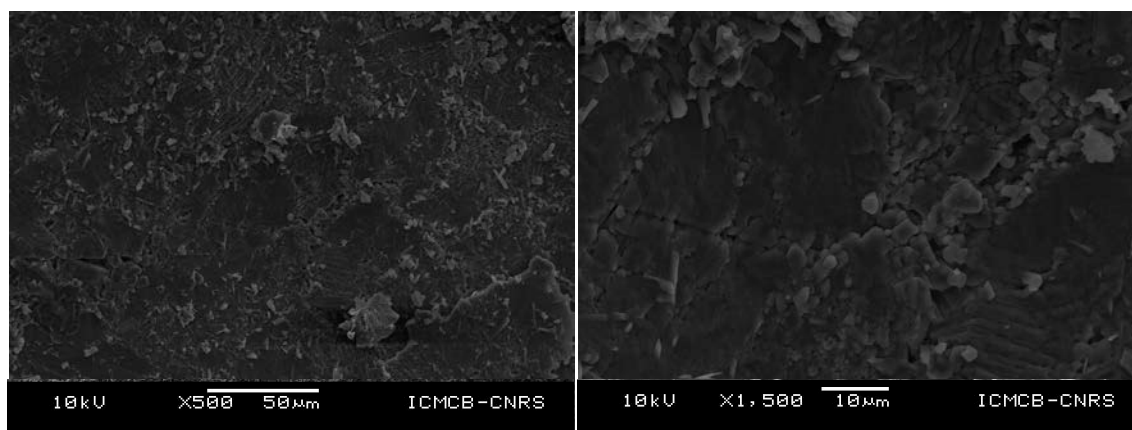


*Figure 112: Fractured pellet observation of  $K_2Cu(CO_3)_2$  sintered at 350 °C*

According to those results (XRD refinement, SEM observations and density measurements), it can be concluded that  $K_2Cu(CO_3)_2$  has been highly densified (>94 %) at very low temperature (down to 300 °C) and short time (10 min). The influence of pressure, vacuum and electric current must be somehow involved in this densification, but also in the stabilization of the phase. As observed previously for  $NH_4FeP_2O_7$ , sintering temperatures applied here are notably above the decomposition temperature of the phase (270 °C according to TGA under air). This example not only confirms the high sintering efficiency of SPS under high pressure at low temperature for a second material family (phosphates and now carbonates), but also confirms the previously observed stabilization effect of the phase in SPS conditions. Confirmation of these two effects in the following will be investigated through the example of the hydrated  $Na_2Cu(CO_3)_2 \cdot 3H_2O$ .

#### 2.4.4.1.2 $Na_2Cu(CO_3)_2 \cdot 3H_2O$

In the case of  $Na_2Cu(CO_3)_2 \cdot 3H_2O$ , the behavior is different. In the present case, the objective is to obtain the anhydrous phase during SPS treatment, while the starting powder is a hydrated phase.

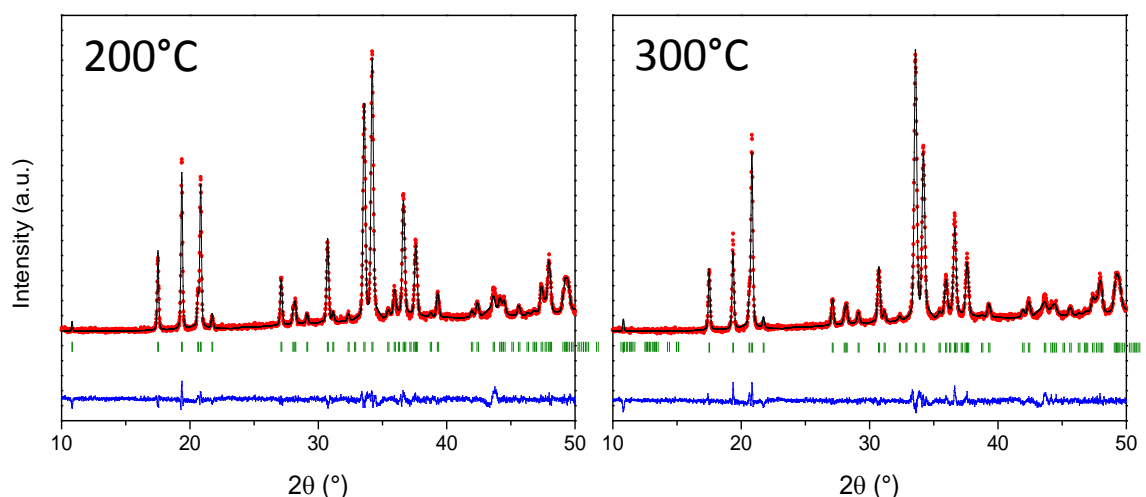


Figure 113: Refined XRD patterns of  $\text{Na}_2\text{Cu}(\text{CO}_3)_2$  pellets sintered at 200 °C and 300 °C in space group  $P2_1/a$  corresponding to an anhydrous phase

As displayed on Figure 113, refinements in space group  $P2_1/a$  which correspond to the anhydrous phase  $\text{Na}_2\text{Cu}(\text{CO}_3)_2$  exhibits a very good fit with experimental data. The only noticeable difference between both pellets is the intensity ratios (around 20 and 34° for example), probably due to some grain growth in the pellet sintered at 300 °C. The total absence of hydrated phase confirms the efficiency of *in-situ* phase transition for both samples. Moreover, the absence of secondary phase is surprising for two reasons:

- Heat treatment performed under air between 160 and 200 °C lead to the appearance of a secondary phase (probably  $\text{NaOH}\cdot\text{H}_2\text{O}$ )
- Decomposition in  $\text{NaCO}_3$  and  $\text{CuO}$  under air occurs at 220 °C

In the present cases, both samples consist of pure anhydrous phase without apparent decomposition or secondary phase. Nonetheless, while treatment under air up to 200 °C were unable to totally remove hydrated phase, the present samples, even sintered in the same temperature condition of 200 °C, shows no trace of remaining  $\text{Na}_2\text{Cu}(\text{CO}_3)_2\cdot 3\text{H}_2\text{O}$ . The total absence of water in the sample has been confirmed by TGA measurement under air on the pellet sintered at 200 °C (Figure 114) which shows a single mass loss from 220 to 300 °C, corresponding to decomposition of the phase observed. Mass losses associated to water release at lower temperatures are absent.

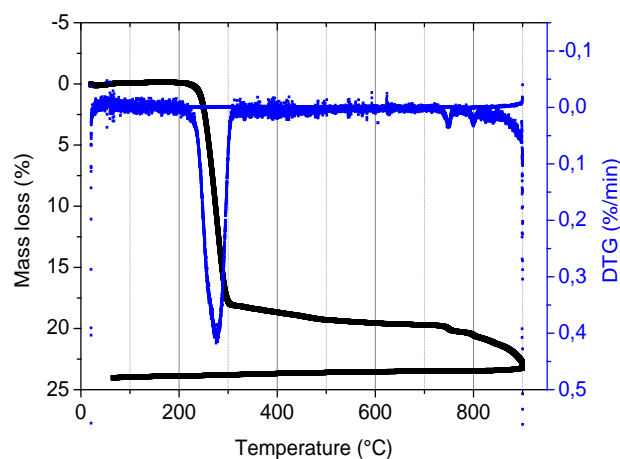


Figure 114: TGA performed on pellet sintered at 200 °C under air

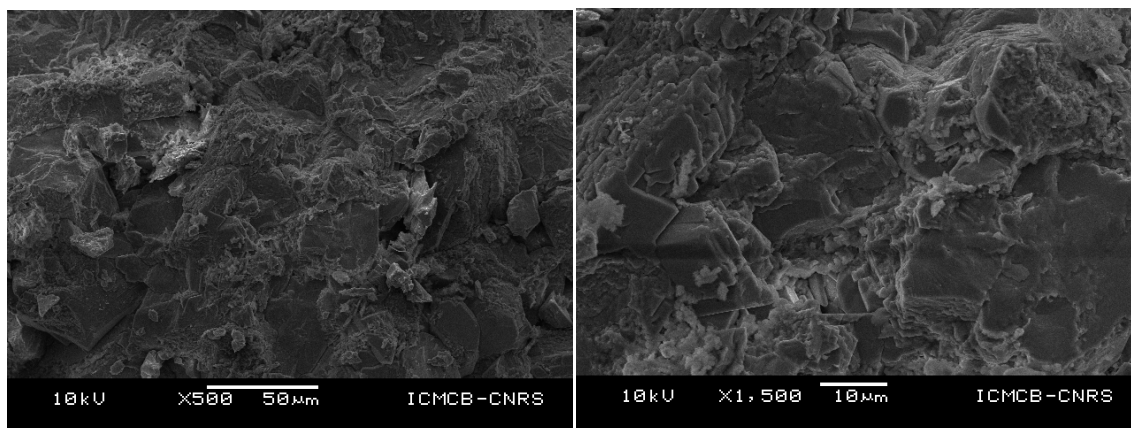
In order to confirm the phase purity, refined lattice parameters are presented in Table 6 and compared to literature values.

Table 13: Refined lattice parameters of pellets sintered at 200 and 300 °C compared to the literature values for single crystal

| Sample   | a (Å)     | b (Å)     | c (Å)     | $\beta$ (Å) |
|--|-----------|-----------|-----------|-------------|
| Na #1 – 200 °C                                       | 6.1728(1) | 8.1778(3) | 5.6478(1) | 116.242(1)  |
| Na #3 – 300 °C                                       | 6.1739(1) | 8.1779(2) | 5.6482(1) | 116.260(1)  |
| $\text{Na}_2\text{Cu}(\text{CO}_3)_2$ <sup>213</sup> | 6.18(2)   | 8.19(2)   | 5.64(2)   | 116.2(2)    |

Both pellets present similar lattice parameters which correspond to the expected values for this anhydrous phase. According to these results, the phase appears pure and can be considered as totally dehydrated. The calculated densities presented in Table 5 have been calculated considering the density of pure  $\text{Na}_2\text{Cu}(\text{CO}_3)_2$ .

These densities are above 96 % and even reach 97.7 % for the sample sintered at 300 °C. This is extremely high for the low temperatures applied during sintering (200 to 300 °C) and the short dwell times used (10 min). SEM observations are displayed on Figure 115 and were taken on fractured pellet sintered at 300 °C.



*Figure 115: SEM picture of fractured pellet sintered at 300 °C*

The high densities measured geometrically seem in good agreement with the very dense microstructure observed in SEM. The microstructure appears homogenous on large scales of few  $\mu\text{m}$ .

As observed for the previous examples, highly densified pellets (from 96.8 to 97.7 %) have been obtained at low temperatures (down to 200 °C) of a carbonate phase. Moreover, we observe here again a phase stabilization beyond the decomposition temperature (220 °C) compared to applied sintering temperature up to 300 °C without visible decomposition. This is the third observation of stabilization of phase in SPS conditions under high pressure. This confirms the previous observations and also confirms the possibility to extend SPS to other materials families. However, some particularity in the present case differs from the previous examples and will be discussed.

#### 2.4.4.2 In-situ dehydration of $\text{Na}_2\text{Cu}(\text{CO}_3)_2 \cdot 3\text{H}_2\text{O}$ into $\text{Na}_2\text{Cu}(\text{CO}_3)_2$

As observed previously, transitions from hydrated to anhydrous form has been observed during SPS treatment. SPS chamber pressure has been recorded during sintering process and is presented on Figure 116. On this same figure is associated the data registered during TGA measurement performed on the powder under air and already presented in Figure 106. As it can be seen on this plot, a massive pressure increase takes place from 70 to 130 °C followed by a slow decrease up to 160 °C. This is likely associated to water release during heating. In parallel, TGA under air shows a water release up to 160 °C but with a maximum that's shifted to higher temperatures. It is then possible to follow dehydration in situ and determine the dehydration

temperature of the phase. It is also noticeable that the water release occurs at lower temperature in SPS conditions than during TGA. This must result from both the application of high pressure (600 MPa) on the powder and the low pressure in the chamber (here from 10 to ~140 Pa) . While it was impossible to obtain the pure anhydrous form with thermal treatment in air, SPS treatments, from 200 to 300 °C, were efficient in realizing this dehydration. This observation, associated with the previous observations on phase stabilization, point out the different phase behavior of materials in SPS conditions as compared to atmospheric conditions. It also means there are possibilities to reach or stabilize phases that may not be obtained in other conditions. This is a remarkable confirmation of the hypothesis that SPS can be used for prospection, by allowing for the sintering of fragile phases, and by stabilizing inaccessible or new ones.

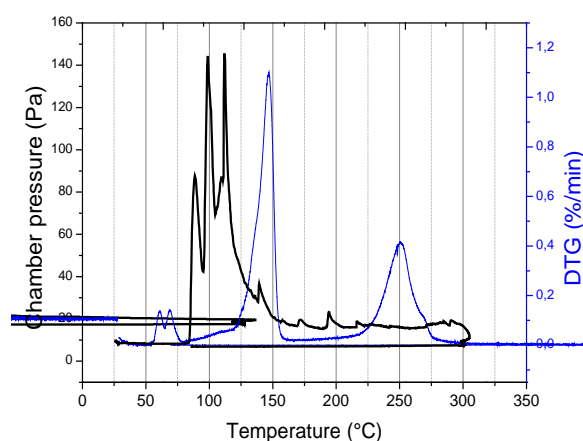


*Figure 116: Chamber pressure versus temperature during sintering at 300 °C associated to DTG measurement of initial powder of hydrate phase*

It has been shown the possibility to follow the dehydration step through chamber pressure in SPS, but it can also be used to determine decomposition temperature of a phase since this is often associated to gas release. In the present case, while DTG shows a peak from 220 to 280 °C, no significant pressure increase is observed in SPS chamber pressure that would be a clue of phase decomposition, even at 300 °C. This is consistent with lattice parameters preservation determined after sintering.

#### 2.4.5 Physical properties

Densification results of both carbonate phases are very good and allow bulk physical properties measurements. This way, magnetic and dielectric measurements have been performed on both samples.

### 2.4.5.1 Magnetic measurements

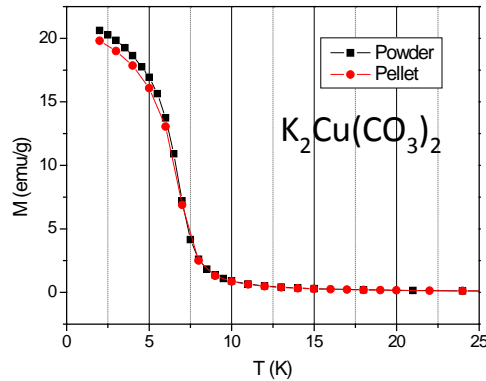


Figure 117: SQUID measurement of  $K_2Cu(CO_3)_2$  pellet under 1 kOe

Figure 117 displays zero field cool measurement of powder and pellet sintered in SPS at 300 °C. Both measurements show a ferromagnetic transition at 6 K as described in literature<sup>208</sup>. Moreover, their mass magnetization are almost the same with 19.8 emu/g for pellet and 20.3 emu/g for powder, which makes for a 2 % difference. This confirms the high phase quality after SPS, during which there was no alteration of the sample's magnetic property, and thus no material decomposition as well.

### 2.4.5.2 Dielectric and magnetocapacitance measurements

#### 2.4.5.2.1 $K_2Cu(CO_3)_2$

Capacitance and dielectric losses have been also measured on a pellet sintered at 300 °C and are displayed on Figure 118. Capacitance decreases from 100 to 2 K with a small slope around 22 K, accompanied by a maximum of dielectric losses. Values for this anomaly are small and difficult to interpret, but this remains present on different samples measured in the same conditions, which seems to confirm the intrinsic nature of this anomaly. It should be stressed that similar features are associated with transition to a ferroelectric state in magnetically driven ferroelectrics. However we were not able, so far, to confirm the existence of a ferroelectric phase in this material.  $C(H)$  measurement at 2 K shows no influence of magnetic field on capacitance. This confirms that the previously presented  $C(H)$  measurement on  $NH_4FeP_2O_7$

exhibits a small diminution of capacitance between 4 and 6 T, which is therefore above noise level.

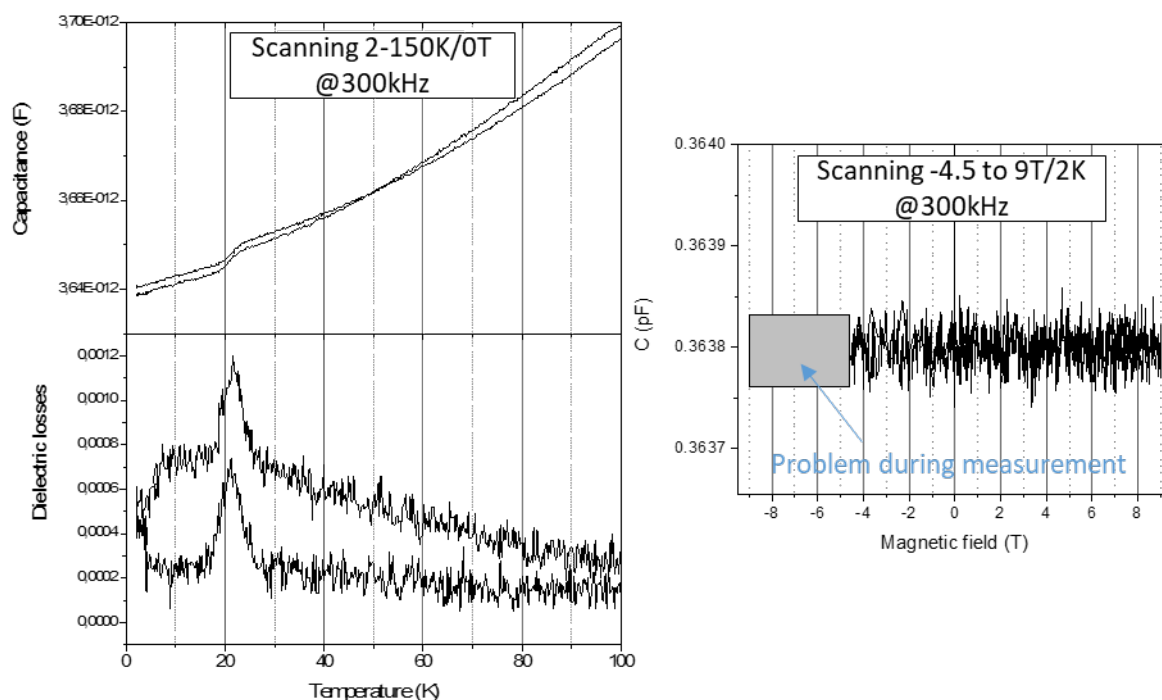


Figure 118: PPMS measurement of capacitance and dielectric losses versus temperature of  $K_2Cu(CO_3)_2$  pellet sintered in SPS

The present signal is too small to perform pyroelectric measurements. Since this carbonate is non-centrosymmetric at room-temperature, measurement of ferroelectric loops were attempted but proved inconclusive. The nature of this anomaly is still undetermined and powder neutron diffraction has been collected to characterize the ferromagnetic structure and discuss the origin of the dielectric anomaly detected in PPMS, but has not been analyzed yet.

#### 2.4.5.2.2 $\text{Na}_2\text{Cu}(\text{CO}_3)_2$

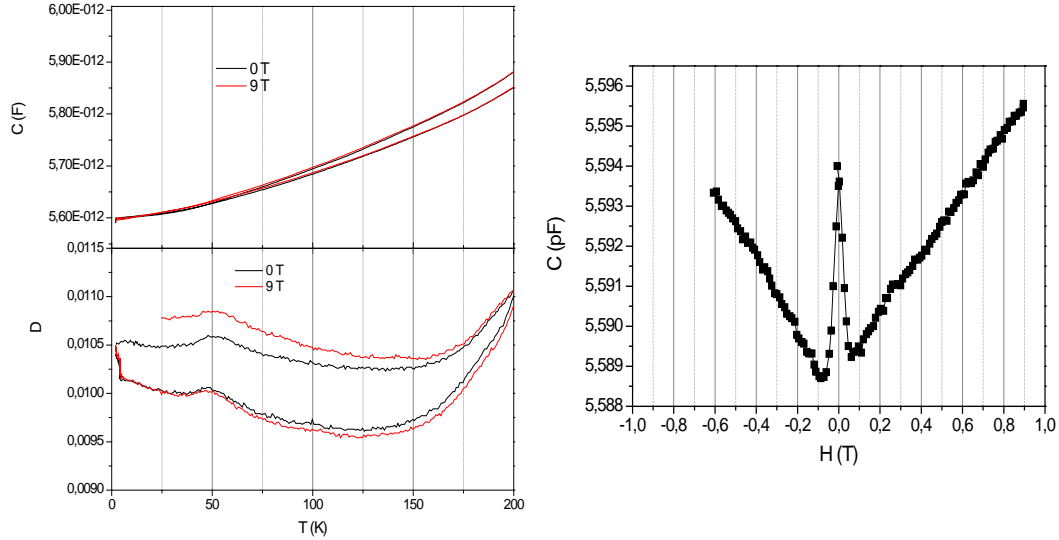


Figure 119: PPMS measurements of  $\text{Na}_2\text{Cu}(\text{CO}_3)_2$  pellet sintered in SPS

Figure 119 displays measurements performed in PPMS on a SPS sintered pellet. On the left are represented capacitance and dielectric losses versus temperature with and without magnetic field. Capacitance decreases with temperature from 200 to 2 K, and losses start to increase above 200 K. An anomaly is detected in the losses between 30 and 65 K with a small increase compared to the rest of the measurement, but no significant signal is observed on capacitance measurements. Between 0 and 9 T, the only difference concerns the beginning of the measurement when heating from 25 K to 200 K but this difference vanishes on the way back to 2 K. No conclusion can be drawn regarding that difference, that is very small in the end, and it seems the effect of magnetic field, if existent, is very weak. On the right part is displayed the magnetic dependence of capacitance at 2 K. Experimental issues with temperature control limited the reliable part of the measurement to the range -0.6 to 0.9 T. Anyway, this plot shows a first decrease of capacitance from 0 to  $\pm 0.1$  T and then an increase up to 0.6/0.9 T, and this behavior is reversible and symmetric. This evolution of capacitance occurs over a range of about 5 fF but is clearly beyond the noise level. The evolution of the capacitance with magnetic field likely corresponds to the spin flop transition that has been reported to occur below 0.1 T<sup>210,214</sup>, and could signal a magnetoelectric coupling.

In this case, such as in other similar systems, the variation of the capacitance is too small to perform further measurements considering our technical possibilities. Further high resolution diffraction measurements could be useful to follow structural evolution with application of magnetic field.

It appears difficult to fully characterize the physical properties of this phase on the basis of the present results. Anyway, such as for the other samples, promising results have been obtained and point out a possible magnetoelectric coupling in  $\text{Na}_2\text{Cu}(\text{CO}_3)_2$ .

#### 2.4.6 Conclusion on carbonates

Both carbonate phases  $\text{K}_2\text{Cu}(\text{CO}_3)_2$  and  $\text{Na}_2\text{Cu}(\text{CO}_3)_2 \cdot 3\text{H}_2\text{O}$  have been successfully synthesized through the development of existing synthesis protocols. In both cases, it was possible to achieve large scale production of powder (according to usual lab scale production). XRD analysis confirmed the high purity of the obtained powders which were then characterized by thermal analysis and magnetic measurement was also performed on K compound which showed a ferromagnetic transition in good agreement with literature data. Thermal stability have been determined and the powders could be used for sintering in SPS. Astonishingly high densities (above 94 % for K compound and 96 % for Na compound) and remarkable phase purities were observed in both cases for sintering dwell not exceeding 10 min. Sintering temperatures applied were extremely low (down to 200 °C for Na compound and 300 °C for K compound) and no phase decomposition has been observed. Moreover, the phase stabilization observed for  $\text{NH}_4\text{FeP}_2\text{O}_7$  compound has been confirmed also in the carbonate phases, which is very promising for SPS sintering. The main information on sintering is the observation of a phase transition from a hydrated to anhydrous phase  $\text{Na}_2\text{Cu}(\text{CO}_3)_2$  with a very high purity, which couldn't be achieved in heat treatment on powder. This paves the way to new opportunities in prospective search using SPS and could lead to the stabilization of phases that are impossible to obtain or to isolate in other environmental conditions.

Finally, dielectric measurement could be performed on the highly dense ceramics. Potassium containing compound did show a small anomaly which resembles the ferroelectric transitions observed in some magnetically driven ferroelectrics. However, no further experimental data could be collected to investigate the nature of this transition. In the case of Na compound, the main observation consists in a capacitance dependence on magnetic field, which is inverted

around the spin flop transition mentioned in the literature. Even if this points out a possible magnetoelectric coupling, the amplitude remains too small to collect additional experimental data and conclude on the nature of this behavior. In both cases, further neutron diffraction measurements could highlight specific structural evolution corresponding to the observed dielectric anomalies.

After these observations, the last presented material is somehow related to  $\text{Na}_2\text{Cu}(\text{CO}_3)_2 \cdot 3\text{H}_2\text{O}$ , in the way that it relies on a hydrated precursor that must be dehydrated during SPS treatment. This situation can provide further information on sintering mechanisms involving a hydrated phase. Furthermore,  $\text{MnSO}_4$ , as a sulfate, represent another chemical family, widening the scope of phases explored in low temperature SPS sintering.

## 2.5. $\text{MnSO}_4$

$\text{MnSO}_4$  has been the first selected candidate of the present work (serendipity lead to  $\text{NH}_4\text{FeP}_2\text{O}_7$  during an exploratory study, while the carbonates were selected subsequently). Because of its composition and magnetic spiral structure<sup>205</sup>,  $\text{MnSO}_4$  is an interesting material when looking for a potentially magnetoelectric phase. Below 16 K,  $\text{MnSO}_4$  transits to an antiferromagnetic phase. At room temperature,  $\text{MnSO}_4$  crystallizes in orthorhombic  $Cmcm$  space group<sup>223</sup>. The structure is based on chains of octahedra linked by  $[\text{SO}_4]^{2-}$  tetrahedra. Below  $T_N$ , magnetic moments order in the structure and a spin frustration between the intra-chain and inter-chain interactions arises. This results in a conical spiral arrangement of spins, which may break the inversion symmetry<sup>205</sup> and induce a magnetically driven polarization.

$\text{MnSO}_4$  represents an important part in the present work, especially through sintering experiments. If a few sintering examples have been presented (and needed) for the three previous materials, much more attempts have been necessary for the sintering of  $\text{MnSO}_4$ , and opened a window on the underlying mechanisms. Therefore a particular attention will be paid to the study of  $\text{MnSO}_4$  Spark Plasma Sintering.

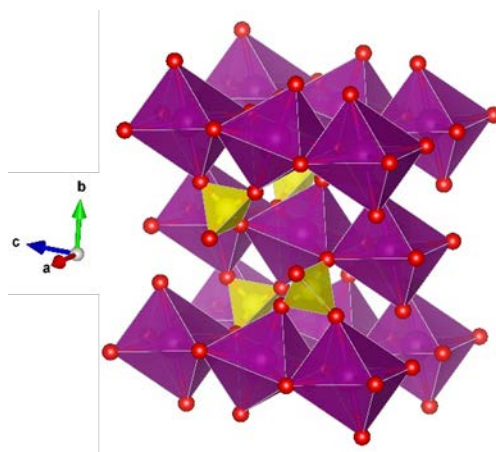


Figure 120: Representation of  $MnSO_4$  crystal structure

In the present work, commercial powder has been used. Since the anhydrous phase is not stable in ambient conditions and hydrates within few hours to days, depending on the atmosphere, most of the work was performed with hydrated powder.

### 2.5.1 Powder characterization

In this work, commercial  $MnSO_4 \cdot xH_2O$  was used as precursor. The different hydrated structures reported in the literature are<sup>224,225</sup>:

- $MnSO_4 \cdot H_2O$ : Monohydrate

A natural mineral named Szmikite, it is obtain by precipitation from saturated solutions at temperature above 24 °C (stable for  $T > 26$  °C). It can also be obtained by heat treatment around 100 °C of the heptahydrate form. It crystallizes in a monoclinic structure. This form is the one used in the present study.

- $MnSO_4 \cdot 2H_2O$ : dihydrate

This form has a very limited thermal stability domain, and could basically be considered as unstable.

- $MnSO_4 \cdot 4H_2O$ : Tetrahydrate

This form is obtained by crystallization after adding alcohol at 95 °C in a highly concentrated solution of manganese sulfate. It crystallizes in a monoclinic form which can easily be heated at 60 °C to turn to the monohydrate phase.

- $\text{MnSO}_4 \cdot 5\text{H}_2\text{O}$ : pentahydrate

This form is obtained at ambient temperature by crystallization of a saturated solution. Its thermal stability range is between +9 °C and +24 °C, and it adopts a triclinic structure

- $\text{MnSO}_4 \cdot 7\text{H}_2\text{O}$ : heptahydrate

A natural mineral called Mallardite, it is obtained by crystallization of a mix of 60 to 70 portions of  $\text{MnSO}_4$  to 100 portions of water. It has a monoclinic structure and is stable only between -10 °C and +9 °C.

In the present work two different powder were used and differ within their hydration and purity level:

- Monohydrate  $\text{MnSO}_4 \cdot \text{H}_2\text{O}$  with > 98 % purity
- Dihydrate  $\text{MnSO}_4 \cdot 2\text{H}_2\text{O}$  with > 99.99 % purity

The actual hydration level is not provided by the supplier of the second powder, and thus both precursors have been investigated by TGA measurement under air (see Figure 121).

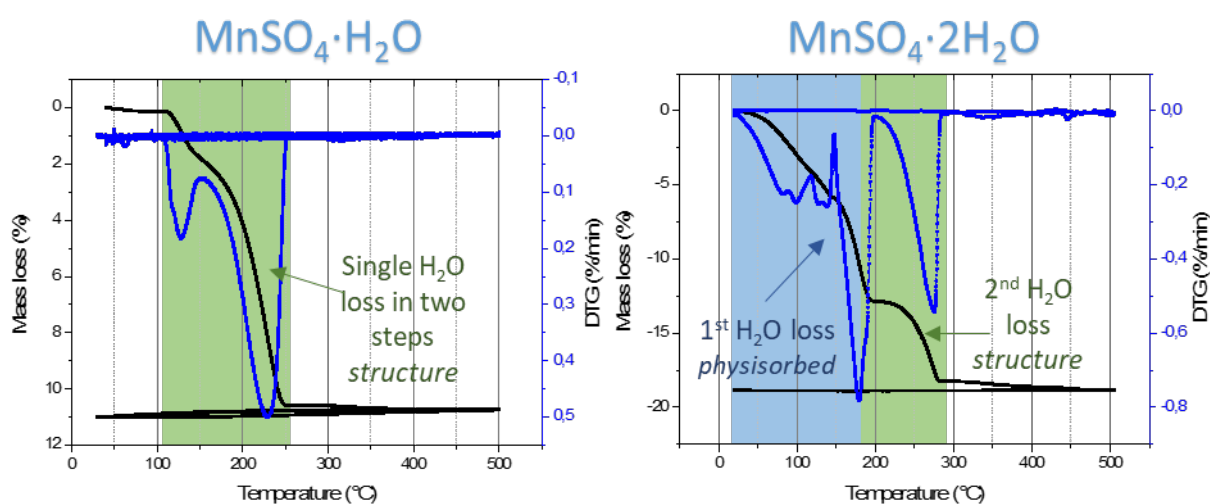


Figure 121: TGA under air of both hydrated powders. Thermal ramps are 3 °C/min and atmosphere is air

Although both powders present different water content, their structure and cell parameters are the same and correspond to  $\text{MnSO}_4 \cdot \text{H}_2\text{O}$  monohydrate structure (see Table 7).

Table 14: Refined and literature values of lattice parameters of both powders used

|  | <b>a (Å)</b> | <b>b (Å)</b> | <b>c (Å)</b> | <b>β (°)</b> |
|--|--------------|--------------|--------------|--------------|
| <b>MnSO<sub>4</sub>·H<sub>2</sub>O</b>                                     | 7.7691(1)    | 7.6464(2)    | 7.1160(2)    | 115.780(2)   |
| <b>MnSO<sub>4</sub>·2H<sub>2</sub>O</b>                                    | 7.7676(1)    | 7.6649(1)    | 7.1232(1)    | 115.846(1)   |
| <i>Literature</i><br><i>MnSO<sub>4</sub>·H<sub>2</sub>O</i> <sup>226</sup> | 7.766        | 7.666        | 7.12         | 115.85       |

*Refinements are performed in A2/a space group in both cases*

The additional water present in the dihydrated powder is considered as adsorbed water on the surfaces and weakly linked to the grains, and therefore, if the composition corresponds to a dihydrate, the structure remains monohydrate. In the following we refer to that one as dihydrate to differentiate from MnSO<sub>4</sub>·H<sub>2</sub>O. TGA measurement (Figure 121) performed on the two powders show different dehydration steps, but in both cases, water can be removed by a 300 °C heat treatment and leads to a phase transition from MnSO<sub>4</sub>·H<sub>2</sub>O (C2/c) to anhydrous MnSO<sub>4</sub> (Cmcm). Anhydrous form is not stable in ambient conditions and is rehydrated within a few days. For a few hours, it can be preserved and used in anhydrous form but must be stored in an oven so that rehydration does not occur.

The room temperature form is referred to as α-MnSO<sub>4</sub>, as it is known to exhibit a reversible phase transition around 380 °C to a high temperature form β-MnSO<sub>4</sub> crystallizing in orthorhombic space group *Pbnm*<sup>227</sup>. a) displays specific heat measurement of dehydrated powder of anhydrous MnSO<sub>4</sub> after a 300 °C firing, and shows two peaks on heating (red line) and one peak on cooling (dark line).

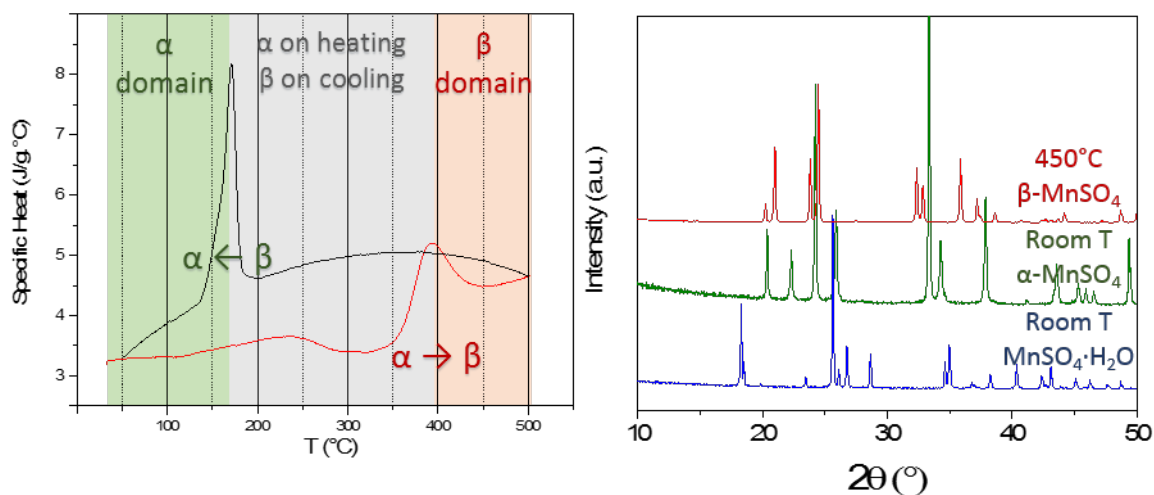
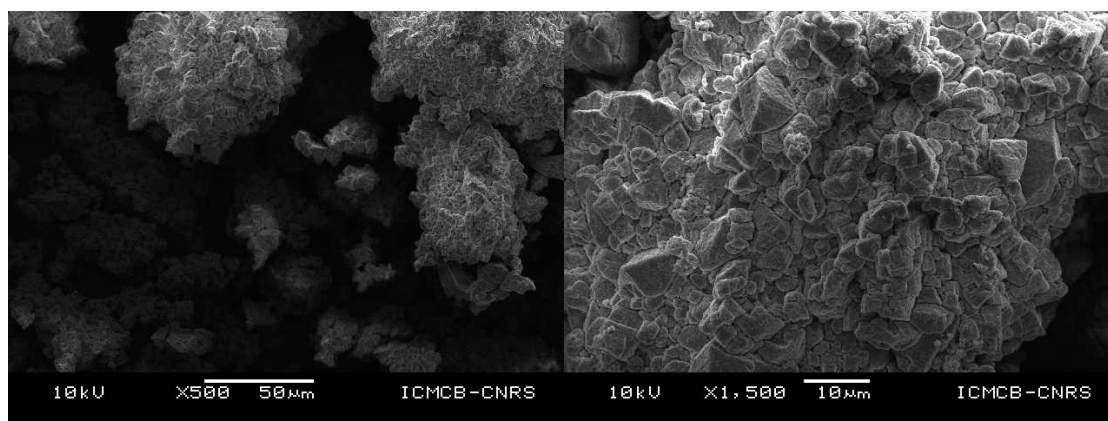


Figure 122: Specific heat measurement performed at 5 °C/min under Ar of dehydrated MnSO<sub>4</sub> and XRD of the three various forms: hydrated MnSO<sub>4</sub>·H<sub>2</sub>O, anhydrous  $\alpha$ -MnSO<sub>4</sub> and high temperature  $\beta$ -MnSO<sub>4</sub>

The first peak likely result from dehydration following a partial rehydration of the sample. A broad peak is visible from 350 to 430 °C and corresponds to the  $\alpha$  to  $\beta$  phase transition reported in literature and also visible on diffraction on Figure 122. XRD patterns show the phase transitions occurring from hydrated to anhydrous  $\alpha$  form, but also from  $\alpha$  to  $\beta$  form. In both cases, no trace of the initial phase is observed. The  $\alpha$  form is totally restored after cooling down to room temperature, confirming that the  $\alpha$  to  $\beta$  transition is reversible, as suggested by thermal analysis.

Microstructure of the powders of anhydrous and monohydrated phases are displayed on Figure 123 and Figure 124 respectively.



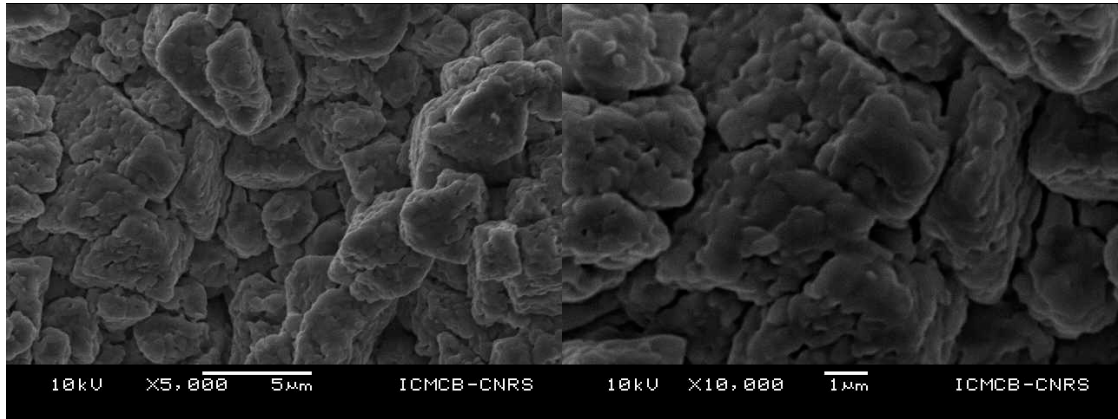


Figure 123: SEM pictures of anhydrous  $MnSO_4$  precursor powder

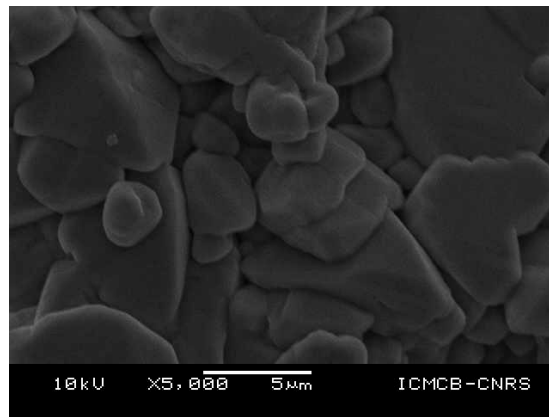
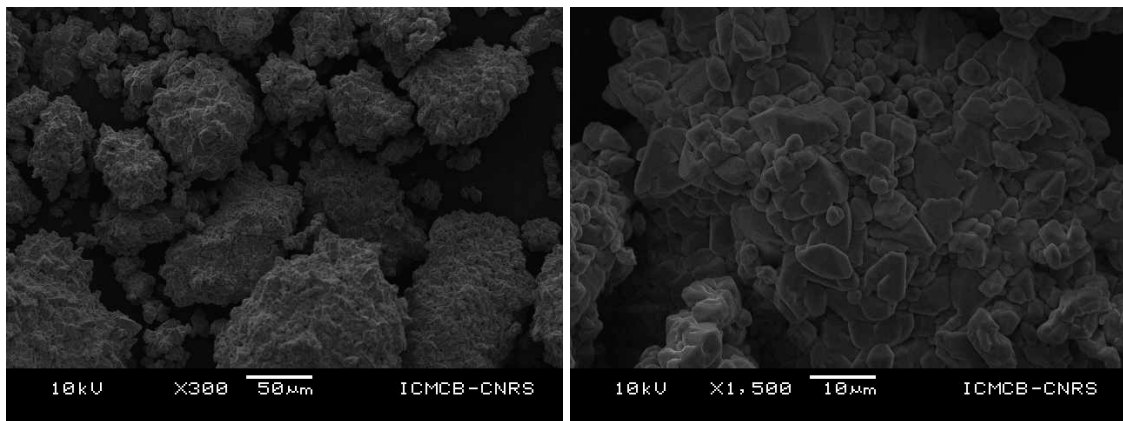


Figure 124: SEM pictures of hydrated  $MnSO_4 \cdot H_2O$  precursor powder

These pictures display micrometer sized grains that are arranged together to form large agglomerates of 50 to 100  $\mu m$ . Dehydration does not seem to affect the overall, but at the grain scale the “scars” of dehydration can be seen at the surface of the grains.

In order to complete the powders characterization, magnetic measurement have been performed on anhydrous powders obtained after 300 °C heat treatment.

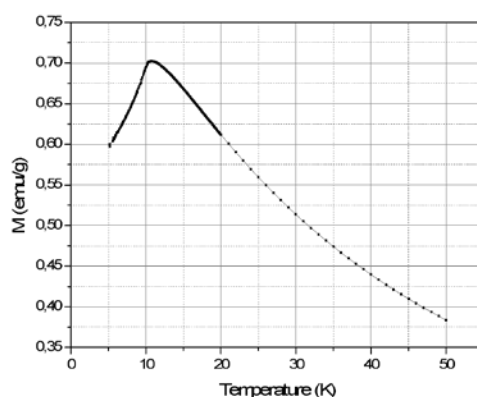


Figure 125: ZFC measurement under 1 kOe of  $\alpha$ -MnSO<sub>4</sub> using SQUID

Antiferromagnetic transition occurs at  $T_N = 11$  K which corresponds to the expected behavior of the anhydrous phase. No transition is observed at 16 K which corresponds to the Neel temperature of the hydrated phase<sup>228</sup>. This confirms the conclusions of XRD and TGA measurements that the phase is fully dehydrated after a heat treatment at 300 °C.

## 2.5.2 Sintering

As depicted previously, Spark Plasma Sintering at low temperature for fragile materials is possible. The high densification levels reached (> 95%) and the temperatures explored (< 400 °C) are very promising in terms of potential development of the technique to densify other compounds not suited for conventional sintering. The success obtained with this method attracted our attention on the mechanisms and parameters involved in such sintering. In order to extend this technique to other types of materials, one has to previously find out the necessary conditions to reach efficient densification at such low temperatures. The main outcome of the results previously described is that low temperature SPS is a different process for each material, even for very close compositions such as K<sub>2</sub>Cu(CO<sub>3</sub>)<sub>2</sub> and Na<sub>2</sub>Cu(CO<sub>3</sub>)<sub>2</sub>. In this work, our first sintering attempts have been performed on MnSO<sub>4</sub>, and identifying the optimal sintering conditions for this sulfate proved the most demanding task. In the following, this material has been used as a reference to investigate the mechanism(s) possibly involved in SPS at low temperature. For the previously discussed materials, only few experiments were necessary

before reaching a good density, giving a limited insight into the sintering mechanism. In the case of  $MnSO_4$  many experiments were performed before any pellet could be obtained in pure and dense form. On this basis, we pursued the exploration of sintering parameters for this material so as to have a wide overview. We'll try to have a global understanding of the sintering mechanisms at work during the densification of this material.

### 2.5.2.1 Effect of initial powder hydration level

As described previously, the precursor for the sintering of  $MnSO_4$  is a hydrated powder that can be either monohydrated or dihydrated (both with the same crystalline structure). In this part, only the monohydrate has been used. Two options are available in terms of powders that can be used for sintering. Either we can reproduce the same process as in the case of  $Na_2Cu(CO_3)_2 \cdot 3H_2O$  and perform *in-situ* dehydration, either we can use anhydrous  $MnSO_4$  powder resulting from heat treatment at 300 °C of hydrated powder. Due to the slow rehydration of the anhydrous powder (few days are necessary to rehydrate the sample), it was possible to use anhydrous powder (either “fresh” or stored at 120°C to prevent rehydration) for sintering.

Both these options have been explored and yielded different sintering result. These are summarized in following table with corresponding sintering conditions and resulting densification of pellets. Densities of pellet were measured geometrically.

Table 15: Experimental sintering conditions and final densification after SPS treatment of  $MnSO_4$  and  $MnSO_4 \cdot H_2O$

| Sample number | Powder      | Temperature (°C) | Pressure (MPa) | Dwell time (min) | Compactness (%) |
|---------------|-------------|------------------|----------------|------------------|-----------------|
| 63            | monohydrate | 400              | 400            | 5                | 82.9*           |
| 32            |             |                  | 100-400        |                  | 93.8            |
| 62            |             |                  | 40-400         |                  | 95.5            |
| 33            |             | 500              | 95.1           |                  |                 |
| 42            | Anhydrous   | 450              | 40-400         | 30               | 88.3            |
| 49            |             |                  | 400            |                  | 92.8            |

(\*) the pellet is a mix of hydrated  $MnSO_4 \cdot H_2O$  and anhydrous  $MnSO_4$

Most of the time, thermal and pressure profile is as follows: pressure is first applied on the powder while room temperature is maintained, then temperature rises when the targeted

pressure is reached. Dwell time starts when temperature reaches its maximum. After dwell time is over, temperature and pressure are both released (scheme view on Figure 126 a). In some cases, it can be interesting to set first the temperature while a pre-dwell pressure is applied. In our case, a 10 mm diameter die is used, thus 40 MPa is the minimum pressure that can be applied, and will be referred to as the contact pressure. When dwell temperature is reached, the target pressure is then applied. This pre-dwell pressure can vary within the range  $40 < P_{\text{pre-dwell}} < P_{\text{dwell}}$ . Dwell time starts when the pressure reaches dwell pressure (Figure 126 b). Such protocol can be useful to favor water release from hydrated powders for instance.

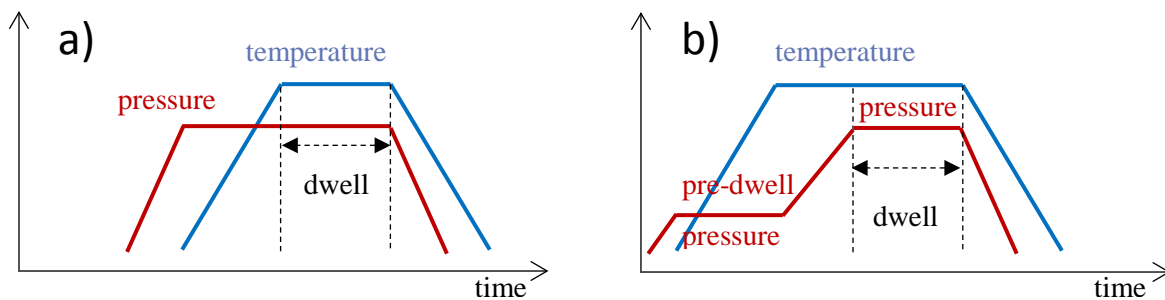


Figure 126: Schematic view of the two different strategies of SPS treatment. In the first case (a) pressure is set first and temperature increases when pressure is stable. In the second case (b), pressure is set lower pressure of the machine (>40 MPa) during heating. Once the temperature is stable at dwell value, pressure can be applied

In Table 8, some pressures are noted by a single or by two values, in relation with the two different processes presented in Figure 126. For instance, here, in the second line of the table, the “100-400 MPa” entry refers to the second process and means that pressure is first set at 100 MPa, then temperature is increased up to 400 °C under this pressure. Once the temperature reaches 400 °C, pressure is increased up to 400 MPa and then dwell time starts. After dwell time is over, pressure and temperature are released. In every cases, pressure ramp is set to 100 MPa/min. Temperature ramp is set at 50 °C/min during heating, and natural cooling is

applied.

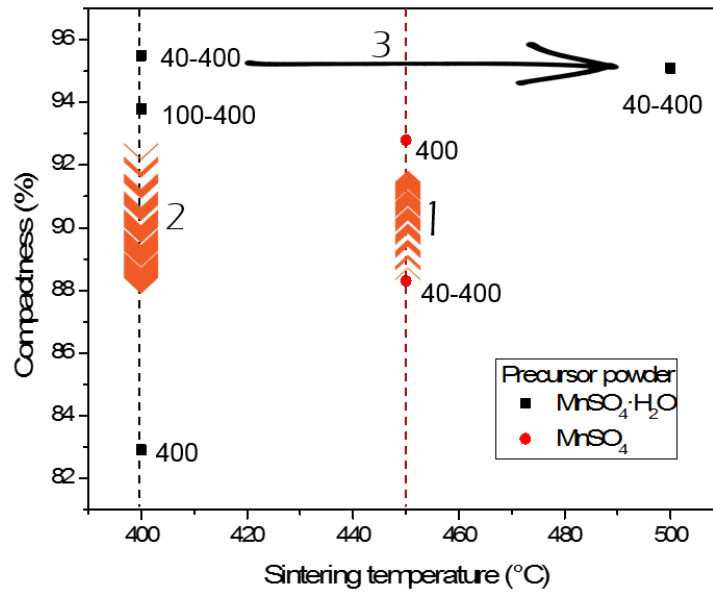


Figure 127: Representation of compactness versus sintering temperatures of MnSO<sub>4</sub>. Black and red dashed lines represent the minimum sintering temperature required for both hydrated (5 min dwell) and anhydrous powders (30 min dwell), respectively. Arrows #1 and #2 show the increase of pre-dwell pressure and the #3 shows the effect of temperature increase

Sintering attempts have been made on MnSO<sub>4</sub>·H<sub>2</sub>O at 350 °C and on MnSO<sub>4</sub> at 400 °C but resulted in compacted but non-cohesive powders that destroyed by mere scratching. This is probably a sign that the resulting pellets suffer from a lack of intergranular bonding. Thus a higher temperature and a longer dwell time are needed to sinter anhydrous MnSO<sub>4</sub>. The minimum required temperatures to sinter both powders are represented by dashed lines, *i.e.* 400 and 450 °C depending on the initial hydration level of the powder. Moreover, 30 min were necessary in the case of anhydrous powders whereas 5 min were sufficient for the hydrated one, with better densities.

Many information can be extracted from Figure 127:

- Sintering can be achieved with high density level (>92%) with anhydrous powder at 450 °C and 400 MPa for 30 min of dwell time
- Higher densities can be obtained at even lower temperature using the monohydrate
- Increasing the temperature to 500 °C (arrow #3) in the case of monohydrate powder does not make a huge difference with sintering at 400 °C. It seems the sintering mechanism is essentially completed at 400 °C and nothing can be gained by operating at higher temperature

- Increasing pre-dwell pressure has a strong impact on final density, but is in opposite ways on monohydrate and dehydrated powders (arrows #1 and #2)

These information highlight the difference between both precursors and the higher reactivity of the monohydrate in SPS conditions. This difference may come from the chemical state at the surfaces of grains, from the crystal structure or from microstructural parameters. The pre-dwell pressure also has a very important impact on sintering. In addition, sample 63 sintered at 400 °C under 400 MPa during 5 min was not totally dehydrated as it can be seen on its XRD pattern (see Figure 128). Thus, the pre-dwell pressure not only has a strong influence on density level but also on dehydration. This effect can be linked to the observation that hydration (and probably the subsequent dehydration) has an influence on sintering too.

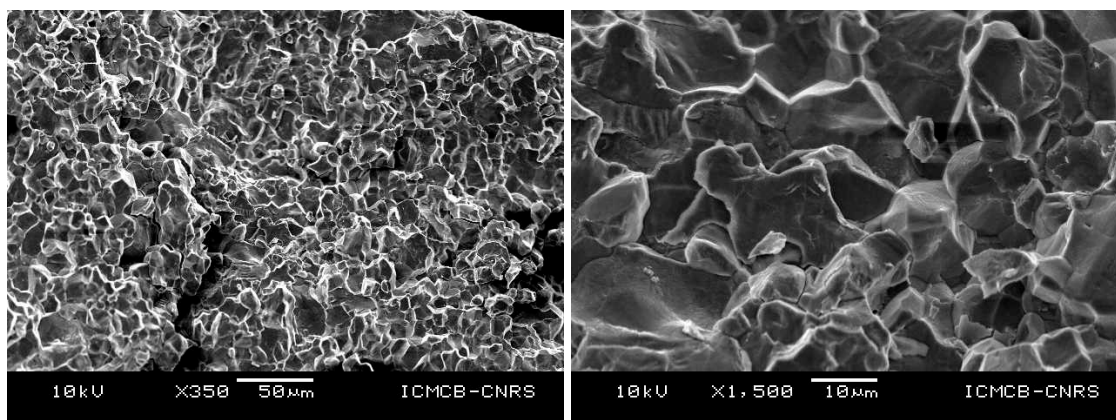


Figure 128: SEM pictures of  $MnSO_4$  pellet sintered at 400 °C - 40/400 MPa - 5 min

Figure 128 displays SEM pictures of an anhydrous pellet of  $MnSO_4$  sintered in two steps, as described in Table 8 (sample 62, 400 °C – 40/400 MPa – 5 min). This sample is the one with the highest measured density (95.5 %) and SEM micrograph shows no open porosity and obviously confirms that densification occurred successfully.

Since the best sintering results have been obtained with the monohydrate precursor, the next parts will only refer to experiments performed with this powder, aiming to highlight the mechanisms involved during sintering.

#### 2.5.2.2 *In-situ* dehydration

It clearly appears that the presence of water has an influence on the sintering process. Moreover, the experimental protocol (depending on when the pressure is applied) has a strong influence

on the final density. For instance in Table 8, the only difference between samples 62 and 63 is the sequence used to apply pressure on the sample. In both case, 400 °C and 400 MPa are applied at dwell and the precursor consists of monohydrate powder. In the case when pressure is set first and then temperature is increased, the resulting pellet consists of a mix of hydrated and anhydrous form. The resulting density is difficult to evaluate in this situation as the exact amount of each phase is not known precisely, and they have different volumic masses (2.94g/cm<sup>3</sup> for the monohydrate, 3.46g/cm<sup>3</sup> for the anhydrous form). When the pressure is applied after reaching the dwell temperature, the resulting pellet has a high density (95.5 %) and the phase is completely anhydrous. In the intermediate case of sample 32, the applied pressure is 100 MPa during heating ramp and when the dwell temperature is reached, pressure is increased to 400 MPa. This leads to a quasi-pure anhydrous phase (see Figure 129) and the density is slightly lower than the previous one (93.8 %). This small difference could possibly be due to the presence of remaining monohydrate phase.

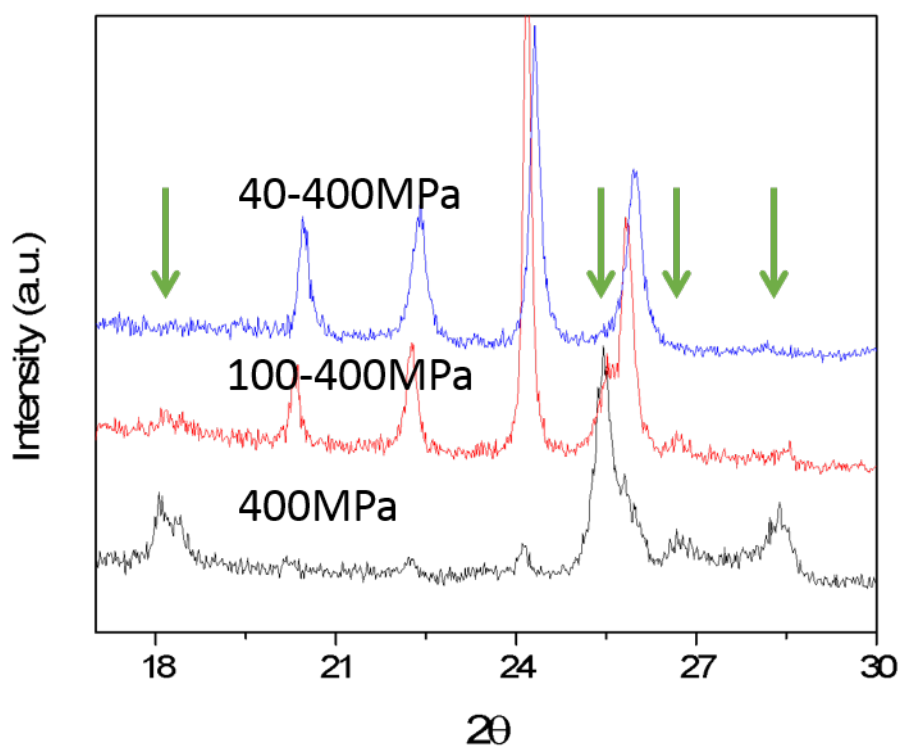


Figure 129: XRD pattern of sample #32 sintered at 400 °C and 100-400 MPa for 5 min. Arrows show the presence of remaining hydrated phase

In Figure 130 is represented the evolution of chamber pressure during SPS sintering of MnSO<sub>4</sub>·H<sub>2</sub>O under various applied pressures, from 40 MPa to 400 MPa (applied from the start).

TGA under air, already displayed in Figure 121, is used here as a reference to compare with the dehydration as observed during SPS. Of course the experimental conditions are different, because the thermal ramp is not the same (3 °C/min versus 50 °C/min) and the atmosphere is also different (under air at ambient pressure for TGA, under dynamic vacuum for SPS), but it is still interesting to use TGA for a qualitative comparison.

When dehydration occurs during SPS experiment, the pressure in the chamber increases. Since subsequent characterization of the pellets excluded decomposition of the target material, it is safe to consider this gas release to be water release associated to dehydration of the precursor powder.

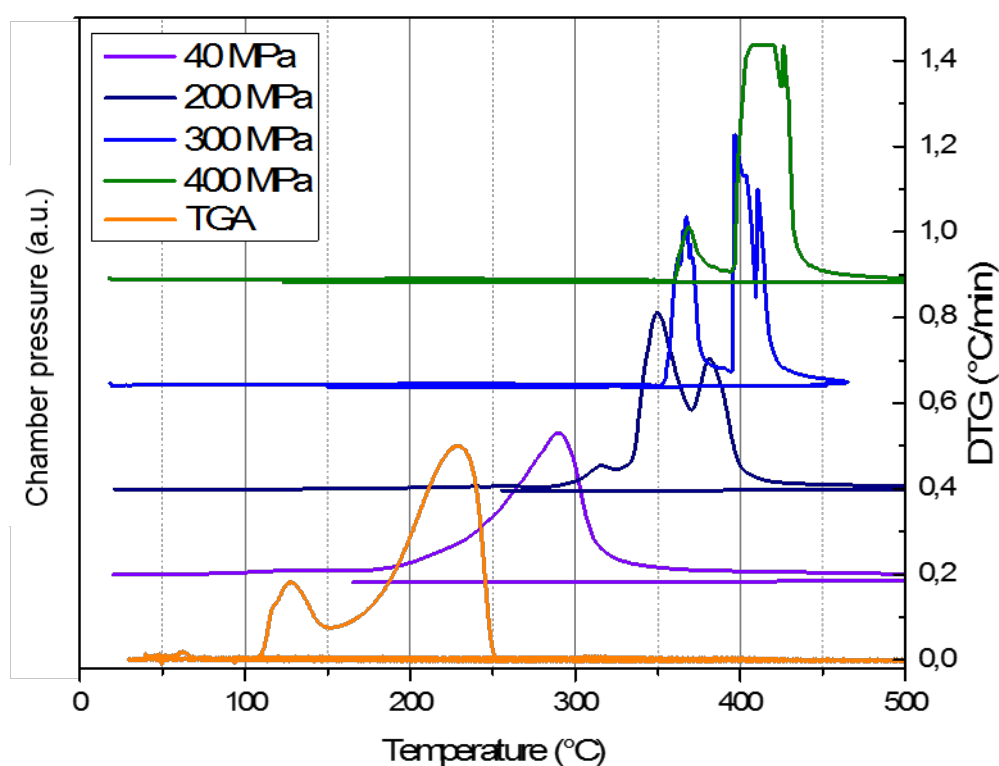


Figure 130: Summary of the water release during SPS experiment on  $\text{MnSO}_4 \cdot \text{H}_2\text{O}$  for various applied pressures; TGA under air in atmospheric pressure is used as reference

When increasing the applied pressure on the powder, dehydration is shifted to higher temperatures. This phenomenon already occurs under a pressure of 40 MPa. At this stage, the maximum of water release is located at 290 °C, which is 60 °C above the maximum of water release observed in TGA. When the pressure is raised up to 200 MPa, water release is separated in two steps. From 40 to 200 MPa, the temperature of the maximum water release increases, but also there is a change of peak shape. At 200 MPa, there are two main peaks at 350 and

380 °C that differ in their intensity, the first one being slightly more intense than the second one. When the pressure is 400 MPa, the two peaks are moved to higher temperatures, respectively ~370 and 415 °C, and the more intense peak becomes the one at 415 °C; *i.e.* the major part of dehydration is moved to higher temperature. It is noteworthy also that dehydration is barely completed at 400°C under 200 MPa, while for higher pressures it is necessary to go beyond 400°C for dehydration to be complete.

Another representation is given in Figure 131 and shows the temperature of dehydration for the different applied pressures, the color scale representing chamber pressure. It is visible that at low applied pressure, not only the dehydration temperature is lowered but it also spans a wider temperature range. At 400 MPa, the temperature range for dehydration is essentially restricted to the peak between 370 and 415 °C. Increasing pressure seems basically to reduce the dehydration temperature range.

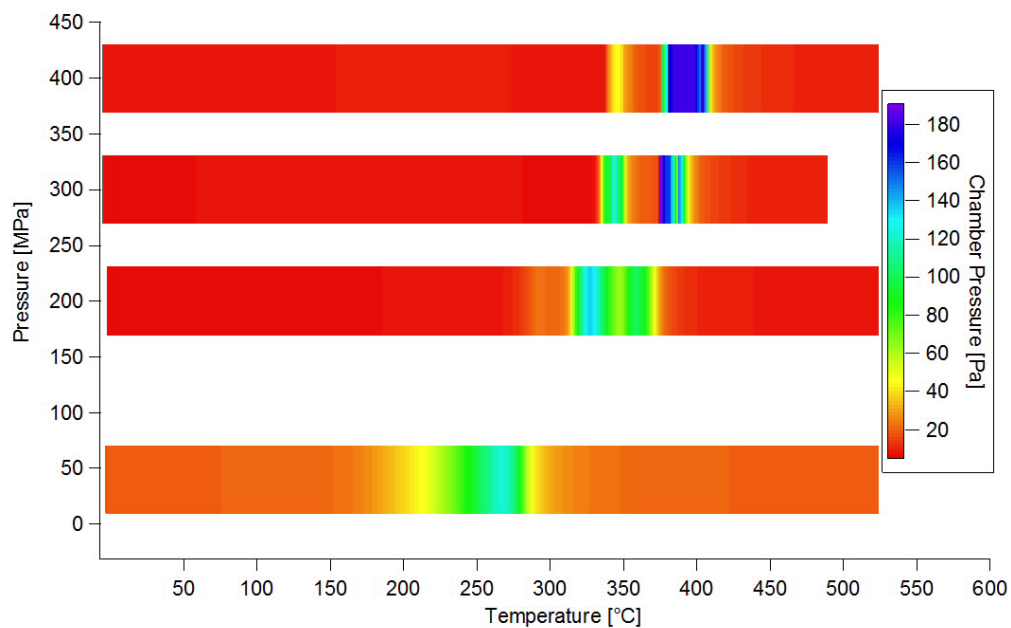


Figure 131: Schematic representation of chamber pressure during sintering of  $MnSO_4 \cdot H_2O$  for different pressures

Thus, the applied pressure while heating the powder has an impact on the dehydration temperature. As a general feature, dehydration is repelled to the higher temperature when a higher pressure is applied. Moreover, the span of temperature on which this dehydration occurs tends to shorten with increasing pressure. These observations explain the presence of the monohydrate phase for a sample sintered under 400 MPa during the whole sintering process,

whereas a sample which has been heated under the lowest pressure (40 MPa) is totally anhydrous. Intermediate pressure of 100 MPa seems to promote *quasi* complete dehydration but a small amount of hydrate phase remains however.

The second observation is the reduction of dehydration temperature span with higher pressures which result in an abrupt water release that can be problematic for the microstructure of the final pellet. In this case, as shown on Figure 132, porosity becomes more important and we know from XRD measurement that water is not totally removed from the sample. Submicrometric pores, probably related to water release, are visible, and cracks even appear in the sample.

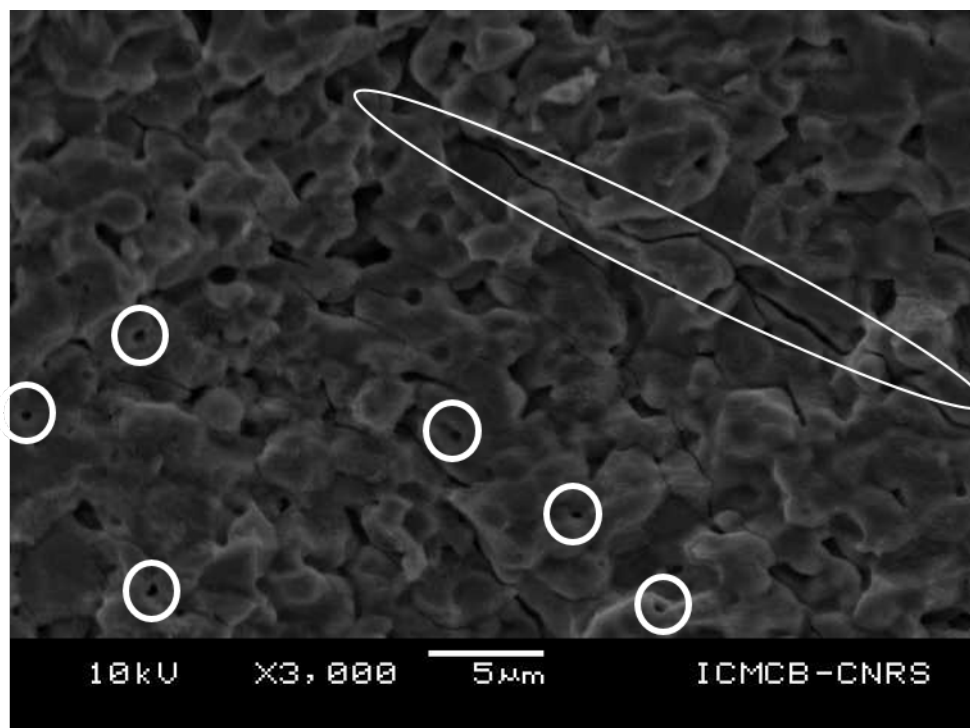


Figure 132: SEM picture of a fractured pellet sintered at 400°C 400MPa for 5 min

These observation explains the result in Table 8 in which the sample sintered at 400 °C with 400 MPa applied during the whole thermal cycle remains hydrated (see Figure 129). This also questions the possibility to sinter the hydrated form  $\text{MnSO}_4 \cdot \text{H}_2\text{O}$ , that will be developed in a further part.

In the case of  $\text{MnSO}_4 \cdot \text{H}_2\text{O}$  used as precursor for the sintering, it is necessary to enable dehydration in order to obtain the desired pure anhydrous phase. According to these results, it is clear that dehydration strongly depends on the applied pressure during heating step, and it

appears that increasing pressure helps stabilizing the hydrated form and repels dehydration to higher temperatures, although the density of the hydrate is lower than that of the anhydrous phase (2.94 compared to 3.46).

### 2.5.2.3 Effect of pressure, temperature and time

Pressure, temperature and time are obviously important parameters for sintering. Their influence has been explored for the sintering of  $\text{MnSO}_4$ , in order to identify the lowest conditions allowing to obtain highly densified ceramics (> 95 %).

#### 2.5.2.3.1 Effect of pressure

Various pressures have been explored in order to identify a range in which the densification could be enhanced without exceeding upper limits above which the mechanical cohesion is put in jeopardy. Although about 100 experiments were ran in this study, the results can be synthesized with the three examples given in Table 9.

*Table 16: Experimental sintering conditions and resulting pellet's density for some  $\text{MnSO}_4$  sample varying pressure*

| Sample number | Temperature (°C) | Pressure (MPa) | Dwell time (min) | Compactness (%) |
|---------------|------------------|----------------|------------------|-----------------|
| 43            | 500              | 40-300         | 5                | 89.1            |
| 48            |                  | 40-400         |                  | 96.0            |
| 06            |                  | 40-500         |                  | broken          |

In these experiments, for the same temperature and time conditions, but also same powder quantity, the only difference is the different pressures applied during sintering. From 300 to 400 MPa, the density increases from 89 % to 96 % of theoretical density. When the pressure reaches 500 MPa, the resulting pellet breaks down when removed from the die. These results have been reproduced on several occasions. As a general result, we never reached 90 % density for pellets sintered at 300 MPa, even at higher temperature and dwell time and all the samples sintered at 500 MPa broke during pellet's manipulation, mainly by delamination. After these observations, 400 MPa was selected for the rest of the work and no more attempts have been performed at a different pressure.

#### 2.5.2.3.2 Effect of temperature

Temperature also has been tested to evaluate its influence on sintering, in order to determine the lowest possible temperature to keep a high densification.

The most significant results of this survey are summarized in Table 10

Table 17: Experimental sintering conditions and resulting pellet's density, crystallite size, for some MnSO<sub>4</sub> sample

| <b>Sample number</b> | <b>Temperature (°C)</b> | <b>Pressure (MPa)</b> | <b>Dwell time (min)</b> | <b>Compactness (%)</b> | <b>Mean crystallite size (nm)</b> |
|----------------------|-------------------------|-----------------------|-------------------------|------------------------|-----------------------------------|
| 33                   | 400                     |                       |                         | 95.5                   | 30                                |
| 72                   | 450                     | 40-400                | 5                       | 95.4                   | 32                                |
| 62                   | 500                     |                       |                         | 95.1                   | -                                 |
| 81                   | 600                     |                       |                         | 96.5                   | 50                                |

Here the evolution of densification with temperature is not very important, with only 1.5 % difference in the temperature range 400 to 600 °C. However, the density of samples sintered between 400 and 500 °C appear identical, while a small increase is observed for the sample sintered at 600 °C.

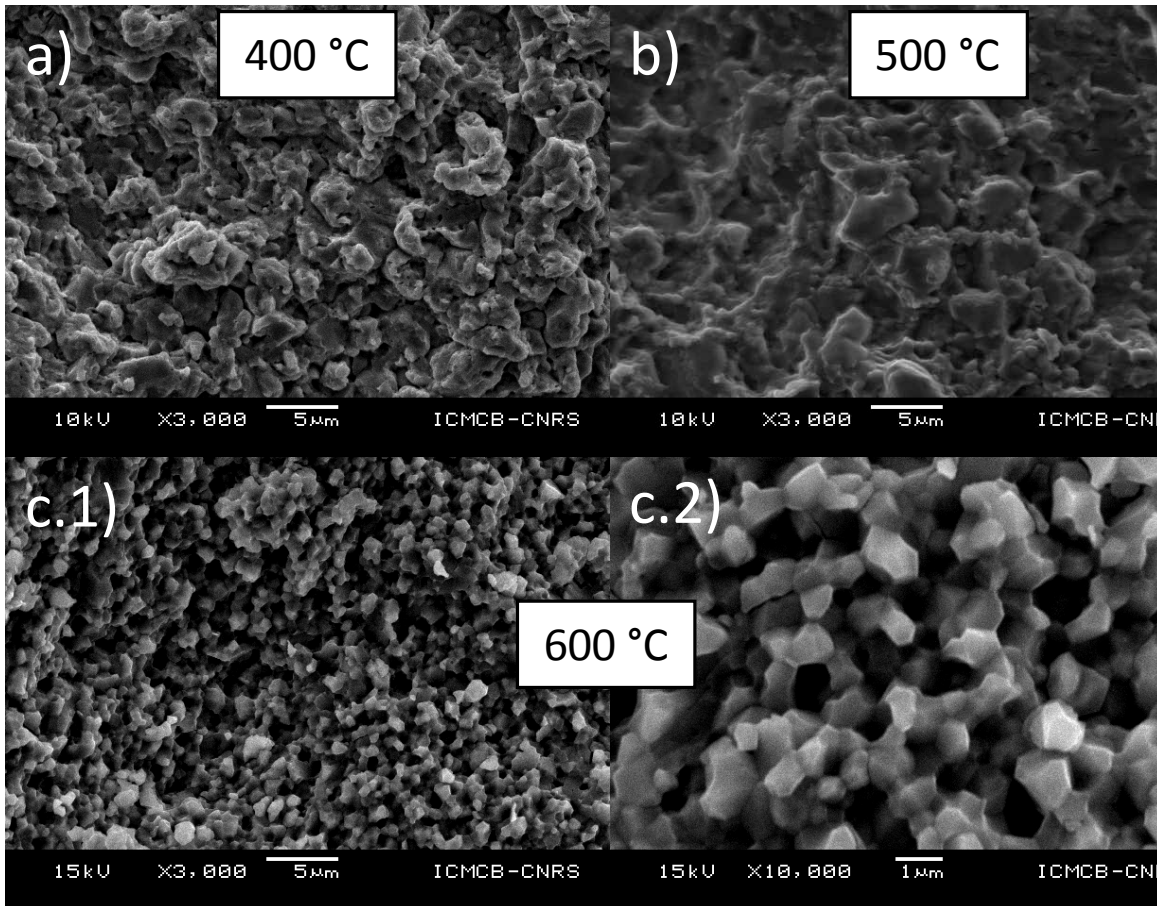


Figure 133: SEM images of  $MnSO_4$  pellets sintered at (a) 400 °C, (b) 500 °C and (c.1 and c.2) 600 °C

On these SEM images are displayed the fractures of three different pellets sintered at different temperatures. The observation of grain shape shows that samples sintered at 400 and 500 °C have the same overall shape, whether grains look slightly bigger at 500 than 400 °C. However, these two samples present the same compact microstructure, while the one sintered at 600 °C looks different. The two first look to be composed of grains of about 1-2 and 4-5  $\mu m$  respectively, with curved shapes, whereas the last one looks to be composed of small grains of about 1  $\mu m$  with nice facets. The remaining porosity in this last case looks to be induced by the fracture. This observation is in the line with the idea that there is activation of some process (diffusion in the solid state, grain growth...) between 500 and 600 °C that makes the density increase and the grains change in shape. A surprising result is the apparent grains size reduction with increasing sintering temperature, according to SEM pictures. However, mean crystallite size extracted from XRD refinements shows a global increase from 30 nm to 50 nm, which is

consistent with a growth expected at higher temperature. No difference is observed between 400 and 450 °C which seems to have only a small influence on growth.

### 2.5.2.3.3 Effect of time

Table 18: Experimental sintering conditions and resulting pellet's density for some MnSO<sub>4</sub> sample varying time

| Sample number | Temperature (°C) | Pressure (MPa) | Dwell time (min) | Compactness (%) | Mean crystallite size (nm) |
|---------------|------------------|----------------|------------------|-----------------|----------------------------|
| 70            | 400              | 40-400         | 10               | 95.3            | 29                         |
| 71            |                  |                | 20               | 95.4            | 32                         |

Increasing the sintering time to 10 and 20 min at 400 °C has been performed for two samples. This leads to a densification level of 95.3 % and 95.4 %, which is only 0.2 % difference with the densification after 5 min (see Table 10, page 207). No evolution of crystallite size has been observed from 5 to 20 min. This is consistent with the microstructure observed on Figure 134 that is quite similar to the one obtained after 5 min. Here, no change in the grain morphology or size can be observed, hence, it seems activation of sintering is reached at 400 °C but no growth mechanism seems to be activated.

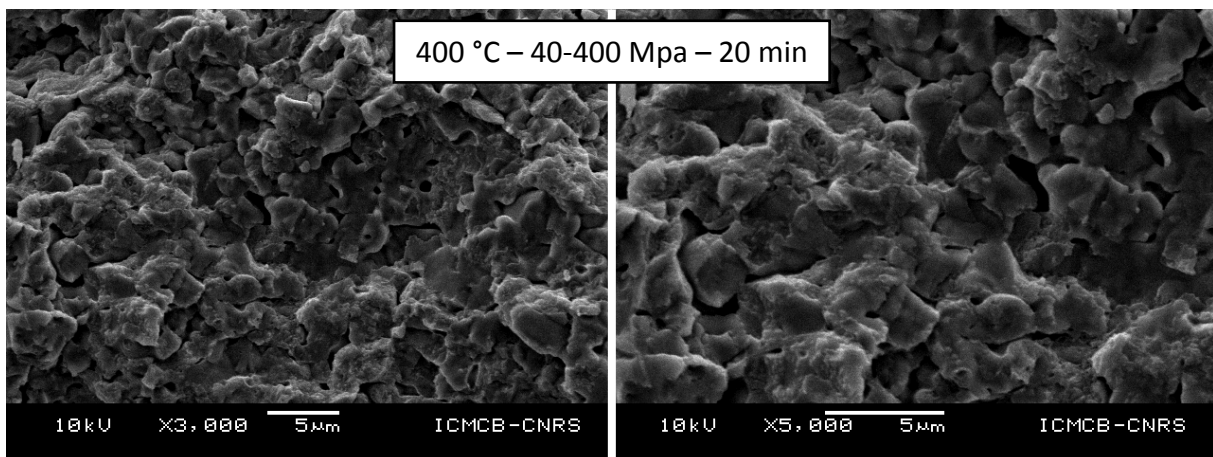


Figure 134: SEM picture on a fracture of a pellet sintered at 400 °C under 400 MPa for 20 min

### 2.5.2.4 Influence of $\alpha$ to $\beta$ transition

#### 2.5.2.4.1 Temperature uncertainty level

Similar sintering experiments have been reproduced in the exact same experimental conditions. Paying attention to the dehydration step is interesting to control the temperature accuracy (see Figure 137).

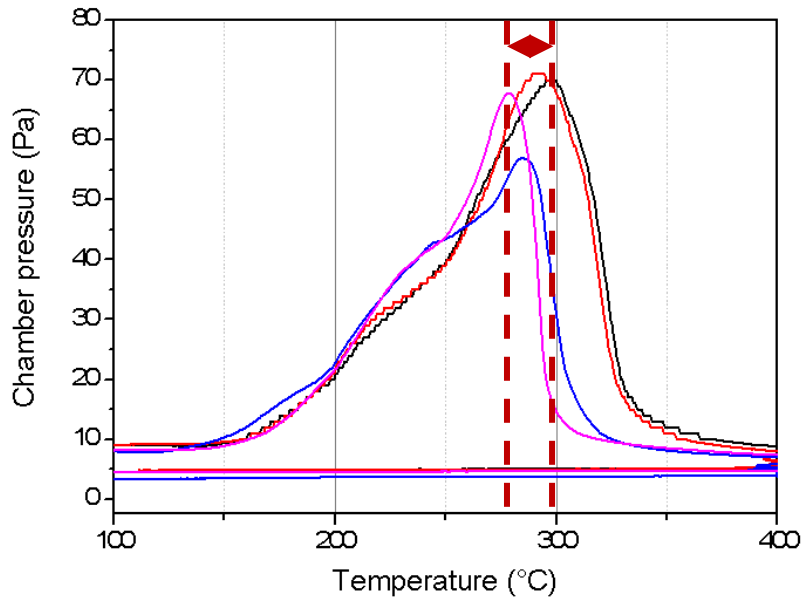


Figure 135: Chamber pressure versus temperature for various  $\text{MnSO}_4 \cdot \text{H}_2\text{O}$  sintering performed at  $400^\circ\text{C}$  under  $40\text{ MPa}$  pressure and  $50^\circ\text{C}/\text{min}$  heating rate and the same amount of powder. Red arrow shows the dehydration temperature range

What is visible here is the difference of temperature for the maximum of pressure associated to dehydration. The maximum dehydration occurs at  $278^\circ\text{C}$  for the lowest temperature and  $298^\circ\text{C}$  for the highest one. According to this observation, any sintering should be considered as taking place in a temperature range spanning  $20^\circ\text{C}$  around the targeted dwell temperature.

Figure 136 is a representation of the die inside the SPS chamber. A small hole in the die is dedicated to the thermocouple. Depending on how the powder and the pistons are centered, and on the thickness of the green sample, its temperature can be read with more or less accuracy. During sintering and pressure application, shrinkage of the powder occurs to form a densified pellet. Here again, a difference between the temperature indicated on the thermocouple and the actual temperature of the sample can result from the increase of sample-thermocouple distance. Temperature measurement variations have already been highlighted in other systems, notably by using magnetic transition affecting the current input while heating the powder in SPS<sup>229</sup>. Combining both phenomena (*i.e.* off centering and shrinkage) can lead to a misevaluation of the sample temperature that cannot be neglected.

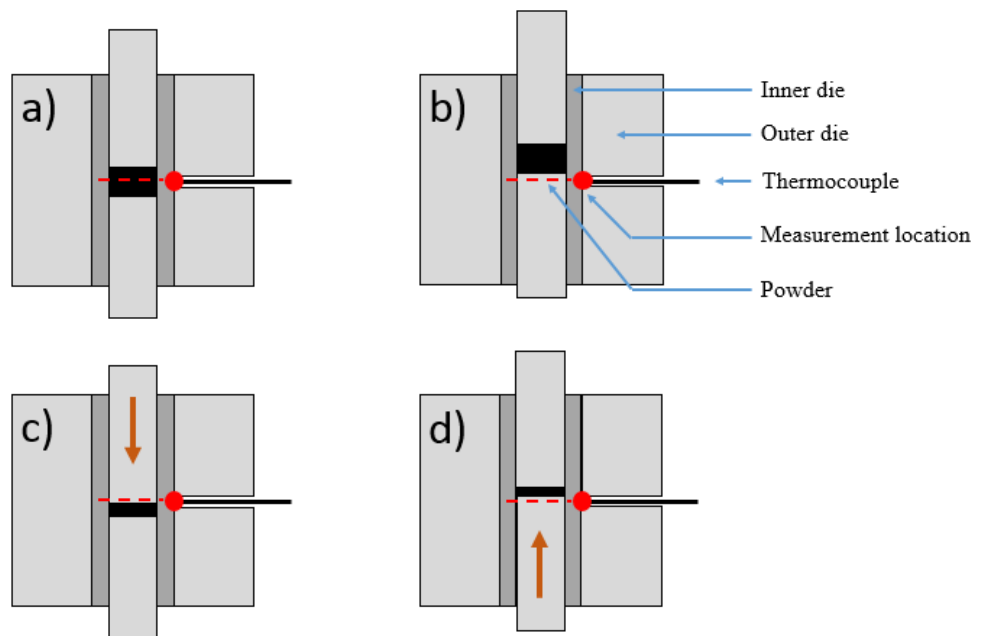


Figure 136: Schematic representation of a SPS die with space for thermocouple. (a) good centering of the powder on the thermocouple, (b) off centering, and shrinkage resulting from (c) top and (d) bottom piston displacement

These information are important to consider when trying to understand the mechanisms of densification in the case of  $\text{MnSO}_4$  and their critical parameters. As discussed previously, attempts performed at  $350\text{ }^\circ\text{C}$  did not lead to sintered pellets. However, sintering at  $380\text{ }^\circ\text{C}$  gave various results, some experiments resulting in sintered pellets while others did not. We know from DSC measurement that the transition from  $\alpha\text{-MnSO}_4$  to  $\beta\text{-MnSO}_4$  occurs above  $370\text{ }^\circ\text{C}$  under atmospheric pressure. When sintering is performed at  $380\text{ }^\circ\text{C}$ , the  $\alpha\text{-}\beta$  transition can occur. It becomes interesting to question the influence of this phase transition on sintering mechanism.

#### 2.5.2.4.2 Evidence of $\beta$ phase transition on sintering

As described in the previous section,  $\alpha\text{-MnSO}_4$  is a low temperature phase and undergoes a reversible transition to a  $\beta$  phase at  $380\text{ }^\circ\text{C}$  under Ar and reverts to the  $\alpha$  phase at  $150\text{ }^\circ\text{C}$  on cooling. At about the same temperature ( $380\text{ }^\circ\text{C}$ ), we demonstrated that the dehydration of the powder (under  $400\text{ MPa}$ ) and its sintering occur. From this point arises a question of the involvement of the  $\alpha\text{-}\beta$  phase transition in the sintering. It has been discussed that phase

transitions of a single phase material taking place within the range of the sintering thermal cycle can have an impact on the resulting densification<sup>155</sup>. It is then possible that the  $\beta$ -MnSO<sub>4</sub> phase is more reactive than  $\alpha$  phase in SPS condition, and/or that the  $\alpha$ - $\beta$  transition occurring at 380 °C favors the sintering.

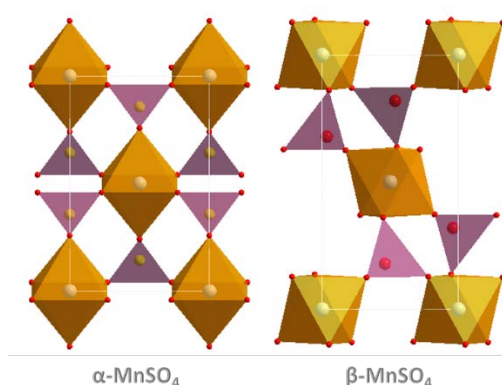


Figure 137: Representation of  $\alpha$ -MnSO<sub>4</sub> and  $\beta$ -MnSO<sub>4</sub> phases along (001)

High temperature  $\beta$  form results from a 45° rotation of octahedra around (001) axis. This result in the reorganization of sulfate tetrahedra and a small increase of lattice volume. From  $\alpha$  to  $\beta$ , the volume changes from 289.6 Å<sup>3</sup> to 299.0 Å<sup>3</sup>, *i.e.* a 3,2% variation which is quite significant. Therefore, due to the lower density of the  $\beta$ -phase, the  $\alpha$ -phase should be stabilized by the application of an external pressure. However, considering that the  $\beta$ -phase has a theoretical density of 3.35 g/cm<sup>-3</sup> at 450°C<sup>227</sup>, while that of the  $\alpha$  phase is 3.46 g/cm<sup>-3</sup> at room temperature, it is difficult to conclude about the effect of pressure. No information about thermal expansion of MnSO<sub>4</sub> has been found in literature, which makes it hard to calculate what would be the theoretical density of  $\alpha$  phase around the transition temperature. Anyway, from 3.46 to 3.35, there is a difference of 3.1 %, and the density of 3.46 for  $\alpha$  phase, taken at 25 °C, must decrease when the temperature will rise to 400 °C. Then one can expect it will get even closer to the  $\beta$  phase density. We can thus assume that pressures of a few hundred of MPa will have a limited influence on the  $\alpha$ - $\beta$  transition temperature.

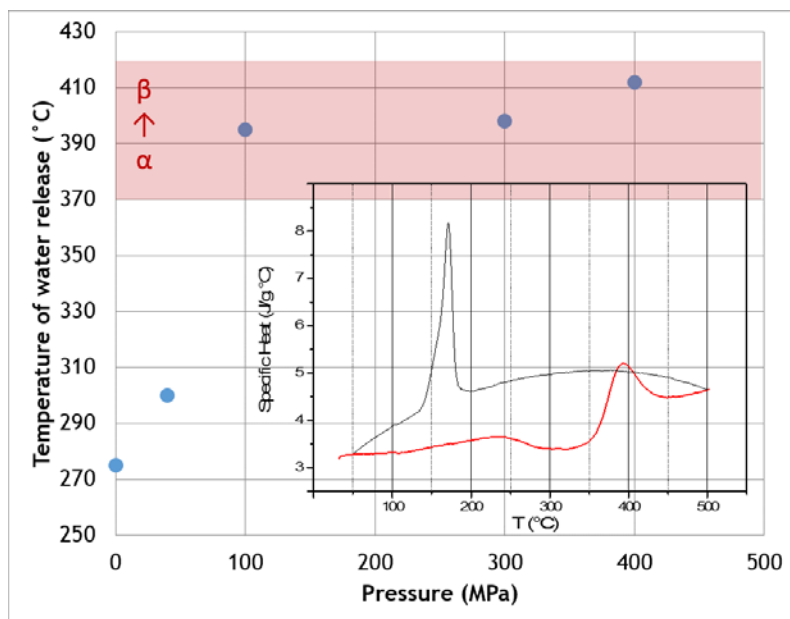


Figure 138: Schematic representation of water release during SPS sintering; blue dots represent the temperature of maximum water release and red box represent the temperature range of  $\alpha$  to  $\beta$  phase transition measured in ambient pressure. Measure at 0 MPa corresponds to the result of TGA measurement. DSC measurement is in the inset

On Figure 138 is represented the temperature of maximum dehydration as detected by monitoring the chamber pressure in SPS, with respect to the pressure applied on the sample. The first point at 0 MPa is the dehydration measured from TGA, used as a reference. After a first increase of the pressure to 40 MPa, a 20 °C increase of the water release temperature is observed. This can be explained by the application of pressure on the sample that slightly stabilizes the monohydrate form. The evolution of dehydration temperature under pressures ranging from 100 to 400 MPa shows a different scheme. The increase of dehydration temperature reaches a plateau at 100 MPa, and after this point, it seems to be essentially constant (it should be reminded here that the dehydration typically takes place over a 20-30° range at the least). The red ribbon represents the zone of phase transition from  $\alpha$  to  $\beta$  taken from DSC measurement.

Beyond the previous observations, no formal proof of the influence of the phase transition can be collected in our experimental conditions, since it is impossible to prove the actual presence of the  $\beta$  phase when SPS experiment is running, and since the  $\alpha$  phase is restored at the end of the experiment. The SPS environment already proved to influence phase transitions and promote a specific chemical reactivity earlier in this work, especially in the case of  $\text{Na}_2\text{Cu}(\text{CO}_3)_2$ . Having no experimental setup to perform XRD under pressure and under the

same vacuum level as the one present in SPS chamber, it is impossible to be sure about the presence of  $\beta$  phase. Anyway, it is interesting to note that dehydration occurs in the same temperature range as the one observed for the  $\alpha$ - $\beta$  phase transition. One could thus consider that the dehydration observed at 400°C under pressure of 100 MPa and above, is actually forced by the transition to  $\beta$ -MnSO<sub>4</sub>, a phase for which no hydrated form is known.

### 2.5.3 Physical properties

Magnetic properties of both materials have been previously reported in literature to be antiferromagnetic with  $T_N$  (MnSO<sub>4</sub>) = 11 K<sup>96-98</sup> and  $T_N$  (MnSO<sub>4</sub>, H<sub>2</sub>O) = 16 K<sup>228</sup>. In order to explore the physical properties of MnSO<sub>4</sub>, magnetic measurement have been performed on both powder and pellet. This phase is known to exhibit a cycloidal spin arrangement<sup>205,231</sup> that can induce magnetoelectric properties. In the opposite, the monohydrate does not display this kind of magnetic structure and appears less interesting in terms of physical properties.

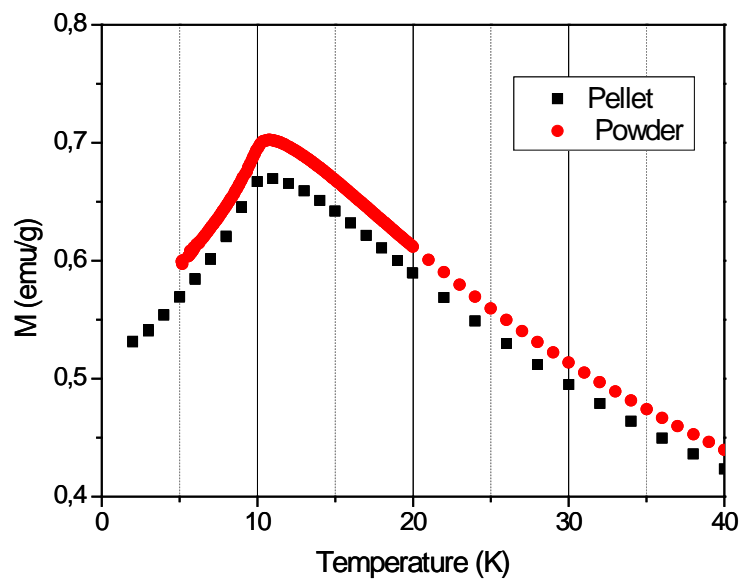


Figure 139: SQUID measurement of MnSO<sub>4</sub> powder and pellet sintered in SPS at 400 °C 400 MPa during 5 min

On Figure 139 is displayed magnetization versus temperature performed on both dehydrated powder and SPS sintered pellet of MnSO<sub>4</sub> (sintering conditions 400 °C – 40-400 MPa – 5 min). On the two samples, the same behavior is found with an antiferromagnetic transition at 11 K and a Weiss temperature of -25 K (in good agreement with literature). In addition to that, no anomaly around 16 K is observed that could be the consequence of the presence of MnSO<sub>4</sub>·H<sub>2</sub>O

in the sample. The mass magnetization of pellet is 0.67 emu/g and powder's is 0.70 emu/g. This makes a difference of 4 % between powder and pellet, which could be explained by a slight difference of crystallinity of the pellet compared to the initial powder. This can be confirmed by checking the X-ray diffraction patterns of both powder and pellet displayed on Figure 140.

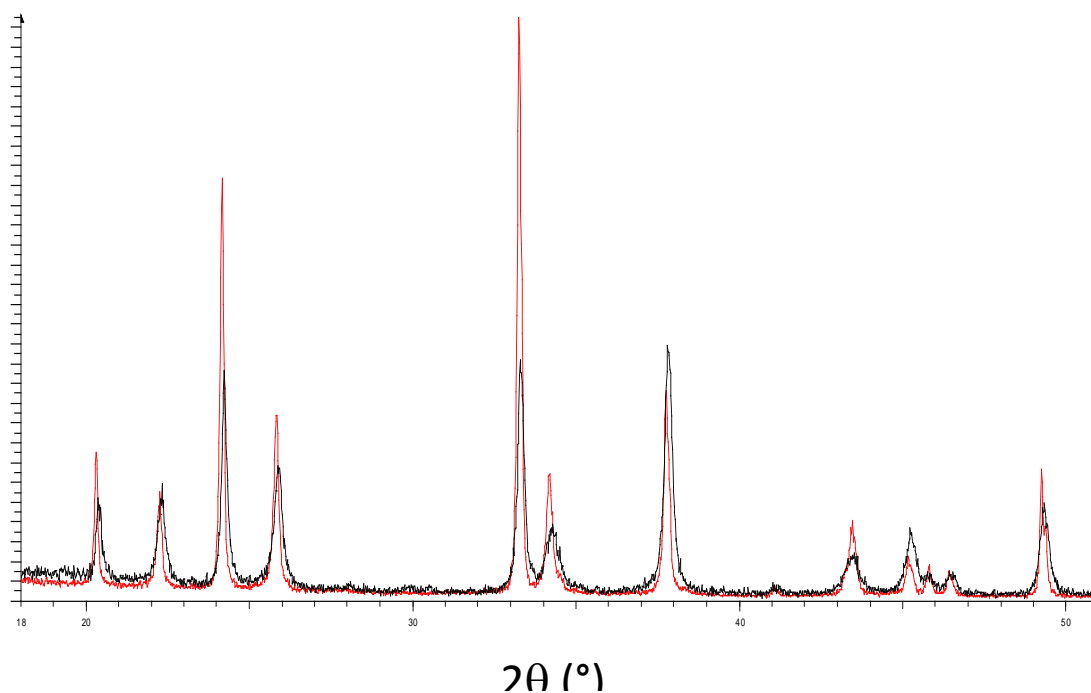


Figure 140: XRD pattern of (red) dehydrated powder and (dark) SPS sintered pellet (400 °C - 400 MPa - 5 min)

The powder and pellet of  $\text{MnSO}_4$  present the same structure, and refined parameters are the same. Anyway, a difference in peak width is clearly visible. Dehydrated powder presents narrower peaks which shows the higher crystallinity level as compared to the diffraction pattern of the pellet. Refined crystallite size are 100 nm for the powder and 30 nm for the pellet. The pellet appears to be composed of smaller crystallites than raw powder. Therefore, the concentration of interfaces increases in the pellet with respect to the parent powder, which results in a decrease of the well crystallized part of the solid. This must result in a decrease of magnetization of the pellet, which is in good agreement with magnetic measurements.

Thus, magnetic measurements confirm phase purity, even with a small decrease of crystallinity of pellets, and dielectric measurement can be performed on pellets in a PPMS in order to reach temperatures down to 2 K, but also to be able to apply magnetic field while measuring the dielectric response, to evaluate a possible magnetoelectric coupling.

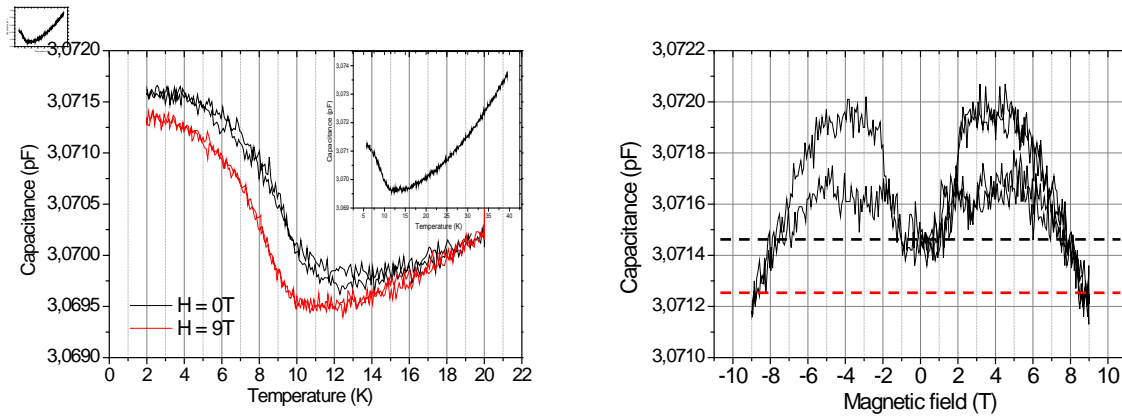


Figure 141: Capacitance measurement versus (left) temperature under applied magnetic field and without field, (inset is full temperature scale to 300 K), and (right) versus magnetic field at 2 K

Figure 141 represents capacitance measurement on a  $\text{MnSO}_4$  pellet. First, it is interesting to note the very low noise level of the measurement that signals a high-quality pellet (thus if interfaces are numerous due to the nano-sized grains, they are of excellent quality), and confirms the very high densification obtained after sintering (95.6 % for this sample). Capacitance first decreases from 300 to 11 K down to 3.07 pF, but starts increasing below 11 K, i.e. right below  $T_N$  as measured from magnetic measurements. While the anomaly does not signal a transition to a ferroelectric state, such a behavior is rather consistent with the helical magnetic structure that can induce a polarization, thus resulting in a high degree of connection between magnetic and electric properties. In addition to these observations, it is also visible that the application of a magnetic field of 9 T on the sample leads to a decrease of the capacitance while preserving the same global behavior. The dielectric anomaly appears at a slightly lower temperature under 9 T than under 0 T however, a trend that is observed in the similar  $\text{MnWO}_4$ . Above 16 K, both measurements (0 or 9 T) become similar with no effect of the applied magnetic field.

Measurement of capacitance versus magnetic field has been performed at 2 K, in the antiferromagnetic state. Between the extrema of 0 and 9 T, the decrease of capacitance observed previously on  $C(T)$  measurement is confirmed, although a non-linear decrease is observed. In addition to this, a hysteresis of capacitance is clearly detected in the range  $\pm 2 - \pm 7$  T. The brutal increase of the capacitance at  $\pm 2$  T likely correspond to a magnetic field induced transition, to a phase that remains stable up to  $\pm 7$  T.  $C(T)$  measurement performed under 0 T after a measurement cycle at 9 T (not displayed) showed no difference with the measurement

performed at 0 T prior to the application of field. In the end, these observations clearly point out the presence of a magnetoelectric coupling in  $\alpha$ -MnSO<sub>4</sub>, a promising finding that appeal for further characterizations. At the moment, it looks difficult to determine the exact nature of the measured anomaly, and the small variation of capacitance hinder any pyrocurrent measurement in our current setups (further confirmed through preliminary attempts).

The origin and nature of the detected dielectric anomaly may be clarified by neutron diffraction measurements that have been performed to this end, but are not yet ready for interpretation. Anyway, MnSO<sub>4</sub> had been previously selected for this study considering its helical magnetic structure that could induce a magnetoelectric coupling. After successful densification without visible decomposition, dielectric measurements clearly confirm the relevance of MnSO<sub>4</sub> as a fragile material, and the possibility to find a magnetoelectric coupling in similar materials, which is one of the objectives of this study.

#### 2.5.3.1 Conclusion on MnSO<sub>4</sub>

Such as in the case of the previous examples of pyrophosphates and the two carbonates, sintering of MnSO<sub>4</sub> has been successfully achieved, from hydrated commercial powder of MnSO<sub>4</sub>·H<sub>2</sub>O with high densification level (> 95 %). The present exploration of operating conditions impact on sintering efficiency highlight the high complexity of sintering mechanisms involved in MnSO<sub>4</sub> Spark Plasma Sintering. From the initial powder hydration level to the presence of a reversible phase transition, and going through the impact of protocol on *in situ* dehydration, many parameters can determine the final sintering level of pellets. Although almost 100 experiments were necessary to determine the possible sintering conditions and the influence of each operating parameter, the final results show both the complexity of the material and the broad tunability of SPS setup.

The present results confirm once more the high efficiency of sintering using SPS setup. MnSO<sub>4</sub> sintering differs from the previous example in the way that sintering has been performed below the decomposition temperature of the phase. However, the very low temperature used, 400 °C, represents a great progress in lowering sintering temperatures.

Finally, the observation of pellets composed of mixed MnSO<sub>4</sub> and MnSO<sub>4</sub>·H<sub>2</sub>O suggests a possible sintering of the hydrated phase. We demonstrated the stabilization of hydrate through

the application of pressure. Thus, using high pressure and lower temperatures could enable the sintering of this phase. Lowering sintering temperature below 350 °C brings to the typical temperature range used in solvothermal sintering, and the presence of water in the phase could be an asset for such sintering. Sintering attempts have been performed using both SPS and solvothermal sintering method, and will be developed in the following section.

## **2.6. Comparison of Spark Plasma Sintering and Solvothermal sintering of $\text{MnSO}_4 \cdot \text{H}_2\text{O}$**

In the present case, fewer experiment were necessary since most of the understanding and the experimental conditions determination has been performed previously. Therefore, highly pure dehydrate,  $\text{MnSO}_4 \cdot 2\text{H}_2\text{O}$ , will be mostly used for both SPS and solvothermal experiments. Only the few first experiments in SPS were performed using the monohydrate and these will be specified. Earlier in section 2.5.1, page 192, have been presented both precursors. Their two major differences are hydration level (1 to 2 water molecules) and their dehydration temperatures. In the case of the dihydrated form, water is released at a higher temperature than for the monohydrate (300 versus 250 °C according to TGA under air, respectively).

### **2.6.1 Spark Plasma Sintering (SPS)**

We have already seen that the pure anhydrous phase can be obtained when heating the hydrated sample at low pressure. When a pressure above 100 MPa is applied, dehydration is repelled to higher temperatures, around 380 °C. Thus, applying pressure during the whole thermal cycle could allow sintering and prevent water release, preserving the hydrated phase.

Table 19: Sintering conditions of  $MnSO_4 \cdot 2H_2O$  samples and final densities of resulting pellets

| Sample number   | Temperature (°C) | Pressure (MPa) | Dwell time (min) | Compactness (%) | XRD on pellet            |
|-----------------|------------------|----------------|------------------|-----------------|--------------------------|
| 89              | 200              |                | 30               | 97.6            | Pure $MnSO_4 \cdot H_2O$ |
| 90              | 200              | 350            | 5                | 97.1            | Pure $MnSO_4 \cdot H_2O$ |
| 91              | 100              |                | 30               | 93.5            | Pure $MnSO_4 \cdot H_2O$ |
| 77(monohydrate) | 200              | 400            | 10               | 96.7            | Pure $MnSO_4 \cdot H_2O$ |

Table 12 summarizes sintering conditions of three different sintering attempts on dihydrate  $MnSO_4 \cdot 2H_2O$  and one on monohydrate  $MnSO_4 \cdot H_2O$ . In the first three examples, conditions have been selected to preserve hydration, through the application of pressure at first step and with a subsequent thermal ramp of 20 °C/min for all samples. The ramps are lower than the one used in the sintering of anhydrous  $MnSO_4$  in order to have a better control of the temperature when reaching the dwell temperature which is noticeably lower. All samples are made of 1 g of powder. The last sample presented in table 5 is a sample sintered using monohydrate powder, which was initially used for a few preliminary attempts on the sintering of  $MnSO_4 \cdot H_2O$ . These attempts motivated the present comparative study with hydrothermal sintering, performed with dihydrate powder. This example of the sintering of the monohydrate was performed in conditions close to those used in the present study, and show that sintering of  $MnSO_4 \cdot H_2O$  can be achieved either from dihydrate or monohydrate precursor. Here the conditions are not strictly comparable but the resulting density is clearly in line with the one obtained from dihydrate samples. Further comparison of the resulting pellets will be presented in the following.

In the three conditions experienced, a dense pellet is obtained at the end of the process, with very good density (all above 93 %). It is very interesting to see it is possible to achieve effective densification at temperatures as low as 100 °C and to obtain ceramic from a hydrated phase. The evolution of density between sintering at 100 °C and 200 °C for 30 min reaches 4 %, which is quite high, especially when going from 93 to 97%. It means the sintering kinetics at 200 °C is way faster than at 100 °C. Even after 5 min of dwell time, density at 200 °C rises up to 97.1 %. Here it looks like sintering is very fast, and most of the densification is achieved after few minutes at the dwell temperature, a situation which is hardly ascribable to a solid-state mechanism, in such conditions. In solvothermal mechanisms, discussed in section 1.1.6.3.2,

page 27, fast densification takes place when a liquid phase is present and participates to the sintering mechanism. Thus, our results confirm the interest of a comparison with solvothermal sintering to explore the mechanism involved in Spark Plasma Sintering of  $\text{MnSO}_4 \cdot \text{H}_2\text{O}$  at low temperature.

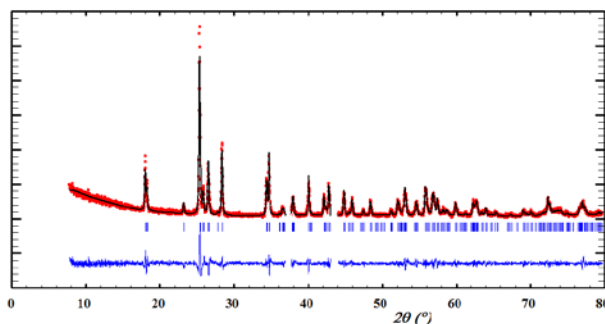


Figure 142: XRD profile refinement of  $\text{MnSO}_4 \cdot \text{H}_2\text{O}$  pellet sintered in SPS at  $100^\circ\text{C}$ , missing parts at  $37^\circ$  and  $44^\circ$  correspond to the sample holder's diffraction signal

Figure 142 represents XRD profile refinement of the pellet obtained after  $100^\circ\text{C}$  and 30 min sintering. It confirms the phase purity of the hydrated phase, with no additional phase detected. Profile refinement gave access to the lattice parameters and a comparison is made with the precursor powder.

Table 20: Lattice parameters refined with XRD patterns for  $\text{MnSO}_4 \cdot 2\text{H}_2\text{O}$  powder and  $\text{MnSO}_4 \cdot \text{H}_2\text{O}$  pellets sintered in SPS

| Sample | a (Å)      | b (Å)      | c (Å)      | V (Å <sup>3</sup> ) |
|--------|------------|------------|------------|---------------------|
| Powder | 7.7675 (1) | 7.6649 (1) | 7.1232 (1) | 381.68 (1)          |
| Pellet | 7.7713 (3) | 7.6616 (2) | 7.1289 (2) | 382.00 (2)          |

it is clear that sintering can be achieved without any significant evolution of the cell parameters with respect to the commercial powder used as a reference.

These results confirm the possibility to sinter the phase at low temperature with conservation of the phase purity and crystallinity. This way, it was possible to obtain this hydrated phase in ceramic form with a good conservation of the material.

In order to confirm the nature of the pellets obtained, TGA have been performed on pellets after sintering for both monohydrate and dihydrate precursors.

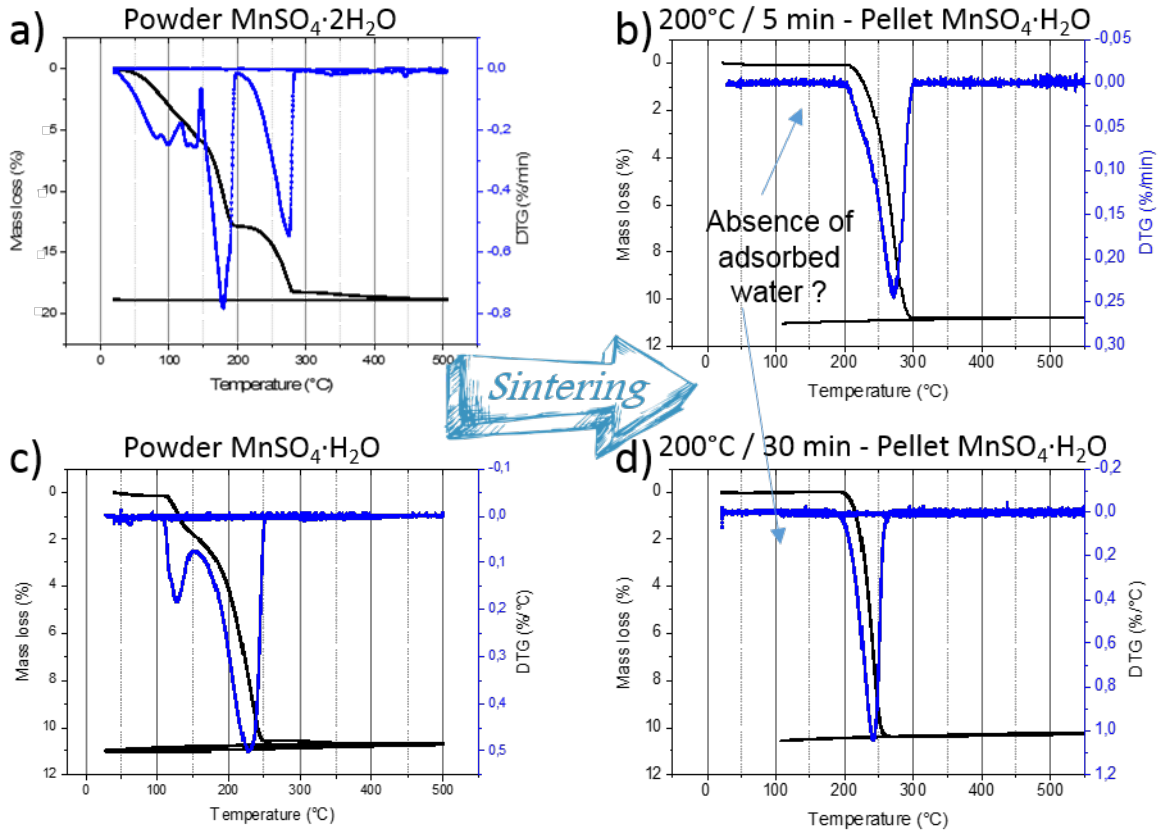


Figure 143: TGA under air of (a) dihydrate powder, (b) 200 °C - 5 min sintered pellet initially from dihydrate powder, (c) monohydrate powder and (d) pellet sintered at 200 °C - 30 min from monohydrate precursor

On Figure 143 is represented the TGA performed on precursors and pellets sintered at 200 °C. In both cases, the final pellet is composed of monohydrate composition (with 10.4 % wt. loss in both cases). However, a difference remains, following sintering, in the temperature of final dehydration, which is correlated to that of the precursor powder corresponding to each pellet. Thus, while TGA confirms that the pellets obtained are constituted of  $\text{MnSO}_4 \cdot \text{H}_2\text{O}$ , it also reveals a surprising “memory” of the parent phase through the dehydration temperature.

On Figure 144 are visible the different microstructures obtained for the three  $\text{MnSO}_4 \cdot \text{H}_2\text{O}$  pellets obtained after sintering of  $\text{MnSO}_4 \cdot 2\text{H}_2\text{O}$ . For the three samples, the microstructures observed on SEM are very dense and consistent with the measured densities. When comparing samples sintered at 200 °C for 5 and 30 min, a difference of microstructure is visible. In the case of sintering at 200 °C for 30 min, the grains are more homogeneous in size (a few  $\mu\text{m}$ ) and shape than the one sintered during 5 min, and some are faceted. In the case of sintering at 100 °C for 30 min, the microstructure is much different, with grain sizes presenting a high polydispersity with small grains of about 100 nm and large ones of 1 to 2  $\mu\text{m}$ .

Here also, different regimes appear, with densification of small grains at 100 °C, and grain growth occurring at 200 °C. A longer dwell time seems to enhance grain crystallization observable through the sharp form of the grains at 200°C and 30 min.

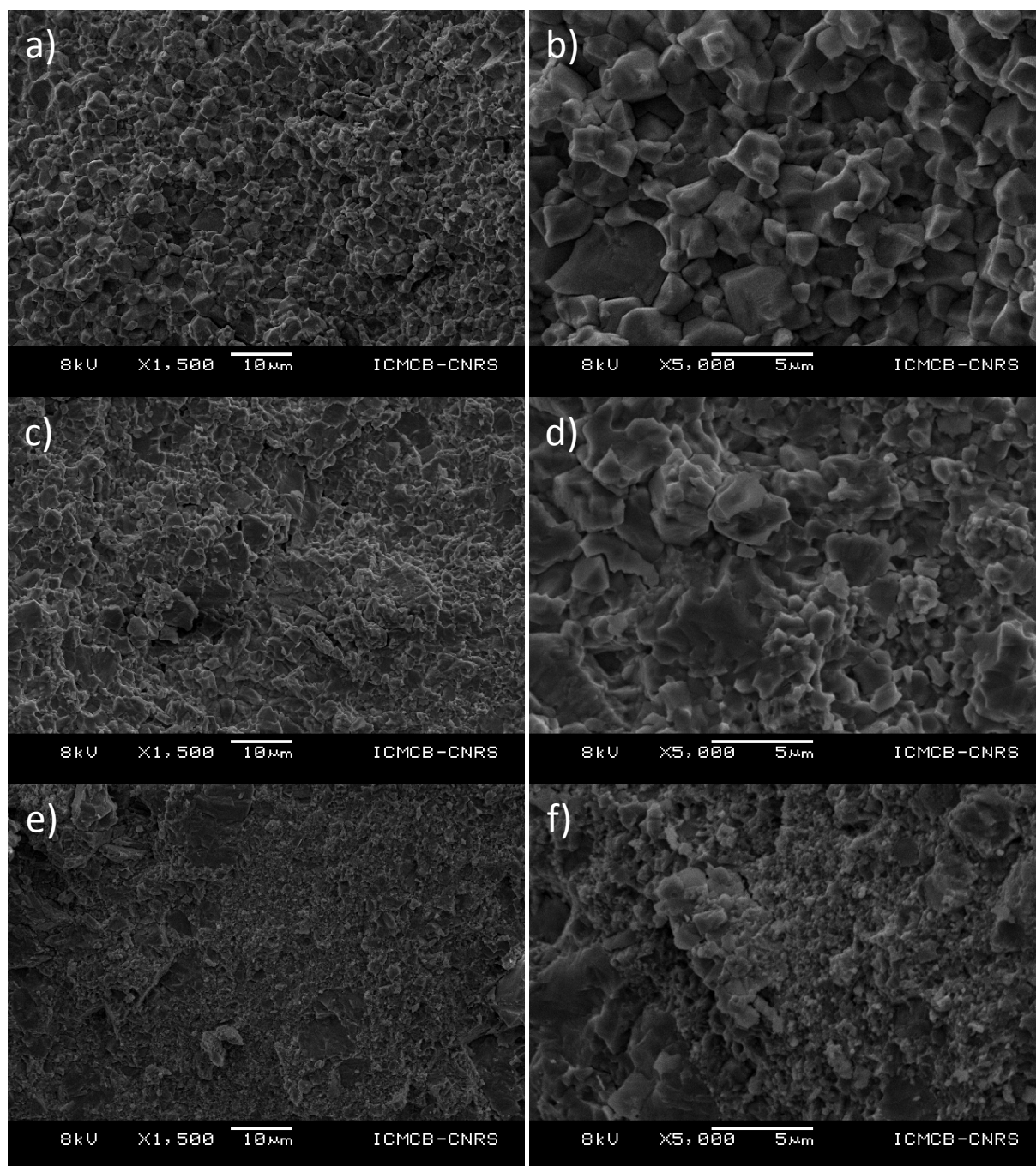


Figure 144: SEM images of  $MnSO_4 \cdot H_2O$  pellets sintered at (a-b) 200 °C/30 min, (c-d) 200 °C/5 min and (e-f) 100 °C/30 min

It is likely that such an effective sintering at such low temperatures can be related to the presence of water in the sample. This idea is also correlated with the previously presented results on the anhydrous phase, for which sintering is possible above 380 °C after dehydration, but impossible

at 350 °C. To give a clearer view of the sintering behavior of the various form of manganese sulfate, a schematic sintering chart is draw in the following.

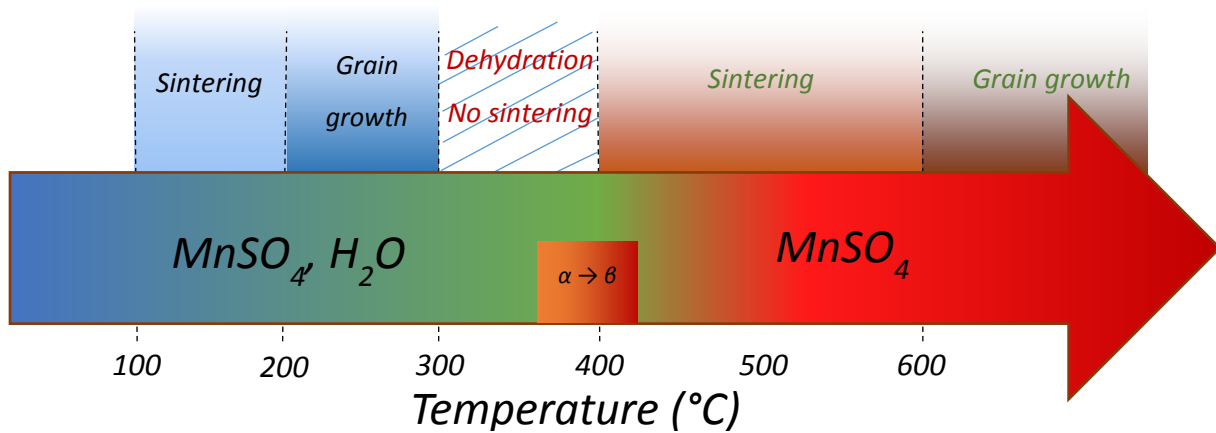


Figure 145: Chart representing the different stability domain of hydrated and anhydrous  $MnSO_4$ . Sintering behavior is summarized in the upper part and  $\alpha$  to  $\beta$  phase transition is represented on the arrow

On Figure 145 is proposed a representation of the sintering behavior of  $MnSO_4$  versus temperature. The interesting part of this chart is the one located at the center, between hydrated and anhydrous forms of manganese sulfate. It is possible to sinter the hydrated form from 100 °C to 200 °C, and then it is possible to sinter anhydrous phase above 380 °C. But it looks that in an intermediate temperature range, sintering is hindered by dehydration, and although compact pellets can be obtained, their cohesiveness is not satisfying.

### 2.6.2 Solvothermal sintering of $MnSO_4 \cdot H_2O$

In the setup used for solvothermal sintering, pressure is applied manually and precision on its value is lower than the one in SPS conditions. This way, direct comparison of densification between SPS and solvothermal sintering experiments performed in the same conditions must take that information into account.

The solvothermal setup we dispose of is quite close to the one described by Yamasaki & *al.*<sup>186</sup> in their first work on hydrothermal hot pressing in 1986. The system has been described in section 1.1.6.3.2 on page 27. Operating conditions for our system are limited to 350 °C and 350 MPa, and thermal ramp is limited to 15 °C/min. SPS sintering of hydrated phase previously presented have then been performed under 350 MPa to be comparable with the applied pressures in solvothermal sintering. Sintering has been performed with commercial powder, without addition of water, the only water available being the one initially present in the sample.

Here again, the dihydrated form of  $\text{MnSO}_4 \cdot 2\text{H}_2\text{O}$  has been used for the sintering. Results are presented in Table 14 below.

Table 21: Hydrothermal sintering conditions of different experiments for  $\text{MnSO}_4 \cdot 2\text{H}_2\text{O}$

| Sample number | Temperature (°C) | Pressure (MPa) | Dwell time (min) | Compactness (%) |
|---------------|------------------|----------------|------------------|-----------------|
| H03           | 200              | 350            | 60               | 95.9            |
| H02           |                  |                | 30               | 95.5            |
| H05           |                  |                | 5                | 94.4            |
| H08           | 150              |                | 30               | 94.9            |
| H07           | 100              |                |                  | 91.2            |

As for SPS sintering, temperatures have been tested from 100 to 200 °C and pressure was always kept constant at 350 MPa. Dwell times has been tuned to see its impact on final sintering. In every case, the experiment resulted in a very cohesive and dense pellet, enabling bulk characterization of density, microstructure and dielectric properties. Compactness up to 96 % is very high for such low temperature and, although slightly smaller, appears in the same range of that of SPS sintered pellets. Both techniques were effective in delivering hydrated  $\text{MnSO}_4 \cdot \text{H}_2\text{O}$  pellets in similar operating conditions. Even in the case of the sample sintered at 100 °C, densification of 91.2 % is obtained, and remains 4.3 % lower the one performed in the same pressure and time conditions but at 200 °C. In SPS, this evolution is comparable (4 % difference between 100 and 200 °C sintering). When comparing samples at 100, 150 and 200 °C, density evolution is not linear. It seems there is a strong increase of density from 91.2 to 94.9 (i.e. 3.7 %) when sintering at 150 °C instead of 100 °C. Increasing temperature up to 200 °C only brings an evolution of density of 0.6 % (95.5 % at 200 °C). Activation of sintering occurs at 100 °C or below, but a strong increase of densification kinetics occurs between 100 and 150 °C.

Increase of dwell time from 5 to 60 min at 200 °C results in an increase of 1.5 % density, which means that even if the densification level still increases with time, the major part of densification occurs in the 5 min after reaching dwell temperature. This is in good agreement with liquid state sintering mechanisms in which densification is fast when liquid phase is present, and the more

the liquid is expelled from the sample (here in the free spaces for water retreat), the more sintering kinetics slows down.

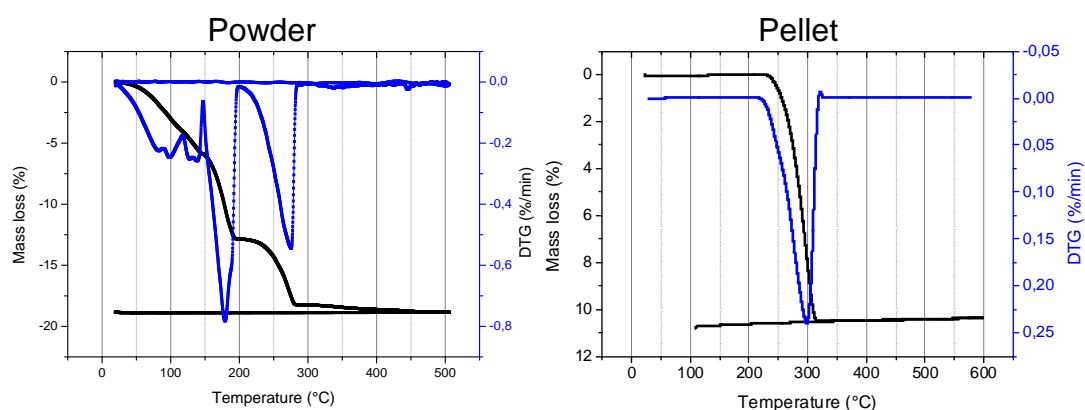


Figure 146: TGA under air of solvothermal sintered pellet of  $\text{MnSO}_4 \cdot \text{H}_2\text{O}$  at  $200\text{ }^\circ\text{C}$  for 30 min and the initial  $\text{MnSO}_4 \cdot 2\text{H}_2\text{O}$  used as precursor

Figure 146 displays the TGA of resulting pellet after  $200\text{ }^\circ\text{C}/30\text{ min}$ . In the precursor powder,  $\text{MnSO}_4$  crystallizes with the monohydrate structure  $\text{MnSO}_4 \cdot \text{H}_2\text{O}$  but is in a dihydrated composition according to TGA. After sintering, such as in the case of SPS, pellet obtained loses 10.5 % of its mass during TGA, which corresponds to a single  $\text{H}_2\text{O}$  per formula unit, which is confirmed by the observation of pure anhydrous phase in XRD (not displayed). This means the final pellet has a composition of pure  $\text{MnSO}_4 \cdot \text{H}_2\text{O}$  with only structural water remaining in the sample. Noticeably, the dehydration temperature of the pellet is found significantly higher than that of commercial monohydrate powder, and even higher than the precursor dihydrated powder.

TGA of the other samples made with solvothermal sintering (not displayed here) present the exact same behavior and mass loss (same peak shift to higher temperature), whatever the sintering conditions explored (temperature and time). This means water release to pass from  $\text{MnSO}_4 \cdot 2\text{H}_2\text{O}$  to  $\text{MnSO}_4 \cdot \text{H}_2\text{O}$  is complete when reaching  $100\text{ }^\circ\text{C}$  (and this water release is probably related to the sintering occurring at this temperature) and no more water loss occurs between  $100$  and  $200\text{ }^\circ\text{C}$ . This is comparable with the results obtained in SPS.

SEM images were taken from these pellets after sintering. Figure 147 displays these images and show a dense microstructure consistent with the measured densities. In all cases, no open porosity can be seen and densification is very good. From samples sintered at  $200\text{ }^\circ\text{C}$  during 5,

30 and 60 min, microstructure evolution can be observed through a small increase of grain size from 3 to 5  $\mu\text{m}$  for 5 min of sintering, up to 5 to 10  $\mu\text{m}$  for 60 min of sintering. The evolution of grain size seems to be similar both in solvothermal and SPS, except the one of the pellet sintered at 100 °C. It is surprisingly dense, with presence of sharper grain edges than in samples sintered at higher temperatures, and this suggest that intragranular porosities have a significant contribution to the final density of this sample.

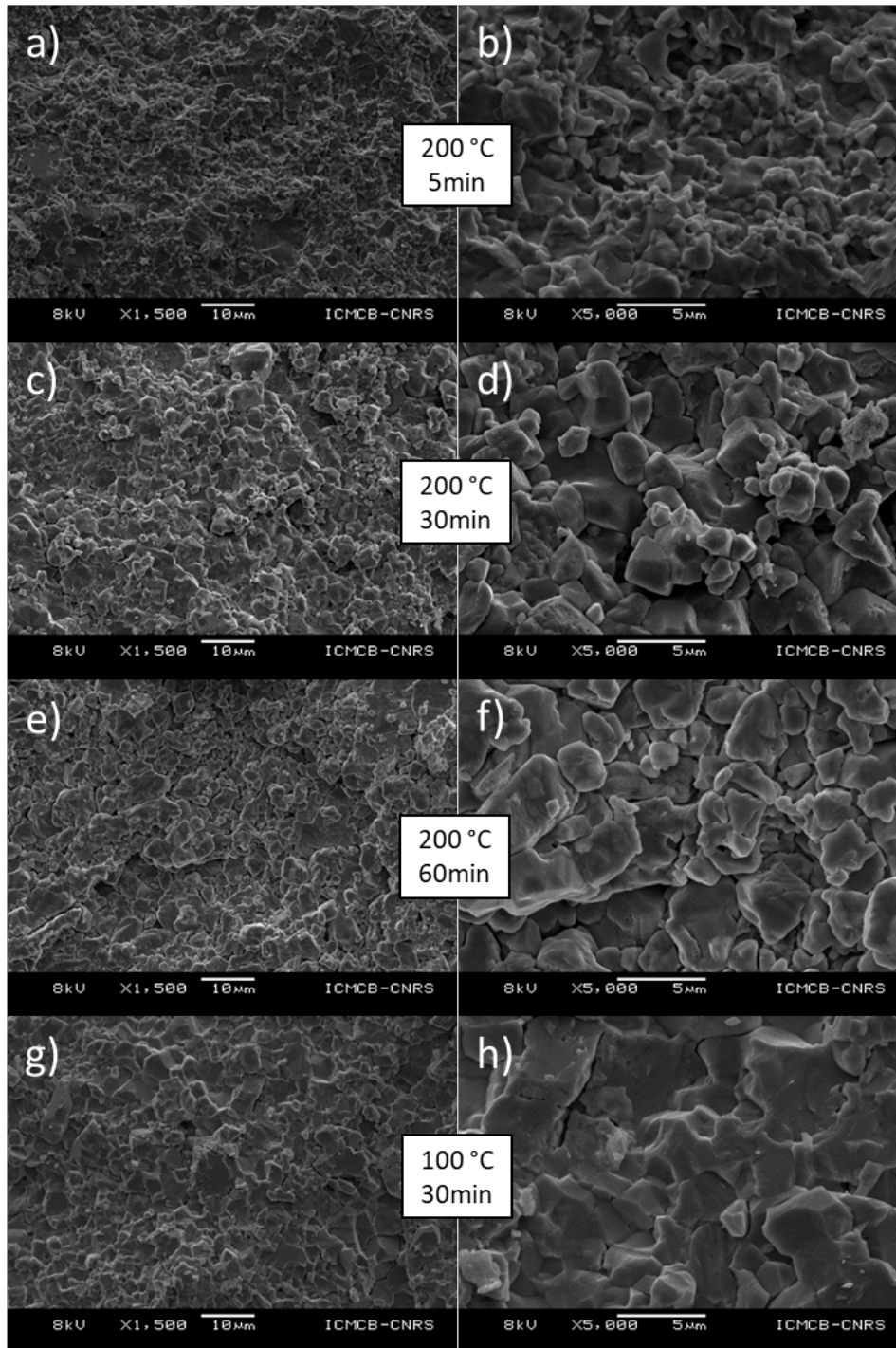


Figure 147: SEM images of pellets fracture of (a-b) 200 °C/5 min (c-d) 200 °C/30 min, (e-f) 200 °C/60 min and (g-h) 100 °C/30 min.

Figure 148 displays an example of higher magnification in the microstructure of pellet sintered at 200 °C for 5 min. On this sample are visible some nano-sized holes in a grain. These ones seem to correspond to the remaining porosity after fast water release that couldn't be removed because of either too high water content, or a too high thermal ramp applied on the sample.

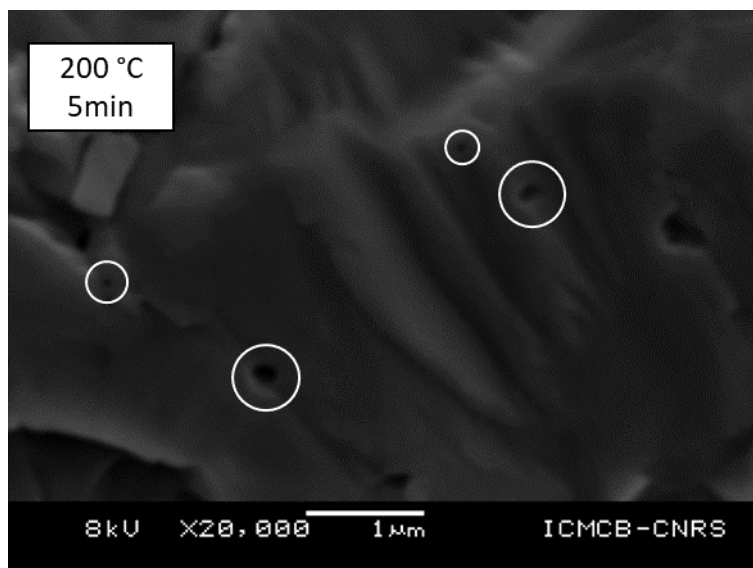


Figure 148: SEM image of THH03 sintered at 200 °C for 5 min, white circles highlight pore locations

### 2.6.3 Discussion on sintering of $\text{MnSO}_4 \cdot \text{H}_2\text{O}$

Sintering of hydrated  $\text{MnSO}_4 \cdot \text{H}_2\text{O}$  has been performed using two different methods, starting from two different hydrated samples, with high densification levels (over 90 %) at temperatures as low as 100 °C.

As presented earlier, both techniques gave comparable densification results. Time dependence of sintering, measured through densification evolution at 200 °C for various dwell times, shows small evolution of the densities for both methods, thus showing the important slowing of sintering kinetics. In the opposite, temperature dependence is more important. In both cases, about 4 % density increase is obtained when increasing sintering temperature from 100 to 200 °C. In solvothermal sintering was also explored 150 °C sintering temperature that gave density close to the one obtained at 200 °C which points out a non-linear behavior of densification versus temperature. It would be interesting to confirm this assertion through a SPS sintering attempt in the same conditions (150 °C – 350 MPa – 30 min) and see if the evolution of densification is the same as for solvothermal sintering.

In the end, this comparative study points out how the two densification methods yield comparable results. It means hydrothermal reactions are likely involved when performing SPS at low temperature. Some observation of hydrothermal reaction have already been evidenced in SPS<sup>232</sup> and support this idea. The remaining question here is the role of electric current,

sintering medium (vacuum in SPS, liquid in solvothermal sintering), which are the major differences between both techniques.

Grain growth and grain shape sharpening are different in the two cases. The biggest difference is observed for samples sintered at 100 °C and 30 min. Solvothermal sintering leads to big grains of few  $\mu\text{m}$ , whereas SPS leads to pellet made of grains of few hundreds of nm. Even if their respective densities are close (91.2 and 93.5 % respectively), it appears the densification process is not strictly the same, especially matter diffusion which seems to be different. For the other conditions however, the difference between SPS and solvothermal results are negligible, which points sintering mechanisms which are either similar or faces the same kind of limitations.

In the end, because of the differences observed at low temperature, it is difficult to confirm that a simple hydrothermal process is responsible for the densification observed in SPS experiments. The use of electric current and the low pressure of the SPS chamber must be involved and somehow responsible for the differences observed between both techniques.

#### 2.6.4 Physical characterization

During this work,  $\text{MnSO}_4 \cdot \text{H}_2\text{O}$  clearly has an important role in sintering. Highly densified pellets have been obtained for the hydrated phase and therefore appear important to characterize. Solvothermal and SPS sintered pellets were measured in the same conditions using PPMS to compare their dielectric behavior.

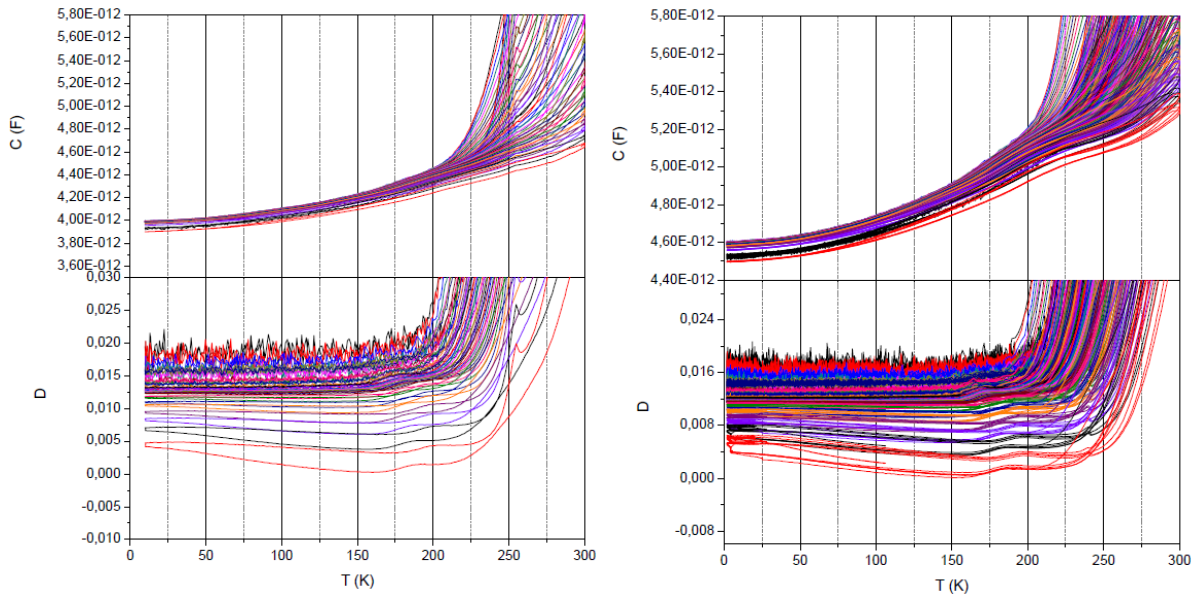


Figure 149: Capacitance and dielectric losses of  $\text{MnSO}_4 \cdot \text{H}_2\text{O}$  performed on pellets sintered in (left) SPS and (right) solvothermal

Both samples have low dielectric losses of 0.02 and below in the range 10-200 K, which demonstrates the high quality of sintering and the high densification of both pellets. In the whole temperature range, no dielectric anomaly is detected. Losses and capacitance become important above 200 K which seems to be related to some conductivity of the samples. Both samples present remarkably similar dielectric properties, and the difference of capacitance can actually be related to different sizes of the samples that were previously broken for the sake of SEM observation.

As explained previously,  $\text{MnSO}_4 \cdot \text{H}_2\text{O}$  has a different magnetic structure than  $\text{MnSO}_4$ . Antiferromagnetic arrangement of  $\text{MnSO}_4 \cdot \text{H}_2\text{O}$  is not expected to exhibit a magnetoelectric coupling and this is verified by the absence of anomaly in the capacitance measurement around  $T_N$  at 16 K.

### 2.6.5 Conclusion on $\text{MnSO}_4 \cdot \text{H}_2\text{O}$

As it could be expected from previous observation of sintering in  $\text{MnSO}_4$  system, it was possible to sinter the hydrated phase  $\text{MnSO}_4 \cdot \text{H}_2\text{O}$  with high densification level (above 90 %) down to a temperature of 100 °C and 30 min of sintering and 350 MPa. This has been both possible through SPS and hydrothermal sintering techniques. The comparative study between these two techniques was useful to highlight some clues of hydrothermal mechanisms involved in the

sintering of the phase during SPS treatment. However, for the lowest temperature explored, 100 °C, the difference is more important than for the higher temperatures. Therefore, there must be a more complex mechanism implying the presence of electric current, and the vacuum atmosphere used for sintering.

These results not only widen the scope of phase that have been sintered in SPS with a first example in the hydrate phases, but also shows the first example of ceramic obtained above 90% of theoretical density at temperature as low as 100 °C. This is a promising result which confirms the potential of SPS at low temperatures, especially for prospection.

Dielectric measurements did not show any particular anomaly, which was expected since the crystal structure of the phase did not give any clue of a possibly interesting observation. The main object in the present work on  $\text{MnSO}_4 \cdot \text{H}_2\text{O}$  concerns the sintering.

## **2.7. Chapter conclusion**

Three main steps have been followed throughout this chapter. First, crystal chemical approach has been developed to find materials which could possibly exhibit interesting (multi)ferroic or magnetoelectric properties in systems that are usually unexplored because of processing issues. The second step, which was the main part of this work, was the experimental synthesis and sintering of samples according to the previously determined objectives. Finally the last step was the measurement of physical properties of the dense ceramic samples obtained.

An important part of the work was dedicated to synthesis, and if it has been described quite fast, it actually represents a big part of working time. It has been dedicated to three materials reported in the literature but which synthesis were performed through pathways inadapted to the production of significant quantities of powder, but which were successfully tweaked. The development of these synthesis, mainly concerning carbonate phases, is a first interesting result since the previous works available were difficult to reproduce and were allowing only small amounts quantities of powders. In view of the development of fragile materials as reliable and sustainable alternative to classic functional materials (oxides...), the availability of efficient and possibly up scalable synthesis methods is a critical step.

The main part concerns the sintering. In all cases, it was very efficient and yielded results beyond expectations. The main conclusions are

- the breathtaking efficiency of Spark Plasma Sintering at low temperatures, between 100 and 400 °C with compactness above 90 %,
- its versatility with the possibility to sinter materials with different compositions and structures (carbonates, pyrophosphate, sulfate, hydrate),
- its specific reactivity with several examples of in situ dehydration and preparation of compounds in ceramic form that could not be obtained in powder form,
- and finally the stabilization of phases at or above their decomposition temperatures (see Figure 150).

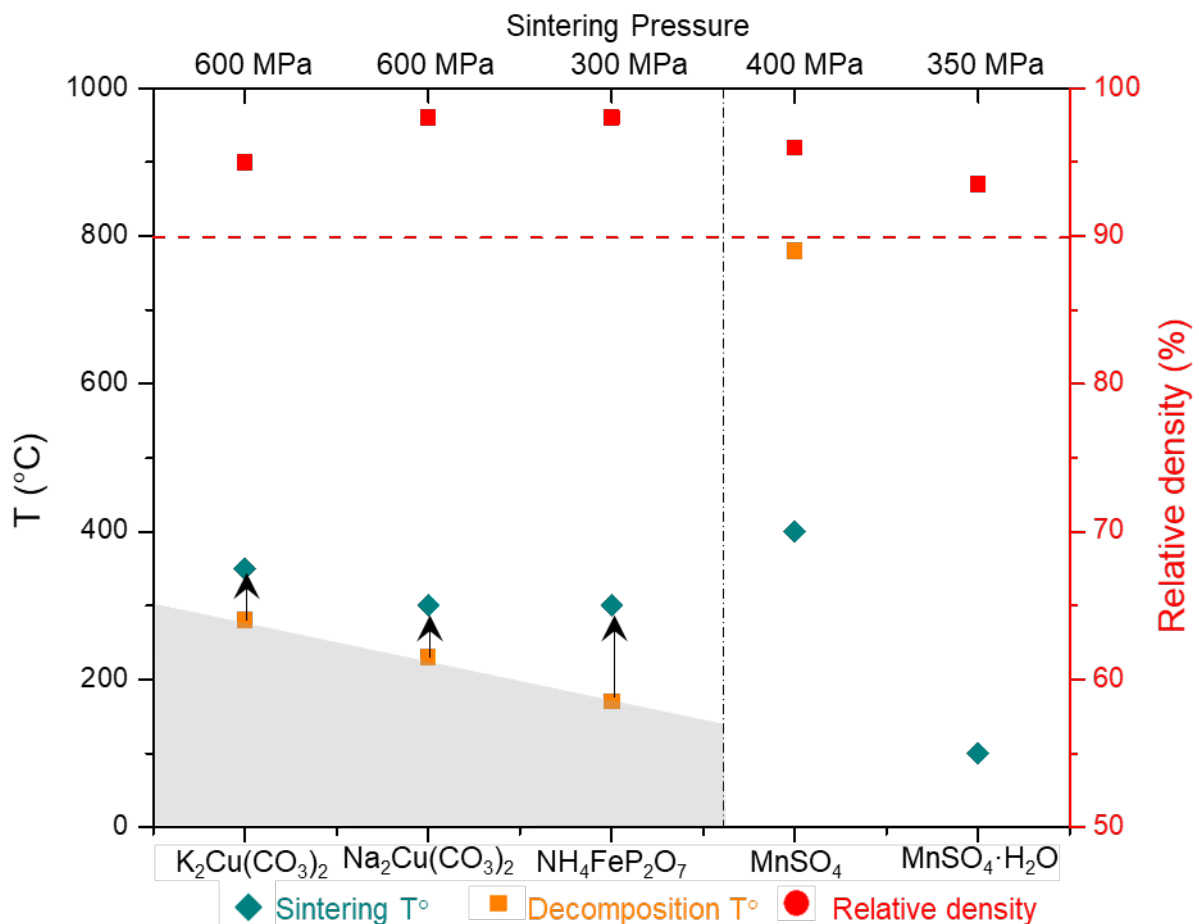


Figure 150: Sintering conditions of temperature and pressure, compared to decomposition temperatures of the various phases, with their corresponding relative densities. Grey area denotes the stability region of the considered materials under air. Pale green area denotes the extra stability in SPS conditions

The examples of  $\text{MnSO}_4$  and  $\text{MnSO}_4 \cdot \text{H}_2\text{O}$  were useful to explore the influence of sintering parameters on the final densities of ceramics, and highlighted complex sintering mechanisms, with the influence of hydration of initial powder, dehydration steps, the presence of phase transition. Sintering of  $\text{MnSO}_4 \cdot \text{H}_2\text{O}$  in hydrothermal conditions was also useful to highlight the similitudes with results obtained in SPS. Through all this work, the opportunity to use SPS as a prospective tool to obtain new ceramics that could not be prepared by other means is more than confirmed.

The exploration of physical properties revealed small dielectric anomalies that were difficult to interpret, that will require further characterization. For all samples, the dielectric measurement confirmed once again the high quality of sintering with very limited dielectric losses in ceramics that are mostly nanostructured. More importantly, in the case of  $\text{MnSO}_4$  and  $\text{Na}_2\text{Cu}(\text{CO}_3)_2$ , the experimental data clearly gives some clues of the presence of magnetoelectric coupling, highlighting the relevancy of fragile materials as functional materials.

Carbonates have been an important part of this work. During this work, attempts were lead on the synthesis of a new ammonium containing compound,  $(\text{NH}_4)_2\text{Cu}(\text{CO}_3)_2$  derived from the two other carbonates cited. The synthesis did not give the expected result, but a molecular material was synthesized. Preliminary observations made on this compound are detailed in a last chapter that extends the potential of low temperature Spark Plasma Sintering.

# Chapter 3: Towards molecular ceramics

Development of SPS sintering at low temperatures down to 100 °C paves the way to new possibilities. Few ceramic materials have been successfully sintered using low temperature, high pressure SPS. In the present work, our attention has been focused on materials from copper carbonate family. Two compounds, containing Na<sup>+</sup> and K<sup>+</sup> have been successively synthesized, sintered and characterized. Other attempts have been made to explore another compound from this series, trying to replace alkaline element with ammonium, NH<sub>4</sub><sup>+</sup>. Such replacement could be interesting in terms of dielectric properties, especially if this ammonium group can possibly be polarized with an asymmetric environment. This has been highlighted in NH<sub>4</sub>CuCl<sub>3</sub> where polarization arises from ammonium groups<sup>202</sup>. Actually, no paper mentions the existence of such composition. Starting from this point, attempts have been made to synthesize it using the same way as the one used for K containing compound. This synthesis quickly lead to highly crystallized material. Obtained crystals are actually a molecular compound, (NH<sub>3</sub>)<sub>2</sub>Cu(COOCH<sub>3</sub>)<sub>2</sub>, otherwise named diamine copper acetate.

In the present chapter, once again, the synthesis, determination, characterization and stabilization of the phase has taken an important amount of experiments, which were possible thanks to the contribution of Vincent Villemot during his bachelor internship.

## 3.1. Synthesis, sintering and characterization of

Synthesis of the phase is realized as described previously for K<sub>2</sub>Cu(CO<sub>3</sub>)<sub>2</sub>, by replacing K<sub>2</sub>CO<sub>3</sub> precursor by (NH<sub>4</sub>)<sub>2</sub>CO<sub>3</sub>. Immediately after filtration, dark purple crystals are obtained.



Figure 151: Picture of crystals obtained after synthesis with average size around 0.5  $\mu\text{m}$

Those crystals can be grinded and characterized by powder XRD and give the pattern presented on Figure 152.

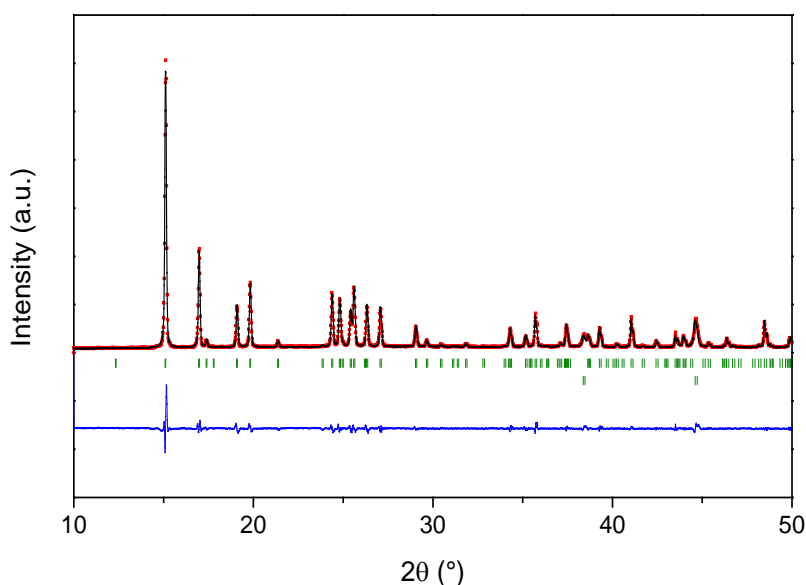


Figure 152: XRD profile refinement on powder of  $(\text{NH}_3)_2\text{Cu}(\text{COOCH}_3)_2$

These crystals exhibit very good crystallinity and phase purity after synthesis. Lattice parameters refinement was then possible and are in good agreement with literature<sup>233</sup>. However, this phase looks very sensitive to temperature and hygrometry. Indeed, after few hours in ambient atmosphere, and because of water vapor, decomposition of the phase occur. A pale blue shell forms little by little around the grains and correspond to another phase that hasn't yet been identified. This shell protects the sample from environmental water and the decomposition slows down after few hours.

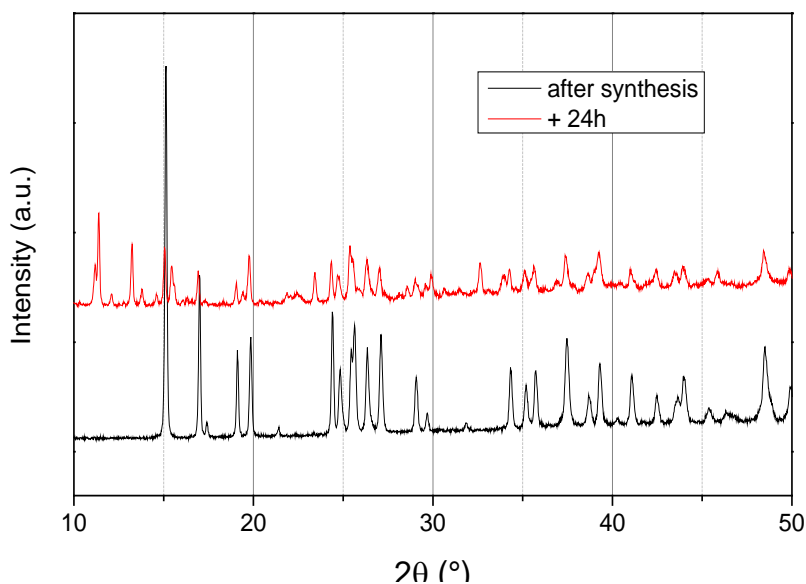


Figure 153: XRD patterns of powder of  $(\text{NH}_3)_2\text{Cu}(\text{COOCH}_3)_2$  (black) after synthesis and (red) after 24h stay in air

Then, powder must be preserved from environmental conditions through storing it in desiccator. Even after few months, no decomposition has been observed.

The only paper referring to this composition deals with its crystal structure<sup>233</sup>. Then, no information about its physical properties has ever been proposed. In order to follow the same scheme as in the previous section, magnetic measurements have been performed on this sample in MPMS down to 2 K.

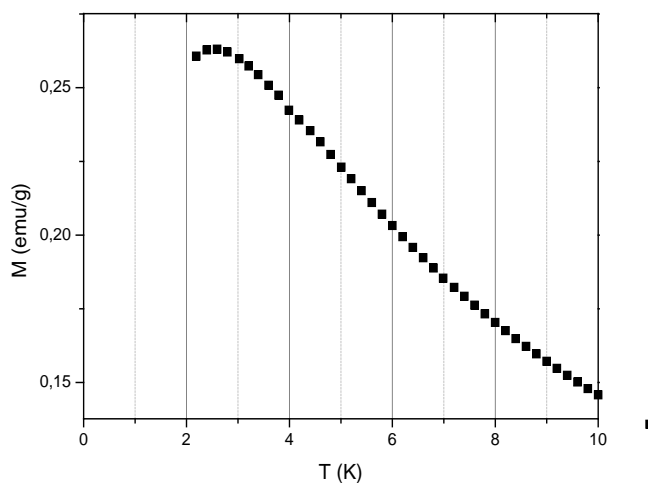


Figure 154: SQUID ZFC measurement of powder after synthesis

Magnetic measurements show an antiferromagnetic transition at 2.8 K with a maximum magnetization of 0.27 emu/g. Both this low transition temperature and low magnetization (with respect to the aforementioned carbonates) results from large Cu-Cu distances in the lattice. The structure of the present compound is made of copper linked to four O<sup>2-</sup> forming a square plan and two NH<sub>3</sub> groups completing the coordinance shell to form an octahedron.

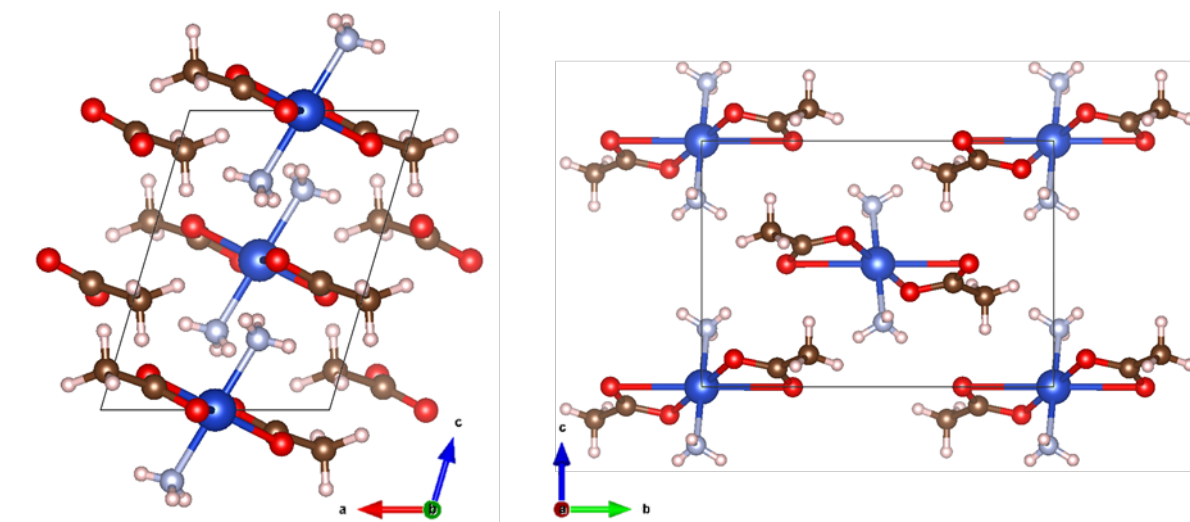


Figure 155: Representations of the molecular structure of  $(\text{NH}_3)_2\text{Cu}(\text{COOCH}_3)_2$  along  $b$  and  $c$  axes

$(\text{NH}_3)_2\text{Cu}(\text{COOCH}_3)_2$  crystallizes in monoclinic space group  $P2_1/c^{233}$  and consists in molecules weakly linked by H-bonding with a smallest Cu-Cu distance along (100) and being 5.43 Å. Such structure, made of weak hydrogen bonding, is then thermally fragile and decomposes at low temperature.

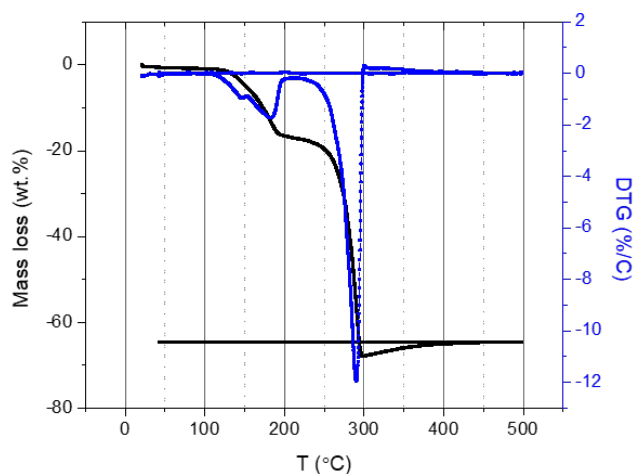


Figure 156: TGA under air of  $(\text{NH}_3)_2\text{Cu}(\text{COOCH}_3)_2$  powder performed at 3 °C/min

TGA measurement performed at 3 °C/min under air shows two mass losses. The first one starting at 110 °C and finishing around 200 °C and the second one being from 250 to 300 °C. After the first mass loss occurring at 110 °C and corresponding in a loss of 17 %, the sample already lost the initial structure and decomposes in non-identified phase (or phases). After the second mass loss, total decomposition occurs. This confirms the low thermal stability induced by weak bonding in the structure.

In order to densify this material, Spark Plasma Sintering was used under the application of high pressure and low temperature to try to stabilize the phase. Pressure was set at 600 MPa, and temperature was set at 300 °C to determine the decomposition point. In order to reduce the interaction between the powder and the surrounding protective foil, tantalum foil was used to cover all the powder's surface.

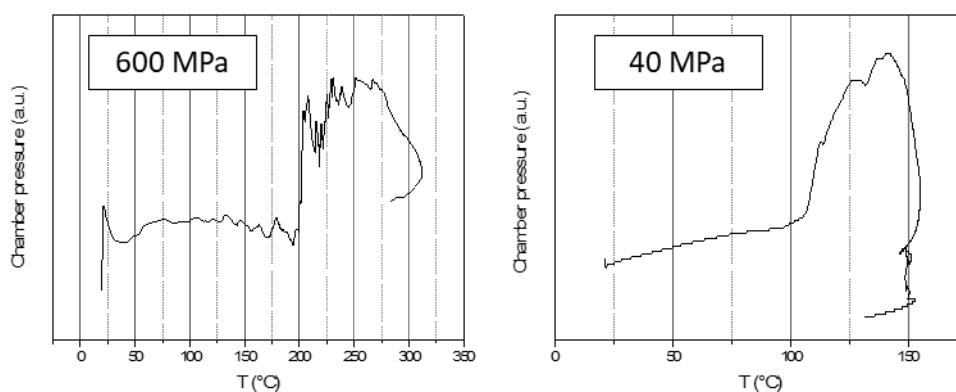


Figure 157: SPS chamber pressure while heating the sample at 300 °C under applied pressure of (left) 600 MPa and (right) 40 MPa

Figure 157 shows the pressure in the SPS chamber when the powder is heated up to 300 °C under 600 MPa and 40 MPa at a constant heating rate of 30 °C/min. After removing the sample from the SPS in both cases, no powder remains, total decomposition of the material occurred. On plotting chamber pressure versus temperature under 600 MPa, it can be seen that chamber pressure is stable up to 200 °C and above this temperature, a massive gas release is observed. This must be due to the decomposition of the material and sets the upper temperature limit to use in order to sinter the sample without decomposition when applying a pressure of 600 MPa. On the other attempt performed under 40 MPa, gas release is observed at 115 °C. This temperature corresponds to decomposition temperature measured in TGA previously.

Comparison of these two results highlights the stabilization effect of applied pressure on the current material. In order to obtain a dense material, *i.e.* to apply the highest sintering temperature achievable without decomposition, maximum pressure of 600 MPa is then the best option.

Sintering has been performed at 180 °C under 600 MPa for 5 min in WC die. Relative density has been measured to be 96.0 %. SEM pictures displayed on Figure 158 shows highly densified microstructure, with no remaining porosity, confirming the measured densification. Because of its intrinsic fragility, the pellet is quite sensitive to the incident electron beam in SEM.

After sintering, pellets, such as the initial powder, is sensitive to atmospheric conditions and has to be stored in a dry space.

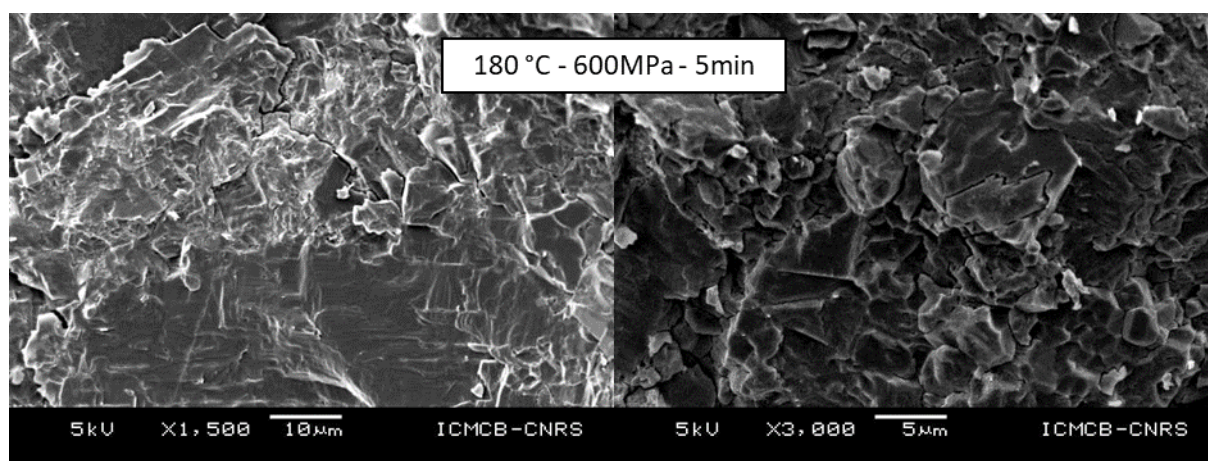


Figure 158: SEM pictures of fractured pellet of  $(\text{NH}_3)_2\text{Cu}(\text{COOCH}_3)_2$  sintered at 180 °C - 600 MPa - 10 min

XRD has been used to confirm the structure of the pellet, and profile refinement gave access to the lattice parameters of both pellet and powder. Refined parameters are summarized in Table 15.

Table 22: Lattice parameters of powder and pellet refined on XRD patterns

| Sample | a (Å)     | b (Å)      | c (Å)     | $\beta$ (deg) |
|--------|-----------|------------|-----------|---------------|
| Powder | 7.5165(1) | 10.2029(1) | 5.4730(1) | 107.255(1)    |
| Pellet | 7.5211(2) | 10.2082(2) | 5.4725(1) | 107.236(1)    |

Refined parameters show differences between powder and pellet below 0.1 %, which demonstrates the high phase quality after sintering. No decomposition seems to occur during sintering at 180 °C and 600 MPa. A high quality, high density pellet is then obtained from this molecular compound.

### **3.2. Physical properties**

Since high density is obtained, dielectric measurements can be performed on this sample. Results are displayed on Figure 159 with both magnetic and dielectric measurements. Magnetic measurement shows a good match between powder and pellet magnetization that confirms property conservation, and then confirms phase purity. Capacitance measurement with respect to temperature show no particular anomaly through all the temperature range explored, but dielectric losses display a peak with a maximum value at 100 K on cooling and 112 K on heating. This small peak is difficult to interpret but may correspond to a very small structural evolution inside the lattice. However, its mere observation is a testimony to the quality of the ceramic. The application of magnetic field brings no significant evolution, although a slight evolution of capacitance is measured. This evolution is also visible on  $M(H)$  measurement at 2 K, where a small evolution of capacitance is found, overall lower than 1 fF. This change of capacitance is too small to be taken into account. The only conclusion about physical properties of this phase we can confirm are the presence of an antiferromagnetic transition at 2.8 K and an anomaly in the dielectric losses at 100 K.

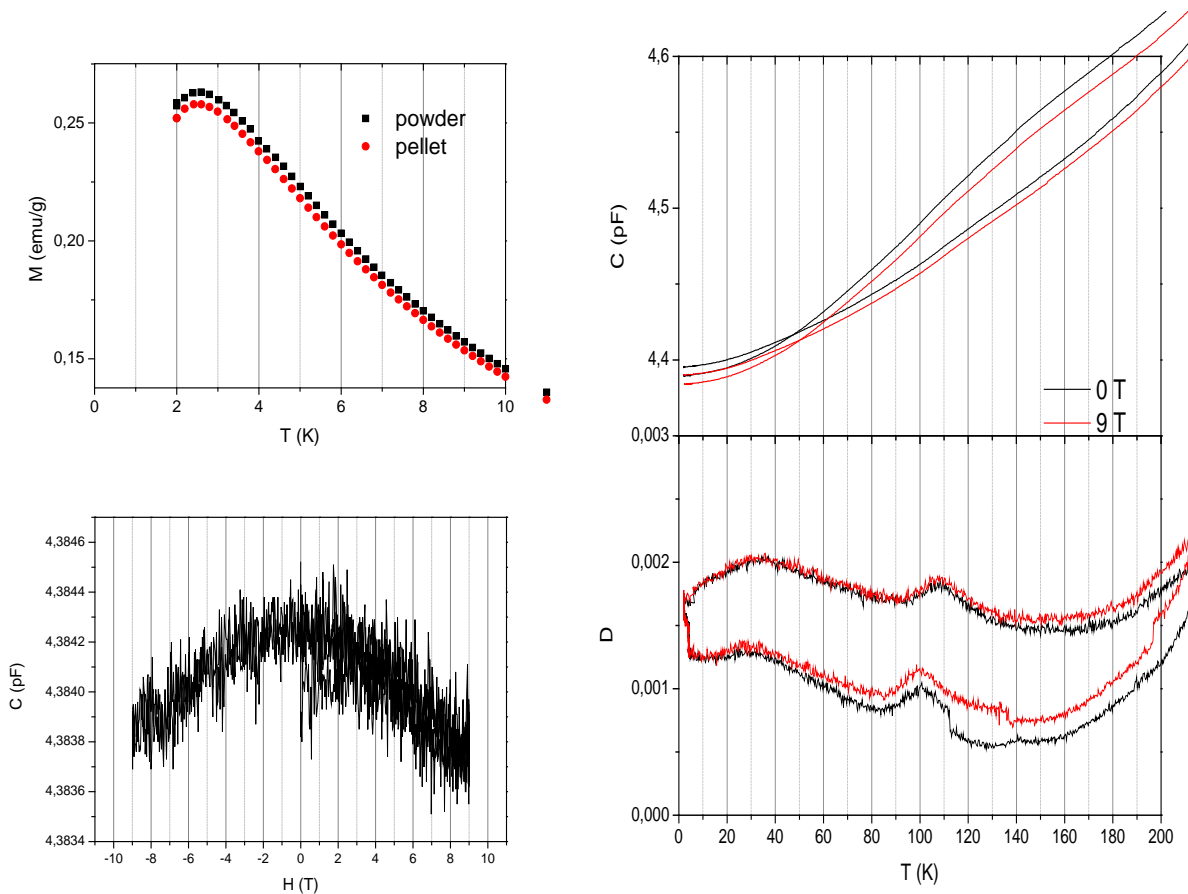


Figure 159:  $(\text{NH}_3)_2\text{Cu}(\text{COOCH}_3)_2$  pellet SQUID and PPMS measurements. Magnetic measurement is performed under 1000 Oe,  $H(T)$  curve is performed at 2 K and 300 kHz. Dielectric measurement displayed has been performed at 300 kHz with and without magnetic field applied on the sample

The main takeaway from the study of  $(\text{NH}_3)_2\text{Cu}(\text{COOCH}_3)_2$  is that it was successfully obtained in ceramic form through Spark Plasma Sintering. The three dimensional cohesion being assured by hydrogen bonds in this materials, this means that the obtained pellet is the first example (to the best of our knowledge) of a *molecular ceramic*.

### 3.3. Towards new materials

In this example, the main purpose is not the existence of an interesting functional property. The real interest here is the unexpected sintering efficiency for such molecular type material. As described all along this work, Spark Plasma Sintering has been used and proved to be very effective at unexpectedly low sintering temperatures. This way, fragile phases decomposing at low temperature (down to 110 C for copper acetate diamine) have been stabilized, sintered, and even purified during SPS treatment. Reaching these temperature range paves the way to a reflection about the possibility to prepare ceramics from materials that were up to now

considered to be impossible to sinter. Now, not only one can consider exploring physical and functional properties of fragile phases of some known materials displaying non-reversible phase transition at low temperatures, but it appears possible to reach high densification for materials such as molecular materials. The main objective of this study, which is to explore and prove that SPS can be used as a prospective tool, has successfully been completed, and the present results on molecular phase largely overrides initial expectations.

In the meantime of this work, a parallel study has been focused on the development of a new sintering technique, aiming to reach low temperature sintering of ceramics using hydrothermal conditions, namely Cold Sintering Process (CSP). High densification levels for a wide panel of compositions have been reached using this technique below 200 C during few tens of minutes. Mechanisms have been explored, and limitations for this technique have been identified<sup>192</sup>. Dissolution is necessary in this process and makes the technique difficult or sometimes impossible to use if different cations have different dissolution behavior. Some materials require further annealing following CSP. This highlights both the interest that is focused on lowering sintering temperature and also the interest to develop various techniques in parallel so that they have different application conditions and can be optimal for different materials, covering a wide scope of phases with their complementarity.

Sintering molecular phases has now been proved to be achievable through the present work, and in the same time, CSP has been used to sinter together ceramics and thermoplastic polymers<sup>234</sup>. Considering these two results now opens, in a technological approach, the possibility to explore new composite materials with a wide range of properties, especially for electronic properties, tunnel barriers for spintronic application or even transparent materials.

## Part conclusion

Through a global approach mixing in the same time synthesis, solid state chemistry, material processing and physical properties investigation, the present work proposed, then demonstrated, the feasibility of accessing new materials properties in various chemical and crystal families, with Spark Plasma Sintering as pillar part. Crystal chemical approach has been developed to select materials with complex structures and possible interesting multiferroic and magnetoelectric properties. Their fragility (essentially limited thermal stability) was the principal issue forbidding the exploration of their electric properties since they could not be obtained in the form of dense ceramic.

It was possible to use Spark Plasma Sintering using uncommon operating conditions, with high pressures applied on the powders, to allow sintering at low temperatures, down to the decompositions temperature range of the phases selected for the study, basically below 400 C. This confirms the initial goal that was to use the SPS technique as a prospective tool for fragile materials. The present results clearly show the possibility for various materials families to access high densities even at low sintering temperature, without any observable decomposition of the phases. Not only that it was possible to efficiently sinter at low temperatures, but it was also possible to use of Spark Plasma Sintering above the phases' decomposition temperatures observed in air. Moreover, and as an unexpected result, it was even possible to obtain through SPS treatment the anhydrous phase  $\text{Na}_2\text{Cu}(\text{CO}_3)_2$  from its hydrated compound. This has proven impossible through classical thermal treatment. Noticeably,  $\text{MnSO}_4$  ceramics were obtained in nanostructured form although the precursor powder was not nanosized. With very short sintering times, below 10 min, high densification above 90 % of theoretical densities were obtained for all the compositions presented and allowed the exploration of physical bulk properties. Even if they mostly remain at a small scale, close to the detection limits of the experimental setups, some clues of magnetoelectric couplings have been highlighted in both  $\text{Na}_2\text{Cu}(\text{CO}_3)_2$  and  $\text{MnSO}_4$ .

This phase,  $\text{MnSO}_4$ , represented the main part of the work conducted on SPS. Through a big amount of experimental sintering attempts, the sintering conditions have been determined and the influencing factors, such as the role of hydration and the moment for the application of

pressure during sintering have been selected so as to maximize material's compactness at the lowest sintering temperature of 400 °C. The possible role of the phase transition has also been discussed. Finally, the presence of water in the powder, appealing for a possible hydrothermal-like behavior during sintering has been explored through a comparative study of  $\text{MnSO}_4 \cdot \text{H}_2\text{O}$  sintering using both hydrothermal sintering and SPS. Clues of this hydrothermal-like mechanism have been evidenced, although this sole mechanism seems insufficient to describe totally the sintering mechanisms of  $\text{MnSO}_4 \cdot \text{H}_2\text{O}$  in SPS. However, sintering has been proven possible down to 100 °C for this phase using both sintering techniques, for a dwell time as short as 30 min and an applied pressure of 350 MPa. This is the first example of the sintering of a purely hydrated phase.

As an interesting perspective, the sintering of a molecular material has been also achieved. Highly dense ceramic has been obtained after very short sintering time and under 600 MPa. This is the first example of molecular ceramic, that paves the wide opportunities for this type of material.

# General conclusion

One of the most important outcome of this work is to highlight of the importance of a systemic approach. Three main aspects have been treated, which are respectively crystal chemistry, material processing and physical properties. The strong links between these three sciences is as important as the sciences themselves and the exploration of each separately from the rest, although echoing deeply-rooted disciplinary traditions, appears likely to miss key points concerning the studied materials. Indeed, precisely because chemical, structural, microstructural and physical properties of materials are strongly interdependent, materials and materials sciences stand at their crossroads, as illustrated by Figure 160<sup>235</sup>.

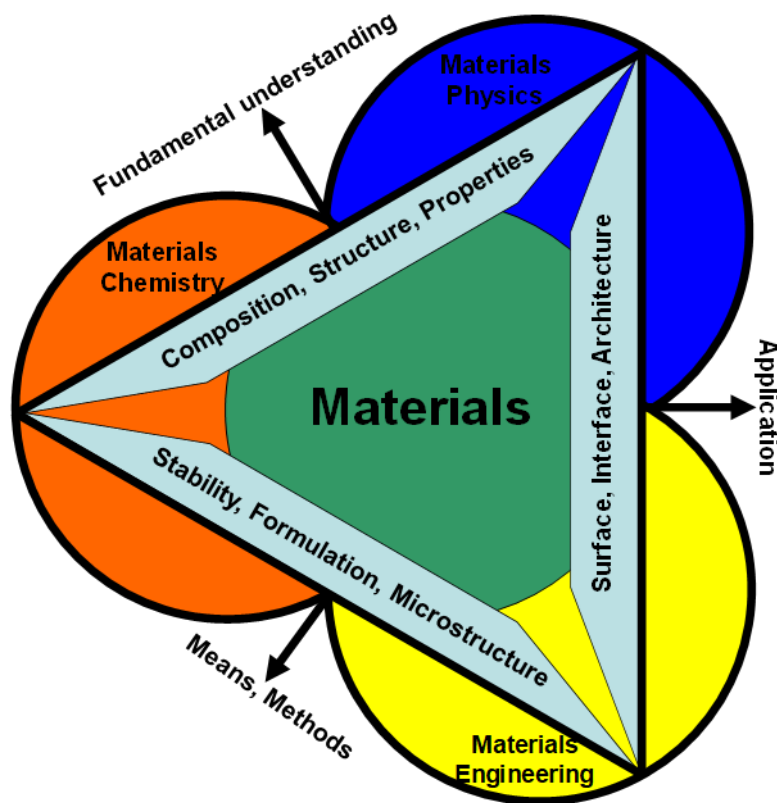


Figure 160: Fields of materials and their interactions

Through this approach then, two research directions have been investigated separately but in fact encompass the same approach. They both concern the synthesis and processing of ceramic materials, allowing the measurement of their structures and ferroic properties. The main difference lies in the key parameter representing the problematic of each study.

In the first part of this work, the synthesis of TTB materials based on  $\text{Ba}_2\text{NdFeNb}_4\text{O}_{15}$  first appears easy to control, and the focus is put on the evolution of crystal structure in connection with relaxor and/or ferroelectric properties.

Three solid solutions have been studied to investigate the influence of lithium accommodation in  $\text{Ba}_2\text{NdFeNb}_4\text{O}_{15}$ . Preliminary structural investigations indicated that one substitution scheme, resumed by the formulation  $\text{Ba}_2\text{Nd}_{1-x/3}\text{Li}_x\text{FeNb}_4\text{O}_{15}$  (NL), is better suited for this purpose. Upon exploration of their dielectric properties a similar evolution, from a relaxor to ferroelectric crossover to a purely relaxor state, was found in the three systems. Unfortunately Rietveld refinements on the most significant representatives of the NL solid solution could not reveal the underlying subtle crystallographic modifications in this system. Nonetheless the dielectric behaviour observed, which had also been evidenced in previous studies, appears in line with the proposed anion driven dielectric properties in these materials.

During the previous study, repeated synthesis of the  $\text{Ba}_2\text{NdFeNb}_4\text{O}_{15}$  compound lead to the observation of irreproducible dielectric behaviors. A meticulous investigation of the synthesis parameters of this phase confirmed that its intrinsic dielectric behavior is a R/FE crossover. The identification of the crucial role of precursor mixing allowed to obtain different samples with either R or R/FE behavior, but also pointed out the tunability of the dielectric behaviour with others synthesis conditions. Finally, XRD diffraction revealed rather identical structural parameters for R and R/FE samples, and preliminary results from precession electron diffraction tomography study, revealed a modulated structure which evolves with the dielectric properties. The survey of satellite peaks revealed a thermal evolution from a commensurate R or FE state to incommensurate modulation, and confirmed the hysteretic behavior of the ferroelectric transition. Preliminary refinements confirmed the influence of the modulation on oxygen positions, and thus the anionic driving force behind  $\text{Ba}_2\text{NdFeNb}_4\text{O}_{15}$  dielectric behaviour. Further data analysis will be necessary to precisely identify the structural origin of ferroelectric properties, but these results are a promising development of the crystal chemical studies of ferroelectric TTB.

In the second part though, the structure of the studied materials is known prior to the study, but useful to determine their potential ferroic properties. The actual issue lies in the processing of these materials in order to obtain measurable samples, as the selected materials are not stable enough to undergo conventional sintering.

Indeed, this second part was dedicated to the prospection for (multi)ferroic and/or magnetoelectric fragile materials through the use of Spark Plasma Sintering. After an explanation of the crystal chemical criteria allowing the presence of these physical properties, several candidate materials have been selected, in order to establish a proof of concept:  $\text{NH}_4\text{FeP}_2\text{O}_7$ ,  $\text{A}_2\text{Cu}(\text{CO}_3)_2$  (A=K, Na) and  $\text{MnSO}_4$ . The carbonates required optimization of the synthesis method, since the published do not provide enough powder for subsequent sintering studies. After characterizing these powders, high pressure (up to 600 MPa), low temperature ( $T \leq 400^\circ\text{C}$ ) sintering has been performed and resulted in all cases in highly dense ceramics, which relative densities beyond 90%. In addition to its impressive efficiency, SPS allowed for the stabilization of phases beyond their decomposition temperatures. Two of the studied materials were sintered from hydrated precursors, through *in situ* dehydration, and one of them,  $\text{Na}_2\text{Cu}(\text{CO}_3)_2$ , that could not be obtained in powder form through solid state route, was successfully processed by SPS into a pure and dense ceramic. Thanks to their successful sintering, the dielectric properties of all the target materials were investigated, and all revealed very small dielectric losses, an additional testimony of the quality of the ceramics. Minor dielectric anomalies were found in  $\text{NH}_4\text{FeP}_2\text{O}_7$  and  $\text{Na}_2\text{Cu}(\text{CO}_3)_2$ , while ferromagnetic  $\text{K}_2\text{Cu}(\text{CO}_3)_2$  displayed what may be a ferroelectric transition, and a dielectric anomaly at the antiferromagnetic transition was observed in  $\text{MnSO}_4$ . In addition, measurement of the magnetic field dependence of the capacitance revealed significant signals in  $\text{Na}_2\text{Cu}(\text{CO}_3)_2$  and  $\text{MnSO}_4$ , with possibly a magnetic field-induced transition in the latter, and these observations strongly suggest the existence of a magnetoelectric coupling in both materials. However, the ordering temperatures are low, and the couplings remain small, but the observation of these properties in a few fragile materials is an incentive for further engagement in their exploration.

The sintering mechanisms involved in  $\text{MnSO}_4$  and  $\text{MnSO}_4 \cdot \text{H}_2\text{O}$  sintering were specifically investigated, and displayed a high level of complexity. The presence of water in the precursor powder and the reversible phase transition to a high temperature phase were found to be crucial in the sintering of  $\alpha\text{-MnSO}_4$  by SPS. A comparative study of SPS and hydrothermal sintering has also been performed on  $\text{MnSO}_4 \cdot \text{H}_2\text{O}$  to identify the similitudes between both sintering methods. The comparison gave some clues of a possible hydrothermal-like mechanism when using SPS at low temperature, and also proved that SPS can be used to sinter hydrated materials.

Finally, a major result is the pure and highly dense pellet obtained from a molecular material,  $(\text{NH}_3)_2\text{Cu}(\text{COOCH}_3)_2$ . This unexpected result could be a breakthrough, as the elaboration of molecular ceramic is unprecedented, and opens new perspectives in terms of functional materials, as such ceramics could be elaborated from functional molecular materials for example. Such ceramics could find application, for instance, in electronic or magnetism, and may also contribute to the development of organic and/or flexible electronics.

In the end, the exploration of low temperature Spark Plasma Sintering provided a proof of its efficiency, confirmed the prospective opportunity lying with fragile ferroic materials and enabled the discovery of molecular ceramics, all these results bearing significant perspectives by themselves. An additional prospect of this research is the development of sustainable functional materials, possibly for substitution purpose or for specific applications. Indeed fragile materials, because of their limited thermal stability, are necessary synthesized and processed at low temperature, and in mild synthesis conditions. This situation will also likely limit their energetical and environmental footprint, but could also favor their integration in flexible devices for example, as the processing conditions of traditional functional materials such as oxides may not compatible with the substrates requested for such devices.

As a more general conclusion, further progress has been made in the investigation of ferroelectric TTB crystal chemistry, and the elaboration of  $\text{Ba}_2\text{NdFeNb}_4\text{O}_{15}$  ceramics displaying a relaxor to ferroelectric crossover or a pure relaxor behavior paves the way for a future step dedicated to the study of the microscopical mechanisms at work. The proof of concept for the use of SPS at very low temperatures has been obtained, as well as the proof of concept for the use of SPS as a prospection tool in the field of fragile ferroic materials. The final chapter which presents the first ever molecular ceramic is the perfect example of the wide possibilities that this exploratory work offers.

Finally, the work presented in this manuscript is an opportunity to enlighten the fertility of the interfaces between Materials Chemistry, Materials Physics and Materials Engineering, especially for prospective researches, thanks to the complimentary cultures of the corresponding communities.

# References

1. European Commission. Report on critical raw materials for the EU. Report of the Ad hoc Working Group on defining critical raw materials, May 2014. European Commission.
2. Aizu, K. Possible species of ferromagnetic, ferroelectric, and ferroelastic crystals. *Phys. Rev. B* **2**, 754–772 (1970).
3. Magneli, A. Crystal structure studies on beta-tungsten oxide. *Ark. foer Kemi* **1**, 513–523 (1949).
4. Capio, C. D., Dearborn, E. F., Bonner, W. A., November, R. & Hannay, C. N. B. Some Characteristics of Niobates Having ‘Filled’ Tetragonal Tungsten Bronze-Like Structures. *Mat. Res. Bull.* **3**, 47–57 (1968).
5. Van Uitert, L. G., Singh, S., Levinstein, H. J., Geusic, J. E. & Bonner, W. A. A new and stable nonlinear optical material. *Appl. Phys. Lett.* **11**, 161–163 (1967).
6. Pan, F. *et al.* Nonstoichiometric Control of Tunnel-Filling Order, Thermal Expansion, and Dielectric Relaxation in Tetragonal Tungsten Bronzes Ba<sub>0.5-x</sub>TaO<sub>3-x</sub>. *Inorg. Chem.* **54**, 8978–8986 (2015).
7. Zhu, X. *et al.* A Crystal-chemical framework for relaxor versus normal ferroelectric behavior in tetragonal tungsten bronzes. *Chem. Mater.* **27**, 3250–3261 (2015).
8. . *Bell Lab. Rec.* **1**, 240 (1926).
9. Jamieson, P. B. Ferroelectric Tungsten Bronze-Type Crystal Structures. I. Barium Strontium Niobate Ba<sub>0.27</sub>Sr<sub>0.75</sub>Nb<sub>2</sub>O<sub>5.78</sub>. *J. Chem. Phys.* **48**, 5048 (1968).
10. Gardner, J. *et al.* Relaxor-to-Ferroelectric Crossover and Disruption of Polar Order in ‘Empty’ Tetragonal Tungsten Bronzes. *Chem. Mater.* **28**, 4616–4627 (2016).
11. Yuan, Y., Chen, X. M. & Wu, Y. J. Diffused ferroelectrics of Ba<sub>6</sub>Ti<sub>2</sub>Nb<sub>8</sub>O<sub>30</sub> and Sr<sub>6</sub>Ti<sub>2</sub>Nb<sub>8</sub>O<sub>30</sub> with filled tungsten-bronze structure. *J. Appl. Phys.* **98**, 84110 (2005).
12. Graetsch, H. a., Pandey, C. S., Schreuer, J., Burianek, M. & Mühlberg, M.

- Incommensurate modulation of calcium barium niobate (CBN28 and Ce:CBN28). *Acta Crystallogr. Sect. B Struct. Sci.* **68**, 101–106 (2012).
13. Josse, M. *et al.* Original Crystal-Chemical Behaviors in (Ba,Sr)<sub>2</sub>Ln(Fe,Nb,Ta)<sub>5</sub>O<sub>15</sub> Tetragonal Tungsten Bronze: Anion-Driven Properties Evidenced by Cationic Substitutions. *Cryst. Growth Des.* **14**, 5428–5435 (2014).
  14. Stennett, M. C. *et al.* Dielectric and structural studies of Ba<sub>2</sub>MTi<sub>2</sub>Nb<sub>3</sub>O<sub>15</sub> (BMTNO<sub>15</sub>, M=Bi<sup>3+</sup>,La<sup>3+</sup>,Nd<sup>3+</sup>,Sm<sup>3+</sup>,Gd<sup>3+</sup>) tetragonal tungsten bronze-structured ceramics. *J. Appl. Phys.* **101**, 1–7 (2007).
  15. Graetsch, H. a., Schreuer, J., Burianek, M. & Mühlberg, M. Thermally induced structural changes in incommensurate calcium barium niobate Ca<sub>0.28</sub>Ba<sub>0.72</sub>Nb<sub>2</sub>O<sub>6</sub> (CBN28). *J. Solid State Chem.* **196**, 255–266 (2012).
  16. Stennett, M. C., Miles, G. C., Sharman, J., Reaney, I. M. & West, A. R. A new family of ferroelectric tetragonal tungsten bronze phases, Ba<sub>2</sub>MTi<sub>2</sub>X<sub>3</sub>O<sub>15</sub>. *J. Eur. Ceram. Soc.* **25**, 2471–2475 (2005).
  17. Gardner, J. & Morrison, F. D. A-site size effect in a family of unfilled ferroelectric tetragonal tungsten bronzes: Ba<sub>4</sub>R<sub>0.67</sub>Nb<sub>10</sub>O<sub>30</sub> (R = La, Nd, Sm, Gd, Dy and Y). *Dalt. Trans.* **43**, 11687 (2014).
  18. Ravez, J., El Alaoui-Belghiti, H., Elaamani, M. & Simon, A. Relations between ionic order or disorder and classical or relaxor ferroelectric behaviour in two lead-free TKWB-type ceramics. *Mater. Lett.* **47**, 159–164 (2001).
  19. Arnold, D. C. & Morrison, F. D. B-cation Effects in Relaxor and Ferroelectric Tetragonal Tungsten Bronzes. *J. Mater. Chem.* **19**, 6485 (2009).
  20. Hu, C., Hou, L., Fang, L. & Liu, L. Preparation and dielectric properties of unfilled tungsten bronze ferroelectrics Ba<sub>4</sub>RETiNb<sub>9</sub>O<sub>30</sub>. *J. Alloys Compd.* (2013). doi:10.1016/j.jallcom.2013.07.164
  21. Lenzo, P. V., Spencer, E. G. & Ballman, A. A. Electro-optic coefficients of ferroelectric strontium barium niobate. *Appl. Phys. Lett.* **11**, 23–24 (1967).

22. Simon, A., Ravez, J. & Maglione, M. The crossover from a ferroelectric to a relaxor state in lead-free solid solutions. *J. Phys. Condens. Matter* **16**, 963–970 (2004).
23. Rotaru, A. & Morrison, F. D. Vogel-Fulcher analysis of relaxor dielectrics with the tetragonal tungsten bronze structure: Ba<sub>6</sub>MNb<sub>9</sub>O<sub>30</sub> (M = Ga, Sc, In). *J. Therm. Anal. Calorim.* **120**, 1249–1259 (2015).
24. Prades, M., Masó, N., Beltrán, H., Cordoncillo, E. & West, A. R. Synthesis, structural characterization, and electrical properties of new oxygen-deficient tetragonal tungsten bronzes Ba<sub>2</sub>NdTi<sub>(2+x)</sub>Nb<sub>(3-x)</sub>O<sub>(15-x/2)</sub>. *Inorg. Chem.* **52**, 1729–36 (2013).
25. Simon, A. & Ravez, J. Solid-state chemistry and non-linear properties of tetragonal tungsten bronzes materials. *Comptes Rendus Chimie* 1268–1276 (2006).
26. Castel, E., Josse, M., Michau, D. & Maglione, M. Flexible relaxor materials: Ba<sub>2</sub>Pr<sub>(x)</sub>Nd<sub>(1-x)</sub>FeNb<sub>4</sub>O<sub>(15)</sub> tetragonal tungsten bronze solid solution. *J. Phys. Condens. Matter* **21**, 452201 (2009).
27. Garcia-Gonzalez, E., Torres-Pardo, A., Jimenez, R. & Gonzalez-Calbet, J. M. Structural singularities in ferroelectric Sr<sub>2</sub>NaNb<sub>5</sub>O<sub>15</sub>. *Chem. Mater.* **19**, 3575–3580 (2007).
28. Choukri, E. *et al.* Dielectric Properties Of Lead Potassium Lithium Niobate (Pb 1,85 K 1,15 Li 0,15 Nb 5 O 15 ) With Tetragonal Tungsten Bronze (TTB) Type Structure. *M. J. Condens. Matter* **12**, 86–91 (2010).
29. Josse, M. *et al.* The Ba<sub>2</sub>LnFeNb<sub>4</sub>O<sub>15</sub> ‘tetragonal tungsten bronze’: Towards RT composite multiferroics. *Solid State Sci.* **11**, 1118–1123 (2009).
30. Castel, E. *et al.* Crystal growth and characterization of tetragonal tungsten bronze FerroNiobates Ba<sub>2</sub>LnFeNb<sub>4</sub>O<sub>15</sub>. *J. Cryst. Growth* **340**, 156–165 (2012).
31. Albino, M. *et al.* Growth and Characterization of Centimeter-Sized Ba<sub>2</sub>LaFeNb<sub>4</sub>O<sub>15</sub> Crystals from High-Temperature Solution under a Controlled Atmosphere. *Eur. J. Inorg. Chem.* 2817–2825 (2013).
32. Albino, M., Veber, P., Pechev, S. & Maglione, M. Growth and Characterization of Ba<sub>2</sub>LnFeNb<sub>4</sub>O<sub>15</sub> (Ln = Pr, Nd, Sm, Eu) Relaxor Single Crystals. *Cryst. Growth Des.* **14**,

- 500–512 (2014).
33. Levin, I. *et al.* Coupling between octahedral tilting and ferroelectric order in tetragonal tungsten bronze-structured dielectrics. *Appl. Phys. Lett.* **89**, 122908 (2006).
  34. Castel, E. Synthèse de nouveaux matériaux multiferroïques au sein de la famille des bronzes quadratiques de formule Ba<sub>2</sub>LnFeNb<sub>4</sub>O<sub>15</sub>. (Universite de Bordeaux, 2008).
  35. Zheludev, I. S. Ferroelectricity and Symmetry. *Solid State Phys.* **26**, 429–464 (1971).
  36. Prakash, H. & Vachaspati. Polarization of Dielectric. *Il nuovo cimientto* **53**, 43–52 (1968).
  37. Curie, P. & Curie, J. Contractions and expansions produced by voltages in hemihedral crystals with inclined faces. *Comptes rendus l'Académie des Sci.* **93**, 1137 (1881).
  38. Lippman, G. . *Ann. Chim. Phys.* **24**, 145 (1881).
  39. Sebald, G. Nouveaux monocristaux à forte conversion piezoelectrique: croissance, modélisation et caractérisation. (2004).
  40. Regulation (EC) No 1907/2006 of the European Parliament and of the Council of 18 December 2006 concerning the Registration, Evaluation, Authorisation and Restriction of Chemicals (REACH), establishing a European Chemicals Agency.
  41. Maeder, M. D., Damjanovic, D. & Setter, N. Lead free piezoelectric materials. *J. Electroceramics* **13**, 385–392 (2004).
  42. Voigt, W. *Lehrbuch der Kristallphysik*. (Teubner, Leipzig, 1910).
  43. Yoon, S. M., Cho, N. J. & Kanazawa, K. Analyzing Spur-Distorted Impedance Spectra for the QCM. *J. Sensors* **Article ID**, 8 pages (2009).
  44. Lang, S. *Sourcebook of pyroelectricity*. (Gordon and Breach science publishers, 1974).
  45. Landau, L. & Lifchitz, E. . *Phys. Stat.* **MIR**, (1967).
  46. Castel, E. Synthèse de nouveaux matériaux multiferroïques au sein de la famille des bronzes quadratiques de formule Ba<sub>2</sub>LnFeNb<sub>4</sub>O<sub>15</sub>. (University of Bordeaux, 2009).
  47. O'Reilly, D. E. & Tsang, T. Deuteron magnetic resonance and proton relaxation times

- in ferroelectric ammonium sulfate. *J. Chem. Phys.* **46**, 1291–1300 (1967).
48. Cao, W. & Cross, L. E. Theory of tetragonal twin structures in ferroelectric perovskites with a first-order phase transition. *Phys. Rev. B* **44**, 5–12 (1991).
  49. Triebwasser, S. Study of the Second-Order Ferroelectric Transition in Tri-Glycine Sulfate. *IBM J.* 212–217 (1958).
  50. Sircon, N. *et al.* Nature of the ferroelectric phase transition in PbTiO<sub>3</sub>. *Phys. Rev. B* **50**, 50 (1994).
  51. Blinc, R. & Žekš, B. Dynamics of order-disorder-type ferroelectrics and antiferroelectrics. *Adv. Phys.* **21**, 693–757 (1972).
  52. Ge, J. *et al.* Dynamic hysteresis and scaling behavior in epitaxial antiferroelectric film. *Thin Solid Films* **584**, 108–111 (2015).
  53. Kanzig, W. Ferroelectrics and antiferroelectrics. in *Solid State Physics* (eds. Seitz, F. & Turnbull, D.) (Academic Press, Inc., New York, 1957).
  54. Cross, L. E. VII. A thermodynamic treatment of ferroelectricity and antiferroelectricity in pseudo-cubic dielectrics. *Philos. Mag.* **1**, 76 (1956).
  55. Pulvari, C. F. Ferrielectricity. *Phys. Rev.* **120**, 1670–1673 (1960).
  56. Pulvari, C. F. & De La Paz, A. S. Phenomenological Theory of Polarization Reversal in Ferrielectric Bi<sub>4</sub>Ti<sub>3</sub>O<sub>12</sub> Single Crystals. *J. Appl. Phys.* **37**, 1754–1763 (1966).
  57. Cross, L. E. Relaxor ferroelectrics : An overview. *Ferroelectrics* **151**, 305–320 (1994).
  58. Bokov, A. A. & Ye, Z. G. Recent progress in relaxor ferroelectrics with perovskite structure. *J. Mater. Sci.* **41**, 31–52 (2006).
  59. Smolenskii, G. A. & Agranovskaya, A. I. Dielectric polarization and losses of some complex compounds. *Zhur. Tekh. Fiz.* **28**, (1958).
  60. Bovtun, V. *et al.* Broad-band dielectric response of PbMg<sub>1/3</sub>Nb<sub>2/3</sub>O<sub>3</sub> relaxor ferroelectrics: Single crystals, ceramics and thin films. *J. Eur. Ceram. Soc.* **26**, 2867–2875 (2006).

61. Cross, L. E. Relaxor ferroelectrics. *Ferroelectrics* **76**, 241–267 (1987).
62. Bokov, V. Q. & Mylnikova, I. E. Ferroelectric properties of monocrystals of new perovskite compounds. *Sov. Physics-Solid State* **2**, 2428–2432 (1961).
63. Randall, C. a., Bhalla, a. S., Shrout, T. R. & Cross, L. E. Classification and consequences of complex lead perovskite ferroelectrics with regard to B-site cation order. *J. Mater. Res.* **5**, 829–834 (1990).
64. Vogel, H. The law of the relation between the viscosity of liquids and the temperature. *Phys. Z* **22**, 645 (1921).
65. Fulcher, G. Analysis of recent measurements of the viscosity of glasses. *J. Am. Ceram. Soc.* **8**, 339 (1925).
66. Viehland, D., Jang, S. J., Cross, L. E. & Wuttig, M. Freezing of the polarization fluctuations in lead magnesium niobate relaxors. *J. Appl. Phys.* **68**, 2916–2921 (1990).
67. Dai, X., Xu, Z. & Viehland, D. The spontaneous relaxor to normal ferroelectric transformation in La-modified lead zirconate titanate. *Philos. Mag. Part B* **70**, 33–48 (1994).
68. Scott, J. F. Ferroelectrics go bananas. *J. Phys. Condens. Matter* **20**, 21001 (2008).
69. Verwerft, M., Van Tendeloo, G., Van Landuyt, J. & Amelinckx, S. A complementary study by electron microscopy of modulated phases in Ba<sub>2</sub>NaNb<sub>5</sub>O<sub>15</sub>. *Ferroelectrics* **88**, 27–36 (1988).
70. Gagou, Y. *et al.* On the nature of phase transitions in the tetragonal tungsten bronze GdK<sub>2</sub>Nb<sub>5</sub>O<sub>15</sub> ceramics. *J. Appl. Phys.* **115**, 0–8 (2014).
71. Aydi, A., Khemakhem, H., Boudaya, C., Simon, A. & Von Der M??hll, R. X-ray and dielectric studies of ferroelectric or relaxor phases in the Ca<sub>1-x</sub>NaxSn<sub>1-x</sub>NbxO<sub>3</sub> system. *Solid State Sci.* **7**, 249–255 (2005).
72. Neurgaonkar, R. R., Oliver, J. R. & Cross, L. E. Ferroelectric properties of tetragonal tungsten bronze single crystals. *Ferroelectrics* **56**, 31–36 (1984).

73. Fang, P. H. & Roth, R. S. Ferroelectric and Ferrimagnetic Properties of  $(\text{Ba}_{6-2x}\text{R}_{2x})(\text{Nb}_{9-x}\text{Fe}_{1+x})\text{O}_{30}$ . *J. Appl. Phys.* **31**, S278 (1960).
74. Heijboer, P. Etude des propriétés diélectriques et structurales de monocristaux et céramiques de structure TTB. (University of Bordeaux, 2014).
75. Roulland, F., Josse, M., Castel, E. & Maglione, M. Influence of ceramic process and Eu content on the composite multiferroic properties of the  $\text{Ba}_{6-2x}\text{Ln}_{2x}\text{Fe}_{1+x}\text{Nb}_{9-x}\text{O}_{30}$  TTB system. *Solid State Sci.* **11**, 1709–1716 (2009).
76. Castel, E. *et al.* In-situ formation of barium ferrite in iron-doped ‘tetragonal tungsten bronze’: Elaboration of room temperature multiferroic composites. *J. Magn. Magn. Mater.* **321**, 1773–1777 (2009).
77. Shannon, R. D. & Prewitt, C. T. Effective ionic radii in oxides and fluorides. *Acta Crystallogr. Sect. B Struct. Crystallogr. Cryst. Chem.* **25**, 925–946 (1969).
78. Le, S., Zhu, S., Zhu, X. & Sun, K. Densification of  $\text{Sm}_{0.2}\text{Ce}_{0.8}\text{O}_{1.9}$  with the addition of lithium oxide as sintering aid. *J. Power Sources* **222**, 367–372 (2013).
79. Villalobos, G. R., Sanghera, J. S. & Aggarwal, I. D. Degradation of magnesium aluminum spinel by lithium fluoride sintering aid. *J. Am. Ceram. Soc.* **88**, 1321–1322 (2005).
80. Potin, A., Ravez, J. & Bonnet, J. P. Liquid-phase sintering of barium titanate with lithium fluoride. *J. Mater. Res.* **2**, 485–488 (1987).
81. Bugaris, D. E. & Zur Loye, H. C. Materials discovery by flux crystal growth: Quaternary and higher order oxides. *Angew. Chemie - Int. Ed.* **51**, 3780–3811 (2012).
82. Albino, M. Synthèse et caractérisation structurale et diélectrique de céramiques et de monocristaux relaxeurs de structure TTB. (2013).
83. Vincent, R. & Midgley, P. A. Double conical beam-rocking system for measurement of integrated electron diffraction intensities. *Ultramicroscopy* **53**, 271–282 (1994).
84. Kolb, U., Gorelik, T., Kübel, C., Otten, M. T. & Hubert, D. Towards automated diffraction tomography: Part I-Data acquisition. *Ultramicroscopy* **107**, 507–513 (2007).

85. Kolb, U., Gorelik, T. & Otten, M. T. Towards automated diffraction tomography. Part II-Cell parameter determination. *Ultramicroscopy* **108**, 763–772 (2008).
86. Palatinus, L., Petříček, V. & Corrêa, C. A. Structure refinement using precession electron diffraction tomography and dynamical diffraction: theory and implementation. *Acta Crystallogr. Sect. A Found. Adv.* **71**, 235–244 (2015).
87. Mugnaioli, E., Gorelik, T. & Kolb, U. ‘Ab initio’ structure solution from electron diffraction data obtained by a combination of automated diffraction tomography and precession technique. *Ultramicroscopy* **109**, 758–765 (2009).
88. Palatinus, L. *et al.* Structure refinement using precession electron diffraction tomography and dynamical diffraction: Tests on experimental data. *Acta Crystallogr. Sect. B Struct. Sci. Cryst. Eng. Mater.* **71**, 740–751 (2015).
89. Palatinus, L. *et al.* Hydrogen positions in single nanocrystals revealed by electron diffraction. *Science (80-. )*. **355**, 166–169 (2017).
90. Steciuk, G. *et al.* Unusual Relaxor Ferroelectric Behavior in Stairlike Aurivillius Phases. *Inorg. Chem.* **55**, 8881–8891 (2016).
91. Hill, N. A. Why are there so few magnetic ferroelectrics? *J. Phys. Chem. B* **104**, 6694–6709 (2000).
92. Hill, N. A. & Filippetti, A. Why are there any magnetic ferroelectrics? *J. Magn. Magn. Mater.* **242–245**, 976–979 (2002).
93. Khomskii, D. I. Multiferroics: different ways to combine magnetism and ferroelectricity 1). *J. Magn. Magn. Mater.* (2004).
94. Spaldin, N. & Fiebig, M. The Renaissance of magnetoelectric multiferroics. *Science (80-. )*. **309**, 391–392 (2005).
95. Kajiwara, Y. *et al.* Transmission of electrical signals by spin-wave interconversion in a magnetic insulator.
96. Lu, J., Pan, D. & Qiao, L. The principle of a virtual amplifier and its application to magnetoelectric measurement system. *Sci. Technol.* 1–11

97. Wadley, P. *et al.* Electrical switching of an antiferromagnet. *Science* (80-. ). **351**, 587–590 (2016).
98. Kosub, T. *et al.* Purely Antiferromagnetic Magnetoelectric Random Access Memory. *Nat. Commun.* 1–7 (2016).
99. Ortega, N., Kumar, A., Scott, J. F. & Katiyar, R. S. Multifunctional magnetoelectric materials for device applications. *J. Phys. Condens. Matter* **27**, 504002 (2015).
100. Dong, S., Liu, J.-M., Cheong, S.-W. & Ren, Z. Multiferroic materials and magnetoelectric physics: symmetry, entanglement, excitation, and topology. *Adv. Phys.* **64**, 519–626 (2015).
101. Ederer, C. & Spaldin, N. A. A new route to magnetic ferroelectrics. *Nat. news views* (2004).
102. Van Aken, B. B., Palstra, T. T. M., Filippetti, A. & Spaldin, N. a. The origin of ferroelectricity in magnetoelectric YMnO<sub>3</sub>. *Nat. Mater.* **3**, 164–170 (2004).
103. Ramesh, R. & Spaldin, N. A. Multiferroics: progress and prospects in thin films. *Nat. Mater.* **6**, 21–29 (2007).
104. Spaldin, N. A., Sang-Wook Cheong & Ramesh, R. Multiferroics : past, present, and future. *Phys. Today* (2010).
105. Curie, P. Sur la symétrie dans les phénomènes physiques, symétrie d'un champ électrique et d'un champ magnétique. *J. Phys. Theor. Appl.* **3**, 395–415 (1894).
106. Landau & Lifshitz. *Electrodynamics of continuous media*. (Pergamon, 1958).
107. Dzyaloshinsky, I. E. K voprosu o magnitno-elektricheskom effekte v antiferromagnetikakh. *J. Exptl. Theor. Phys.* **37**, 881–882 (1959).
108. Astrov, D. N. The magnetoelectric effect in antiferromagnetics. *Sov. Phys. JETP* **11**, 708–709 (1960).
109. Folen, V. J., Rado, G. T. & Stalder, E. W. Anisotropy of the magnetoelectric effect in Cr<sub>2</sub>O<sub>3</sub>. *Phys. Rev. Lett.* **6**, 607 (1961).

110. Ascher, E., Rieder, H., Schmid, H. & Stössel, H. Some properties of ferromagnetoelectric nickel-iodine boracite, Ni<sub>3</sub>B<sub>7</sub>O<sub>13</sub>I. *J. Appl. Phys.* **37**, 1404–1405 (1966).
111. Schmid, H. Ferroelectrics Multi-ferroic magnetoelectrics. *Ferroelectrics* **162**, 317–338 (1994).
112. Rivera, J. P. A short review of the magnetoelectric effect and related experimental techniques on single phase (multi-) ferroics. *Eur. Phys. J. B* **71**, 299–313 (2009).
113. Hill, N. A. Why Are There so Few Magnetic Ferroelectrics? *J. Phys. Chem.B* **104**, 6694–6709 (2000).
114. Rondinelli, J. M., Eidelson, A. S. & Spaldin, N. A. Non-d 0 Mn-driven ferroelectricity in antiferromagnetic BaMnO<sub>3</sub>. *Phys. Rev B* **79**, 205119 (2009).
115. Eerenstein, W., Mathur, N. D. & Scott, J. F. Multi-ferroic and magnetoelectric materials and interfaces. *Nature* **442**, (2006).
116. Khomskii, D. Classifying multiferroics: Mechanisms and effects. *Physics (College Park, Md)*. **2**, (2009).
117. Zvezdin, a. K. *et al.* Magnetoelectric effects in gadolinium iron borate GdFe<sub>3</sub>(BO<sub>3</sub>)<sub>4</sub>. *Lett. to J. Exp. Theor. Phys.* **81**, 272–276 (2005).
118. von Wartburg, W. The magnetic structure of magnetoelectric nickel-iodine boracite Ni<sub>3</sub>B<sub>7</sub>O<sub>13</sub>I. *Phys. Status Solidi* **21**, 557–568 (1974).
119. Roberts, S. Dielectric and piezoelectric properties of barium titanate. *Phys. Rev.* **71**, 890–895 (1947).
120. Watanabe, T. & Kohn, K. Magnetoelectric effect and low temperature transition of PbFe<sub>0.5</sub>Nb<sub>0.5</sub>O<sub>3</sub> single crystal. *Phase Transitions* **15**, 57–68 (1989).
121. Raevski, I. P. *et al.* Studies of Ferroelectric and Magnetic Phase Transitions in Multiferroic PbFe<sub>0.5</sub>Ta<sub>0.5</sub>O<sub>3</sub>. *Ferroelectrics* **475**, 52–60 (2015).
122. Isupov, V. A. *Ferroelectric and Antiferroelectric Perovskites PbB' 0.5 B'' 0.5 O 3*. *Ferroelectrics* **289**, (2003).

123. Fabini, D. H. *et al.* Dynamic Stereochemical Activity of the Sn<sup>2+</sup> Lone Pair in Perovskite CsSnBr<sub>3</sub>. *J. Am. Chem. Soc.* **138**, 11820–11832 (2016).
124. Hochheimer, H. D. *et al.* Study of the ferroelectric phase transition of TlGaSe<sub>2</sub> by dielectric, calorimetric, infrared and X-ray diffraction measurements. *J. Phys. Condens. Matter* **73**, 257–263 (1988).
125. Bos, J.-W. G., Colin, C. V. & Palstra, T. T. M. Magnetoelectric coupling in the cubic ferrimagnet Cu<sub>2</sub>OSeO<sub>3</sub>. *Phys. Rev. B* **78**, 94416 (2008).
126. Bunting, E. N., Shelton, G. R. & Creamer, A. S. Properties of barium-strontium titanate dielectrics. *J. Am. Ceram. Soc.* **30**, 114–125 (1947).
127. Hill, N. a. & Rabe, K. M. First-principles investigation of ferromagnetism and ferroelectricity in bismuth manganite. *Phys. Rev. B* **59**, 8759 (1999).
128. Li, M., Ning, M., Ma, Y., Wu, Q. & Ong, C. K. Room temperature ferroelectric, ferromagnetic and magnetoelectric properties of Ba-doped BiFeO<sub>3</sub> thin films. *J. Phys. D. Appl. Phys.* **40**, 1603–1607 (2007).
129. Brink, J. van den & Khomskii, D. I. Multiferroicity due to charge ordering. *J. physics. Condens. matter* **20**, (2008).
130. Ikeda, N. *et al.* Ferroelectricity from iron valence ordering in the charge-frustrated system LuFe<sub>2</sub>O<sub>4</sub>. *Nature* **436**, 1136–1138 (2005).
131. Fujimura, N., Ishida, T., Yoshimura, T. & Ito, T. Epitaxially grown YMnO<sub>3</sub> film: New candidate for nonvolatile memory devices. *Appl. Phys. Lett.* **69**, 1011–1013 (1996).
132. Kimura, T. *et al.* Magnetic control of ferroelectric polarization. *Nature* **426**, 55–58 (2003).
133. Hur, N. *et al.* Electric polarization reversal and memory in a multiferroic material induced by magnetic fields. *Nature* **429**, 392–395 (2004).
134. Sawada, S., Shiroishi, Y., Yamamoto, A., Takashige, M. & Matsuo, M. Ferroelectricity in Rb<sub>2</sub>ZnCl<sub>4</sub>. *J. Phys. Soc. Japan* **43**, 2099–2100 (1997).

135. Levanyuk, A. P. & Sannikov, D. G. Improper ferroelectrics. *Sov. Phys. Uspekhi* **17**, 199–214 (1974).
136. Kimura, T. Spiral Magnets as Magnetoelectrics. *Annu. Rev. Mater. Res.* **37**, 387–413 (2007).
137. Tokura, Y. & Seki, S. Multiferroics with spiral spin orders. *Adv. Mater.* **22**, 1554–1565 (2010).
138. Yamasaki, Y. *et al.* Magnetic reversal of the ferroelectric polarization in a multiferroic spinel oxide. *Phys. Rev. Lett.* **96**, 1–4 (2006).
139. Ishiwata, S., Taguchi, Y. & Murakawa, H. Low Magnetic-Field Control of Electric Polarization Vector in a Helimagnet. *Science (80-. )*. **319**, (2008).
140. Seki, S., Onose, Y. & Tokura, Y. Spin-driven ferroelectricity in triangular lattice antiferromagnets ACrO<sub>2</sub> (A=Cu, Ag, Li, or Na). *Phys. Rev. Lett.* **101**, 1–4 (2008).
141. Van Suchtelen, J. Product Properties : a New Application of Composite Materials. *Philips Res. Repts* **27**, 28–37 (1972).
142. Nan, C. W. Magnetoelectric effect in composites of piezoelectric and piezomagnetic phases. *Phys. Rev. B* **50**, 6082–6088 (1994).
143. Sallagoity, D. *et al.* Synthesis of dense arrays of multiferroic CoFe<sub>2</sub>O<sub>4</sub>–PbZr<sub>0.52</sub>Ti<sub>0.48</sub>O<sub>3</sub> core/shell nanocables. *RSC Adv.* **6**, 106716–106722 (2016).
144. Greve, H. *et al.* Low damping resonant magnetoelectric sensors. *Appl. Phys. Lett.* **97**, 152503 (2010).
145. Yan, L. *et al.* Review of magnetoelectric perovskite-spinel self-assembled nanocomposite thin films. *J. Mater. Sci.* **44**, 5080–5094 (2009).
146. Piraux, L. *et al.* Template approach for novel magnetic-ferroelectric nanocomposites. *Appl. Phys. Express* **4**, (2011).
147. Jaffari, G. H. *et al.* Effect of densification on the ferroelectric response of Ba<sub>0.4</sub>Sr<sub>0.6</sub>TiO<sub>3</sub>. *Solid State Commun.* **205**, 46–50 (2015).

148. Fantozzi, G., Le Gallet, S. & Niepce, J.-C. *Sciences et Technologies Ceramiques*. (EDP Sciences, 2016).
149. Tadic, D., Beckmann, F., Schwarz, K. & Epple, M. A novel method to produce hydroxyapatite objects with interconnecting porosity that avoids sintering. *Biomaterials* **25**, 3335–3340 (2004).
150. Wang, S. F. *et al.* Transparent ceramics: Processing, materials and applications. *Prog. Solid State Chem.* **41**, 20–54 (2013).
151. German, R. M. *Sintering theory and practice*. (Wiley, 1996).
152. German, R. M. *Sintering: from empirical observations to scientific principles*. (Elsevier, 2014).
153. Challa, S. R. *et al.* Relating rates of catalyst sintering to the disappearance of individual nanoparticles during Ostwald ripening. *J. Am. Chem. Soc.* **133**, 20672–20675 (2011).
154. Bernache-Assollant, D., Ababou, A., Champion, E. & Heughebaert, M. Sintering of calcium phosphate hydroxyapatite  $\text{Ca}_{10}(\text{PO}_4)_6(\text{OH})_2$  I. Calcination and particle growth. *J. Eur. Ceram. Soc.* **23**, 229–241 (2003).
155. Bousquet, C. *et al.* Tuning  $\text{Al}_2\text{O}_3$  crystallinity under supercritical fluid conditions: Effect on sintering. *J. Eur. Ceram. Soc.* **28**, 223–228 (2008).
156. Coble, R. L. Sintering Alumina: Effect of Atmospheres. *J. Am. Ceram. Soc.* **45**, 123–127 (1962).
157. Mackenzie, J. K. & Shuttleworth, R. A phenomenological theory of sintering. *Proc. Phys. Soc. Sect. B* **62**, 833–852 (1949).
158. Murray, P. L., Livey, D. & Williams, J. Hot pressing of ceramics. *Ceram. Fabr. Process.* 147–171 (1958).
159. Mangsen, G. E., Lambertson, W. A. & Best, B. Hot Pressing of Aluminium Oxide. *J. Am. Ceram. Soc.* **43**, 55–59 (1960).
160. Vasilos, T. Hot Pressing of Fused Silica. *J. Am. Ceram. Soc.* **43**, 517–519 (1960).

161. McClelland, J. D. A Plastic Flow Model of Hot Pressing. *J. Am. Ceram. Soc.* **44**, 526 (1961).
162. Coble, R. L. & Ellis, J. S. Hot-Pressing Alumina-Mechanisms Transport. *J. Am. Ceram. Soc.* **46**, 438–441 (1963).
163. Zhang, G., Deng, Z., Kondo, N., Yang, J. & Ohji, T. Reactive Hot Pressing of ZrB<sub>2</sub>-SiC Composites. *J. Am. Ceram. Soc.* **83**, 2330–2332 (2000).
164. Wang, W., Fu, Z., Wang, H. & Yuan, R. Influence of hot pressing sintering temperature and time on microstructure and mechanical properties of TiB<sub>2</sub> ceramics. *J. Eur. Ceram. Soc.* **22**, 1045–1049 (2002).
165. Wu, W. W., Zhang, G. J., Kan, Y. M. & Wang, P. L. Reactive hot pressing of ZrB<sub>2</sub>-SiC-ZrC ultra high-temperature ceramics at 1800°C. *J. Am. Ceram. Soc.* **89**, 2967–2969 (2006).
166. Zhang, W. *et al.* Improvement of optical properties of Nd:YAG transparent ceramics by post-annealing and post hot isostatic pressing. *Opt. Mater. (Amst)*. **35**, 2405–2410 (2013).
167. Bocanegra-Bernal, M. H. Hot isostatic pressing (HIP) technology and its applications to metals and ceramics. *J. Mater. Sci.* **39**, 6399–6420 (2004).
168. Agrawal, D. (Material R. I. Microwave Sintering of Ceramics, Composites, and Metallic Materials, and Melting of Glasses. *Trans. Indian Ceram. Soc.* **65**, 129–144 (2006).
169. Brosnan, K. H., Messing, G. L. & Agrawal, D. K. Microwave Sintering of Alumina at 2.45 GHz. *J. Am. Ceram. Soc.* **86**, 1307 (2003).
170. Tokita, M. Chapter 11.2.3 - Spark Plasma Sintering (SPS) Method, system and applications. in *Handbook of Advanced Ceramics (Second Edition)* (ed. Somiya, S.) 1149 (Academic Press, Oxford, 2013).
171. Grasso, S., Kim, B. N., Hu, C., Maizza, G. & Sakka, Y. Highly transparent pure alumina fabricated by high-pressure spark plasma sintering. *J. Am. Ceram. Soc.* **93**, 2460–2462 (2010).

172. Anselmi-Tamburini, U., Garay, J. E. & Munir, Z. A. Fast low-temperature consolidation of bulk nanometric ceramic materials. *Scr. Mater.* **54**, 823–828 (2006).
173. Anselmi-Tamburini, U., Gennari, S., Garay, J. E. & Munir, Z. A. Fundamental investigations on the spark plasma sintering/synthesis process II. Modeling of current and temperature distributions. *Mater. Sci. Eng. A* **394**, 139–148 (2005).
174. Munir, Z. A., Anselmi-Tamburini, U. & Ohyanagi, M. The effect of electric field and pressure on the synthesis and consolidation of materials: A review of the spark plasma sintering method. *J. Mater. Sci.* **41**, 763–777 (2006).
175. Shen, Z., Johnsson, M., Zhao, Z. & Nygren, M. Spark Plasma Sintering of Alumina. *J. Am. Ceram. Soc.* **85**, 1921–1927 (2002).
176. Gauthier, V., Bernard, F., Gaffet, E., Munir, Z. A. & Larpin, J. P. Structural evolution during mechanical alloying and annealing of a Nb-25at% Al alloy. *Intermetallics* **9**, 571–580 (2001).
177. Kim, H. C., Shon, I. J., Garay, J. E. & Munir, Z. A. Consolidation and properties of binderless sub-micron tungsten carbide by field-activated sintering. *Int. J. Refract. Met. Hard Mater.* **22**, 257–264 (2004).
178. Omori, M. Sintering, consolidation, reaction and crystal growth by the spark plasma system (SPS). *Mater. Sci. Eng. A* **287**, 183–188 (2000).
179. Oh, S. T., Tajima, K. I., Ando, M. & Ohji, T. Strengthening of porous alumina by pulse electric current sintering and nanocomposite processing. *J. Am. Ceram. Soc.* **83**, 1314–1316 (2000).
180. Schwarz, S., Thron, A. M., Rufner, J., Van Benthem, K. & Guillon, O. Low temperature sintering of nanocrystalline zinc oxide: Effect of heating rate achieved by field assisted sintering/spark plasma sintering. *J. Am. Ceram. Soc.* **95**, 2451–2457 (2012).
181. Olevsky, E. A., Kandukuri, S. & Froyen, L. Consolidation enhancement in spark-plasma sintering: Impact of high heating rates. *J. Appl. Phys.* **102**, (2007).
182. Massoni, N. *et al.* Sintering of synthetic barytocalcite BaCa(CO<sub>3</sub>)<sub>2</sub>, kutnahorite

- CaMn(CO<sub>3</sub>)<sub>2</sub> and rhodochrosite MnCO<sub>3</sub> for carbon-14 sequestration. *J. Eur. Ceram. Soc.* **35**, 297–308 (2015).
183. Monchoux, J.-P., Dollé, M., Rozier, P. & Galy, J. Reaction kinetics during synthesis of CuxV<sub>2</sub>O<sub>5</sub> and AgyV<sub>2</sub>O<sub>5</sub> by spark plasma sintering. *Solid State Ionics* **182**, 24–31 (2011).
184. Harrison, T. M. & Watson, E. B. Kinetics of zircon dissolution and zirconium diffusion in granitic melts of variable water content. *Contrib. to Mineral. Petrol.* **84**, 66–72 (1983).
185. Corker, D. L., Whatmore, R. W., Ringgaard, E. & Wolny, W. W. Liquid-phase sintering of PZT ceramics. *J. Eur. Ceram. Soc.* **20**, 2039–2045 (2000).
186. Yamasaki, N., Yanagisawa, K., Nishioka, M. & Kanahara, S. A hydrothermal hot-pressing method: apparatus and application. *J. Mater. ...* **5**, 355–356 (1986).
187. Yanagisawa, K., Ioku, K. & Yamasaki, N. Formation of Anatase Porous Ceramics by Hydrothermal Hot-Pressing of Amorphous Titania Spheres. *J. Am. Ceram. Soc.* **80**, 1303–1306 (1997).
188. Yamasaki, N., Weiping, T. & Jiajun, K. Low-temperature sintering of calcium carbonate by a hydrothermal hot-pressing technique. *J. Mater. Sci. Lett.* **11**, 934–936 (1992).
189. Yamasaki, N., Kai, T., Nishioka, M., Yanagisawa, K. & Ioku, K. Porous hydroxyapatite ceramics prepared by hydrothermal hot-pressing. *J. Mater. Sci. Lett.* **9**, 1150–1151 (1990).
190. Yanagisawa, K., Nishioka, M., Ioku, K. & Yamasaki, N. Densification of silica gels by hydrothermal hot-pressing. *J. Mater. Sci. Lett.* **12**, 1073–1075 (1993).
191. Guo, J. *et al.* Cold Sintering Process of Composites: Bridging the Processing Temperature Gap of Ceramic and Polymer Materials. *Adv. Funct. Mater.* **26**, 1–7 (2016).
192. Guo, H., Baker, A., Guo, J. & Randall, C. A. Cold Sintering Process: A Novel Technique for Low-Temperature Ceramic Processing of Ferroelectrics. *J. Am. Ceram. Soc.* **19**, 1–19 (2016).
193. Vakifahmetoglu, C. *et al.* Reactive Hydrothermal Liquid-Phase Densification (rHLPD)

- of Ceramics? A Study of the BaTiO<sub>3</sub>[TiO<sub>2</sub>] Composite System. *J. Am. Ceram. Soc.* **99**, 3893–3901 (2016).
194. Yu, H., Liu, J., Zhang, W. & Zhang, S. Ultra-low sintering temperature ceramics for LTCC applications: a review. *J. Mater. Sci. Mater. Electron.* **26**, 9414–9423 (2015).
  195. Matthias, B. T. & Remeika, J. P. Ferroelectricity in ammonium sulfate. *Phys. Rev.* **103**, 262 (1956).
  196. Belkouch, J., Monceaux, L., Bordes, E. & Courtine, P. Comparative structural study of mixed metals pyrophosphates. *Mater. Res. Bull.* **30**, 149–160 (1995).
  197. Alfonso, B. F. *et al.* On the crystal structure and thermal decomposition of ammonium-iron(iii) bis(hydrogenphosphate). *Dalt. Trans.* **39**, 1791–1796 (2010).
  198. Dvoncova, E. & Lii, K.-H. Synthesis, crystal structure, and magnetic susceptibilities of CsFeP<sub>2</sub>O<sub>7</sub> and RbFeP<sub>2</sub>O<sub>7</sub>. *J. solid state Chem.* **105**, 279–286 (1993).
  199. Terebilenko, K. V. *et al.* Structure and magnetic properties of AgFeP<sub>2</sub>O<sub>7</sub>. *J. Solid State Chem.* (2010).
  200. Tekin, B. & Güler, H. The synthesis and characterization of NH<sub>4</sub>FeP<sub>2</sub>O<sub>7</sub>, NaCaPO<sub>4</sub>, WP<sub>2</sub>O<sub>7</sub> compounds using microwave energy. *J. Balikesir Univ. Inst. Sci. Technol.* **9**, 68–76 (2007).
  201. Gentil, S. *et al.* Synthesis, structure and magnetic susceptibility of KCrP<sub>2</sub>O<sub>7</sub>, a potential antiferromagnetic magnetoelectric. *Ferroelectrics* **204**, 35–44 (1997).
  202. Kinyon, J. S., Clark, R., Dalal, N. S., Choi, E. S. & Zhou, H. Ferroelectricity in the gapless quantum antiferromagnet NH<sub>4</sub>CuCl<sub>3</sub>. *Phys. Rev. B* **92**, 144103 (2015).
  203. Josse, M. *et al.* Dielectric study of unexpected transitions in Multiferroic Mn<sub>1-x</sub>(Mg,Zn)<sub>x</sub>WO<sub>4</sub> ceramics. *Ferroelectrics* (2012).
  204. Arkenbout, A. H., Palstra, T. T. M., Siegrist, T. & Kimura, T. Ferroelectricity in the cycloidal spiral magnetic phase of MnWO<sub>4</sub>. *Phys. Rev. B - Condens. Matter Mater. Phys.* (2006). doi:10.1103/PhysRevB.74.184431

205. Will, G., Frazer, B. C., Shirane, G., Cox, D. E. & Brown, P. J. Magnetic structure of MnSO<sub>4</sub>. *Phys. Rev.* **140**, 2139–2142 (1965).
206. Legrand, E., Hautecler, S., Wegener, W. & Will, G. Magnetic phase transition in MnSO<sub>4</sub>. *J. Magn. Magn. Mater.* **18**, 529–530 (1980).
207. Gregson, A. K. & Moxon, N. T. Average and Single-Crystal Magnetic Properties of Potassium Bis(carbonato)cuprate(II): A Three-Dimensional Ferromagnet. *Inorg. Chem.* **21**, 3464–3466 (1982).
208. Farrand, A., Gregson, A., Skelton, B. & White, A. Crystal structure of the ferromagnetic polymer potassium Bis(carbonato)cuprate(II). *Aust. J. Chem.* **33**, 431–434 (1980).
209. Figgis, B. N., Reynolds, P. A., White, A. H. & Williams, G. A. The electronic structure of copper in the polymer potassium bis(carbonato)cuprate(II) as determined from precise X-ray diffraction data. *Journal of the Chemical Society, Dalton Transactions* (1981).
210. Gregson, A. K. & Moxon, N. T. Single-Crystal Magnetic Properties of Sodium Bis(carbonato)cuprate(II): Three-Dimensional Antiferromagnet. *Inorg. Chem.* **20**, 78–81 (1981).
211. Wetchakun, N. & Incessungvorn, B. Influence of calcination temperature on anatase to rutile phase transformation in TiO<sub>2</sub> nanoparticles synthesized by the modified sol-gel method. *Mater. Lett.* **82**, 195–198 (2012).
212. Riou, D., Nguyen, N., Benloucif, R. & Raveau, B. LiFeP<sub>2</sub>O<sub>7</sub> : Structure and magnetic properties. *Mater. Res. Bull.* **25**, 1363–1369 (1990).
213. Healy, P. C. & White, A. H. Crystal Structure and Physical Properties of Anhydrous Sodium Copper. *J. Chem. Soc. Dalt. Trans.* 1913–1917 (1972).
214. Gregson, A. K. & Healey, P. C. Ferromagnetic interactions in sodium bis(carbonato)cuprate(II). *Inorg. Chem.* **17**, 2969–2970 (1978).
215. Gregson, A. K., Moxon, N. T., Weller, R. R. & Hatfield, W. E. Ferromagnetic Exchange Coupling in Sodium Biscarbonatocuprate(II) Trihydrate. *Aust. J. Chem.* **35**, 1537–1541 (1982).

216. Nelyubina, Y. V, Korlyukov, A. A., Fedyanin, I. V & Lyssenko, K. A. Extremely Long Cu ... O Contact as a Possible Pathway for Magnetic Interactions in  $\text{Na}_2\text{Cu}(\text{CO}_3)_2$ . *Inorg. Chem.* **52**, 14355–14363 (2013).
217. Deville. Mémoire sur les combinaisons des carbonates métalliques avec les carbonates alcalins et ammoniacaux. *Ann. Chim. Phys.* (1856).
218. Reynolds, W. C. Chemical properties of condensed solutions of certain salts Part I. Double potassium carbonates. *J. Chem. Soc. Trans.* **73**, 262–267 (1898).
219. Pickering, S. U. Potassium cupricarbonates. *J. Chem. Soc. Trans.* **94**, 800–811 (1911).
220. Applebey, M. P. & Lane, K. W. Double Carbonates of Sodium and Potassium with the Heavy Metals. *J. Chem. Soc.* **113**, 609–622 (1918).
221. Deville. Mémoire sur les combinaisons des carbonates métalliques avec les carbonates alcalins et ammoniacaux. *Ann. Chim. Phys.* **33**, 75 (1851).
222. Mosset, A., Bonnet, J. J. & Galy, J. Structure cristalline de la chalconatronite synthétique :  $\text{Na}_2\text{Cu}(\text{CO}_3)_2 \cdot 3\text{H}_2\text{O}$ . *Zeitschrift für Krist.* **148**, 165–177 (1978).
223. Will, G. The crystal structure of  $\text{MnSO}_4$ . *Acta Crystallogr.* **19**, 854–857 (1965).
224. *Pascal, tome Manganese et Zinc.*
225. Narayanchar, P., Basaveswara Rao, P. & Aneesuddin, M. DTA studies on preparation of  $\text{MnSO}_4$  by reacting pyrite and pyrolusite at high temperatures. *J. Therm. Anal.* **35**, 1553–1560 (1989).
226. le Fur, Y., Coing-Boyat, J. & Bassi, G. Structure des sulfates monohydrates, monocliniques, des métaux de transition,  $\text{MSO}_4 \cdot (\text{H}_2\text{O})$  (M = Mn, Fe, Co, Ni et Zn). *Comptes Rendus Hebd. des Seances l'Academie des Sci. Ser. C, Sci. Chim.* **262**, 632–635 (1966).
227. Kirfel, A. & Will, G. New high temperature phase of  $\text{MnSO}_4$ . *High Temp. - high Press.* **6**, 525–527 (1974).
228. Allain, Y., Krebs, J. P. & De Gunzbourg, J. Magnetic study of the manganous sulfates

- MnSO<sub>4</sub> and MnSO<sub>4</sub>.H<sub>2</sub>O. *J. Appl. Phys.* **39**, 1124–1125 (1968).
229. Mani, M. K., Viola, G., Hall, J. P., Grasso, S. & Reece, M. J. Observation of Curie transition during spark plasma sintering of ferromagnetic materials. *J. Magn. Magn. Mater.* **382**, 202–205 (2015).
230. Lecomte, M., de Gunzbourg, J., Teyrol, M., Miedan-Gros., A. & Allain, Y. Magnetic transitions in manganese sulfates Mn SO<sub>4</sub> and Mn SO<sub>4</sub>.H<sub>2</sub>O. *Solid State Communications* (1972).
231. Will, G., Frazer, B. C., Shirane, G., Cox, D. E. & Brown, P. J. Cycloidal Spin Configuration of Orthorhombic MnSO<sub>4</sub>. *J. Appl. Phys.* **36**, 1095 (1965).
232. Liu, Y., Eriksson, M., Jin, Z., Nygren, M. & Shen, Z. Micro-hydrothermal reactions mediated grain growth during spark plasma sintering of a carbonate-containing hydroxyapatite nanopowder. *J. Eur. Ceram. Soc.* **34**, 4395–4401 (2014).
233. Euler, H., Kutzke, H., Barbier, B. & Kirfel, A. Refinement of crystal structure of copper acetate diammine, Cu(CH<sub>3</sub>COO)<sub>2</sub>, 2NH<sub>3</sub>. *Z. Krist.* **224**, 725–726 (2009).
234. Baker, A., Guo, H., Guo, J. & Randall, C. Utilizing the Cold Sintering Process for Flexible-Printable Electroceramic Device Fabrication. *J. Am. Ceram. Soc.* **3**, 1–3 (2016).
235. Josse, M. Des fluorures aux ferroïques, l’empire de la cristalochimie. (2012).
236. Spaldin, N. A., Fiebig, M. & Mostovoy, M. The toroidal moment in condensed-matter physics and its relation to the magnetoelectric effect. *J. Phys. Condens. Matter* **20**, 434203 (2008).
237. Bernache-Assollant, D. & Bonnet, J.-P. Frittage : aspects physico-chimiques Partie 2 : frittage en phase liquide. *Techniques de l’ingénieur* (2005).

THÈSE PRÉSENTÉE  
POUR OBTENIR LE GRADE DE  
**DOCTEUR DE**  
**L'UNIVERSITÉ DE BORDEAUX**

ÉCOLE DOCTORALE DES SCIENCES CHIMIQUES  
SPÉCIALITÉ : Chimie et Physico-Chimie des Matériaux

Par **Thomas HERRISSON DE BEAUVOIR**

---

**Cristallochimie prospective : relaxeurs, ferroïques et SPS basse  
température**

---

Sous la direction de : Michaël JOSSE

Soutenue le 26 Septembre 2017

Membres du Jury :

|                                |   |            |
|--------------------------------|---|------------|
| <b>Mr RANDALL Clive</b>        | Professeur, MRI, State College            | Rapporteur |
| <b>Mr ESTOURNES Claude</b>     | Directeur de Recherche, CIRIMAT, Toulouse | Rapporteur |
| <b>Mr ALARY Jean-André</b>     | R&D manager, IMERYS                       | Examineur  |
| <b>Mme ELISSALDE Catherine</b> | Directrice de Recherche, ICMCB            | Examineur  |
| <b>Mr MAGLIONE Mario</b>       | Directeur de Recherche, ICMCB             | Examineur  |
| <b>Mr JOSSE Michaël</b>        | Maitre de conférences, ICMCB              | Directeur  |

# Introduction

Les matériaux diélectriques et magnétiques ont un nombre important d'applications, de l'énorme usage en tant que condensateurs en électronique à usage quotidien (ordinateurs, téléphones, ...), aux utilisations en tant que capteurs piézoélectriques, stockage magnétique, sonars, imagerie médicale, optique non linéaire, ou plus largement dans les télécommunications. Ils sont donc de nos jours à la fois très important dans la vie courante comme pour des applications de hautes technologies. Le besoin de réduction de taille des constituants, tout en conservant le même niveau de qualité technique, est plus que jamais un enjeu majeur. Parmi ces matériaux se trouvent les matériaux ferroïques, multiferroïques et magnétoélectriques, qui représentent des candidats prometteurs pour le développement de nouveaux types de mémoires par spintronique. Développer de nouveaux matériaux implique la mise en commun de ressources, compétences et cultures variées, comprenant les interactions entre chimie du solide, science des matériaux et physique qui doivent alors être parfaitement synchrones pour fonctionner de concert. Au-delà de la recherche de nouveaux matériaux à propriétés inédites, d'autres challenges doivent être relevés par cette approche, comme :

- ✓ L'utilisation de constituants non critiques
- ✓ L'utilisation de procédés à empreinte environnementale limitée
- ✓ Le développement de matériaux et de procédés compatibles avec les nouvelles générations de matériaux (polymères fonctionnels, matériaux moléculaires, ...) et de nouveaux dispositifs (organiques, flexibles, électroniques solubles, ...)
- ✓ Le développement de matériaux favorisant des procédés renouvelables, à travers la recyclabilité ou au moins par la simplification des étapes de retraitement

Une façon de créer une rupture scientifique et technologique, donc, d'améliorer sensiblement dans différents types de domaine interconnectés, est d'explorer au-delà des limites habituelles (pluridisciplinaire) de ce domaine. C'est le domaine de la recherche prospective, qui est généralement une approche à haut risque, car l'exploration de territoires inconnus peut prendre du temps et même échouer à fournir les résultats attendus, comme toute activité de recherche mais avec une plus grande probabilité. Cependant, une telle approche peut également révéler de grandes

possibilités inattendues et n'implique pas nécessairement l'exploration de territoires vierges. En effet, le contexte évolutif et les découvertes inattendues peuvent faire revivre le potentiel de territoires explorés partiellement ou même profondément (ou perçus de comme tel), qui peuvent contenir des ressources utiles par rapport aux défis mentionnés ci-dessus.

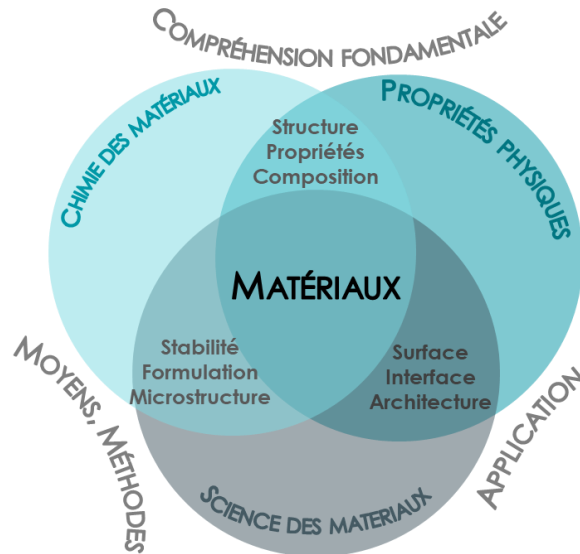


Figure 1: Composantes des matériaux et leurs interactions

Dans le présent travail, l'intérêt central porte sur les matériaux ferroïques. Ceux-ci ont la particularité de posséder une polarisation spontanée, une magnétisation ou une déformation qui peut être inversée par l'application d'un champ externe. Les propriétés ferroïques sont les fondements de nombreuses applications et la compréhension de leur fonctionnement fondamental est une étape préalable et essentielle avant toute utilisation. Le lien étroit entre les propriétés ferroïques, la structure cristalline et la composition chimique implique que les études de diffraction et les approches cristallographiques sont particulièrement bien adaptées à l'étude des matériaux ferroïques. Une fois que le lien a été établi entre les aspects chimiques des cristaux et les propriétés, ou lorsqu'il est établi, il est possible de concevoir un matériau à des fins spécifiques. À ce stade, combler le fossé entre la chimie et la physique induit le développement du traitement des matériaux. Les trois aspects (chimie/cristallographie, science des matériaux et propriétés physiques) représentent les principaux piliers de la présente étude. Comme nous l'avons souligné précédemment, des recherches prospectives seront entreprises dans ce travail et, pour atténuer

leurs risques, deux sujets de recherche différents seront étudiés, l'étude des crossovers de relaxeur à ferroélectriques dans les niobates de structure bronze quadratiques de tungstène (*tetragonal tungsten bronze* en anglais, abrégés TTB) et le développement de frittage par *Spark Plasma Sintering* (SPS) à faibles températures de matériaux thermodynamiquement fragiles. Le premier est un sujet original et bien établi, mais avec des facettes (presque) inexplorées, qui comporte des risques limités, alors que le second est à haut risque, à haute récompense et totalement nouveau, ce qui peut avoir un potentiel de rupture.

Dans une première partie, l'intérêt sera porté sur la compréhension du fondement chimique cristallin des matériaux ferroélectriques cristallisant dans la structure TTB. Ces matériaux représentent l'une des classes les plus importantes de matériaux ferroélectriques, mais possèdent également des propriétés optiques non linéaire et de conduction ionique. Les observations précédentes de modulations structurales aperiodiques dans ces matériaux ont été récemment liées à des propriétés diélectriques. De plus, l'utilisation de la technique XRD n'a pas pu résoudre la structure de ces matériaux et le lien structure-propriété reste flou. L'exploration de la solution solide est un outil puissant pour étudier les relations structure-propriétés. Un second chapitre sera consacré à l'exploration des solutions solides et à leur caractérisation afin d'étudier l'évolution des propriétés structurales et diélectriques de  $\text{Ba}_2\text{NdFeNb}_4\text{O}_{15}$  substitué au Li. Trois schémas de substitution différents seront présentés, qui ont été conçus afin d'identifier le rôle cristallographique du lithium, autrement insaisissable dans les études de diffraction des rayons X. Lors de la découverte de relations inattendues entre les conditions de traitement et les propriétés diélectriques, un troisième chapitre sera spécifiquement consacré à leur étude, y compris un rapport préliminaire d'une étude cristallographique au moyen de la diffraction d'électrons.

Après une première partie dédiée à l'exploration de la chimie cristalline des TTBs, une deuxième partie sera consacrée à la prospection de nouveaux matériaux fragiles ferroïques, multiferroïques ou magnétoélectriques à l'aide de la technique SPS (*Spark Plasma Sintering*). Les matériaux fragiles désignent ici des matériaux présentant une stabilité thermique limitée, ce qui interdit leur frittage par des moyens classiques. La caractérisation des propriétés diélectriques de ces matériaux, en recherche prospective, est entravée par leur indisponibilité sous forme céramique. Le présent travail vise à établir une preuve de concept concernant le frittage de matériaux fragiles par SPS basse température, afin de permettre le développement de recherches prospectives sur ces

matériaux. Un chapitre mettra en évidence les critères chimiques cristallins qui seront nécessaires pour sélectionner les matériaux candidats intéressants et présentera les résultats expérimentaux associés à la densification des quatre matériaux sélectionnés. Une attention particulière sera portée au frittage du sulfate de manganèse, à travers lequel les mécanismes de frittage impliqués dans le SPS à basse température seront étudiés. Dans ces travaux, le SPS sera effectué dans des conditions inhabituelles en tentant d'obtenir des échantillons mesurables denses, pour l'étude ultérieure de leurs propriétés physiques. Un fort accent sera mis sur le comportement et la stabilité de différents matériaux lors du frittage par rapport aux différents paramètres SPS. Dans un troisième et dernier chapitre, des résultats inattendus issus de cette étude exploratoire du SPS à basse température seront présentés. Ces résultats peuvent constituer une percée significative dans le domaine des matériaux céramiques.

# Partie 1 : Etude cristallochimique du crossover relaxeur / ferroélectrique dans les TTB de la famille de $\text{Ba}_2\text{NdFeNb}_4\text{O}_{15}$

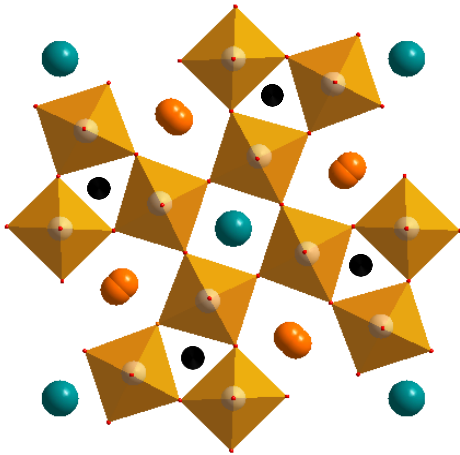


Figure 2: Représentation de la maille TTB selon la direction  $\langle 001 \rangle$

La synthèse de trois solutions solides a été réalisée avec succès par voie solide :



La haute cristallinité et l'absence de phase secondaire ont été mises en évidence par DRX. Alors que la solution solide BNL montre une augmentation linéaire constante des paramètres du réseau cohérente avec l'insertion de grands ions  $\text{Ba}^{2+}$  dans le réseau, l'influence des modifications cationiques dans les deux autres solutions solides conduit à des valeurs constantes des paramètres de maille. Ces résultats suggèrent une bonne accommodation de Ba pour la solution solide BNL et l'absence d'évolution pour les solutions solides LFN et NL confirment les tendances attendues, c'est donc un indice de la bonne insertion de Li dans la phase.

Des mesures diélectriques ont été réalisées et toutes conduisent à l'observation de la même évolution à partir d'échantillons à faible teneur en Li présentant à la fois des transitions relaxeur (R) et ferroélectrique

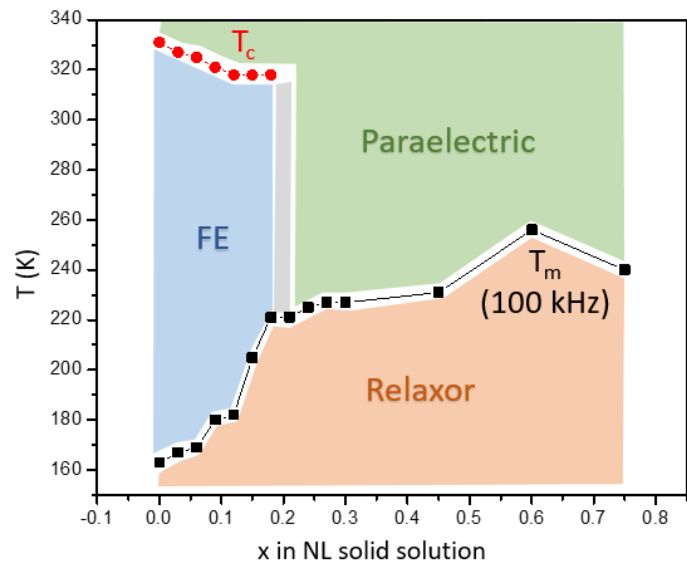


Figure 3: Diagramme de phase diélectrique de la solution solide NL

(FE) à des échantillons à forte teneur en Li présentant une phase R pure. Dans la solution NL, la transition de l'un à l'autre a été particulièrement identifiée pour  $x$  entre 0,18 et 0,21.

Afin d'identifier l'origine structurale des deux propriétés diélectriques différentes observées, des affinements de Rietveld ont été réalisés sur des échantillons de solution solide NL dans les deux régimes (R / FE et R). La présence de Li étant presque indétectable par DRX, en particulier pour les faibles quantités. Cette observation conduit à la conclusion qu'aucune différence notable ne peut être mise en évidence à partir de ces données et suggère, en accord avec la littérature et les travaux antérieurs, la forte influence du réseau d'oxygène sur les propriétés diélectriques.

Au cours de cette étude, l'observation de réponses diélectriques inattendues sur  $x = 0$  conduit à s'interroger sur la sensibilité de la phase à la procédure de synthèse et sur l'influence de différentes étapes de synthèse sur ces propriétés.

L'ajustement des paramètres de synthèse de la phase mère  $\text{Ba}_2\text{NdFeNb}_4\text{O}_{15}$  conduit à l'observation de la même variété de réponses diélectriques que dans les solutions solides. Ce résultat très surprenant devient un grand atout dans la recherche de la relation structure / propriété. Après avoir identifié la forte influence des conditions de broyage sur les propriétés résultantes, sans aucune différence structurale ou associée à la composition, d'autres traitements thermiques ont été réalisés et la réponse crossover (R / FE) a été déterminée comme étant la réponse intrinsèque.

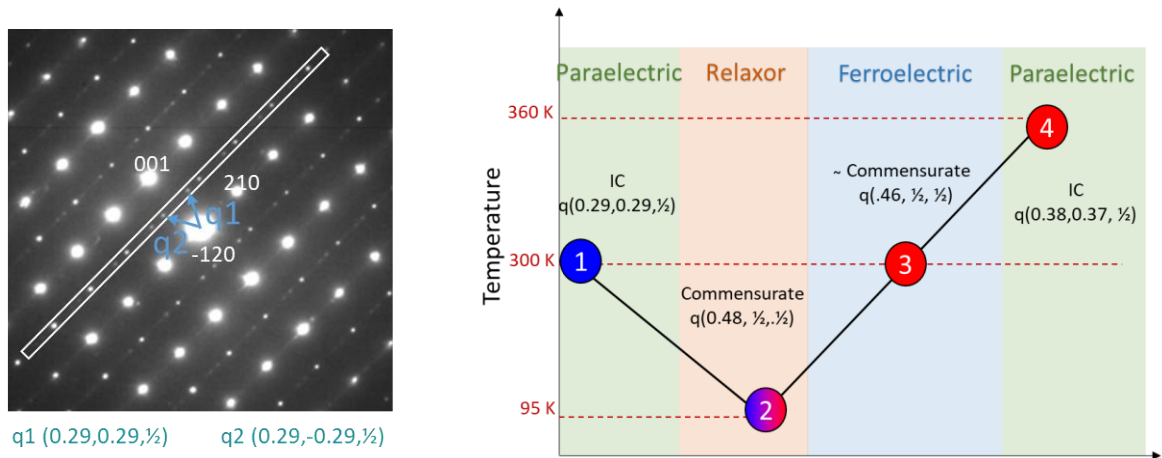


Figure 4: (gauche) SAED selon  $\langle -120 \rangle$  montrant des satellites à vecteurs de modulation incommensurable et (droite) évolution de la modulation structurale au sein de la structure TTb en fonction de la température dans les différentes phases diélectriques (IC : incommensurable)

Cependant, aucune différence n'a été observée dans les affinements DRX sur poudre qui pourrait expliquer les différents comportements diélectriques, ni les transitions de phase des états PE à FE ou R. L'utilisation d'une technique de diffraction d'électrons récemment développée, appelée tomographie électronique en précession en mode diffraction (PEDT), a permis d'observer des pics satellite dans la structure 3D supposée, indiquant ainsi la présence d'une structure modulée. Le suivi en température de ces satellites a permis de mettre en évidence un lien entre propriétés diélectriques et modulations structurales de type commensurable/incommensurable. La description complète de ces structures modulées n'a pas pu être menée à terme puisque ces résultats sont encore préliminaires mais constituent un moyen prometteur pour explorer ces matériaux afin de comprendre les mécanismes structuraux responsables de leurs propriétés diélectriques.

## **Partie 2 : Recherche prospective de matériaux ferroïques, multiferroïques et magnétoélectriques par frittage *Spark Plasma Sintering (SPS)***

Trois étapes principales ont été suivies tout au long de ce chapitre. Tout d'abord, une approche cristallographique a été développée pour trouver des matériaux qui pourraient éventuellement présenter des propriétés (multi) ferroïques ou magnétoélectriques intéressantes dans des systèmes qui sont habituellement inexplorés en raison de la difficulté de leur mise en forme (frittage par exemple). La deuxième étape, qui était la partie principale de ce travail, était la synthèse et le frittage des échantillons selon les objectifs précédemment déterminés. Enfin, la dernière étape a été la mesure des propriétés physiques des échantillons de céramique dense obtenus.

Une partie importante du travail a été consacrée à la synthèse qui représente une grande partie du temps consacré à ce travail. Il a été dédié à trois matériaux rapportés dans la littérature mais dont la synthèse a été réalisée par des voies inadaptées à la production de quantités significatives de poudre, mais qui ont été ajustées avec succès. Le développement de ces synthèses, principalement en ce qui concerne les phases carbonatées ( $A_2Cu(CO_3)_2$  avec  $A = Na, K$ ), est un premier résultat intéressant car les travaux antérieurs disponibles étaient difficiles à reproduire et ne permettaient que de petites quantités de poudres (quelques centaines de microgrammes). Compte tenu du développement de matériaux fragiles comme alternative fiable et durable aux matériaux fonctionnels classiques (oxydes ...), la disponibilité de méthodes de synthèse efficaces et éventuellement évolutives est une étape critique.

La partie principale concerne le frittage. Dans tous les cas, il a été très efficace et a donné des résultats au-delà des attentes. Les principales conclusions sont :

- ✓ L'utilisation de constituants non critiques
- ✓ L'utilisation de procédés à empreinte environnementale limitée
- ✓ Le développement de matériaux et de procédés compatibles avec les nouvelles générations de matériaux (polymères fonctionnels, matériaux moléculaires, ...) et de nouveaux dispositifs (organiques, flexibles, électroniques solubles, ...)

- ✓ Le développement de matériaux favorisant des procédés renouvelables, à travers la recyclabilité ou au moins par la simplification des étapes de retraitement

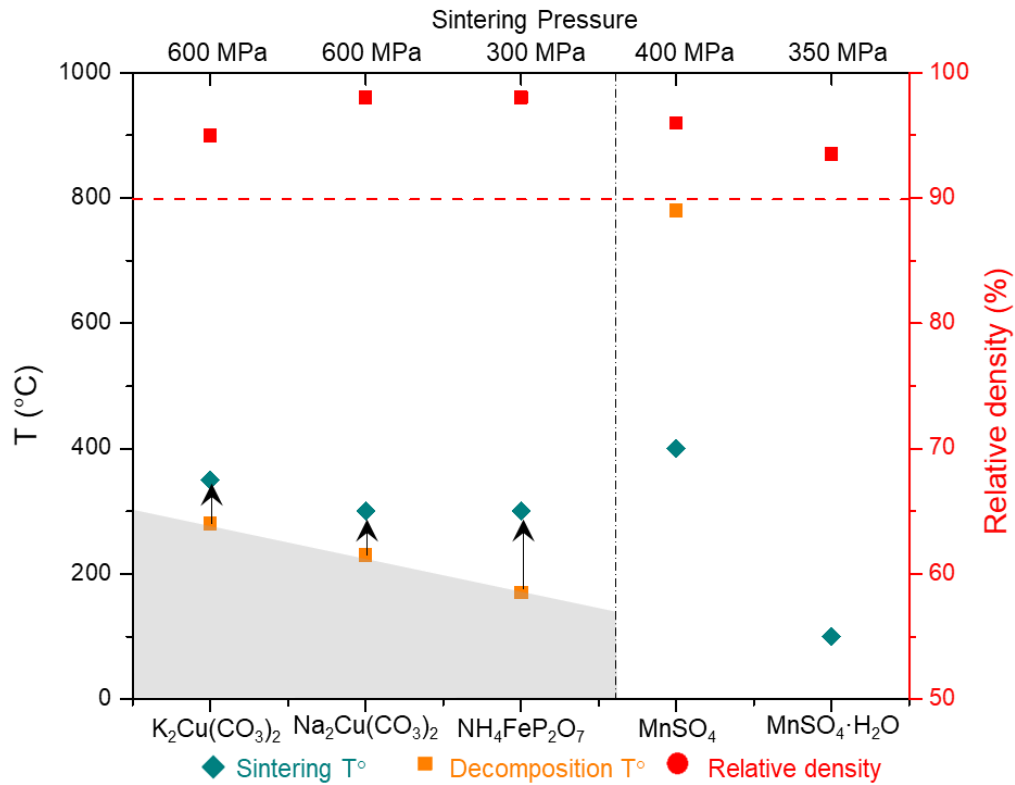


Figure 5: Températures et pressions de frittage comparées aux températures de décomposition des différents matériaux, ainsi que leur densité relative. La zone grise correspond au domaine de stabilité sous air des matériaux étudiés. Les flèches montrent l'accroissement de stabilité.

Les exemples de  $MnSO_4$  et  $MnSO_4 \cdot H_2O$  ont été utiles pour explorer l'influence des paramètres de frittage sur les densités finales des céramiques et ont mis en évidence des mécanismes de frittage complexes avec l'influence de l'hydratation de la poudre initiale, les étapes de déshydratation, la présence de transition de phase. Le frittage de  $MnSO_4 \cdot H_2O$  dans des conditions hydrothermales était également utile pour mettre en évidence les similitudes avec les résultats obtenus dans le SPS. Tout au long de ce travail, la possibilité d'utiliser le SPS comme outil prospectif pour obtenir de nouvelles céramiques qui ne pourraient pas être préparées par d'autres moyens est plus que confirmée.

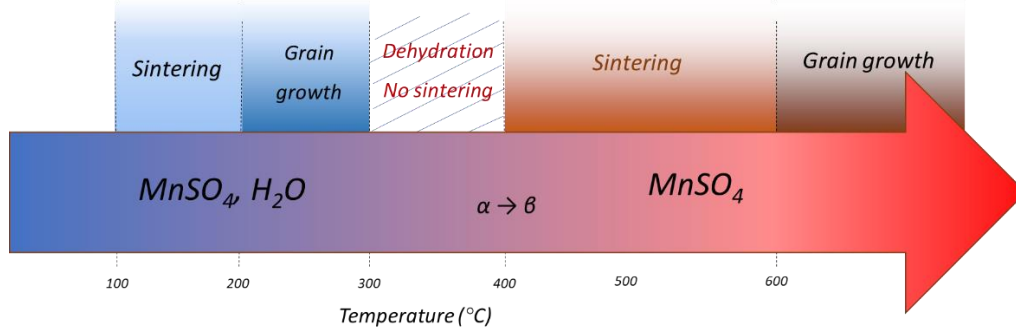


Figure 6: Schéma général du frittage de  $MnSO_4$  et  $MnSO_4 \cdot H_2O$  à différentes températures pour des pressions ajustées

L'exploration des propriétés physiques a révélé de petites anomalies diélectriques difficiles à interpréter, qui nécessiteront une caractérisation plus poussée. Pour tous les échantillons, la mesure diélectrique confirme une fois de plus la grande qualité du frittage avec des pertes diélectriques très limitées dans les céramiques majoritairement nanostructurées. Plus important encore, dans le cas de  $MnSO_4$  et  $Na_2Cu(CO_3)_2$ , les données expérimentales donnent clairement des indices de la présence de couplages magnétoélectriques, mettant en évidence la pertinence des matériaux fragiles en tant que matériaux fonctionnels.

Les carbonates ont été une partie importante de ce travail, et des tentatives ont été menées sur la synthèse d'un nouveau composé contenant de l'ammonium,  $(NH_4)_2Cu(CO_3)_2$  dérivé des deux autres carbonates cités. La synthèse n'a pas donné le résultat attendu, mais un matériau moléculaire a été synthétisé de composition  $(NH_3)_2Cu(COOCH_3)_2$ .

Le présent travail a ensuite démontré la faisabilité de l'accès à de nouvelles propriétés de matériaux dans diverses familles de matériaux et de structures, avec le SPS comme point central. Une approche cristallographique a été développée pour sélectionner des matériaux avec des structures complexes et des propriétés multiferroïques et magnétoélectriques intéressantes. Leur fragilité (stabilité thermique limitée) était le principal enjeu interdisant l'exploration de leurs propriétés électriques puisqu'elles ne pouvaient pas être obtenues sous forme de céramiques denses.

Il a été possible d'utiliser le SPS en utilisant des conditions de fonctionnement inhabituelles, avec des pressions élevées appliquées sur les poudres, pour permettre le frittage à basse température jusqu'à la température de décomposition des phases sélectionnée pour l'étude. Les présents résultats montrent clairement la possibilité pour diverses familles de matériaux d'accéder à des densités élevées même à basse température de frittage ( $< 400$  °C), sans décomposition observable

des phases. Non seulement il était possible de fritter efficacement à basse température, mais il était également possible d'utiliser le SPS au-dessus des températures de décomposition des phases observées dans l'air. De plus, et comme résultat inattendu, il était même possible d'obtenir par traitement SPS la phase anhydre  $\text{Na}_2\text{Cu}(\text{CO}_3)_2$  à partir de son composé hydraté. Cela s'est avéré impossible grâce à un traitement thermique classique. Notamment, les céramiques  $\text{MnSO}_4$  ont été obtenues sous forme nanostructurée bien que la poudre de précurseur ne le soit pas. Avec des temps de frittage très courts, en dessous de 10 min, une densification élevée supérieure à 90% a été obtenue pour toutes les compositions présentées et a permis d'explorer les propriétés physiques. Même s'ils restent pour la plupart à petite échelle, proches des limites de détection des configurations expérimentales, certains indices d'accouplements magnétoélectriques ont été mis en évidence à la fois dans  $\text{Na}_2\text{Cu}(\text{CO}_3)_2$  et  $\text{MnSO}_4$ .

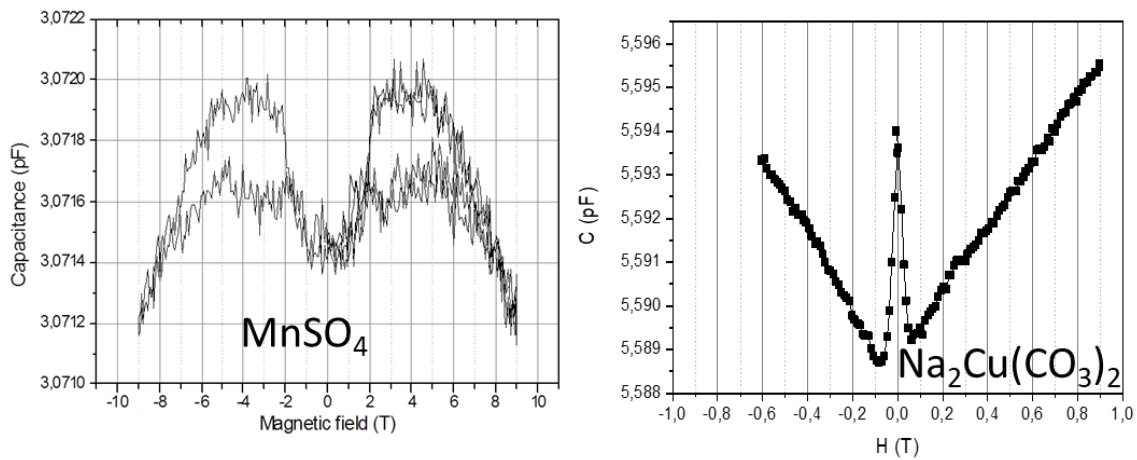


Figure 7: Mesures magneto-capacitives sur céramiques de  $\text{MnSO}_4$  et  $\text{Na}_2\text{Cu}(\text{CO}_3)_2$  à 2 K montrant une dépendance de la capacité en fonction du champ magnétique

Cette phase,  $\text{MnSO}_4$ , représentait la partie principale du travail mené sur le SPS. Les conditions de frittage ont été déterminées par une grande quantité de tentatives expérimentales de frittage et les facteurs d'influence tels que le rôle de l'hydratation et le moment d'application de la pression lors du frittage ont été choisis de manière à maximiser la compacité du matériau à la température de frittage la plus basse de  $400^\circ\text{C}$ . Le rôle possible de la transition de phase a également été discuté. Enfin, la présence d'eau dans la poudre, attirant un éventuel comportement hydrothermal pendant le frittage, a été explorée par une étude comparative du frittage  $\text{MnSO}_4 \cdot \text{H}_2\text{O}$  utilisant à la fois le frittage hydrothermal et le SPS. Des indices de ce mécanisme de type hydrothermal ont été

mis en évidence, bien que ce seul mécanisme semble insuffisant pour décrire totalement les mécanismes de frittage de  $\text{MnSO}_4 \cdot \text{H}_2\text{O}$  dans le SPS. Cependant, le frittage a été prouvé possible à partir de  $100^\circ\text{C}$  pour cette phase en utilisant les deux techniques de frittage (SPS et hydrothermal), pour un temps de palier aussi court que 30 min et une pression appliquée de 350 MPa. C'est le premier exemple de frittage d'une phase purement hydratée.

En tant que perspective intéressante, le frittage d'un matériau moléculaire a également été réalisé. La céramique très dense a été obtenue après un temps de frittage très court (5 min seulement) et sous 600 MPa. C'est le premier exemple de céramique moléculaire, qui ouvre de larges possibilités pour ce type de matériau.

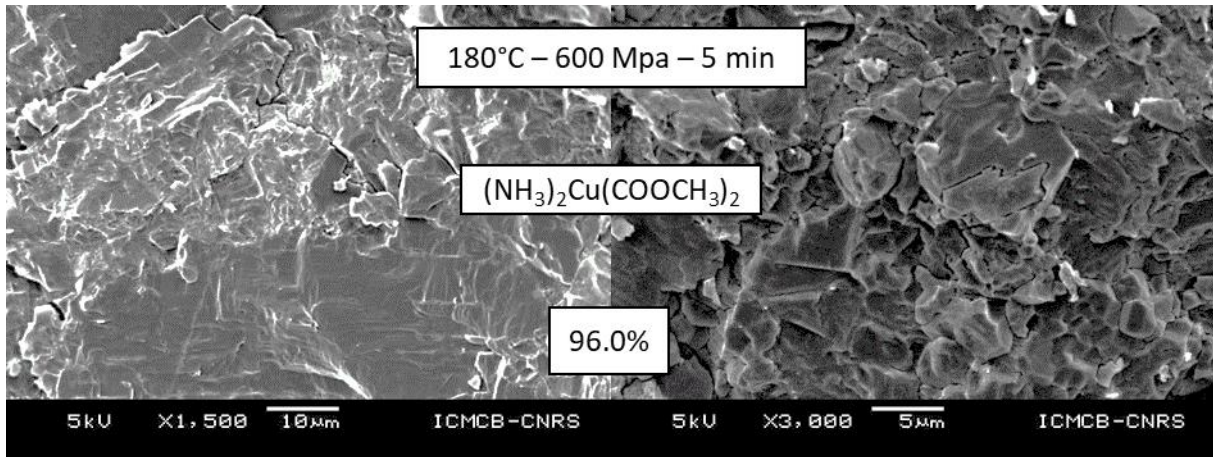


Figure 8: Image MEB de céramique moléculaire obtenue après frittage SPS

# Conclusion

L'un des résultats les plus importants de ce travail est de souligner l'importance d'une approche systémique. Trois aspects principaux ont été traités, qui sont respectivement la chimie des cristaux, la science des matériaux et les propriétés physiques. Les liens forts entre ces trois sciences sont aussi importants que les sciences elles-mêmes et l'exploration de chacune séparément des autres, bien que faisant écho à des traditions disciplinaires profondément enracinées, semble insuffisante pour comprendre des points essentiels concernant les matériaux étudiés. En effet, précisément parce que les propriétés chimiques, structurales, microstructurales et physiques des matériaux sont fortement interdépendantes, les sciences des matériaux et les matériaux sont à leur croisée.

Dans cette approche, deux directions de recherche ont été étudiées séparément, mais couvrent en fait la même approche. Ils concernent tous deux la synthèse et le traitement des matériaux céramiques, permettant la mesure de leurs structures et propriétés ferroïques. La principale différence réside dans le paramètre clé représentant la problématique de chaque étude.

Dans la première partie de ce travail, la synthèse des matériaux TTB à base de  $\text{Ba}_2\text{NdFeNb}_4\text{O}_{15}$  semble d'abord facile à contrôler et l'accent est mis sur l'évolution de la structure cristalline en relation avec les propriétés relaxantes et / ou ferroélectriques.

Trois solutions solides ont été étudiées pour étudier l'influence de l'accommodation du lithium dans  $\text{Ba}_2\text{NdFeNb}_4\text{O}_{15}$ . Des études structurales préliminaires ont indiqué qu'un schéma de substitution, repris par la formulation  $\text{Ba}_2\text{Nd}_{1-x/3}\text{Li}_x\text{FeNb}_4\text{O}_{15}$  (NL), est mieux adapté à cette fin. Lors de l'exploration de leurs propriétés diélectriques, une évolution similaire, d'un crossover relaxeur/ferroélectrique à un état purement relaxeur, a été trouvée dans les trois systèmes. Malheureusement, les affinements de Rietveld sur les représentants les plus significatifs de la solution solide de NL n'ont pas pu révéler les modifications cristallographiques subtiles sous-jacentes de ce système. Néanmoins, le comportement diélectrique observé, qui avait également été mis en évidence dans des études antérieures, apparaît en accord avec les propriétés diélectriques anioniques proposées dans ces matériaux.

Au cours de l'étude précédente, la synthèse répétée du composé  $\text{Ba}_2\text{NdFeNb}_4\text{O}_{15}$  a conduit à l'observation de comportements diélectriques non reproductibles. Une étude méticuleuse des paramètres de synthèse de cette phase a confirmé que son comportement diélectrique intrinsèque est un croisement R / FE. L'identification du rôle crucial du mélange de précurseurs a permis d'obtenir différents échantillons avec un comportement R ou R / FE, mais a également souligné l'accordabilité du comportement diélectrique avec d'autres conditions de synthèse. Enfin, la DRX a révélé des paramètres structuraux assez identiques pour les échantillons R et R / FE, et les résultats préliminaires de l'étude de tomographie par diffraction électronique en précession ont révélé une structure modulée qui évolue avec les propriétés diélectriques. L'étude des pics de satellites a révélé une évolution thermique allant d'un état proportionnel R ou FE à une modulation incommensurable et a confirmé le comportement hystérétique de la transition ferroélectrique. Les affinements préliminaires ont confirmé l'influence de la modulation sur les positions de l'oxygène, et donc la force motrice anionique derrière le comportement diélectrique  $\text{Ba}_2\text{NdFeNb}_4\text{O}_{15}$ . D'autres analyses de données seront nécessaires pour identifier précisément l'origine structurale des propriétés ferroélectriques, mais ces résultats constituent un développement prometteur des études cristallographiques des TTB ferroélectriques.

Dans la deuxième partie cependant, la structure des matériaux étudiés est connue avant l'étude, mais utile pour déterminer leurs propriétés ferroïques potentielles. Le véritable problème réside dans le traitement de ces matériaux afin d'obtenir des échantillons mesurables, car les matériaux sélectionnés ne sont pas suffisamment stables pour subir un frittage conventionnel.

En effet, cette deuxième partie a été consacrée à la prospection de matériaux fragiles (multi) ferroïques et / ou magnétoélectriques par l'utilisation du *Spark Plasma Sintering*. Après une explication des critères cristallographiques permettant la présence de ces propriétés physiques, plusieurs matériaux candidats ont été sélectionnés, afin d'établir une preuve de concept :  $\text{NH}_4\text{FeP}_2\text{O}_7$ ,  $\text{A}_2\text{Cu}(\text{CO}_3)_2$  ( $\text{A} = \text{K}, \text{Na}$ ) et  $\text{MnSO}_4$ . Etant donné que les informations disponibles dans la littérature ne permettent pas l'obtention de de quantité de poudre suffisante pour les études de frittage ultérieures, les carbonates ont nécessité une étape d'optimisation de la méthode de synthèse. Après caractérisation de ces poudres, un frittage à haute pression (jusqu'à 600 MPa), à basse température ( $T \leq 400^\circ \text{C}$ ) a été réalisé et a abouti dans tous les cas à des céramiques très denses, dont les densités relatives dépassent 90%. En plus de son efficacité impressionnante, le

SPS a permis la stabilisation des phases au-delà de leurs températures de décomposition. Deux des matériaux étudiés ont été frittés à partir de précurseurs hydratés, par déshydratation in situ, et l'un d'entre eux,  $\text{Na}_2\text{Cu}(\text{CO}_3)_2$ , qui n'a pas pu être obtenu sous forme de poudre par voie solide a été traité avec succès par SPS en une céramique pure et dense. Grâce à leur frittage réussi, les propriétés diélectriques de tous les matériaux cibles ont été étudiées et ont révélé de très faibles pertes diélectriques, un témoignage supplémentaire de la qualité des céramiques. Des anomalies diélectriques mineures ont été observées dans  $\text{NH}_4\text{FeP}_2\text{O}_7$  et  $\text{Na}_2\text{Cu}(\text{CO}_3)_2$ , tandis que le composé ferromagnétique  $\text{K}_2\text{Cu}(\text{CO}_3)_2$  a montré ce qui pourrait être une transition ferroélectrique et une anomalie diélectrique à la transition antiferromagnétique a été observée dans  $\text{MnSO}_4$ . De plus, la mesure de la dépendance au champ magnétique de la capacité a révélé des signaux significatifs dans  $\text{Na}_2\text{Cu}(\text{CO}_3)_2$  et  $\text{MnSO}_4$ , avec éventuellement une transition induite par le champ magnétique dans ces derniers, et ces observations suggèrent fortement l'existence d'un couplage magnétoélectrique dans les deux matériaux. Cependant, les températures de mise en ordre et les couplages restent faibles, mais l'observation de ces propriétés dans quelques matériaux fragiles est une incitation à s'engager davantage dans leur exploration.

Les mécanismes de frittage impliqués dans le frittage de  $\text{MnSO}_4$  et  $\text{MnSO}_4 \cdot \text{H}_2\text{O}$  ont été spécifiquement étudiés, et présentaient un haut niveau de complexité. La présence d'eau dans la poudre de précurseur et la transition de phase réversible à une phase à haute température se sont révélées cruciales pour le frittage de  $\alpha\text{-MnSO}_4$  par SPS. Une étude comparative du SPS et du frittage hydrothermal a également été réalisée sur  $\text{MnSO}_4 \cdot \text{H}_2\text{O}$  pour identifier les similitudes entre les deux méthodes de frittage. La comparaison a donné quelques indices d'un possible mécanisme de type hydrothermal lors de l'utilisation de SPS à basse température, et a également prouvé que le SPS peut être utilisé pour fritter les matériaux hydratés.

Enfin, un résultat majeur est le granulé pur et très dense obtenu à partir d'un matériau moléculaire,  $(\text{NH}_3)_2\text{Cu}(\text{COOCH}_3)_2$ . Ce résultat inattendu pourrait être une percée, car l'élaboration de la céramique moléculaire est sans précédent et ouvre de nouvelles perspectives en termes de matériaux fonctionnels, car de telles céramiques pourraient être élaborées à partir de matériaux moléculaires fonctionnels par exemple. De telles céramiques pourraient trouver une application, par exemple, dans l'électronique ou le magnétisme, et peuvent également contribuer au développement d'une électronique organique et / ou flexible.

En fin de compte, l'exploration du SPS à basse température a prouvé son efficacité, confirmé l'opportunité potentielle de matériaux ferroïques fragiles et permis la découverte de céramiques moléculaires, tous ces résultats ayant eux-mêmes des perspectives significatives. Une perspective supplémentaire de cette recherche est le développement de matériaux fonctionnels durables, éventuellement à des fins de substitution ou pour des applications spécifiques. En effet, les matériaux fragiles, en raison de leur stabilité thermique limitée, sont nécessairement synthétisés et traités à basse température et dans des conditions de synthèse douces. Cette situation limitera également leur empreinte énergétique et environnementale mais pourrait également favoriser leur intégration dans des dispositifs flexibles par exemple car les conditions de traitement des matériaux fonctionnels traditionnels tels que les oxydes peuvent ne pas être compatibles avec les substrats demandés pour ces dispositifs.

L'étude de la chimie des cristaux de TTB ferroélectriques a permis d'approfondir l'étude de la céramique  $\text{Ba}_2\text{NdFeNb}_4\text{O}_{15}$ , qui présente un comportement crossover relaxeur / ferroélectrique ou un comportement purement relaxeur, ouvrant la voie à une future étape consacrée à l'étude de la chimie des mécanismes microscopiques en jeu. La preuve de concept pour l'utilisation de SPS à de très basses températures a été obtenue, ainsi que la preuve de concept pour l'utilisation du SPS comme outil de prospection dans le domaine des matériaux ferroïques fragiles. Le dernier chapitre qui présente la toute première céramique moléculaire est l'exemple parfait des larges possibilités offertes par ce travail exploratoire.

Enfin, le travail présenté dans ce manuscrit est une occasion d'éclairer la fertilité des interfaces entre la chimie des matériaux, la physique des matériaux et l'ingénierie des matériaux, en particulier pour les recherches prospectives, grâce aux cultures complémentaires des communautés correspondantes.

## **Titre : Cristallochimie prospective : relaxeurs, ferroïques et SPS basse température**

**Résumé :** Les travaux présents ici portent sur l'étude et la prospection de matériaux ferroïques. Cette étude consiste en une approche revêtant plusieurs aspects que sont la chimie du solide, la physique du solide et la science des matériaux. Deux parties sont développées, avec deux approches différentes. La première se concentre sur les liens entre composition/structure/propriétés dans des matériaux de la famille des TTB dérivés de  $Ba_2NdFeNb_4O_{15}$  à travers l'étude de solutions solides à base de Li et l'étude de l'impact des différents paramètres de synthèse sur la nature de l'anomalie diélectrique mesurées sur pastilles densifiées. La mise en évidence de modulation structurale dans cette famille de matériaux semble être en lien direct avec l'observation des variations de propriétés diélectriques. L'utilisation de diffraction électronique notamment permet la mise en évidence de ces modulations structurales et leur évolution en température. Dans une seconde partie, l'approche consiste à utiliser le Spark Plasma Sintering (SPS) comme technique de densification pour des matériaux dits "fragiles" mais aussi d'explorer des propriétés diélectriques jusqu'alors inaccessibles, sur matériaux massifs. Le développement de la technique SPS à basse température permet ainsi non seulement de densifier à basse température des matériaux fragiles, mais aussi d'obtenir des phases inaccessibles dans des conditions de températures similaires par traitement thermique conventionnel. De même, l'obtention de céramique moléculaire de très haute densité a pu être réalisée, malgré des températures de décomposition extrêmement faible (100 °C).

**Mots clés :** Frittage ; Spark Plasma Sintering ; Électrocéramique ; Structure module ; Bronze quadratique de tungstène

---

## **Title : Prospective crystal-chemistry : relaxors, ferroics and low temperature SPS**

**Abstract :** The present work focuses on the prospection and understanding study of ferroic materials. It consists in a multiple aspect approach, including materials chemistry, materials physics and materials processing. Two parts compose this work, with two different approaches. The first one focuses on the links between composition, structure and properties in materials belonging to the TTB family, more specifically derived from  $Ba_2NdFeNb_4O_{15}$ , through the exploration of Li containing solid solutions, and the impact of synthesis parameters on measured dielectric anomalies on dense samples. The observation of structural modulation in these materials seems to be closely related to the observation of dielectric anomalies variations. Using electron diffraction techniques allowed the evidence of such anomalies and the following of their thermal evolution. In a second part, the approach consists in using Spark Plasma Sintering (SPS) as a densification technique for so called "fragile" materials but also explore dielectric properties impossible to experimentally measure thus far. Developing low temperature SPS technique not only allows to densify ceramics at low temperatures fragile materials, but also to obtain inaccessible phases in similar temperature conditions using conventional thermal treatments. Moreover, sintering of molecular ceramic at very high density was possible, even if its decomposition temperature is extremely low (100 °C).

**Keywords :** Sintering ; Spark Plasma Sintering ; Electroceramic ; Modulated structure, Tetragonal Tungsten Bronze